ISSN 1811-1165 (Print)
ISSN 2413-2179 (Online)

EURASIAN PHYSICAL TECHNICAL JOURNAL

VOLUME 23, NO. 1(55), 2026

phtj.buketov.edu.kz

EURASIAN PHYSICAL TECHNICAL JOURNAL

p - ISSN 1811-1165
e - ISSN 2413-2179

Volume 23, No. 1(55), 2026

Journal Founder:

NON-PROFIT LIMITED COMPANY
«KARAGANDA NATIONAL RESEARCH
UNIVERSITY NAMED AFTER ACADEMICIAN
YE.A. BUKETOV»

https://phtj.buketov.edu.kz

www.facebook.com/groups/1103109540750967

Registration Certificate No.4382-Zh,
November 7, 2003.

Re-registration Certificate No.KZ32VPY00135738,
November 28, 2025 issued by the Information
Committee of the Ministry of Culture and Information
of the Republic of Kazakhstan

Contact information:

Editorial board of EAPhTJ
(Build. 2, room 216)
Karaganda Buketov University
Universitetskaya Str.28, Karaganda,
Kazakhstan, 100024
Subscription index: 75240

Tel: +7(7212) 77-04-03
Fax: +7(7212) 35-63-98
E-mail: ephtj@mail.ru,
ephtj2021@gmail.com

Signed to print 19.03.2026
Format 60x84 1/8. Offset paper.
Volume 20.13 p.sh. Circulation 300 copies.
Order No. 30.

Printed in the Publishing House of
Karaganda National Research University
named after academician Ye.A. Buketov

Tel. +7 (7212) 35-63-16.
E-mail: printed@karnu-buketov.edu.kz

EDITOR-IN-CHIEF

Sakipova S.E., Buketov Karaganda National Research University, Karaganda, Kazakhstan

ISSUE EDITOR

Kozlovskiy A.L., L.N. Gumilyov Eurasian National University, Astana, Kazakhstan

EDITORIAL BOARD

Aringazin A.K., L.N. Gumilyov Eurasian National University, Astana, Kazakhstan

Dzhumanov S., Institute of Nuclear Physics, Uzbekistan Academy of Sciences, Tashkent, Uzbekistan

Hançerlioğullari A., Kastamonu Üniversitesi, Kastamonu, Turkey

Ibrayev N.Kh., Institute of Molecular Nanophotonics, Buketov Karaganda National Research University, Karaganda, Kazakhstan

Jakovics A., Institute of Numerical Modelling, University of Latvia, Riga, Latvia

Kucherenko M.G., Director of the Laser and Information Biophysics Centre, Orenburg State University, Orenburg, Russia

Kuritnyk I.P., Department of Electronics and Automation, High school in Oswiecim, Poland

Kushpil S., Heavy Ion Group, Nuclear Physics Institute of the Czech Academy of Science, Řež near Prague, Czech Republic

Miau J.J., Department of Aeronautics and Astronautics, National Cheng Kung University, Tainan, Taiwan

Miroshnichenko A.S., Department of Physics and Astronomy, University of North Carolina at Greensboro, North Carolina, USA

Saulebekov A.O., Kazakhstan Branch of Lomonosov Moscow State University, Astana, Kazakhstan

Senyut V.T., Joint Institute of Mechanical Engineering of National Academy of Sciences of Belarus, Minsk, Belarus

Shrager E.R., National Research Tomsk State University, Tomsk, Russia

Stoev M., South-West University «Neofit Rilski», Blagoevgrad, Bulgaria

Suprun T., Institute of Engineering Thermophysics of NASU, Kyiv, Ukraine

Trubitsyn A.A., Ryazan State Radio Engineering University, Ryazan, Russia

Zeinidenov A.K., Buketov Karaganda National Research University, Karaganda, Kazakhstan

TECHNICAL EDITOR

Kambarova Zh.T., Buketov Karaganda National Research University, Karaganda, Kazakhstan

© Buketov Karaganda National Research University, 2026

Eurasian Physical Technical Journal, 2026, Vol. 23, No. 1(55)

CONTENTS

PHYSICS AND ASTRONOMY

.

Dear authors and readers!
Dear colleagues!

In the preface, we traditionally inform the authors and readers about the most important achievements of the Eurasian Physical Technical Journal at the moment.

Thanks to our authors and the qualified work of the editorial board members, the journal continues to be indexed in the Scopus database in all four scientific areas with a max percentile 26% on the Engineering. These indicators were achieved thanks to the objective and highly qualified examination of materials by our reviewers, which guarantees the quality of published articles.

Website statistics show that the review period for articles from their receipt on the website to the publication date is up to six months. This fact is due to the relatively large number of applications received, and despite the fact that 63% of articles were rejected, a queue for consideration is forming. Therefore, authors are advised to upload articles in accordance with the 2006 submission and publication schedule, which is available on the website's home page. The journal's website also displays the number of views of abstracts or the entire article. Some articles receive quite a few views; the highest number of views per article in a year was 1,417. The Cite Score Tracker, which is directly related to the number of citations an article receives, has shown positive dynamics in recent months at 1.3-1.4. Each author can contribute to improving the dynamics of this important citation indicator.

Let's move on to the contents of this issue, which features 17 articles by scientists co-authored with colleagues from Kazakhstan, Uzbekistan, Russia, Iraq, the UK, Mongolia, and elsewhere.

The "Materials Science" section presents new, original research results on the properties of materials exposed to various external factors. These results make it possible to obtain "high-quality coatings with improved wear and corrosion resistance" and determine "the influence of residual stresses on the microstructure and mechanical properties of metal coatings obtained by electrolytic friction," confirming "the excellent thermal stability and high suitability of silicon heterojunction solar cells for space energy applications."

The "Energy" section features articles on a wide range of current energy issues. The authors used modern software to model the properties of a free-piston Stirling engine in an isothermal approximation; assess the reliability and performance of a thermal power plant; analyze the atomization and combustion dynamics of biodiesel and fossil diesel fuel droplets in turbulent gas flows; and examine the thermal stability of a two-component gravel structure at high temperatures. Also relevant are the results of an experimental study of the thermal regime of a small-scale biogas plant using solar energy.

The "Engineering Developments" section presents the results of research aimed at improving the efficiency of technical devices and technologies. For example, the technology of "electrohydraulic drilling in hard soils" is discussed. In three articles authors based on modeling the flow of a highly viscous viscoelastic fluid in a pipe, develop a method for reducing the pipe's hydraulic resistance by suppressing small-scale vortex structures; propose flow motion in an annular space to improve heat transfer efficiency and optimize heat exchanger design in the oil and gas industry; and analyze pressure and energy changes within a hydraulic pulse chamber to predict the dynamic behavior of the system and the operational stability of hydraulic pulse systems.

The Physics and Astronomy section presents the results of research into physical characteristics ranging from micro-nanoscopic processes to macroscopic processes in the space. The first article examines "the half-lives of alpha decay of heavy and superheavy nuclei with atomic numbers greater than 82 are systematically investigated using three quantum tunneling approaches." Next three articles in this section are devoted to study of the astrophysical signals and macroscopic phenomena. Observation of a massive star-forming region revealed two hot cores caused by the presence of a chemically rich environment for the early stage of star formation of massive stars; the study of phonon dynamics in the solid crust of neutron stars and their relationship to large-scale structural instabilities allowed for the development of models of the dynamics of the neutron star crust; molecular emission analysis revealed a compact and dense methanol component located at the peak of the continuum, suggesting that a massive protostar is actively accreting into a compact disk-shell system surrounded by a hot core. The latest paper investigates cooling methods for photovoltaic panels using copper nanoparticles and shows that for monocrystalline panels, the best increase in power output is achieved using nanofluid at a certain concentration.

Unfortunately, in real life, bright and joyful events alternate with dark ones. So, at the beginning of the year, we experienced a very sad event. On February 22, 2026, Zeynulla Zhanabayevich Zhanabayev, Doctor of Physical and Mathematical Sciences and Professor of the al-Farabi Kazakh National University, passed away suddenly. Zeynulla Zhanabayevich was the initiator and co-founder of the Eurasian Physical Technical Journal and a long-standing member of the editorial board since 2004. He always played an active role in the preparation of successive issues, providing valuable advice and recommendations, and ensuring the quality of the published articles.

Professor Z. Zh. Zhanabaev combined his impeccable teaching with active research, as evidenced by his monographs and international publications in highly regarded journals. He developed the foundations of a unique structural theory of hydrodynamic turbulence. Creating a new scientific field in Kazakhstan in the field of nonlinear information phenomena and semiconductor optoelectronics, Professor Zhanabaev was the first to formulate information-entropy criteria for the self-organization of open systems in nonlinear physics and astrophysics. Recently, his research has focused on semiconductor nanostructures and gas sensors. He led the ongoing grant-funded research project "Coherence and Saturation of a Laser Sensor Signal," which explores the fundamental and applied aspects of laser measurement systems.

In 2023, the Z. Zhanabayev Research Center for Science Data in Astrophysics was established at Al-Farabi Kazakh National University. Its activities are aimed at developing interdisciplinary research in astrophysics, nonlinear physics, and data analysis, as well as training highly qualified specialists for the next generation. Under his supervision, 9 Candidate of Sciences dissertations, 3 doctoral dissertations, and 7 internationally recognized PhD dissertations were successfully defended.

Professor Z. Zhanabaev's creative achievements and dedication to science, invaluable contribution to the training of highly qualified specialists, and outstanding achievements in the development of nonlinear physics and astrophysics have been recognized with the Al-Farabi Grand Gold Medal.

The bright memory about Zeynulla Zhanabaevich Zhanabaev as outstanding scientist, kind mentor, and wise academic advisor will forever remain in the hearts of all who had the privilege of knowing him.

The main legacy of this outstanding scientist is the continued development of his ideas and principles in the works of his students, whose articles are published in almost every issue of our journal, including this one.

We hope the presented articles will not only be interesting but also useful in preparing new publications for researchers, teachers, graduate students, and postgraduates.

Please remember to cite the articles published in our journal.

And we look forward to seeing you among our readers and authors in the future.

With respect and hope for fruitful collaboration,
Editor-in-Chief, Professor Sakipova S.E.
March, 2026

EURASIAN PHYSICAL TECHNICAL JOURNAL

2026, Volume 23, No. 1 (55)

https://doi.org/10.31489/2026N1/6-14

Received: 16/02/2025 Revised: 14/01/2026 Accepted: 19/03/2026

Research Article

UDC 621.793: 669.14

ELECTRIC ARC SPRAYING WITH COPPER-PLATED WIRE SV08G2S ON GRADE 45 STEEL: FORMATION OF THE STRUCTURE AND PROPERTIES OF PROTECTIVE COATINGS

Sagdoldina Zh.B. [1,2], Leonidova A.B.*[2], Zhassulan A.Zh.[2],
Shynarbek A.B.[2], Ibragimov N.K.[2], Mukhametov Y.M.[2]

[1] Sarsen Amanzholov East Kazakhstan University, Ust-Kamenogorsk, Kazakhstan

[2] Shakarim University, Semey, Kazakhstan

*Corresponding author: aiymleonidova1994@gmail.com

Abstract. *The paper investigates the influence of electric arc spraying process parameters using copper-plated Sv08G2S wire on the structure and performance characteristics of coatings formed on grade 45 steel. Spraying was performed at varying voltages and wire feed speeds, followed by a comprehensive analysis of the structure and properties of the resulting coatings. The best coating characteristics were achieved at 40 V, 280 A and a wire feed speed of 100 mm/s: the resulting coating exhibited a relatively dense and uniform structure, high microhardness (277.6 HV), minimal mass loss due to abrasive wear (0.018 g), and enhanced corrosion resistance. Electrochemical tests in a 3.5 wt.% NaCl solution revealed a positive shift of the corrosion potential to −0.318 V (vs. Ag/AgCl) and a low corrosion current density of* 4.61×10^{-5} *A/cm², corresponding to a corrosion rate of 0.54 mm/year. It is shown that voltage is one of the key parameters in supersonic arc metallization, governing arc stability, spray uniformity, and coating quality, whereas increasing the current and wire feed speed resulted in a thicker sprayed layer but promoted pore formation and reduced structural homogeneity. Overall, optimization of spraying parameters enables the formation of high-quality coatings with improved wear and corrosion resistance, thereby increasing the service life of steel components in practical applications.*

Keywords: electric arc spraying, copper-plated wire, grade 45 steel, microhardness, corrosion resistance, wear resistance.

1. Introduction

Grade 45 steel is one of the most widely used carbon structural steels in mechanical engineering, power engineering, and related industries for the manufacture of components due to its combination of strength, affordability, and manufacturability [1]. During operation, under conditions of friction and abrasive action, parts made of grade 45 steel (such as shafts and gears in thermal power plant equipment) undergo accelerated wear, significantly reducing their service life. To enhance the durability and reliability of such components, surface modification methods must be applied to improve their performance characteristics. Among existing technologies, thermal spraying (TS) is of particular interest as it allows the formation of functional coatings without significant thermal deformation of the substrate or changes in the structure of the base material [2, 3]. A key advantage of this technology is the wide selection of usable materials, which ensures versatility in addressing tasks related to improving wear and corrosion resistance. The main types of thermal spraying include flame, detonation, plasma, cold gas-dynamic, electric arc spraying, and other methods [4–12]. Among these, electric arc spraying (EAS) has attracted particular attention from researchers due to its technological simplicity, low cost, and high productivity. According to technical and economic estimates, coatings obtained by this method are 3–10 times cheaper than similar coatings applied by other thermal spray methods, while maintaining comparable performance characteristics [10–14]. The efficiency of electric arc spraying is largely determined by process parameters, including the material feed rate, current, voltage, air pressure, and spraying distance. These factors directly influence the coating's structure, porosity, microhardness, and adhesion to the substrate [11, 15–18]. In recent years, particular attention has been paid to optimizing spraying conditions, which has significantly improved the wear and corrosion resistance of coatings [18–23].

Along with process parameters, the choice of spray material is a key factor. Among metallic coating materials, copper and its alloys are of particular interest due to their high ductility and excellent thermal and electrical conductivity. When using copper-plated wire, the copper layer facilitates stable arc formation, improves the thermal regime of the process, and ensures more uniform coating deposition. In addition, copper-plated coatings demonstrate high corrosion resistance and can enhance the mechanical properties of the surface. Thus, pseudo-alloys of the Cu–Fe system obtained by arc spraying form dense coatings with low porosity, a microhardness of approximately 2,1 ± 0,7 GPa, and high resistance in aggressive environments, including a 3% NaCl solution [24]. The use of copper-plated wire in arc spraying combines technological simplicity and cost-effectiveness, ensuring the formation of coatings with a range of protective and functional properties.

Thus, the potential of copper-based coatings is confirmed by modern research on composites based on them, which demonstrate improved wear resistance and corrosion protection. The purpose of this study is to identify the formation patterns of copper-plated Sv08G2S wire coatings on the surface of grade 45 steel, with the aim of improving its performance.

2. Materials and Research Methods

In this study, grade 45 steel and copper-plated Sv08G2S wire were used. Their chemical composition (in wt.%) is shown in Table 1 according to GOST 1050–2013. Electric arc spraying was carried out using a Metalcoat system (Figure 1) comprising an Arc Spray Torch (model 100AD) and a power source with control console (model VCH 400 AIR and DC), produced by Metalcoat. The process parameters for arc spraying are given in Table 2. For the experiment, a round disk specimen (66 mm in diameter and 5 mm thick) was prepared and subsequently divided into four equal sectors. Three of these sectors were used for coating deposition and subsequent analyses. Prior to coating, each specimen's surface was ground with 120-grit abrasive paper and then sandblasted, resulting in an initial surface roughness of 0,94 ± 0,12 µm.

Table 1. Chemical composition of materials (wt.%)

Material	C	Si	Mn	S	P	Ni	Cr	Cu
Steel 45	0,42–0,50	0,17–0,37	0,5–0,8	≤0,035	≤0,03	≤0,3	≤0,25	≤0,25
Sv08G2S	0,05–0,11	0,70–0,95	1,8–2,1	≤0,025	≤0,03	≤0,25	≤0,20	≤0,25

After spraying the copper-plated wire onto the grade 45 steel surface, a comprehensive study of the coating's structure and properties was conducted. Coating morphology was examined using a JSM-6390LV scanning electron microscope (JEOL, Tokyo, Japan). To study the coating's structure and porosity, a cross-section of a coated sample was prepared by grinding with abrasive paper up to 2500 grit, followed by polishing on felt wheels using diamond pastes with particle sizes of 0,3 µm and 0,1 µm. Coating porosity was then assessed by analyzing SEM cross-sectional images using ImageJ software (version 1.54d). Surface roughness measurements were performed using an Anytester HY2300 profilometer (Hefei, China). Roughness values (Ra) were determined as the average of 10 measurements taken at different points on the surface. Coating microhardness was measured using an HLV-1DT Vickers microhardness tester with a 1 N indenter load and a dwell time of 10 s. Abrasive wear tests were conducted in accordance with GOST 23.208–79. Electro corundum abrasive (grain size 16-P as per GOST 3647–80) with a relative moisture content of no more than 0.15% was used. The roller rotation frequency was 60 ± 2 min^{-1}, and the sample load was 44,1 ± 0,25 N. According to GOST 23.208–79, since the test material's microhardness did not exceed 400 HV, the number of revolutions was set to 600. Upon completion of the tests, the samples were blown with compressed air, wiped with alcohol, dried, and weighed on an analytical balance with an accuracy of 0.001 g.

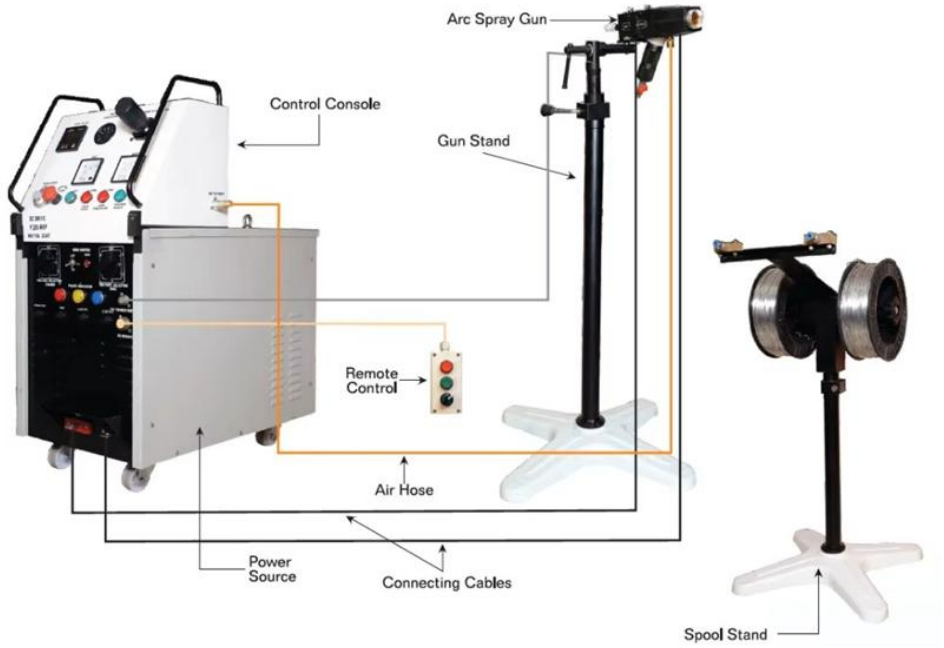

Fig.1. Metalcoat electric arc spraying system.

Table 2. Parameters of the electric arc spraying process.

Sample	U (V)	Wire feed speed (mm/s)	I (A)	Air pressure (MPa)	Distance (mm)	Spraying time (s)
No. 1	30	150	350	0.4	150	5
No. 2	40	100	280	0.4	150	5
No. 3	20	120	300	0.4	150	5

Corrosion resistance was assessed by potentiodynamic polarization using a CS300M potentiostat–galvanostat (Corrtest Instruments, Wuhan, China) with a CS936 flat corrosion cell in a standard three-electrode setup. The working electrode was a coated or uncoated sample with an exposed area of 1 cm². A saturated Ag/AgCl electrode served as the reference and a platinum mesh as the counter-electrode. Tests were carried out in a 3,5 wt% NaCl solution at 25 °C (room temperature). Before polarization, the open-circuit potential was stabilized for 30 min. The corrosion test was performed according to ASTM G5–13.

3. Results and Discussion

Figure 2 shows cross-sectional images of the coatings. As shown in Figure 2 (a–c), the coating thickness varies depending on the process parameters (Table 3). The coating on sample No. 1 has a significant thickness of 778,74 ± 9,26 μm and shows increased layer waviness along the edges. This effect is due to the combination of high current (350 A) and high wire feed speed (150 mm/s), which accelerate the particles and increase the material flow rate, resulting in more material being deposited in a short time. Sample No. 2 exhibited the most uniform structure, with a consistently distributed coating and a thickness of 604,04 ± 15,94 μm. The coating–substrate interface in sample 2 was clearly defined and even. Sample No. 3 had the smallest coating thickness, 326,70 ± 36,03 μm.

The moderate wire feed speed (120 mm/s) combined with the low voltage (20 V) led to incomplete atomization of the material, causing some of the wire to be wasted and preventing proper coating formation on the sample surface. Coating No. 1 is characterized by a low porosity (1.65%) but a relatively large average pore size of 0,863 ± 0,347 μm (Table 3). This is due to the intense deposition of molten particles at high current and high wire feed speed. The resulting jet turbulence and incomplete overlap of individual splat zones contribute to the formation of isolated large pores.

For sample No. 2, the combination of high voltage (40 V) and low wire feed speed produced a large number of small, closed pores. This explains its higher overall porosity (2,575%), with an average pore size of

0,325 ± 0,535 µm. A higher voltage increases the energy transferred to the particles and prolongs their time in a molten state in the spray plume.

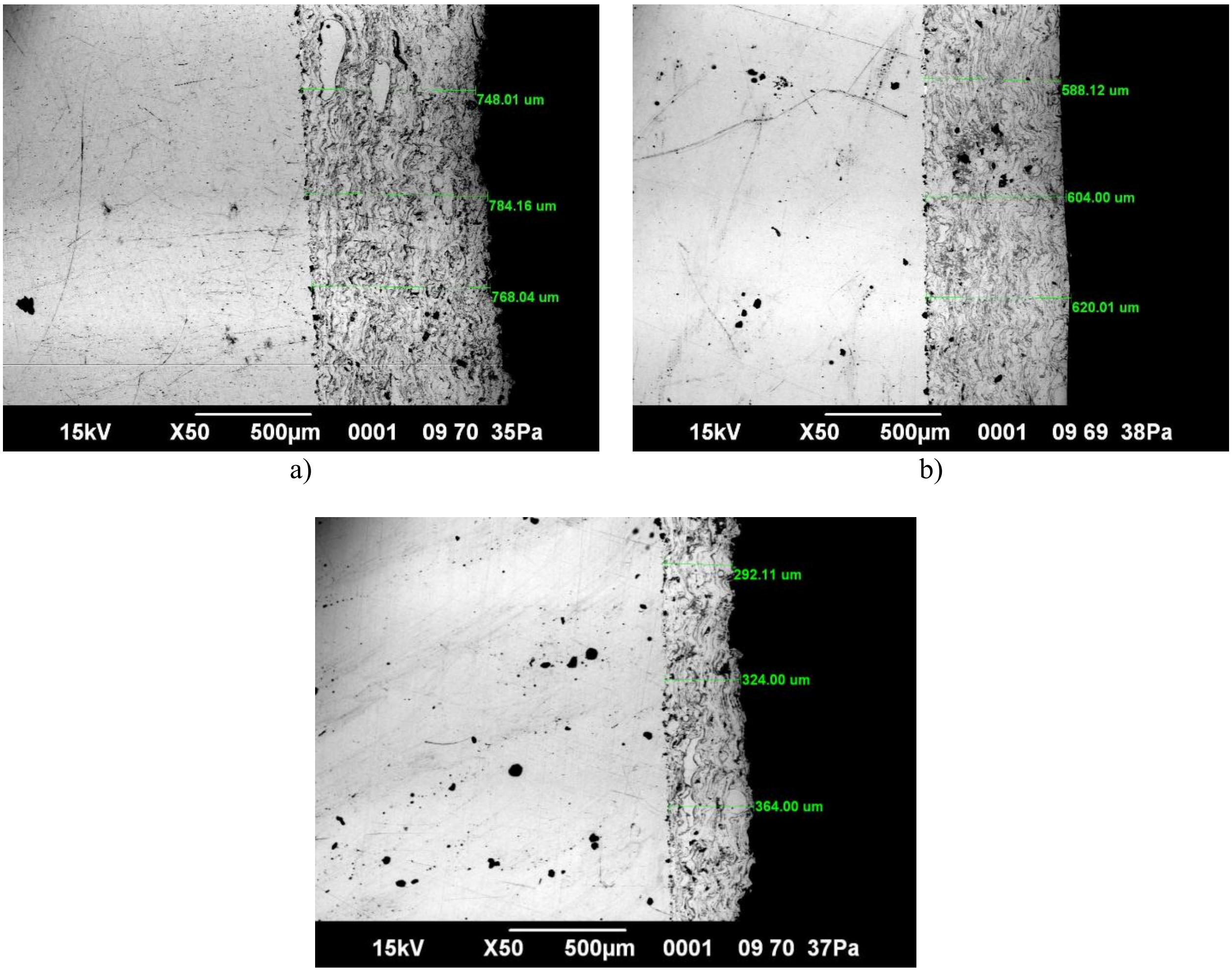

a) b)

c)

Fig.2. Cross-sectional images of coatings: (a) sample No. 1; (b) sample No. 2; (c) sample No. 3.

Table 3. Coating characteristics.

Sample	Coating thickness (µm)	Average pore size (µm)	Porosity (%)	Roughness Ra (µm)
No. 1	778,74 ± 9,26	0,863 ± 0,347	1,165	11,48 ± 2,01
No. 2	604,04 ± 15,94	0,325 ± 0,535	2,575	7,70 ± 1,41
No. 3	326,70 ± 36,03	0,146 ± 0,264	0,953	5,28 ± 0,68

This raises the likelihood of chemical interaction with oxygen, leading to the formation of oxides and gaseous products. These oxides and gases become incorporated into the molten phase or are released during solidification, remaining as closed or semi-open pores within the coating. Sample No. 3 is characterized by the lowest porosity (0,953%) and the smallest average pore size, 0,146 ± 0,264 µm. Reducing the particle dispersion energy lowers the likelihood of air entrapment and defect formation, resulting in only very small pores. The low voltage (20 V) decreases the degree of particle melting and the residence time of particles in the arc, which minimizes oxidation and gas inclusion formation; as a result, the overall porosity of the coating is minimal. Similar correlations between spraying parameters and coating porosity have been reported in the literature [24-26].

Table 3 also presents the surface roughness (Ra) values for the samples. After coating application, the roughness increased significantly: for sample No. 1, Ra = 11,48 ± 2,01 µm; for sample No. 2, Ra = 7,70 ± 1,41 µm; and for sample No. 3, Ra = 5,28 ± 0,68 µm. Sample No. 1 had the highest roughness, while sample No. 3 had the lowest, indicating that the process parameters significantly influence the formation of the surface microrelief. Voltage plays a key role in supersonic arc spraying, as it affects arc stability and intensity. At an optimal voltage, the arc remains stable, facilitating uniform metal spraying and the formation of a high-quality coating. If the voltage is too low, the arc can become unstable and intermittent, leading to an uneven coating [12–15]. Surface roughness and coating porosity are also key factors in wear mechanisms and can influence the development of abrasive wear. The abrasive wear test results are presented in Table 4. Sample No. 3 showed the greatest mass loss, indicating the lowest wear resistance of the coating produced under those spraying conditions. This is possibly due to the highly porous structure of that coating. During abrasive wear, the pores can facilitate accelerated material removal, leading to greater mass loss. In contrast, the minimal mass loss observed for sample No. 2 (0,018 g) demonstrates the effectiveness of the chosen spraying parameters in ensuring high wear resistance of the coating.

Table 4. Results of coating abrasive wear testing.

Sample	Mass before (g)	Mass after (g)	Mass loss (g)
No. 1	28,555	28,530	0,025
No. 2	31,556	31,538	0,18
No. 3	24,972	24,936	0,036

The microhardness measurements of the samples are shown in Figure 3. These average values (with corresponding errors) indicate a substantial increase in surface microhardness compared to the original grade 45 steel. The coating microhardness exceeds that of the uncoated material (grade 45 steel, ~190 HV). In particular, sample No. 1 had a microhardness of 242,87 ± 10,89 HV; sample No. 2, 277.62 ± 4,67 HV; and sample No. 3, 272.81 ± 10,52 HV. These data demonstrate an improvement in the surface's strength characteristics after applying the coatings.

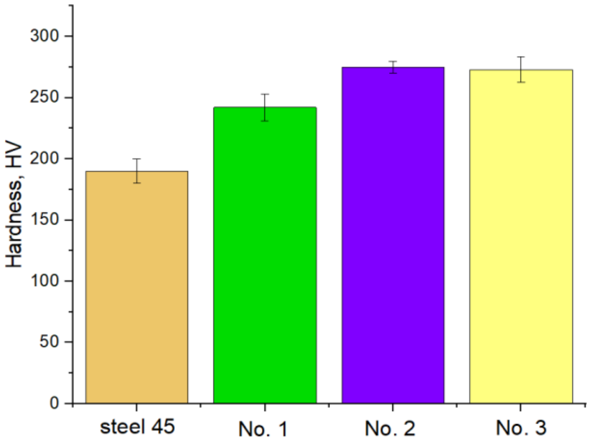

Fig. 3. Microhardness values of the samples.

The increased microhardness of the coatings (relative to the original steel) can be attributed to specific features of the electric arc metallization process. Specifically, when molten metal particles impact the substrate surface, they are rapidly cooled by the cold compressed air jet, causing nearly instantaneous solidification and the formation of a structure with higher microhardness [27]. In sample No. 1, the high current (350 A) led to significant heat input in the spray zone, potentially causing particle overheating, burnout of alloying elements, and intense oxidation of the molten surface. The increased wire feed speed (150 mm/s) reduced the specific energy per unit mass of metal, limiting the extent of uniform melting. The combination of these factors resulted in a coating with partially unmelted and overheated particles, yielding a relatively low microhardness of 242,87 ± 10,89 HV for sample No. 1.

Sample No. 2 exhibited an optimal balance of voltage (40 V) and current (280 A) at a moderate wire feed speed (100 mm/s). As a result, the specific heating energy was sufficient for complete particle melting, leading to the formation of a dense coating structure with the maximum microhardness (277,62 ± 4,67 HV) among the samples. Sample No. 3 was characterized by minimal heat input, which affected the morphology of the resulting coating. In its structure, dense inclusions visually resembling unmelted material were observed (Figure 2c). These inclusions were uniformly distributed across the cross-section and reduced the overall porosity. As a result of these structural features, sample No. 3 still demonstrated a high microhardness of 272,81 ± 10,52 HV. It can be seen that the balance between the applied arc energy, wire feed speed, and cooling conditions largely determines the coating microhardness. Additionally, factors such as the degree of particle melting, the likelihood of particle overheating and oxidation, and the coating's porosity significantly influence the final microhardness.

Figure 4 shows the polarization curves of grade 45 steel samples in a 3.5% NaCl solution. The uncoated steel sample exhibited a more negative corrosion potential and a higher corrosion current density, indicating low resistance to the chloride environment. After applying the copper-plated wire arc spray coating, a positive shift in corrosion potential and a decrease in current density were observed. This indicates a reduction in the steel's thermodynamic susceptibility to corrosion and a slowing of the electrochemical processes.

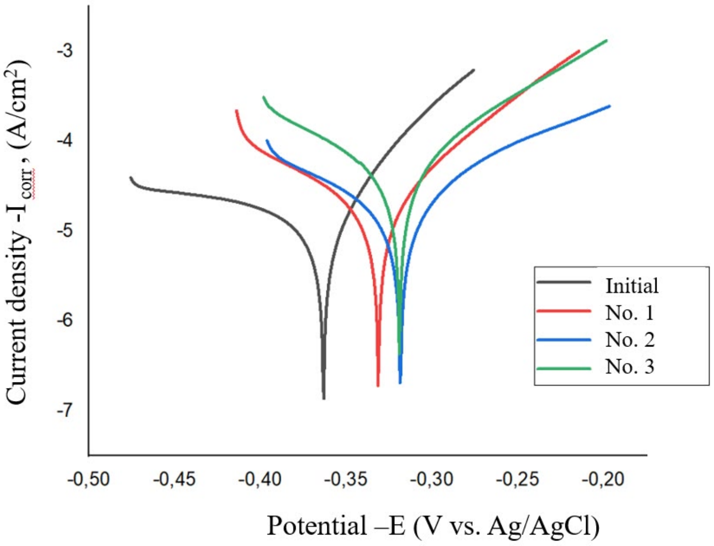

Fig. 4. Potentiodynamic polarization curves of grade 45 steel samples in 3.5% NaCl solution

The most positive shift in corrosion potential and the lowest corrosion current density was observed for sample No. 2, which was obtained with the following parameters: arc air pressure 0,4 MPa, air pressure 0,2 MPa, 40 V, and 280 A. This implies the formation of a denser, less porous coating structure, providing the best corrosion protection. Therefore, the spraying parameters used for sample No. 2 can be considered optimal for producing coatings with enhanced corrosion resistance. The obtained results are consistent with previous studies of arc spray coatings on carbon steels. In particular, the coating thickness (604 ± 15.9 μm) and microhardness (277.6 ± 4.7 HV) observed under optimal spraying conditions (40 V, 280 A, wire feed 100 mm/s) are comparable to the values reported by other authors [28-30]. Moreover, similar to previous studies, the use of wire with this coating resulted in a coating with low porosity, improved wear resistance, and high corrosion resistance in a 3.5% NaCl solution. These comparisons confirm that the selected process parameters are effective in improving the performance and durability of components made of grade 45 steel.

4. Conclusions

This research broadens the potential practical applications of electric arc spraying with copper-plated Sv08G2S wire on grade 45 steel under various spraying conditions.

Process parameters significantly affect the formation of the coating's structure and properties, including its thickness, porosity, surface roughness, microhardness, wear resistance, and corrosion behavior.

Optimal coating characteristics were obtained at 40 V, 280 A and a wire feed rate of 100 mm/s (sample No. 2). Under these conditions, the average coating thickness was 604 ± 15,9 μm, the maximum microhardness was 277,6 ± 4,7 HV, the mass loss due to abrasive wear was minimal (0,018 g), and the coating exhibited high corrosion resistance in a 3,5% NaCl solution.

The coating thickness across the tested modes varied from 327 μm to 779 μm, depending on the spraying parameters. Increasing the current and wire feed speed increased the coating thickness, but also led to larger pores and reduced structural homogeneity. Overall, the results confirm that electric arc spraying with copper-plated wire is an accessible and effective method for improving the performance characteristics and durability of grade 45 steel components in mechanical engineering and related applications.

Conflict of interest statement. The authors declare that the re-search was conducted in the absence of any commercial or financial relationships that could be construed as a potential conflict of interest.

CRediT author statement.
Leonidova A.B.: conceptualization, methodology; **Shynarbek A.B.**: investigation; **Zhassulan A.Zh.**: data curation, visualization; **Ibragimov N.K.**: resources; validation; **Mukhametov Y.M.**: formal analysis; **Leonidova A.B.**: writing-original draft; **Sagdoldina Zh.B.**: writing-review and editing, supervision, project administration. All authors have read and approved the final version of the manuscript.

Funding

This research has been funded by the Committee of Science of the Ministry of Science and Higher Education of the Republic of Kazakhstan (Grant No. BR24992870).

References

1 Li Y., Liu S., Wang Y., Wei Y., Han L., Zhi H., & Yang X. (2023) Effects of process parameters on the microstructure and mechanical properties of AISI 1045 steel prepared by selective laser melting. *Materials Today Communications,* 37, 107287. https://doi.org/10.1016/j.mtcomm.2023.107287

2 Su X., Zhu X., Fu Y., Xiao S., & Liu Y. (2024) Comparative Analysis of Tribological Behavior of 45 Steel under Intensive Quenching-High-Temperature Tempering and Queenching-Tempering Process. *Applied Sciences*, 14(13), 5942. https://doi.org/10.3390/app14135942

3 Davis J. R. (2004) Handbook of thermal spray technology. *ASM international*. Available at: https://books.google.kz/books?id=S0PryYc9T70C&lpg=PA128&ots=m93YUXnCp&dq=Davis%2C%20J.%20R.%20

4 Oksa M., Turunen E., Suhonen T., Varis T., & Hannula S. P. (2011) Optimization and characterization of high velocity oxy-fuel sprayed coatings: techniques, materials, and applications. *Coatings*, 1(1), 17-52. https://doi.org/10.3390/coatings1010017

5 Sunitha K., & Vasudev H. (2022) A short note on the various thermal spray coating processes and effect of post-treatment on Ni-based coatings. *Materials Today: Proceedings*, 50, 1452-1457. https://doi.org/10.1016/j.matpr.2021.09.017

6 Łatka L., Pawłowski L., Winnicki M., Sokołowski P., Małachowska A., & Kozerski S. (2020) Review of functionally graded thermal sprayed coatings. *Applied Sciences*, 10(15), 5153. https://doi.org/10.3390/app10155153

7 Rakhadilov B., Buitkenov D., Sagdoldina Z., Idrisheva Z., Zhamanbayeva M., & Kakimzhanov D. (2021) Preparation and characterization of NiCr/NiCr-Al2O3/Al2O3 multilayer gradient coatings by gas detonation spraying. *Coatings*, 11(12), 1524. https://doi.org/10.3390/coatings11121524

8 Kengesbekov A., Rakhadilov B., Sagdoldina Z., Buitkenov D., Dosymov Y., & Kylyshkanov M. (2022) Improving the efficiency of air plasma spraying of titanium nitride powder. *Coatings*, 12(11), 1644. https://doi.org/10.3390/coatings12111644

9 Fukumoto M. (2008) The current status of thermal spraying in Asia. *Journal of Thermal Spray Technology*, 17(1), 5-13. https://doi.org/10.1007/s11666-008-9154-8

10 Tejero-Martin D., Rezvani Rad M., McDonald A., & Hussain T. (2019) Beyond traditional coatings: a review on thermal-sprayed functional and smart coatings. *Journal of Thermal Spray Technology*, 28(4), 598-644. https://doi.org/10.1007/s11666-019-00857-1

11 Rakhadilov B., Magazov N., Kakimzhanov D., Apsezhanova A., Molbossynov Y., & Kengesbekov A. (2024) Influence of spraying process parameters on the characteristics of steel coatings produced by arc spraying method. *Coatings*, 14(9), 1145. https://doi.org/10.3390/coatings14091145

12 Malek M.H.A., Saad N. H., Abas S. K., & Shah N. B. M. (2014). Critical process and performance parameters of thermal arc spray coating. *International Journal of Materials Engineering Innovation*, 5(1), 12-27. https://doi.org/10.1504/IJMATEI.2014.059489

13 Hauer M., Ripsch B., Gericke A., Krömmer W., & Henkel K.-M. (2023) Advanced Analyses of Heating Elements Manufactured by an Optimized Arc Spraying Process. *Coatings*, 13(10), 1701. https://doi.org/10.3390/coatings13101701

14 Devaraj S., McDonald A., & Chandra S. (2021). Metallization of porous polyethylene using a wire-arc spray process for heat transfer applications. *Journal of Thermal Spray Technology,* 30(1), 145-156. https://doi.org/10.1007/s11666-020-01119-1

15 Tillmann W., Abdulgader M., Wirtz A., Milz M.P., Biermann D., & Walther F. (2022) The Effect of Argon as Atomization Gas on the Microstructure, Machine Hammer Peening Post-Treatment, and Corrosion Behavior of Twin Wire Arc Sprayed (TWAS) ZnAl4 Coatings. *Coatings,* 12(1), 32. https://doi.org/10.3390/coatings12010032

16 Ndumia J. N., Kang M., Gbenontin B. V., Lin J., Liu J., Li H., & Nyambura S. M. (2023) Optimizing parameters of arc-sprayed Fe-based coatings using the response surface methodology. *Journal of Thermal Spray Technology,* 32(7), 2202-2220. https://doi.org/10.1007/s11666-023-01621-2

17 Pham T.H., Nguyen V.T., Le T.Q., Nguyen T.A., Pham T.L., Nguyen T.P., Dao B.T., Ly Q.C., & Le D.T. (2021) Influence of electric arc spraying parameters on the porosity and adhesion strength of Al-Mg alloy coating. *Proceeding of the Intern. Conf. on Advanced Mechanical Engineering, Automation and Sustainable Development*, 655 – 659. Springer International Publishing. https://doi.org/10.1007/978-3-030-99666-6_94

18 Rakhadilov B., Buitkenov D., Apsezhanova A., Kakimzhanov D., Nabioldina A., & Magazov N. (2025) Selection of Optimal Process Parameters for Arc Metallization. *Coatings*, 15(3), 300. https://doi.org/10.3390/coatings15030300

19 Ndumia J.N., Kang M., Gbenontin B.V., Lin J., & Nyambura S. M. (2021). A Review on the Wear, Corrosion and High-Temperature Resistant Properties of Wire Arc-Sprayed Fe-Based Coatings. *Nanomaterials*, 11(10), 2527. https://doi.org/10.3390/nano11102527

20 Wang S., Guo T., Xu G., & Ding F. (2023) Corrosion behavior and mechanism of electric arc-sprayed Al-Mg coating and Zn-Al-Mg pseudo-alloy coatings. *Surface and Coatings Technology*, 475, 130126. https://doi.org/10.1016/j.surfcoat.2023.130126

21 Cooke K., Oliver G., Buchanan V., & Palmer N. (2007) Optimisation of the electric wire arc-spraying process for improved wear resistance of sugar mill roller shells. *Surface and Coatings Technology*, 202(1), 185-188. https://doi.org/10.1016/j.surfcoat.2007.05.015

22 Bang J., & Lee E. (2023) Evaluation of the Mechanical and Corrosion Behavior of Twin Wire Arc Sprayed Ni-Al Coatings with Different Al and Mo Content. *Coatings*, 13(6), 1069. https://doi.org/10.3390/coatings13061069

23 Yury K., Filippov M., Makarov A., Malygina I., Soboleva N., Fantozzi D., Andrea M., Koivuluoto H., & Vuoristo P. (2018). Arc-Sprayed Fe-Based Coatings from Cored Wires for Wear and Corrosion Protection in Power Engineering. *Coatings*, 8(2), 71. https://doi.org/10.3390/coatings8020071

24 Borisov Y. S., Vigilianska N. V., Iantsevitch C. V., & Demianov I. A. (2023) Corrosion resistance of pseudoalloy copper-iron coatings obtained by electric arc spraying. *Materials Science*, 59(2), 223-227. https://doi.org/10.1007/s11003-024-00766-x

25 Boronenkov V., & Korobov Y. (2016). Fundamentals of arc spraying. *Physical and Chemical Regularities*; Springer: Berlin/Heidelberg, Germany. https://doi.org/10.1007/978-3-319-22306-3

26 Tamaki R., & Yamakawa M. (2018) Elucidation of mechanism for reducing porosity in electric arc spraying through CFD. *Proceeding of the Intern. Conf.on Computational Science,* 418 - 428. Springer International Publishing. https://doi.org/10.1007/978-3-319-93698-7_32

27 Rakhadilov B., Shynarbek A., Kusainov R., Kakimzhanov D., Ormanbekov K., & Zhassulan A. (2024) Study of compressed air pressure on the properties of coatings obtained by supersonic metallization. *Journal of Theoretical and Applied Physics*, 18(6). https://doi.org/10.57647/j.jtap.2024.1806.77

28 Isakov S. A., & Lezhava A.G. (2016) Determination of optimal parameters for obtaining metal coatings by electric arc metallization using a current source with a falling volt-ampere characteristic. In New Functional Materials, Modern Technologies and Research Methods (pp. 17-18). https://www.elibrary.ru/download/elibrary_29831895_26071298.pdf [in Russian].

29 Kolyada V. S., & Shakhov V. A. (2017) New technologies and equipment for the restoration of concaves of Claas Tucano combines. Izvestiya Orenburgskogo gosudarstvennogo agrariannogo universiteta, (1 (63)), 80-82. https://cyberleninka.ru/article/n/novye-tehnologii-i-oborudovanie-dlya-vosstanovleniya-podbarabaniy-kombaynov-claas-tucano/viewer [in Russian].

30 Koroteyev A. O., Kulikov V. P., & Dolyachko V. P. (2017) Characteristics of the selection of welding wire for arc welding in Ar+ CO_2 with two-jet coaxal supply of shielding gases to the arc zone. Bulletin of the Belarusian-Russian University, (3 (56)), 65-73. https://cyberleninka.ru/article/n/osobennosti-vybora-svarochnyh-provolok-pri-dugovoy-svarke-v-srede-ar-co2-s-dvuhstruynoy-koaksalnoy-podachey-zaschitnyh-gazov-v-zonu/viewer [in Russian].

AUTHORS' INFORMATION

Sagdoldina, Zhuldyz – PhD, Associate Professor, Sarsen Amanzholov East Kazakhstan State University, Ust-Kamenogorsk, Kazakhstan; Senior Lecturer, Department of Technical Physics and Thermal Power Engineering, Shakarim University, Semey, Kazakhstan; Scopus ID: 24476592900; https://orcid.org/000-0001-6421-2000; sagdoldina@mail.ru

Leonidova, Aiym – PhD student, Research School of Physical and Chemical Sciences, Department of Technical Physics and Heat Power Engineering, Shakarim University, Semey, Kazakhstan; Scopus ID: 60013968800; https://orcid.org/0009-0008-2981-2041; aiymleonidova1994@gmail.com

Zhassulan, Ainur – PhD student, Engineering Center, Research School of Physical and Chemical Sciences, Department of Technical Physics and Heat Power Engineering, Shakarim University, Semey, Kazakhstan; Scopus ID: 58837450200; https://orcid.org/0009-0001-5887-0135; a.zhassulan@shakarim.kz

Shynarbek, Aibek – PhD student, Engineering Center, Shakarim University, Semey, Kazakhstan; Scopus ID: 58838202500; https://orcid.org/0009-0009-2877-5178; Shinarbekov16@gmail.com

Ibragimov, Nadir - Candidate of Technical Sciences, Senior Lecturer, Research School of Engineering, Department of Bioengineering Systems, Shakarim University, Semey, Kazakhstan; Scopus ID: 57188718716; https://orcid.org/0000-0001-9607-823X; n.ibragimov@shakarim.kz

Mukhametov, Yeldos - PhD, Head of the Department, Graduate school of STEAM education, Department of Physics and Informatics, Shakarim University, Semey, Kazakhstan; Scopus ID:59654975600; https://orcid.org/0000-0001-7818-8160; y.mukhametov@shakarim.kz

EURASIAN PHYSICAL TECHNICAL JOURNAL

2026, Volume 23, No. 1 (55)

https://doi.org/10.31489/2026N1/15-23

Received: 30/09/2025 Revised: 20/01/2026 Accepted: 19/03/2026

Research Article

UDC 539.374.1, 539.381, 539.4.012, 621.735.3:621.983.31

STUDY OF THE INFLUENCE OF INTERNAL STRESSES ON THE MICROSTRUCTURE OF COATINGS DURING ELECTROLYTIC RUBBING

Gimaltdinov I.[1], Sadykov M.[1], Adigamov N.[1], Kalimullin M.[1], Voinash S.[2], Vornacheva I.[3], Malikov V.[4]

[1] Kazan State Agrarian University, Kazan, Russian Federation
[2] RUDN University, Moscow, Russian Federation
[3] South-West State University, Kursk, Russian Federation
[4] Altai State University, Barnaul, Russian Federation

*Corresponding author: osys11@gmail.com

Abstract. *The paper studies the effect of residual stresses on the microstructure and mechanical properties of metal coatings formed by electrolytic rubbing. The dependence of the internal stress level on the current density, anode rotation speed, electrolyte composition and deposited layer thickness is established. It is shown that with an increase in current density from 50 to 100* A/dm^2 *and a deposition rate of up to 16.6 μm/min, residual stresses vary within 23–34* kg/mm^2*. The addition of ascorbic acid, nickel and manganese chlorides promotes an increase in stresses by 5–10% and simultaneously increases the microhardness of the coatings. A decrease in residual stresses is noted upon reaching a layer thickness of 0.03–0.04 mm, followed by stabilization at a level of 10–12* kg/mm^2*. The results of the work can be used to optimize technological modes of restoration and hardening of agricultural machinery parts, ensuring increased accuracy and quality of metal coatings.*

Keywords: residual stresses, microstructure, elastic deformation, anode, cathode, deposited layer.

1. Introduction

The process of restoring agricultural machinery parts using electrolytic rubbing allows for the formation of metal coatings with specified physical and mechanical properties. However, during the deposition of the metal layer, residual stresses arise in the coating, which significantly impact its performance characteristics, including strength, hardness, and adhesion. The magnitude and nature of these internal stresses are determined by a combination of process parameters, the most important of which are current density, electrolyte composition, substrate geometry, and anode rotation speed [1, 2, 3]. Residual stresses can be either positive or negative. Compressive stresses prevent crack propagation and increase the durability of the coating, while tensile stresses increase the risk of failure. During the manufacturing process, materials undergo uneven deformation due to external influences such as uneven mechanical strain, temperature changes, or phase transitions. Uneven deformation often results in residual stresses [4]. Residual stresses have a significant impact on the strength and other mechanical properties of products and can cause defects such as deformations and cracks during use; these defects ultimately impact the condition of the products and their service life. Therefore, strength analysis and deformation prediction during processing, as well as the assessment of future residual stresses, are pressing issues in modern industrial and scientific research [4].

Theoretical and experimental studies have shown that residual tensile stress deteriorates the fatigue life of a component [5]. Xiao et al. [6, 7] modeled the parameters of residual stress during the study of the grinding process of the surface of a titanium part and also conducted studies on the formation mechanism of residual stress. Huang et al. [8] proposed methods to study the grinding process during the abrasive process, and the residual stress of the workpiece surface after processing was determined during the experiments. Li et al. [9] used molecular dynamics methods to simulate the grinding process of single-crystal silicon. They were able to describe the distribution of residual stress after grinding, and it was also found that reducing subsurface damage during grinding can improve the service life of the workpiece. Wang et al. [10] analyzed the influence mechanism of residual compressive stress on the occurrence of fatigue cracks, estimated the residual compressive stress as a negative load and found that the presence of residual compressive stress reduces the actual average stress of the workpiece and plays an important role in delaying the occurrence of fatigue cracks. Wang et al. [10] analyzed the mechanism of influence of residual compressive stress on the growth of fatigue cracks and found that the presence of residual compressive stress can significantly reduce the intensity of crack formation in the workpiece.

Experiments conducted show that factors limiting the effect of residual stress on fatigue life exist [11, 12]. The conducted modeling can be used to study residual stress and its effect on fatigue life. However, most residual stress simulations can only simulate the formation of residual stress during processing [13] and cannot describe the full mechanism by which residual stress influences fatigue life. An improved technique based on recording the deformations of cylindrical samples and mathematical modeling of the electrolytic process for the precise quantitative determination of residual stresses and stress control has been developed [14-16].

The aim of this study is to analyze the influence of process parameters on the level of residual stresses in order to rationalize the electrolytic rubbing process and improve the quality of restored metal coatings.

2. Materials and Methods

The residual stresses in electrolytic coatings were determined using a method based on recording the elastic deformation of a sample cathode with controlled geometry, allowing for a quantitative assessment of the level of internal stresses in the layer being formed. A cylindrical sample cathode with a given diameter is shown in Figure 1. The prepared sample is placed in a cylindrical housing, after which an anode is installed in the device. Galvanic deposition of metal is performed on the inner surface of the sample cathode, which allows for reproducing the actual conditions of coating formation and conducting a subsequent analysis of the residual stresses that arise [17,18].

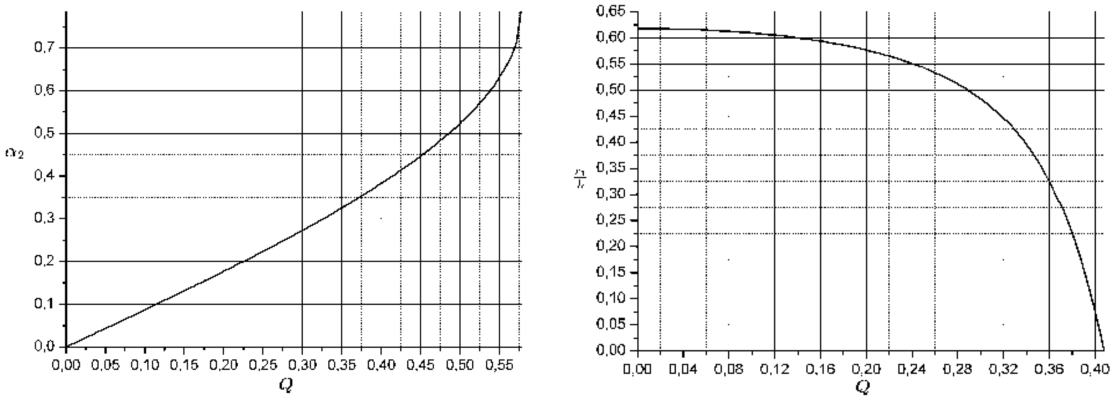

a b

Fig.1. a) Sample assembled with cathode inside cylinder; b) Cathode-sample

After the coating had been deposited and cooled, the substrate (cathode sample), Figure 2, was removed, resulting in elastic deformation of the sample under the action of internal (residual) stresses in the deposit. The resulting deflection was characterized by the value f, measured along the centerline of the cylinder cross-section. To determine the residual stresses in the coating, a classical assumption was used, according to which the internal stresses in the deposit are modeled by an equivalent system of external (reverse) stresses capable of causing similar deformation in the absence of other effects [19,20]. This makes it possible to use the superposition principle to derive a calculation formula that establishes a relationship between the measured deflection and the level of residual stresses in the coating.

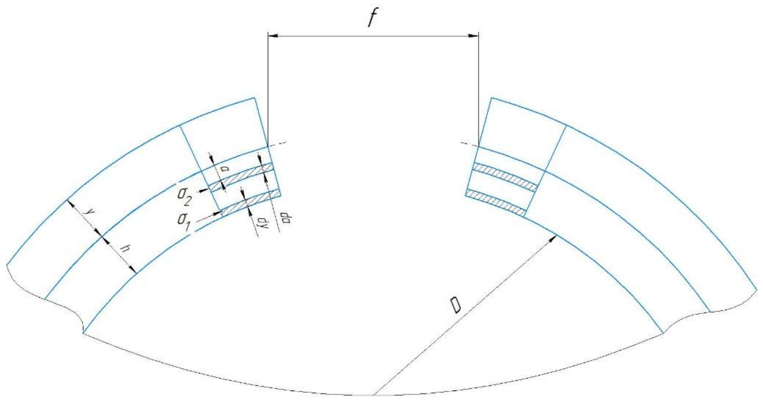

Fig.2. Scheme for calculating residual stresses in coatings

In the process of successive build-up of the coating, when a layer of thickness *da* is deposited, its own stresses are formed in it σ_1 (a). The application of a subsequent layer of thickness dy leads to a change in the stress state in the previously formed layers of the coating. As a result of this, the stresses in the layer located at a distance a from the rod-coating interface consist of two components: primary σ_1 (a), arising directly during the deposition of this layer, and additional σ_2 (a), caused by the action of subsequent layers.

$$\sigma_{tot}(a) = \sigma_1(a) + \sigma_2(a). \tag{1}$$

When a coating element of thickness *da* is deposited, stresses arise in it $\sigma_1(a)$, creating a bending moment about the neutral axis. Because the attitude (h+a)/R0=0.33≤10, the position of the neutral axis can be taken to coincide with the geometric axis of the section. Then the elementary bending moment is determined by the expression:

$$dM = \frac{1}{2}\sigma_1(a)b(h+a)da. \tag{2}$$

According to solid mechanics, the increment of bending moment can be described through the change in the lock opening using the following relation:

$$dM = \frac{E \cdot I_x}{2\pi R^2}df, \tag{3}$$

where E is the modulus of elasticity,

I_x- axial moment of inertia equal to

$$I_x = \frac{b(h+a)^3}{12}, \tag{4}$$

df- increment of the lock solution.

Representing (4) in (3) and assuming that (3) is equal to (2), we obtain

$$\sigma_1(a) = \frac{E}{12\pi R^2} \cdot \frac{df}{da}(a). \tag{5}$$

Deposition of a layer of thickness dy, located at a distance y from the rod-coating interface and characterized by stress σ1(y) leads to the occurrence of a bending moment $dM(y)$ and axial force $dN(y)$, affecting the cross-section at the level (h+y).

$$dM(y) = \frac{1}{2}\sigma_1(y)b(h+y)dy, \tag{6}$$

$$dN(y) = \sigma_1(y)b \cdot dy \tag{7}$$

Bending moment that occurs $dM(y)$ leads to the formation of additional stresses in the previously deposited layer of thickness da

$$d\,\sigma_{2M}(a)=\frac{dM(y)\cdot 12}{b(h+y)^3}\cdot\frac{h-y+2a}{2}, \tag{8}$$

taking into account expression (6), equation (8) can be transformed to the following form:

$$d\sigma_{2M}(a)=\frac{12}{b(h+y)^3}\cdot\frac{h-y+2a}{2}\cdot\frac{1}{2}\sigma_1(y)b(h+y)\cdot dy=\sigma_1(y)\cdot 3\cdot\frac{h-y+2a}{(h+y)^2}dy. \tag{9}$$

Tension $\sigma_1(y)$, included in equation (9) is defined similarly and has the following form:

$$\sigma_1(y)=\frac{E}{12\pi R^2}(h+y)^2\cdot\frac{df}{dy}(y). \tag{10}$$

In this case, expression (9), taking into account (10), is transformed to the following form:

$$d\sigma_{2M}(a)=\frac{E}{12\pi R^2}(h+y)^2\cdot 3\cdot\frac{h-y+2a}{(h+y)^2}\cdot\frac{df}{dy}(y)=\frac{3E(h-y+2a)}{12\pi R^2}\cdot\frac{df}{dy}(y). \tag{11}$$

Total change in stress in the layer da due to the action of a bending moment $dM(y)$ equals:

$$\sigma_{2M}(a)=\int_0^a d\,\sigma_{2M}(a)=\frac{3E}{12\pi R^2}\int_0^a(h-y+2a)df=\frac{3E}{12\pi R^2}\left[(h+a)f(a)+\int_0^a f(y)dy\right]. \tag{12}$$

Under the action of axial force $dN(y)$ in a layer da additional stresses are formed

$$\sigma_{2N}(a)=\frac{dN(y)}{b(h+y)}. \tag{13}$$

Taking into account expressions (7), (13) will take the form:

$$\sigma_{2N}(a)=\frac{\sigma_2(y)dyb}{b(h+y)}. \tag{14}$$

Substituting expression (10) for $\sigma_1(y)$ we will receive:

$$d\sigma_{2N}(a)=\frac{E(h+y)^2}{12\pi R^2(h+y)}\cdot\frac{df}{dy}dy. \tag{15}$$

Total voltage changes $\sigma_{2N}(a)$ in a layer da equals:

$$\sigma_{2N}(a)=\int_0^a d\,\sigma_{2N}(a)=\frac{E}{12\pi R^2}\cdot \tag{16}$$

Total stress in the layer da arising under the action of a bending moment $dM(y)$ and axial force $dN(y)$ is defined by the following expression:

$$\sigma_{2N}(a)=\sigma_{2M}(a)+\sigma_{2N}(a)=\frac{3E}{12\pi R^2}\left[(h+a)f(a)+\int_0^a f(y)dy\right]+\frac{E}{12\pi R^2}\left[(h+a)f(a)-\int_0^a f(y)dy\right]=\frac{E}{12\pi R^2}\left[4(h+a)\cdot f(a)+2\int_0^a f(y)dy\right]. \tag{17}$$

Total stress in the layerda equals:

$$\sigma_{tot}(a)=\sigma_1(a)+\sigma_2(a)=\frac{E}{12\pi R^2}(h+a)^2\frac{df}{da}(a)+\frac{E}{12\pi R^2}\left[4(h+a)\cdot f(a)+2\int_0^a f(y)dy\right]=\frac{E}{12\pi R^2}\left[(h+a)^2\frac{df}{da}(a)+4(h+a)\cdot f(a)+2\int_0^a f(y)dy\right]. \tag{18}$$

Thus:

$$\sigma_{tot}(a)=\frac{E}{12\pi R^2}\left[(h+a)^2\frac{df}{da}\cdot(a)+4(h+a)f(a)+2\int_0^a f(y)dy\right]. \tag{19}$$

Formula (18) describes the stresses in the coating: the first term is the stress from applying the layer da, the second and third are stresses from the interaction of this layer with the previous ones and the resulting bending. In the practical part of the study, the substrate was made of sheet iron 0.7 mm thick and 10 mm wide. In all the experiments, the substrate diameter was 120 mm. The thickness of the lining and coating was measured with an accuracy of 0.001 mm. Differential curves were taken for deposition from 0 to 0.1 mm with an interval of 0.01 mm. The deposition time was calculated using the formula and refined experimentally. The standard electrolytic deposition method was used to obtain coatings. Etching of the substrate with nitric acid did not cause additional stresses.

In electrolytically deposited iron films, the dependence of the residual stress on the thickness of the deposited layer demonstrates a pattern similar to that observed in bulk iron samples. Significant internal stresses are formed in the boundary layers directly in contact with the substrate. Depending on the electrolysis parameters, such as current density ($D_{к}$) and sedimentation rate (V), the magnitude of residual stresses varies in the range from 34 $\frac{\mathrm{kg}}{\mathrm{mm}^2}$($D_{к} = 150\ \frac{\mathrm{A}}{\mathrm{dm}^2}$ and V=40 $\frac{\mathrm{ob}}{\mathrm{min}}$) до 23 $\frac{\mathrm{kg}}{\mathrm{mm}^2}$($D_{к} = 50\ \frac{\mathrm{A}}{\mathrm{dm}^2}$ и V=20 $\frac{\mathrm{ob}}{\mathrm{min}}$).

When the thickness of the deposited layer reaches 0.03-0.04 mm, a sharp decrease in internal stresses is observed, after which, up to a thickness of 0.1 mm, their insignificant growth is noted. An increase in current density during electrolytic rubbing of iron does not have a significant effect on the magnitude of the internal stresses formed. According to the research data, under stationary conditions of electrolysis at a current density of 50 A/dm^2, in sediments with a thickness of 0.05 mm, internal stresses of the order of 12 $\mathrm{kg/mm}^2$. Application of the anodic-jet deposition method at a similar current density (50 A/dm^2) leads to the formation of stresses of the same thickness (0.05 mm) in sediments 12 $\mathrm{kg/mm}^2$. Precipitates obtained by electrolytic rubbing at a current density 150 $\mathrm{A/dm}^2$ and a thickness of 0.05 mm, are characterized by residual stresses equal to 12 $\mathrm{kg/mm}^2$. The difference in the values of residual stresses obtained at different current densities is insignificant.

3. Results and Discussion

The origin of internal stresses in iron electrolytic deposits is associated with a complex of factors. Firstly, it is associated with the absorption of hydrogen, which is released at the cathode simultaneously with iron ions during electro crystallization. Secondly, the mechanism of capture (occlusion) of iron hydroxide particles by the growing metal film plays an important role. Thirdly, the level of internal stresses is affected by increased cathodic polarization observed during iron electrodeposition.

Figure 3 shows a graphical interpretation of the dependence of the cathode deformation (f), expressed in millimeters, on the thickness of the deposited layer (α), measured in micrometers. The abscissa (x) axis shows the values of the deposited layer thickness in the range from 20 to 100 μm, and the ordinate (y) axis shows the corresponding values of the cathode deformation, varying from 1 to 2 mm. The experimental data are presented on the graph as five discrete points marked with special markers. For clarity, the points are connected by a blue trend line, demonstrating the general tendency of the change in the cathode deformation depending on the thickness of the deposited layer.

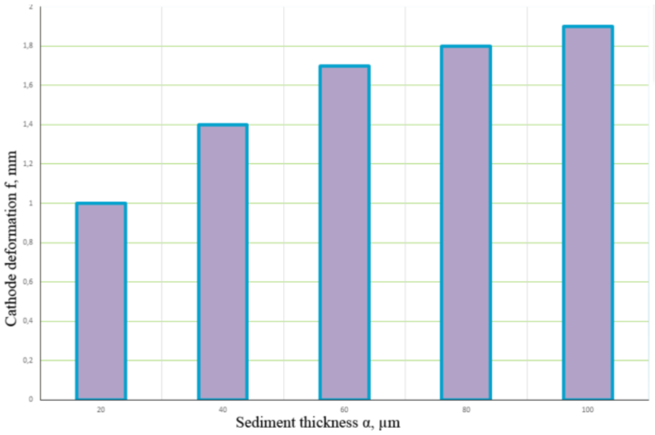

Fig. 3. Dependence of cathode deformation f (in mm) on deposit thickness α (in μm)

The analysis of the presented graphical dependence reveals the presence of a direct correlation between the thickness of the deposited layer and the degree of deformation of the cathode. With an increase in the thickness of the deposited layer, a proportional increase in the deformation of the cathode is observed: from 1 mm at a layer thickness of 20 µm to 1.9 mm at a thickness of 100 µm. The dependence visually observed on the graph has a close to linear character, which indicates a directly proportional relationship between the increase in the thickness of the deposit and the growth of the degree of deformation of the cathode. The obtained results are of high practical importance for the optimization of technological processes associated with the use of cathodes. Knowledge of the nature of the influence of the thickness of the deposited layer on the deformation of the cathode makes it possible to more accurately control the process parameters in order to achieve the specified deformation characteristics.

Figure 4 shows the dependence of the deformation curve (α), crystallization stressesσ_1 (a), tensions, caused by the influence of overlying layers $\sigma_2(a)$ and residual stress $\sigma_{tot}(a)$, from the sediment thickness (α), expressed in micrometers (µm). All types of stress are presented в kg/mm^2. Analysis of graphical data reveals different dynamics of changes in internal stresses depending on the thickness of the deposited layer (α). Residual stress curve $\sigma_{tot}(a)$ shows a sharp decline from 25 кг/мм^2 at $\alpha=0$ µm to 10 kg/mm^2 at α=40 µm, after which stabilization is observed in the range 10-12 kg/mm^2. A similar trend, but with a more pronounced decline (от 28 до 2-3 kg/mm^2), characteristic of crystallization stresses $\sigma_1(a)$, in the thickness range from 0 to 40 µm, after which their values also stabilize.

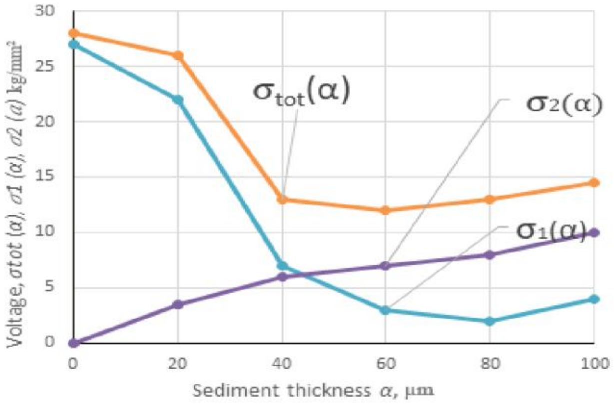

Fig. 4. Deformation curve (a) and corresponding crystallization stresses $\sigma_1(a)$, stresses of the impact of overlying layers $\sigma_2(a)$ and residual stress $\sigma_{tot}(a)$

In turn, the stresses caused by the influence of the overlying layers $\sigma_2(a)$, demonstrate monotonous growth от 0 до 10 kg/mm^2 proportionally to the increase in the thickness of the deposited layer from 0 до 100 µm. Thus, in the initial stages of sedimentation (α <40 µm) the dominant contribution to the formation of the internal stress state is made by crystallization stresses, whereas with further growth of the sediment thickness (α> 40 µm) the determining role is played by the stress induced by the overlying layers. The obtained results are of practical interest for predicting the mechanical behavior of the material and optimizing the technological parameters of deposition in order to achieve the specified properties. The insignificant increase in residual stresses observed in iron deposits obtained by electrolytic rubbing can be explained by a combination of two factors. Firstly, the deposits formed by electrolytic rubbing are characterized by a low tendency to hydrogenation, which minimizes the influence of hydrogen in the formation of internal stresses. Secondly, such deposits, as a rule, have an increased structural defectiveness, in particular, a tendency to form microcracks, which also helps to reduce the level of residual stresses. The effect of such an electrochemical parameter as the current density on the cathode on the value of residual stresses in electrolytic iron obtained by electrolytic rubbing is shown in Figure 5.

In the range of current densities 50–150 A/dm² an increase in residual stresses is observed, but when exceeded 150 A/dm² they are reduced. In thin coatings (0.01 mm, anode speed 20 ob/min) voltage increases from 16.2 to 29.2 kg/mm² with increasing current density, whereas for layers (>0.05 mm) the effect of current density becomes insignificant. In thin layers, residual stresses depend on the substrate, and their relaxation through microcracks is difficult, whereas in thickened layers, stresses relax through microcracks, weakening the dependence on current density at thicknesses >0.04 mm. Iron deposits with residual stresses 12–15 kg/mm² demonstrate stability due to partial stress relaxation and compensating properties of the material. Increasing the rotation speed of the anode with 20 to 40 ob/min leads to an increase in residual stresses: in thin layers (0.01 mm, 150 A/dm²) with 29.2 to 32 kg/mm², and in thick ones (0.1 mm) with 17.7 to 20 kg/mm². Acceleration of the anode reduces the crystal growth time, forming a fine-grained structure with increased strength and an increase in internal stresses. Refining the grains increases the area of the boundaries between them, facilitating the release of dislocations and the growth of internal tensile stresses.

Figure 6 shows the dependence of residual stresses on the deposit thickness (in the range of 0.05 - 0.1 mm) obtained from electrolytes with various additives. Analysis of the graphical data shows that the introduction of ascorbic acid, manganese chloride and nickel additives leads to an increase in residual stresses in the deposits.

1- 600 g/l $FeCl_2 \cdot 4H_2O$; pH=1; $D_к = 150\frac{\text{A}}{gm^2}; V = 20\frac{ob}{min}$.

2- 600 g/l $FeCl_2 \cdot 4H_2O$; pH=1; $0{,}5\frac{g}{l}C_6H_8O_6$; $D_к = 150\frac{\text{A}}{dm^2}; V = 20\frac{ob}{min}$.

3- 600 g/l $FeCl_2 \cdot 4H_2O$; pH=1; $0{,}5\frac{g}{l}C_6H_8O_6$; $25\frac{g}{l}NiCl_26H_2O$; $D_к = 150\frac{\text{A}}{dm^2}; V = 20\frac{ob}{min}$.

600 g/l $FeCl_2 \cdot 4H_2O$; pH=1; $0{,}5\frac{g}{l}C_6H_8O_6$; $25\frac{g}{l}MnCl_24H_2O$; $D_к = 150\frac{\text{A}}{dm^2}; V = 20\frac{ob}{min}$.

Addition of ascorbic acid to the electrolyte reduces layering and cracking in the deposits, increasing residual stresses due to improved mechanical properties.

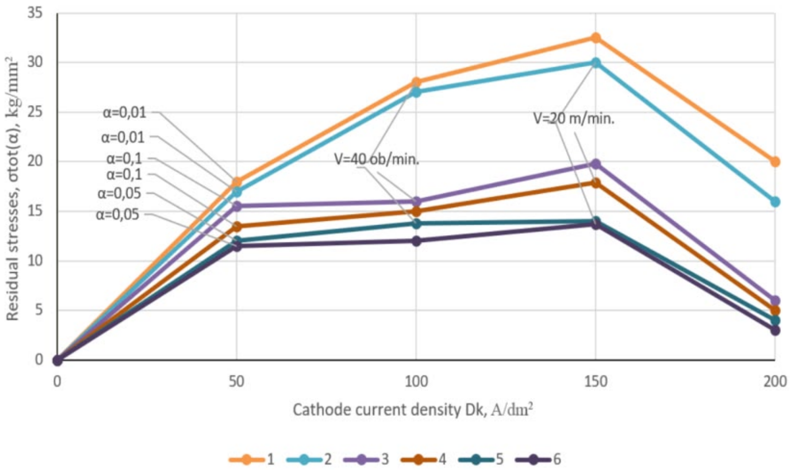

Fig. 5. Effect of cathode current density on residual stresses in iron deposits at different deposit thicknesses and anode rotation speeds

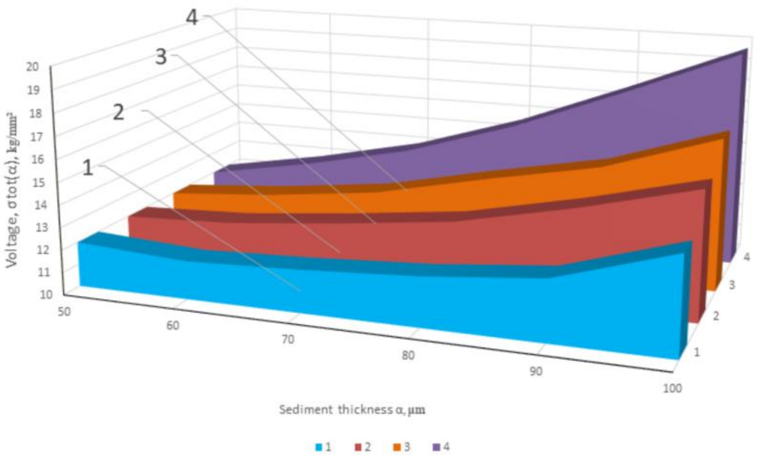

Fig. 6. Dependence of residual stresses on sediment thickness

Additions of nickel and manganese chlorides increase residual stresses due to the formation of chemical compounds during ion discharge, simultaneously improving the mechanical properties of the deposits. A slight increase in stresses from the additives is compensated by an increase in microhardness and an improvement in the results of the technological bending test.

4. Conclusion

The study demonstrated a significant influence of residual stresses on the properties of coatings obtained by electrolytic rubbing. It was found that at a current density of 50–100 A/dm² residual stresses vary from 23 to 34 kg/mm² depending on the sedimentation rate and layer thickness. When the sediment thickness reaches 0.03–0.04 mm, the stresses decrease sharply and then stabilize at the level 10–12 kg/mm². Additives to the electrolyte, such as ascorbic acid, nickel and manganese chlorides, increase residual stresses by 5–10%, while improving the microhardness and strength characteristics of the deposits. The proportional increase in cathode deformation, varying from 1 to 1.9 mm with an increase in the layer thickness from 20 to 100 µm, indicates a linear relationship between the deposited layer thickness and the stress state. The data obtained allow us to more accurately predict the mechanical behavior of the coatings and optimize the deposition process parameters.

Conflict of interest statement

The authors declare that they have no conflict of interest in relation to this research, whether financial, personal, authorship or otherwise, that could affect the research and its results presented in this paper.

CRediT author statement

Gimaltdinov I.: Conceptualization, Methodology; **Sadykov M. and Adigamov N.:** Software; **Kalimullin M. and Voinash S.:** Validation; **Vornacheva I**.: Writing - Review & Editing; **Malikov V**.: Supervision.
The final manuscript was read and approved by all authors.

Acknowledgements

The work was supported by a grant (No. 143/2024 - PD dated 16.12.2024) to young candidates of science (postdoctoral students) with the aim of defending a doctoral dissertation, performing research work, and performing labor functions in scientific and educational organizations of the Republic of Tatarstan.

References

1 Sadykov M., Gimaltdinov I., Adigamov N., Zagidullin R., Zalyakaeva D. (2024) Theory and practice of substantiation of electroplating modes by electrolytic rubbing. *AIP Conf. Proc.*, 3154, 020054. DOI: 10.1063/5.0201265.

2 Sadykov M.R., Gimaltdinov I.Kh. (2024) Restoration of machine parts by electrolytic rubbing. *L. Machinery and equipment for the village,* 324, 37-41. https://doi.org/10.33267 / 2072-9642-2024-6-37-41

3 Lee R.I. (2018) Model of contact stresses and durability of metal-polymer roller bearings. *Adhesives. Sealants. Technologies,* 3, 33 – 37. https://doi.org/10.1134/S1995421218040123

4 Jiang G., Haiyang F., Bo P. (2021) Recent progress of residual stress measurement methods: A review. *Chinese Journal of Aeronautics,* 34(2), 54-78. https://doi.org/10.1016/j.cja.2019.10.010

5 Guijian X., Benqiang C. (2022) Fatigue life analysis of aero-engine blades for abrasive belt grinding considering residual stress. *Engineering Failure Analysis,* 131, 105846. https://doi.org/10.1016/j.engfailanal.2021.105846

6 Guijian X., Kangkang S. (2021) Comprehensive investigation into the effects of relative grinding direction on abrasive belt grinding process. *Journal of Manufacturing Processes,* 62, 753-761. https://doi.org/10.1016/j.jmapro.2020.12.073

7 Na X., Weijun H., Yongjian Z. (2020) High cycle fatigue behavior of a low carbon alloy steel: The influence of vacuum carburizing treatment. *Engineering Failure Analysis,* 109, 104215. https://doi.org/10.1016/j.engfailanal.2019.104215

8 Huang Y. (2021) Research progress of aero-engine blade materials and anti-fatigue grinding technology. *J. Aero-Eng. Mater.,* 41(4), 17-35. https://doi.org/10.11868/j.issn.1005-5053.2021.000058

9 Penghui L., Xiaoguang G. (2021) Effects of grinding speeds on the subsurface damage of single crystal silicon based on molecular dynamics simulations. *Applied Surface Science,* 554, 149668. https://doi.org/10.1016/j.apsusc.2021.149668

10 Dharmesh K., Idapalapati S. (2022) Influence of residual stress distribution and microstructural characteristics on fatigue failure mechanism in Ni-based Superalloy. *Fatigue & Fracture of Engineering Materials & Structures,* 44 (5), 159574. https://doi.org/10.1111/ffe.13454

11 Yun H. (2021) Research on the fatigue failure behavior of 1Cr17Ni2 blades ground by abrasive belt with passivation treatment. *Engineering Failure Analysis,* 129, 105670. https://doi.org/10.1016/j.engfailanal.2021.105670

12 Zhang X.C., Zhang Y.K. (2010) Improvement of fatigue life of Ti–6Al–4V alloy by laser shock peening, *Materials Science and Engineering,* 527 (15), 3411-3415. https://doi.org/10.1016/j.msea.2010.01.076

13 Xiangfan N., Weifeng H. (2020) Experimental study and fatigue life prediction on high cycle fatigue performance of laser-peened TC4 titanium alloy. *Materials Science and Engineering: A,* 822, 141658. https://doi.org/10.1016/j.msea.2021.141658

14 Li R.I. (2018) Model of the Contact Stresses and Endurance of Metal–Polymer Roller Bearings. *Polymer Science,* 11(4), 382-386. https://doi.org/10.1134/S1995421218040123

15 Malokhatko E.Yu. (2024) Effect of internal mechanical stresses in a multilayer structure on displacement for various designs of microelectromechanical membranes. *St. Petersburg State Polytechnical University Journal. Physics and Mathematics,* 17, 121-124. https://doi.org/10.18721/JPM.173.223

16 Kablov E.N. (2021) The Influence of Internal Stresses on the Aging of Polymer Composite Materials: a Review. *Mechanics of Composite Materials,* 57 (5), 565-576. https://doi.org/10.1007/s11029-021-09979-7

17 Tkacheva A.V. (2024) Effect of combined thermal action of electric arc welding with aluminothermic backfill on internal stresses in a steel plate. News of higher educational institutions. *Ferrous metallurgy,* 67 (5), 604 – 611. https://doi.org/10.17073/0368-0797-2024-5-604-611

18 Smirnov A.N. (2016) Effect of the degree of deformation of welded joints of carbon steels on the structural-phase state and internal stress fields. *Welding and diagnostics,* 3, 25-28. Available at: https://www.elibrary.ru/item.asp?id=26901508

19 Kuryntsev S.V. (2020) Analysis of the influence of the welding type on the phase composition and internal stresses of welded joints of austenitic and duplex steels. *Science-intensive technologies in mechanical engineering,* 3(105), 3-11. https://doi.org/10.30987 / 2223-4608-2020-3-3-11

20 Gaskarov I.R., Farkhshatov M.N., Saifullin R.N. (2022) Cylindrical interfaces repair technique using electric resistance welding of metal powder materials. *Results in Engineering,* 16, 100699. https://doi.org/10.1016/j.rineng.2022.100699

AUTHORS' INFORMATION

Gimaltdinov, Ildus Khafizovich – Candidate of Technical Sciences, Associate Professor, Acting Head of the Department of Machine Operation and Repair, Kazan State Agrarian University, Kazan, Russian Federation; https://orcid.org/0000-0003-2297-8950; kafedrarm@yandex.ru

Sadykov, Marat Rashitovich – Assistant of the Department of Machine Operation and Repair, Kazan State Agrarian University, Kazan, Russian Federation; https://orcid.org/0009-0003-9335-6080; marat3012@yandex.ru

Adigamov, Nail Rashatovich – Doctor of Technical Sciences, Professor of the Department of Machine Operation and Repair, Kazan State Agrarian University, Kazan, Russian Federation; https://orcid.org/0009-0007-3647-1858; n-adigamov@rambler.ru

Kalimullin, Marat Nazipovich – Doctor of Technical Sciences, Associate Professor of the Department of Machine Operation and Repair, Kazan State Agrarian University, Kazan, Russian Federation; https://orcid.org/0000-0001-6867-3103; marat-kmn@yandex.ru

Voinash, Sergey Aleksandrovich – Assistant at the Department of Architecture and Restoration, RUDN University, Moscow, Russian Federation; https://orcid.org/0000-0001-5239-9883; sergeyvoinash@yandex.ru

Vornacheva, Irina Valerievna – Candidate of Technical Sciences, Associate Professor, South-West State University, Kursk, Russian Federation; https://orcid.org/0009-0003-5511-235X; vornairina2008@yandex.ru

Malikov, Vladimir Nickolaevich – Candidate of Technical Sciences, Associate Professor, Department of General and Experimental physics, Altai State University, Barnaul, Altai Territory, Russian Federation; https://orcid.org/0000-0003-0351-4843; osys11@gmail.com

EURASIAN PHYSICAL TECHNICAL JOURNAL

2026, Volume 23, No. 1 (55)

https://doi.org/10.31489/2026N1/24-33

Received: 17/11/2025 Revised: 24/02/2026 Accepted: 19/03/2026

Research Article

UDC 539.232; 538.915; 535.215.6; 536.4; 620.91

PHOTOVOLTAIC PROPERTIES OF SILICON HETEROJUNCTION SOLAR CELLS FABRICATED ON BORON-DOPED SILICON WAFERS UNDER EXTRATERRESTRIAL ILLUMINATION

Utamuradova Sh.B.[1], Terukov E.I.[2], Ataboev O.K.[1*], Kabulov R.R.[3],
Panaiotti I.E.[2], Uzakbayeva N.S.[4]

[1] Semiconductor Physics and Microelectronics Research Institute, Tashkent, Uzbekistan
[2] Ioffe Institute, Russian Academy of Sciences, St. Petersburg, Russia
[3] Physical-technical Institute Uzbekistan Academy of Sciences, Tashkent, Uzbekistan
[4] Nukus state technical university, Nukus, Uzbekistan

*Corresponding author: omonboy12@mail.ru

Abstract. *The temperature coefficient is a key performance indicator for assessing the operational stability of solar cells used for power generation in both terrestrial and space environments. In recent years, silicon heterojunction solar cells employing hydrogenated amorphous silicon passivating layers have attracted significant attention owing to their high conversion efficiency and excellent surface passivation quality achieved at low processing temperatures. However, to ensure their reliable and stable operation in extraterrestrial conditions, it is essential to investigate not only the effects of radiation but also the influence of temperature variations on their photovoltaic performance. In this study, the illuminated current–voltage characteristics of heterojunction solar cells fabricated on boron-doped single-crystalline silicon wafers were experimentally investigated under Air Mass Zero spectrum across a wide temperature range of 173–373 K. The results revealed that the short-circuit current density exhibited a positive temperature coefficient of +(0.077±0.003) %/K, whereas the open-circuit voltage decreased linearly with a coefficient of – (0.23±0.002) %/K as temperature increased. The temperature coefficients of the conversion efficiency and fill factor were determined to be – (0.23±0.007) %/K and – (0.075±0.004) %/K, respectively. The experimentally obtained temperature coefficient of the maximum output power – (0.231±0.008) %/K was found to be lower than that of conventional Al-BSF solar cells (−0.39%/K) and other single-crystalline silicon–based photovoltaic technologies, confirming the excellent thermal stability and high suitability of silicon heterojunction solar cells for space power applications.*

Keywords: heterojunction, hydrogenated amorphous silicon, Air Mass Zero spectrum, light current-voltage characteristics, temperature coefficient, open-circuit voltage, conversion efficiency.

1. Introduction

It is well known that reliable broadband Internet access and data transmission, particularly in remote regions where stable communication networks are lacking, can be achieved through the deployment of global low Earth orbit (LEO, 500–2000 km altitude) satellite communication systems [1-3]. The continuous and efficient operation of such satellites depends on the availability of highly reliable power supply systems. In these spacecraft, electrical energy is primarily generated by photovoltaic (PV) modules [4, 5]. Therefore, enhancing the efficiency, radiation resistance, and thermal stability of PV modules is essential to ensure the long-term and stable operation of satellite communication systems in LEO [6].

Since the launch of the first Soviet satellite, *Sputnik 1*, in 1957, interest in solar cells (SCs) has increased significantly [4]. One year later, in 1958, Si-based SCs were used for the first time aboard the *Vanguard-1* satellite launched by the United States [7]. Since then, Si SCs have been widely adopted as the primary power source for spacecraft because of their long-term operational stability, mature fabrication technology, and favorable power-to-mass ratio [4, 8, 9]. This trend continued until the 1990s, when the development of Si-based SCs for space applications was largely discontinued, and research efforts shifted toward III–V compound semiconductor-based SCs, which subsequently began to dominate the space market [5, 7]. At present, the most widely used semiconductor materials for space applications - particularly in geostationary Earth orbit (GEO, at an altitude of approximately 35.786 km above Earth's surface) - are GaAs-based multijunction SCs, such as GaInP/GaInAs/Ge [5] and AlInGaP/AlInGaAs/InGaAs/Ge [10]. However, the production cost of these SCs is considerably higher than that of their Si-based counterparts, primarily due to the complex technological processes required for their fabrication [5, 11]. In addition, the brittle nature of GaAs compounds further complicates large-scale manufacturing and handling. These factors have limited the widespread adoption of GaAs-based SCs for terrestrial applications and, in particular, for use in LEO missions, where cost efficiency and structural robustness are of critical importance [4].

Currently, among Si-based PV technologies, Si heterojunction (HJT) SCs have emerged as the most efficient option. A record conversion efficiency of 27.8% has been achieved for n-type heterojunction back-contact (HBC) SCs with an active area of 134 cm^2, developed by LONGi Laboratory under standard test conditions (1 sun, AM1.5G, 100 mW/cm^2) [12]. This represents the highest efficiency reported for any single-junction Si-based SC and is comparable to that of state-of-the-art single-junction GaAs SCs (29.1%) [12, 13]. Moreover, HJT SCs exhibit a higher bifacial coefficient compared with other Si-based PV technologies [13]. Owing to the use of low-temperature hydrogenated amorphous silicon (a-Si:H) passivating layers and low Si consumption, HJT SCs achieve exceptionally high open-circuit voltages (up to 752 mV) and low temperature coefficients (< 0.3%/°C for n-type wafers). These characteristics provide a significant advantage over other Si-based PV technologies such as PERC (Passivated Emitter and Rear Cell), TOPCon (Tunnel Oxide Passivated Contact), and conventional Al-BSF (Aluminum Back Surface Field), which currently dominate terrestrial PV manufacturing [14-16]. In contrast, these alternative technologies generally require high-temperature processing (> 600 °C) [15]. The combination of superior efficiency, low-temperature fabrication, and outstanding thermal stability makes HJT SCs highly promising candidates for space PV applications. In extraterrestrial environments - particularly in LEO, the performance of SCs is affected not only by high-energy particle irradiation but also by extreme cyclic temperature fluctuations (160–400 K) [8, 17]. Therefore, a comprehensive study of the temperature-dependent behavior of HJT SCs under extraterrestrial solar illumination is essential for evaluating their reliability and long-term operational stability in future spacecraft power systems.

In this study, the temperature dependence of the PV performances of HJT SCs based on boron-doped p-type crystalline Si (c-Si) wafers were investigated under Air Mass Zero (AM0) spectrum (136.7 mW/cm^2) in the temperature range of 173–373 K.

2. Material preparation and methods

2.1 Sample preparation

The studied p-type Si HJT SCs were fabricated at the R&D Center of Thin film technologies in Energetics, Saint-Petersburg, Russia. To conduct experiments, Si HJT SCs (Fig. 1) were created on boron-doped p-type c-Si wafers grown by the Czochralski method, with an acceptor concentration of $3 \cdot 10^{16}$ cm^{-3}, a thickness of ~165 μm, crystallographic orientation (100). In the c-Si wafer, the concentrations of oxygen and carbon, as well as density of dislocation were approximately $4.5 \cdot 10^{17}$ cm^{-3}, $3 \cdot 10^{16}$ cm^{-3} and 500 cm^{-2}, respectively. The wafers were acquired from SAS Sunrise and are commonly used in the fabrication of PERC SCs. Before depositing intrinsic and doped a-Si:H layers onto the p-type c-Si wafers to form the heterojunctions, the wafers underwent a wet chemical cleaning procedure. Afterward, the c-Si wafers were subjected to pyramidal surface texturing to enhance light absorption [18]. Subsequently, thin intrinsic a-Si:H layers were deposited on both the front and rear surfaces of the textured p-type c-Si wafers using Very High Frequency Plasma-Enhanced Chemical Vapor Deposition (VHF PECVD) method. The purpose of this layer is to passivate dangling bonds (by forming Si–H bonds) on the c-Si surfaces [19]. Using the same method to form a p-n-junction, n-type a-Si:H layer was deposited on the front side, and to create the back-surface field

(BSF), p-type a-Si:H layer was deposited on the rear side of i-a-Si:H deposited p-type c-Si wafer. All intrinsic and doped a-Si:H layers were deposited at a low temperature of 180–185°C and a frequency of 40.68 MHz. Further, transparent and conductive Sn-doped In_2O_3 (ITO) layers (90 wt.% In_2O_3 and 10 wt.% SnO_2) were deposited on the front and rear surfaces of the photosensitive heterostructures using Radio-Frequency (RF) magnetron sputtering. To collect photogenerated charge carriers from the heterostructure surfaces, low-temperature silver (Ag) paste with "Busbar" type contacts was screen-printed onto both the front and rear sides of the photosensitive heterostructures with subsequent curing. The "Busbar" type contacts had the following dimensions, measured using a KLA/Tencor Alpha-Step D-120 profilometer: a height of ~25 μm, a width of ~45 μm, and a pitch of ~1.36 mm**.** A cross-sectional view of the finished HJT SCs based on p-type c-Si wafer is shown in Fig. 1.

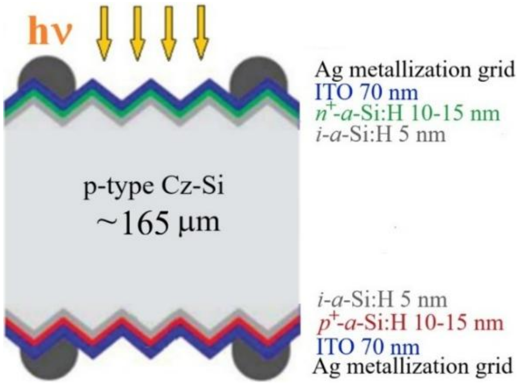

Fig. 1. A cross-sectional view of the HJT SCs based on p-type c-Si wafer.

2.2 Characterization and measurement of performances

As reported in [20, 21], in order to improve the overall efficiency of PV modules compared with conventional full-cell designs, standard SCs are divided into half-cells, which reduces the cell current and minimize resistive losses. This design also prevents the performance degradation of PV modules under partial shading conditions, which would otherwise increase resistance and potentially lead to module failure [21]. Therefore, two main techniques are currently employed for SC separation: laser scribing with mechanical cleaving (LSMC) and thermal laser separation (TLS) [20]. In the present study, p-type c-Si-based samples with an area of 1 × 1 cm^2 were cut from full-sized high-efficiency HJT SCs (15.6 × 15.6 cm^2) using the LSMC method for experimental investigation. No additional passivation of the lateral surfaces or edge isolation was performed after laser cutting. A solid-state "MiniMaker2" diode laser, with a wavelength of 1064 nm was used for cutting the samples. During laser scribing, the laser parameters were set as follows: a scribing speed of 200 mm/s, a pulse repetition rate of 25 kHz, and a pulse duration of 20 ns. The scribing process was carried out on the rear side of the p-n-junction, which helped to reduce potential damage to the contact layers and maintain photoelectric conversion efficiency.

To study the effect of temperature on the PV performance of p-type c-Si HJT SCs, light J-V curves were measured using a liquid nitrogen cryostat (Janis VPF-100). During the measurements, the samples were illuminated with a class AAA pulsed solar simulator (SS-80AAA simulator) under AM0 spectrum (136.7 mW/cm^2). The short-circuit current density and open-circuit voltage were recorded using a Keithley SM2460 Source Meter. Temperature stabilization during the measurements was maintained by the liquid nitrogen cryostat, equipped with a Lake Shore Model 335 temperature controller. Each light J-V measurement was conducted after the target temperature was reached and maintained for 4-5 minutes under the AM0 spectrum. Temperature coefficients of the output parameters of the HJT SCs, such as open-circuit voltage (V_{oc}), short-circuit current density (J_{sc}), fill factor (FF), maximum power (P_{max}) and conversion efficiency **(**η**)** were extracted from the slopes of the linear regions of the experimental temperature-dependent curves. For the present investigation, about 20 HJT SCs were fabricated. These samples exhibited similar parameters within a margin of error of no more than 2%. Among them, three representative samples were selected for temperature-dependent measurements, and their results are presented in this study.

This study focuses on characterizing the temperature-dependent performance of p-type c-Si HJT SCs without considering radiation effects.

3. Results and discussion

To investigate the influence of temperature on the PV parameters of the illuminated J-V curves of HJT SCs based on p-type c-Si, measurements were carried out under AM0 spectrum (136.7 mW/cm²) in the temperature range of 173–373 K (Fig. 2). As shown in Fig. 2, temperature has a significant effect on the shape of the illuminated J-V curves. In particular, the J_{sc} increases slightly with rising temperature, whereas the V_{oc} exhibits a pronounced decrease. It can also be seen from Fig. 2 that, at elevated temperatures, the influence of the series resistance (R_s) on the J-V curve shape becomes less pronounced, as a noticeable increase in J_{sc} is observed in this range. To determine the temperature dependence of each PV parameter of the p-type HJT SCs, namely the V_{oc}, J_{sc}, FF, P_{max} and η, their variations with temperature were analyzed.

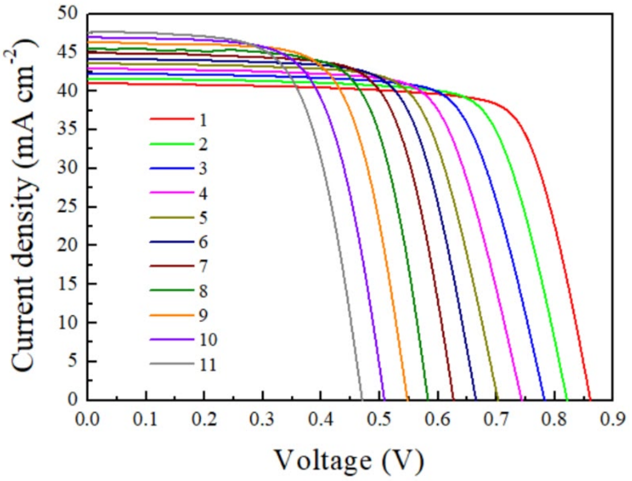

Fig. 2. Light J-V curves of HJT SCs based on p-type c-Si wafer under AM0 spectrum (136.7 mW/cm^2) in the temperature range of 173–373 K. T, K: 1 – 173, 2 – 193, 3 – 213, 4 – 233, 5 – 253, 6 – 273, 7 – 293, 8 – 313, 9 – 333, 10 – 353, 11 – 373.

Fig. 3 *a*) presents the temperature dependence of the J_{SC} for the p-type c-Si HJT SCs under AM0 spectrum in the temperature range of 173–373 K. The experimental results demonstrate a linear increase in J_{SC} with rising temperature.

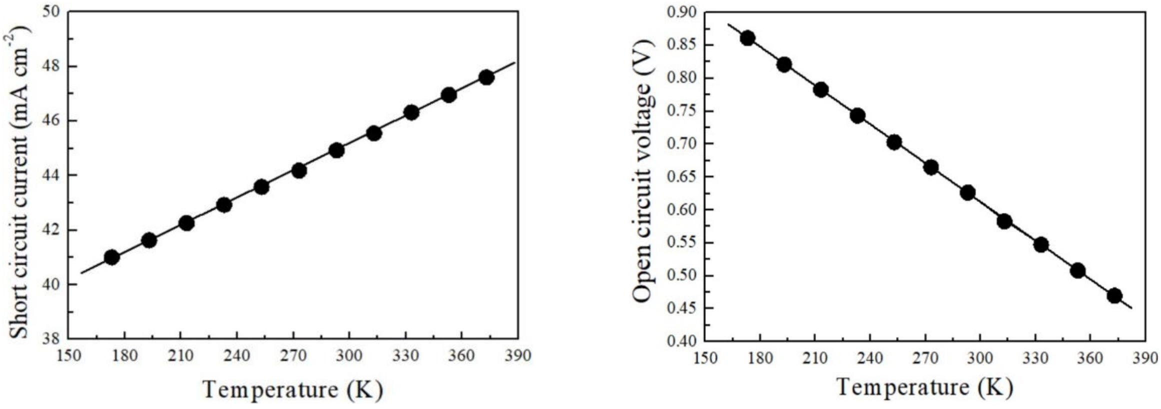

a) *b)*

Fig. 3. Temperature dependence of short-circuit current density (*a*) and open-circuit voltage (*b*) of HJT SCs based on p-type c-Si wafer under AM0 spectrum (136.7 mW/cm^2).

For example, the J_{SC} value increased at a rate of approximately 0.032 mA/K, from 41.1 mA/cm^2 to about 47.5 mA/cm^2 in the range of 173 – 373 K. It is well known that the bandgap of c-Si narrows with increasing temperature [22], causing a redshift of the absorption edge toward longer wavelengths. Consequently, the wafer absorbs a broader range of the infrared spectrum, enhancing electron–hole pair generation in the photoactive region [16, 23]. Based on the experimental data, the temperature coefficient (TC) of the short-circuit current density (TCJ_{SC}) for the p-type c-Si HJT SCs was determined from the slope of the linear region of the $J_{SC}(T)$ dependence. The calculated TCJ_{SC} value was +(0.077±0.003) %/K, which is in good agreement with previously reported results [14-16]. Fig. 3 *b*) presents the experimental results of the temperature dependence of the open-circuit voltage - $V_{oc}(T)$, for the p-type c-Si HJT SCs under AM0 spectrum in the temperature range of 173–373 K. As shown in Fig. 3 *b*), the experimental value of the V_{oc} decreases linearly with increasing temperature. Specifically, V_{oc} decreases from 0.861 V at 173 K to 0.47 V at 373 K. The observed reduction in V_{oc} with increasing temperature is mainly caused by the temperature-dependent narrowing of the Si bandgap [22], which leads to an exponential increase in the reverse saturation current density (J_0) due to the higher intrinsic carrier concentration (n_i) [24].

According to our previous studies [25, 26], the temperature dependence of V_{oc} can be expressed as

$$V_{oc}(T)=\frac{E_g(T)}{q}-\frac{kT}{q}\ln\left\{\frac{N_{C0}N_{V0}}{\left[\frac{J_{SC}(T)}{q\left[\frac{D}{L_{diff}}tanh\left(\frac{d}{L_{diff}}\right)+S(T)\right]}\right]\left[N_a(T)+\frac{J_{SC}(T)}{q\left[\frac{D}{L_{diff}}tanh\left(\frac{d}{L_{diff}}\right)+S(T)\right]}\right]}\left(\frac{T}{T_0}\right)^3\right\} \qquad (1)$$

where, D –ambipolar diffusion coefficient, d –base thickness, L_{diff} –minority carrier diffusion length, N_a –acceptor concentration, N_{C0} and N_{V0} – effective density of states in conduction and valence band at T_0=300 K, S –total surface recombination velocity ($S=S_0+S_d$), S_0 and S_d –surface recombination velocity on the front and rear surfaces of wafer, respectively.

According to Equation (1), the parameters of the light J–V curves of the p-type c-Si HJT SCs, such as J_{SC}, total recombination velocity (S), including both surface ($S=S_0+S_d$) and bulk $\tau(T)$ components at different temperatures, proposed in [27, 28], N_a and L_{diff} exhibit a tendency to increase with temperature. Within the investigated temperature range, the S in the p-type c-Si HJT SC increased from 12.8 cm/s at 173 K to 24.2 cm/s at 373 K, which is in good agreement with the data reported in [29]. The S, incorporating both surface ($S=S_0+S_d$) and bulk $\tau(T)$ contributions at various temperatures, was evaluated using the approach proposed in [25-27]. The S noticeably increased from 9.65 cm/s to 18.6 cm/s after laser cutting at room temperature. The combined temperature-dependent variations of these parameters contribute to the observed decrease in V_{oc}.

The temperature coefficient of the open-circuit voltage (TCV_{oc}) for the p-type c-Si HJT SCs was determined from the slope of the linear region of the experimental $V_{oc}(T)$ dependence. The obtained value of TCV_{oc} was –(0.23±0.002)%/K in the temperature range of 173–373 K. Notably, this value is significantly lower than those reported for other c-Si-based PV technologies. It is also slightly smaller than the TCV_{oc} (–0.254%/K) obtained for n-type Si HJT SCs in [14-16], which can be attributed to the full rear-side silver (Ag) metallization in that structure. Such metallization hinders heat dissipation, thereby increasing the thermal sensitivity of the device. In addition, the TCV_{oc} of p-type c-Si HJT SCs also depends on the illumination level. According to [14-16], as the illumination intensity increases, the absolute value of TCV_{oc} decreases. Therefore, the relatively low TCV_{oc} observed in this study can be explained by measurements performed under the AM0 spectrum (136.7 mW/cm^2). A smaller (less negative) TCV_{oc} reflects enhanced thermal stability, as the SC maintains a higher V_{oc} with increasing temperature.

Fig. 4 *a*) presents the experimental results of the temperature dependence of the fill factor - $FF(T)$, for the p-type c-Si HJT SCs under AM0 spectrum (136.7 mW/cm^2). The FF is defined as follows [23]:

$$FF=\frac{J_mV_m}{J_{sc}V_{oc}}, \qquad (2)$$

where, J_m and V_m are the current density and voltage at the maximum power point, respectively.

It can be seen from Fig. 4 *a*) the FF of the p-type c-Si HJT SCs decreases almost linearly from about 77.3% to 65.7% as the temperature increases from 173 K to 373 K. Within this temperature range, the series resistance (R_s) slightly decreases from about 3.43 $\Omega\cdot cm^2$ to 1.65 $\Omega\cdot cm^2$, as shown in Fig. 4 *b*). In the investigated temperature range, the shunt resistance (R_{sh}) exhibits only minor variations with temperature, as a results, a noticeable reduction in FF is observed at elevated temperatures.

The R_s of the p-type c-Si HJT SCs is determined from the linear region of the J-V curve near the V_{oc} point, while the R_{sh} is extracted from the linear region close to the J_{sc} point [30]. The total R_s comprises several resistive components connected in series with the p-n-junction, including the bulk resistances of the p- and n-type semiconductor regions, the metal–semiconductor contact resistances, and resistances of the front and rear metal contacts. The R_{sh} represents leakage current pathways through pinholes, surface recombination currents, tunneling via bulk defects, and peripheral leakage at the device edges [31].

It is well known that both the R_s and R_{sh} strongly influence the FF of SCs. To achieve a high FF, R_s must be minimized, while R_{sh} should be maximized [31]. In the present study, a clear decrease in R_s with increasing temperature was observed, which under typical conditions should result in an increase in FF. However, the experimental results revealed the opposite trend FF decreased with temperature. One of the main reasons for this discrepancy is the simultaneous slight reduction in R_{sh} due to parasitic leakage paths through the p-n-junction at elevated temperatures, and linear decrease in V_{oc} with temperature. According to Equation (2), FF is positively correlated with V_{oc}, therefore, the decrease in V_{oc} leads to a corresponding reduction in FF. As a result, the combined effect of decreasing R_{sh} and V_{oc} causes the deterioration of FF with increasing temperature, which is consistent with the experimental observations reported by other researchers [32].

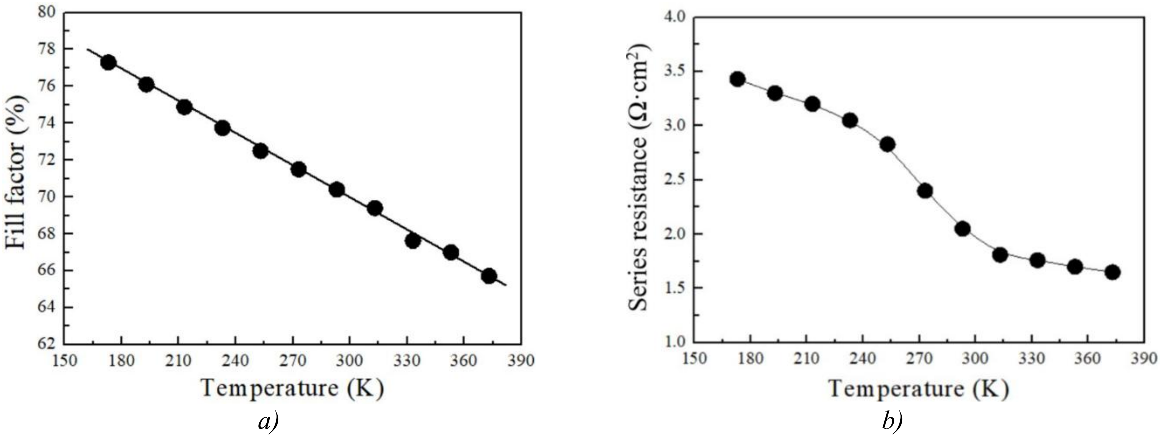

a)　　*b)*

Fig. 4. Temperature dependence of fill factor (*a*) and series resistance (*b*) of HJT SCs based on p-type c-Si wafer under AM0 spectrum (136.7 mW/cm^2).

The temperature coefficient of the fill factor ($TCFF$), determined from the slope of the linear region of the $FF(T)$ dependence, was found to be – (0.075±0.004) %/K in the temperature range of 173–373 K. To evaluate the contribution of V_{oc} and R_s to the $TCFF$ of p-type c-Si HJT SCs, the following expression was used, as described in [33].

$$\frac{1}{FF}\frac{dFF}{dT} = (1 - 1.02FF_0)\left(\frac{1}{V_{oc}}\frac{dV_{oc}}{dT} - \frac{1}{T}\right) - \frac{R_s}{\frac{V_{oc}}{I_{sc}} - R_s}\left(\frac{1}{R_s}\frac{dR_s}{dT}\right), \quad (3)$$

where,

$$FF_0 = \frac{\frac{qV_{oc}}{nkT} - ln\left(\frac{qV_{oc}}{nkT} + 0.72\right)}{\frac{qV_{oc}}{nkT} + 1}, \quad (4)$$

FF_0 is the FF in the absence of the R_s and R_{sh}, n −diode ideality factor, T − cell temperature, respectively.

From Eq. (3), it can be seen that the first term represents the contribution of the V_{oc} to the $TCFF$, while the second term reflects the contribution of the R_s to the $TCFF$. For the studied SCs, the analysis showed that the contribution of the V_{oc} to the $TCFF$ is dominant, accounting for more than 60%. Therefore, the observed decrease in FF with increasing temperature can be explained by the strong temperature dependence of V_{oc}, which, as mentioned earlier, is primarily governed by the effective intrinsic carrier concentration ($n_{i.eff}$) that increases at elevated temperatures due to bandgap narrowing [22]. Fig. 5 shows the temperature dependence of the maximum power $P_{\max}(T)$ (a) and the conversion efficiency $\eta(T)$ (b) for the p-type c-Si HJT SCs under AM0 spectrum (136.7 mW/cm²). The $P_{\max}$ value is defined as the product of J_{sc}, V_{oc} and FF. As shown in Fig. 5 a)**,** the maximum power ($P_{\max}$) of the p-type c-Si HJT SCs decreases linearly from approximately 27.3 mW/cm² to 14.7 mW/cm² as the temperature increases from 173 K to 373 K. This behavior of $P_{\max}$ is primarily attributed to the temperature dependencies of key PV parameters such as J_{sc}, V_{oc}, FF and R_s, which collectively exert the most significant influence on the $P_{\max}(T)$ characteristics [34].

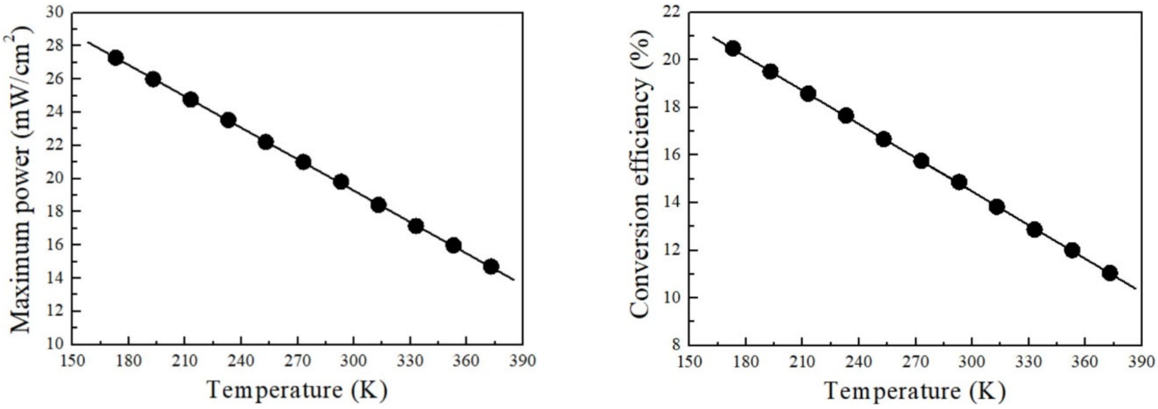

a) *b)*

Fig. 5. Temperature dependence of the maximum power (a) and conversion efficiency (b) of p-type c-Si HJT SCs under AM0 spectrum (136.7 mW/cm²) in the temperature range of 173–373 K.

The temperature coefficient of the P_{max} (TCP_{max}) was determined to be – (0.231±0.008) %/K in the investigated temperature range. The relatively low TCP_{max} of HJT SCs, compared with other Si-based PV technologies, can be attributed to the presence of intrinsic a-Si:H passivation layers on both surfaces of the c-Si wafer, which effectively suppress recombination losses of photogenerated charge carriers. This structural design leads to a reduction in the TCV_{oc}, which contributes more than 60% to the overall variation in the TCP_{max} and therefore plays a dominant role compared to other PV parameters such as J_{sc} and FF [15]. Owing to the excellent surface passivation provided by the intrinsic a-Si:H layers, low temperature HJT SCs currently achieve record-high V_{oc} (up to 752 mV) [12], which in turn accounts for their relatively low TCP_{max} values [14]. Fig. 5 b) presents the experimental results of the temperature dependence of the conversion efficiency, $\eta(T)$ of the p-type c-Si HJT SCs under AM0 spectrum (136.7 mW/cm²). The conversion efficiency η is defined as the ratio of the maximum power (P_{max}) to the incident light power (P_{rad}), which can be expressed by the following equation [31]:

$$\eta = \frac{P_{max}}{P_{rad}} \cdot 100\% = \frac{J_{sc}V_{oc}FF}{P_{rad}} \cdot 100\%, \tag{5}$$

where, P_{rad}= 136.7 mW/cm^2.

As shown in Fig. 5 b), the $\eta(T)$ of the p-type c-Si HJT SCs follows a trend similar to that of the P_{max}. As the temperature increased from 173 K to 373 K, the η value decreases linearly from 20.5% to 11.1%. The reduction in η with increasing temperature is primarily attributed to the temperature dependence of the key PV parameters of the SCs: V_{oc}, FF, and to a lesser extent, J_{sc}, since the η is defined by Eq. (5). It should also be noted that the η of the SCs under the AM0 spectrum is lower than under AM1.5G conditions. This difference primarily arises because the AM0 spectrum lacks atmospheric absorption, resulting in a higher proportion of ultraviolet (UV) and infrared (IR) radiation, which are less efficiently converted into electrical energy. This occurs because the spectral response, or internal quantum efficiency (IQE) of SCs is significantly lower in these regions of the solar spectrum [35]. After laser cutting, the η of the p-type HJT SCs was determined to be 14.9% under AM0 and 16.3% under AM1.5G spectrum at room temperature.

4. Conclusion

In this study, the light J-V curves of HJT SCs fabricated on boron-doped p-type c-Si wafers were experimentally investigated under extraterrestrial AM0 spectrum (136.7 mW/cm²) over the temperature range of 173–373 K. The experimental results revealed a linear increase in the J_{sc} with rising temperature, whereas the V_{oc}, FF and P_{max} exhibited a linear decrease.

The TCs of the key PV parameters were determined as follows: the J_{sc} exhibited a positive temperature coefficient of +(0.077±0.003) %/K, while the V_{oc} and FF showed negative coefficients of –(0.23±0.002)%/K and –(0.075±0.004)%/K, respectively, within the investigated temperature range. The maximum power reached 27.3 mW/cm² at 173 K, with a corresponding power temperature coefficient (TCP_{max}) of –(0.231±0.008)%/K - one of the lowest values reported for Si-based PV technologies. This remarkably low temperature coefficient demonstrates the excellent thermal stability of p-type c-Si HJT SCs, primarily attributed to the effective surface passivation provided by the intrinsic a-Si:H layers on both wafer surfaces.

It is well established that n-type Si-based SCs are predominantly used in terrestrial PV applications due to their high conversion efficiency and superior surface passivation quality. However, for space applications, transitioning to p-type Si wafers offer distinct advantages, as they exhibit greater radiation tolerance, reduced susceptibility to radiation-induced degradation, and a lower TCP_{max}. These characteristics are critical for ensuring long-term operational stability and reliability in harsh extraterrestrial environments. Consequently, p-type c-Si HJT SCs represent highly promising candidates for power generation in small satellite platforms (CubeSats) and other spacecraft operating in LEO, where wide temperature fluctuations and stringent energy efficiency requirements make thermal robustness a key design consideration.

Conflict of interest statement

The authors declare that they have no conflict of interest in relation to this research, whether financial, personal, authorship or otherwise, that could affect the research and its results presented in this paper.

CRediT author statement

Utamuradova Sh.B.: Conceptualization, Writing – original draft; **Terukov E.I.:** Resources, Supervision, Writing – review & editing; **Ataboev O.K., Kabulov R.R.:** Investigation, Writing – original draft; **Panaiotti I.E.:** Formal analysis, Writing – review & editing; **Uzakbayeva N.S.:** Investigation, Methodology.

The final manuscript was read and approved by all authors.

Acknowledgements

The authors are grateful to the staff of the R&D Center for Thin Film Technologies in Energetics, Ioffe Institute, and Zh.I. Alferov St. Petersburg National Research Academic University for valuable assistance in the process of creating and studying HJT SCs, as well as to the staff of the Semiconductor Physics and Microelectronics research institute for valuable advice when discussing the research results.

References

1 Aljohani A.J., Mirza J., Ghafoor S.A. (2021) A novel regeneration technique for free space optical communication systems. *IEEE Communications Letters,* 25(1), 196–199. https://doi.org/10.1109/LCOMM.2020.3029591

2 Kalinovskii V.S., Terukov E.I., Abolmasov S.N., Prudchenko K.K., Kontrosh E.V., Tolkachev I.A., Kochergin A.V., Titov A.S., Ataboev O.K. (2023) Studies of degradation silicon heterojunction solar cells by 1 MeV electrons irradiation. *Applied Solar Energy,* 59(5), 604–611. https://doi.org/10.3103/S0003701X23600984

3 Utamuradova Sh.B., Terukov E.I., Ataboev O.K., Panaiotti I.E., Kabulov R.R., Troshin A.V. (2025) Influence of 1 MeV electron irradiation on the output parameters of silicon heterojunction solar cells. *Nuclear Instruments and methods in physics research section B: Beam interactions with materials and atoms*, 560, 165630. https://doi.org/10.1016/j.nimb.2025.165630

4 Verduci R., Romano V., Brunetti G., Nia N.Y., Carlo A.D., D'Angelo G., Ciminelli C. (2022) Solar energy in space applications: review and technology. *Advanced Energy Materials*, 12(29), 2200125. https://doi.org/10.1002/aenm.202200125

5 Li J., Aierken A., Liu Y., Zhuang Y., Yang X., Mo J.H., Fan R.K., Chen Q.Y., Zhang S.Y., Huang Y.M., Zhang Q. (2021) A brief review of high efficiency III-V solar cells for space application. *Frontiers in Physics*, 8, 631925. https://doi.org/10.3389/fphy.2020.631925

6 Yamaguchi M., Takamoto T., Araki K., Ekins-Daukes N. (2005) Multi-junction III-V solar cells: Current status and future potential. *Solar Energy*, 79(1), 78–85. https://doi.org/10.1016/j.solener.2004.09.0186

7 Suzuki A., Kaneiwa M., Saga T., Matsuda S. (1999) Progress and future view of silicon space solar cells in Japan. *IEEE Transactions on Electron Devices*, 46(10), 2126–2132. https://doi.org/10.1109/16.792007

8 Rehman, A.U., Lee, S.H. & Lee, S.H. (2016) Silicon space solar cells: progression and radiation-resistance analysis. *Journal of the Korean Physical Society,* 68, 593–598. https://doi.org/10.3938/jkps.68.593

9 Kaltenbrunner M., Adam G., Glowacki E.D., Drack M., Schwödiauer R., Leonat L., Apaydin D.H., Groiss H., Scharber M.C., White M.S., Sariciftci N.S., Bauer S. (2015) Flexible high power-per-weight perovskite solar cells with chromium oxide-metal contacts for improved stability in air. *Nature Materials*, 14, 1032-1039. https://doi.org/10.1038/nmat4388

10 Fernandez J., Janz S., Suwito D., Oliva E., Dimroht F. (2008) Advanced concepts for high- efficiency germanium photovoltaic cells. *Proceeding of the 33rd IEEE Photovoltaic Specialists Conference*, San Diego, CA, USA. https://doi.org/10.1109/PVSC.2008.4922631

11 Nishioka K., Takamoto T., Agui T., Kaneiwa M., Uraoka Y., Fuyuki T. (2006) Evaluation of InGaP/InGaAs/Ge triple-junction solar cell and optimization of solar cell's structure focusing on series resistance for high-efficiency concentrator photovoltaic systems. *Solar Energy Materials and Solar Cells*, 90(9), 1308–1321, https://doi.org/10.1016/j.solmat.2005.08.003

12 Green M.A., Dunlop E.D., Yoshita M., Kopidakis N., Bothe K., Siefer G., Hao X., Jiang J.Y. (2025) Solar cell efficiency tables (Version 66). *Progress in Photovoltaics: Research and applications*, 33(7), 795–810. https://doi.org/10.1002/pip.3919

13 Joseph K.L.V., Rosana N.T.M., Kumar J.A., Samrot A.V. (2025) Commercial bifacial silicon solar cells – Characteristics, module topology and passivation technique for high electrical output: An overview. *Results in Engineering,* 26, 104971. https://doi.org/10.1016/j.rineng.2025.104971

14 Le A.H.T., Dreon J., Michel J.I., Boccard M., Bullock J., Borojevic N., Hameiri Z. (2022) Temperature-dependent performance of silicon heterojunction solar cells with transition-metal-oxide-based selective contacts. *Progress in Photovoltaics: Research and applications*, 30, 981–993. https://doi.org/10.1002/pip.3509

15 Le A.H.T., Basnet R., Yan D., Chen W., Nandakumar N., Duttagupta Sh., Seif J.P., Hameiri Z. (2021) Temperature-dependence performance of silicon solar cells with polysilicon passivating contacts. *Solar Energy Materials and Solar Cells*, 225, 111020. https://doi.org/10.1016/j.solmat.2021.111020

16 Haschke J., Seif J.P., Riesen Y., Tomasi A., Cattin J., Tous L., Choulat P., Aleman M., Cornagliotti E., Uruena A., Russell R., Duerinckx F., Champliaud J., Levrat J., Abdallah A.A., Aissa B., Tabet N., Wyrsch N., Despeisse M., Szlufcik J., Wolf S.D., Ballif C. (2017) The impact of silicon solar cell architecture and cell interconnection on energy yield in hot and sunny climates. *Energy and environmental science*, 10(5), 1–11. https://doi.org/10.1039/C7EE00286F

17 Cardinaletti I., Vangerven T., Nagels S., Cornelissen R., Schreurs D., Hruby J., Vodnik J., Devisscher D., Kesters J., D'Haen J., Franquet A., Spampinato V., Conard T., Maes W., Deferme W., Manca J.V. (2018) Organic and perovskite solar cells for space application. *Solar Energy Materials and Solar Cells*, 182, 121-127. https://doi.org/10.1016/j.solmat.2018.03.024

18. Ataboev O.K., Terukov E.I., Shelopin G.G., Kabulov R.R. (2021) Wet chemical treatment of monocrystalline silicon wafer surfaces. *Applied Solar Energy*, 57(5), 363–369. https://doi.org/10.3103/S0003701X21050042

19 Hammann B., Schindler F., Schön J., Kwapil W., Schubert M.C., Glunz S.W. (2025) Review on hydrogen in silicon solar cells: From its origin to its detrimental effects. *Solar Energy Materials and Solar Cells*, 282, 113432. https://doi.org/10.1016/j.solmat.2025.113432

20 Han H., Jia X., Ma C., Wu Y. (2022) A novel laser scribing method combined with the thermal stress cleaving for the crystalline silicon solar cell separation in mass production. *Solar Energy Materials and Solar Cells*, 240, 111714. https://doi.org/10.1016/j.solmat.2022.111714

21 Witteck R., Hinken D., Schulte-Huxel H., Vogt M.R., Müller J., Blankemeyer S., Köntges M., Bothe K., Brendel R. (2016) Optimized interconnection of passivated emitter and rear cells by experimentally verified modeling. *IEEE Journal of Photovoltaics*, 6(2), 432-439. https://doi.org/10.1109/JPHOTOV.2016.2514706

22 Bludau W., Onton A., Heinke W. (1974) Temperature dependence of the band gap of silicon. *Journal of Applied Physics,* 45(4), 1846–1848. https://doi.org/10.1063/1.1663501

23 Ataboev O.K., Kabulov R.R., Matchanov N.A., Egamov S.R. (2019) Influence of temperature on the output parameters of a photovoltaic module based on amorphous hydrogenated silicon. *Applied solar energy*, 55(3), 159–167. https://doi.org/10.3103/S0003701X19030022

24 Löper P., Pysch D., Richter A., Hermle M., Janz S., Zacharias M., Glunz S.W. (2012) Analysis of the temperature dependence of the open-circuit voltage. *Energy Procedia*, 27, 135-142. https://doi.org/10.1016/j.egypro.2012.07.041

25 Utamuradova Sh.B., Terukov E.I., Ataboev O.K., Panaiotti I.E., Baranov A.I., Mikhaylov O.P. (2025) A study on the influence of temperature on the output parameters of silicon heterojunction solar cells. *Journal of computational electronics*, 24, 162. https://doi.org/10.1007/s10825-025-02400

26 Ataboev O.K., Utamuradova Sh.B., Panaiotti I.E., Terukov E.I., Malevskiy D.A., Baranov A.I., Troshin A.V. (2026) Temperature dependence of photovoltaic performance of silicon heterojunction solar cells based on gallium- and

phosphorous-doped silicon wafers. *Radiation Physics and Chemistry*, 240, 113407. https://doi.org/10.1016/j.radphyschem.2025.113407

27 Panaiotti I.E., Terukov E.I. (2019) A study of the effect of radiation on recombination loss in heterojunction solar cells based on single-crystal silicon. *Technical physics letters*, 45(3),193–196. https://doi.org/10.1134/S106378501903012X

28 Panaiotti I.E., Terukov E.I., Shakhrai I.S. (2020) A method for calculating operating characteristics of silicon heterojunction solar cells with arbitrary parameters of crystalline wafers. *Technical physics letters*, 46, 835–837. https://doi.org/10.1134/S1063785020090072

29 Bernardini S., Bertoni M.I. (2019) Insights into the degradation of amorphous silicon passivation layer for heterojunction solar cells. *Physica status solidi (a)*, 216(4), 1800705. https://doi.org/10.1002/pssa.201800705

30 Singh P., Ravindra N.M. (2012) Analysis of series and shunt resistance in silicon solar cells using single and double exponential models. *Emerging materials research,* 1(1), 33 – 38. https://doi.org/10.1680/emr.11.00008

31 Fahrenbruch A.L., Bube R.H., (1983). *Fundamentals of solar cells. Photovoltaic solar energy conversion*. London. https://doi.org/10.1016/B978-0-12-247680-8.X5001-4

32 Büyükbaş-Uluşan A., Turan R., Altındal Ş. (2025) On the investigation of current transport mechanisms (CTMs) of the crystalline Si solar cells utilizing current/voltage (I-V) characteristics in temperature range of 110-380 K. *Journal of materials science: Materials in electronics*, 36, 1173. https://doi.org/10.1007/s10854-025-15235-7

33 Durpe O., Vaillon R., Green M.A. (2015) Physics of the temperature coefficients of solar cells. *Solar Energy Materials and Solar Cells*, 140, 92-100. https://doi.org/10.1016/j.solmat.2015.03.025

34 Green M.A. (2003). General temperature dependence of solar cell performance and implications for device modelling. *Progress in Photovoltaics: Research and Applications*, 11(5), 333-340. https://doi.org/10.1002/pip.496

35 Woodyard J.R., Landis G.A. (1991) Radiation resistance of thin-film solar cells for space photovoltaic power. *Solar cells*, 31(4), 297. https://doi.org/10.1016/0379-6787(91)90103-V

AUTHORS' INFORMATION:

Utamuradova, Sharifa Bekmuradovna – DSc, Professor, Semiconductor Physics and Microelectronics research institute, Tashkent, Uzbekistan; Scopus Author ID: 6506286512; https://orcid.org/0000-0002-1718-1122; sh-utamuradova@yandex.com

Terukov, Evgeniy Ivanovich – DSc, Professor, Ioffe Institute, Russian Academy of Sciences, St. Petersburg, Russia; Scopus Author ID: 9236174500; https://orcid.org/0000-0002-5226-1101; eug.terukov@mail.ioffe.ru

Ataboev, Omonboy Kurbanboevich – PhD, Senior researcher, Semiconductor Physics and Microelectronics research institute, Tashkent, Uzbekistan; Scopus Author ID: 54890775800; https://orcid.org/0000-0002-5226-1101; omonboy12@mail.ru

Kabulov, Rustam Rashidovich – PhD, Senior researcher, Physical-technical Institute Uzbekistan Academy of Sciences, Tashkent, Uzbekistan; Scopus Author ID: 6602800668; https://orcid.org/0000-0003-3157-9038; krr1982@bk.ru

Panaiotti, Irina Evgenevna – PhD, Senior researcher, Ioffe Institute, Russian Academy of Sciences, St. Petersburg, Russia; Scopus Author ID: 6504074762; https://orcid.org/0000-0003-1233-7973; panaiotti@mail.ioffe.ru

Uzakbayeva, Nargiza Sansizbayevna – Master, Senior Lecturer, Nukus state technical university, Nukus, Uzbekistan; https://orcid.org/0009-0008-3900-2421; nargizauzakbaeva4@gmail.com

EURASIAN PHYSICAL TECHNICAL JOURNAL

2026, Volume 23, No.1 (55)

https://doi.org/10.31489/2026N1/34-47

Received: 16/09/2025 Revised: 08/02/2026 Accepted: 19/03/2026

Original Research Article

UDC 536.8

PHYSICAL PROPERTIES OF A FREE-PISTON STIRLING ENGINE WITH A REVERSIBLE CHEMICAL REACTION OF DIOXSIDE NITROGEN ↔ TETRAOXSIDE NITROGEN IN THE WORKING GAS

Sabdenov K. O., Konysbekova G. K.

L.N. Gumilyov Eurasian National University, Astana, Republic of Kazakhstan

**Corresponding author*: gulbarshyn_1991@mail.ru

Abstract. *Simulation is used to study the properties of a free-piston Stirling engine in the isothermal approximation. The working substance is a chemically reacting gas mixture, in which mutual conversion of nitrogen dioxide and nitrogen tetroxide can occur in the reversible reaction* $2NO_2 \leftrightarrow N_2O_4$*. In the cooler, the exothermic reaction* $2NO_2 \rightarrow N_2O_4$ *occurs, in the heater at a high temperature, the endothermic reaction* $N_2O_4 \rightarrow 2NO_2$ *occurs. Two cases are compared: 1) the above chemical reaction occurs in the working gas, and 2) the working gas is chemically inert. The engine efficiency* η_{eng} *is higher in the first case over the range of heater temperature change from 90 to 130 °C, and where* η_{eng} *increases from 0.345 to 0.383. In this case,* η_{eng} *turns out to be higher than that calculated using the Carnot formula with the same maximum and minimum temperatures. High efficiency is achieved thanks to the engine's ability to produce negative E. Schrödinger entropy.*

Keywords: free-piston Stirling engine, working gas with a reversible chemical reaction, nitrogen dioxide and nitrogen tetroxide.

1. Introduction

In recent scientific works [1-8] much attention has been paid to the production of mechanical work or electrical energy in thermodynamic systems with a reversible chemical reaction. The results of works [1, 2] predict the possibility of increasing the efficiency of thermodynamic cycles due to the reversible chemical reaction occurring in the working gas. In such cycles, under certain conditions, chemical work plays a significant role in the energy balance; it facilitates the conversion of heat into mechanical work. Using the properties of reversible chemical reactions to increase the efficiency of energy systems and production is not new. Substances where such reactions can occur are considered as energy accumulators in thermal power plants and other types of electricity production from low-potential heat sources [3-8]. Due to the reversibility of electrochemical reactions and thermodynamic cycles based on them, modern storage batteries exist [7, 8]. There are also earlier theoretical works [9-11] that show the possibility of creating Stirling engines with a reversible chemical reaction in the working gas and which will have a significantly higher efficiency than similar engines, but with a chemically inert working gas.

To achieve high efficiency in thermodynamic cycles with a reversible chemical reaction and a gas working substance, several conditions must be met [1, 2]:

– at the compression stage, the gas must have a high molecular weight, and at the expansion stage, a low one;

– the value of chemical work must be such as to completely or partially compensate for the heat release in the reverse chemical reaction in the cooler; this reduces the amount of heat released into the surrounding space;

– the temperatures of the heater and cooler should not differ greatly; this determines the condition for the existence of the cycle.

In [2], the analysis of the Stirling cycle with a reversible chemical reaction was carried out under the assumption of equilibrium processes in all four of its sections. Under the condition of the existence of a cycle, a reversible chemical reaction behaves as a periodic reaction, and the heat engine becomes similar to a biological object. In the simplest model, a chemical reaction is represented as a mutual transformation of two substances; the relative concentration of one of the substances g_A is added to the familiar thermodynamic parameters of pressure p, temperature T and specific volume υ. Then the cycle under consideration is depicted in three-dimensional space (Fig. 1, a), and it can be projected onto the well-known two-dimensional plane (Fig. 1, b). To analyze thermodynamic cycles with multicomponent reversible chemical reactions, it is necessary to move to a space of even higher dimensionality.

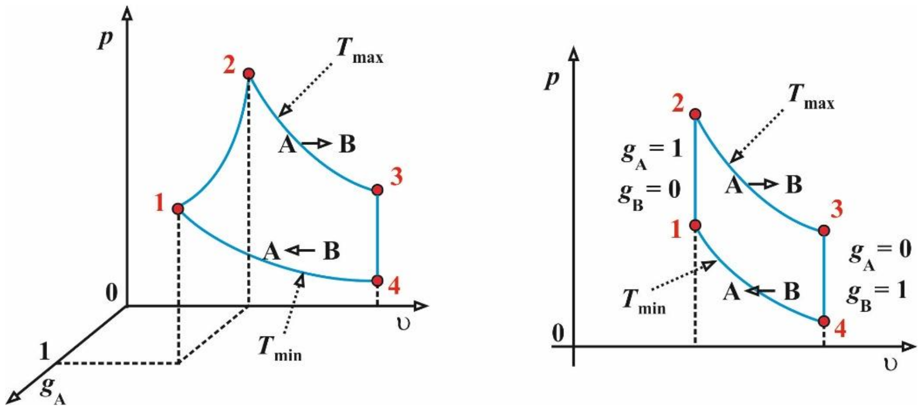

a) b)

Fig. 1. Ideal Stirling cycle with reversible chemical reaction A ↔ B (a) in three-dimensional space of variables p-υ-g_A and its projection onto the p-υ plane (b).

Such consideration of cycles in a multidimensional space of variables allows us to better understand the thermodynamic properties of heat engines with reversible chemical reactions; for example, in [7, 8] it is proposed to use the coordinates of temperature T, entropy S and Gibbs free energy G; the convenience of using the Gibbs energy as the third coordinate is manifested in its direct dependence on the concentration g_A.

According to the results of studies [1, 2], under certain conditions the efficiency of a heat engine can approach 1, and this indicates the possibility of creating better methods for producing electricity, especially from low-potential heat sources. Such theoretical conclusions need to be verified on physical experimental devices or on their virtual computer models. In this paper, the second method, also known as a computational experiment, is chosen. In particular, the operation of a Stirling engine with a free working piston is studied on the basis of a computer model. Its first mathematical model in the isothermal approximation was proposed in [12] and has since become the basis for many theoretical and experimental studies [13-18]. The isothermal approximation means accepting the assumption of a constant working gas temperature in the heater and cooler. The general name "Stirling engine" unites a wide class of mechanical devices operating on the basis of the thermodynamic Stirling cycle [18, 19]. Their mathematical models are represented by several differential equations, and they have (or should have) periodic solutions only when one parameter is not equal to one, and such a parameter is the ratio of the maximum temperature T_{max} (heater) to the minimum temperature T_{min} (cooler) $\Theta = T_{max}/T_{min}$ The models are also characterized by other physical and/or parameters, and may not have periodic solutions when $\Theta \neq 1$. But the fulfillment of this inequality is mandatory for the existence of periodic solutions.

The aim of this work is to search for and identify opportunities to achieve high efficiency in a Stirling engine with a reversible chemical reaction in the working gas $2NO_2 \leftrightarrow N_2O_4$. For this purpose, it is necessary at the first stage to conduct a simulation of the operation of a β-type engine, which will allow us to verify the main theoretical results of earlier studies [2, 9, 11].

2. Engine design diagram

The general design of the Stirling engine is shown in Fig. 2, where cooler 6 is the compression volume V_c, and heater 7 is the expansion volume V_e. In volumes V_c and V_e, constant values of temperature T_c and T_e are maintained. They are taken as the minimum and maximum temperature in the engine. The masses of gas in each of the specified volumes are equal to m_c and m_e, respectively. The mass exchange is performed at the rate of mass change in the regenerator m'_r, it is equal to the rates of mass change in the cooler $m'_c = m'_r$ and the heater $m'_c = m'_r$.

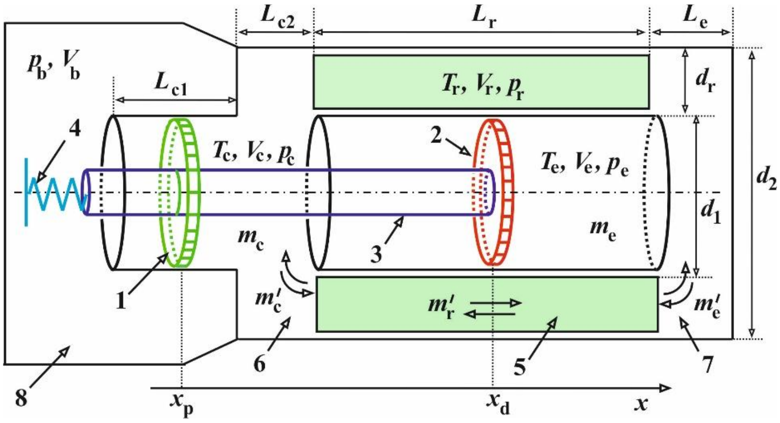

Fig. 2. Simplified diagram of a Stirling engine with a free piston; 1 – working piston; 2 – displacer; 3 – displacer rod; 4 – spring; 5 – regenerator; 6 – cooler; 7 – heater; 8 – buffer space.

Regenerator 5 is an independent part of the engine; it is characterized by its own physical and geometric parameters. Buffer space 8 with volume V_b and pressure p_b is borrowed from work [12], but later studies [21] show its frequent negative impact on engine operation. In the future, the buffer space will be excluded from the model, if necessary, by the limit transition $V_b \to \infty$. Thus, the engine will be considered to consist of three main parts: a heater, a cooler and a regenerator. The working piston 1 in the cooler moves freely along the rod 3 of the displacer 2, the latter two are rigidly connected to each other, and one of the ends of the rod with a diameter d_{rod} is attached to a spring 4 with a stiffness coefficient k_d (coefficient of rigidity of the displacer spring). The displacer can move freely inside the cylinder surrounded by a cylindrical regenerator with a length L_r (L_r and A_r – length and area of the working section of the regenerator) and a working space width d_r. When the working piston moves, an electric current is generated by a linear generator; in Fig. 2, the linear generator is not shown, but its feedback on the operation of the machine is taken into account by the damping coefficient D_p. The parameter D_p depends on the generator design and the properties of the electrical load connected to it, but for the steady-state operating mode of the engine with a constant frequency, it can be considered a freely variable parameter [12].

3. Equations of the free-piston Stirling engine model

The regenerator is represented by a narrow and long channel in the space between two coaxial cylinders with diameters d_1 and $d_2 = d_1 + 2d_r$. The average velocity of one-dimensional gas movement in it with density ρ_r and in the direction of the x coordinate is designated u. For cases of flows when the density of the medium changes slightly with pressure, this velocity is found from the equation of conservation of momentum [21]:

$$\frac{\partial u}{\partial t} + u\frac{\partial u}{\partial x} = -\frac{1}{\rho_r}\frac{\partial p}{\partial x} - \frac{1}{8}\cdot\frac{\zeta\Pi}{A_r}|u|u - \frac{1}{2}\delta(x - x_0)K_r|u|u. \qquad (1)$$

The delta-function $\delta(x - x_0)$ models a sudden change in momentum in a local region folded into a point with coordinate x_0. In typical Stirling machines, the thermal expansion of the gas is small, the pressure also changes little and the compressibility of the gas is insignificant. Therefore, the derivative of the density with respect to time is a small value, compared to convective transfer. As a result, the density ρ_r and the velocity u can only be functions of time. Therefore, instead of (1), we can consider the equation [21]:

$$L_r \frac{du}{dt} = \frac{1}{\rho_r} \Delta p - \frac{1}{8} \zeta \frac{L_r \Pi}{A_r} |u| u - \frac{1}{2} K_r |u| u \,. \tag{2}$$

The pressure difference $\Delta p > 0$ if the gas flows from left to right. For a regenerator (Fig. 2) enclosed in the space between coaxial cylinders, the ratio of the perimeter to the flow area is $\Pi/A_r = 2/d_r$ (height of the working section of the regenerator) (in [21] the erroneous 4 was used instead of 2). The most accurate heater and cooler model should include non-steady-state temperature equations in all parts of the engine [22]. But now the study of the influence of a reversible chemical reaction on the technical characteristics of a free-piston Stirling engine is fundamental. Therefore, the case of constant temperature is considered below, i.e. the isothermal approximation is used [12–14]. The model includes equations of motion of the displacer, piston and gas in the regenerator. The coordinate of the displacer x_d with mass m_d is measured from the equilibrium position $x_{d,0}$, the initial coordinate of the piston x_p with mass m_p coincides with the reference point of the coordinate x. The thickness of the piston and displacer is neglected. Thus, there are notations:

– initial position of the piston $x_{p,0} = 0$;

– initial volume of coolant

$$V_{c,0} = \frac{\pi d_1^2}{4} \frac{L_{c,1} + L_r}{2} + \frac{\pi d_2^2}{4} L_{c,2} - A_{rod} x_{d,0} \,,$$

– cross-sectional area of the rod A_{rod} cross-sectional area of the rod (displacer) and the initial position of the displacer $x_{d,0}$,

$$A_{rod} = \frac{\pi d_{rod}^2}{4}, \qquad x_{d,0} = \frac{L_{c,1} + L_r}{2} + L_{c,2} \,;$$

– initial volume of heater,

$$V_{e,0} = \frac{\pi d_1^2}{4} \frac{L_r}{2} + \frac{\pi d_2^2}{4} L_e \,.$$

As can be seen, the initial position of the displacer $x_{d,0}$ coincides with the coordinate of the center of the regenerator. The gas in the buffer volume is compressed and expanded under adiabatic conditions with an adiabatic index of γ. The external and initial pressure is denoted by p_0.

The equations of motion of the displacer (taking into account the friction force with the coefficient D_d) and the piston have the form

$$m_d \frac{d^2 x_d}{dt^2} + D_d \frac{dx_d}{dt} + k_d (x_d - x_{d,0}) = p_b A_{rod} + p_c A_p - p_e A_d \,, \tag{3}$$

$$m_p \frac{d^2 x_p}{dt^2} + D_p \frac{dx_p}{dt} = (p_b - p_c) A_p \,. \tag{4}$$

The areas of the piston A_p cross-sectional area of the working piston, and the displacer A_d cross-sectional area of the displacer;

are equal

$$A_d = \frac{\pi d_1^2}{4}, \qquad A_p = \frac{\pi (d_1^2 - d_{rod}^2)}{4} \,.$$

Equations (3) and (4) are supplemented by formulas for determining pressures:

$$p_b = p_0 \left(\frac{V_{b,0}}{V_b} \right)^{\gamma}, \qquad p_c = \frac{R_{g,c} T_c}{V_c} m_c \,, \qquad p_e = \frac{R_{g,e} T_e}{V_e} m_e \,. \tag{5}$$

A change in the chemical composition of the gas leads to a change in the gas constant, the gas composition is different in the heater and cooler. Accordingly, two designations are introduced for the gas constant: $R_{g,c}$ and $R_{g,e}$. The volumes contained in (5) are found using the formulas

$$V_c = V_{c,0} + A_p (x_d - x_{d,0} - x_p), \tag{6}$$

$$V_{\mathrm{e}} = V_{\mathrm{e},0} - A_{\mathrm{d}}(x_{\mathrm{d}} - x_{\mathrm{d},0}), \quad V_{\mathrm{b}} = V_{\mathrm{b},0} + A_{\mathrm{rod}}(x_{\mathrm{d}} - x_{\mathrm{d},0}) + A_{\mathrm{p}}x_{\mathrm{p}}.$$

The masses of gas in the displacer m_{c} and the heater m_{e} are determined by solving the equations

$$\frac{dm_{\mathrm{c}}}{dt} = -m'_{\mathrm{r}}, \quad \frac{dm_{\mathrm{e}}}{dt} = m'_{\mathrm{r}}. \tag{7}$$

The mass flow rate of gas in the regenerator m'_{r} is found from equation (2) and this issue is discussed below. The pressure p_{r} and temperature T_{r} in the regenerator are taken as the average values in the heater and cooler:

$$p_{\mathrm{r}} = \frac{p_{\mathrm{e}} + p_{\mathrm{c}}}{2}, \quad T_{\mathrm{r}} = \frac{T_{\mathrm{e}} + T_{\mathrm{c}}}{2}. \tag{8}$$

Equalities (8) mean the adoption of a linear dependence on the x coordinate of the change in pressure and temperature in the regenerator. Then the gas density in the regenerator ρ_{r} is determined from the equation of state

$$\rho_{\mathrm{r}} = \frac{p_{\mathrm{r}}}{T_{\mathrm{r}}R_{\mathrm{g}}}, \tag{9}$$

where the average gas constant R_{g} is defined as $R_{\mathrm{g}} = (R_{\mathrm{g,c}} + R_{\mathrm{g,e}})/2$.

Equation (9) is necessary to find the mass of gas in the regenerator m_{r}. The density ρ_{r} can be determined more accurately by calculating its average value using the linear functions $p(x)$ and $T(x)$ and the equation of state of the gas for the regenerator [12]. But such averaging, leading to a complex expression, does not provide significant advantages over (9). In Figure 2, between the regenerator and the volumes V_{c} and V_{e}, there are local sections of gas flow reversal; they are included in the regenerator and are characterized by the coefficient K_{r}.

Equation (2) can also be written for the mass flow rate $m'_{\mathrm{r}}(t) = u(t)\rho_{\mathrm{r}}A_{\mathrm{r}}$. Using this definition and taking into account the constancy of the density ρ_{r}, we write the equation for the flow rate,

$$\frac{dm'_{\mathrm{r}}}{dt} = \frac{A_{\mathrm{r}}}{L_{\mathrm{r}}}\Delta p - \frac{1}{2}\frac{K_{\Sigma}|m'_{\mathrm{r}}|}{m_{\mathrm{r}}}m'_{\mathrm{r}}, \tag{10}$$

$$K_{\Sigma} = K_{\mathrm{r}} + \frac{L_{\mathrm{r}}}{2d_{\mathrm{r}}}\zeta, \quad m_{\mathrm{r}} = \rho_{\mathrm{r}}L_{\mathrm{r}}A_{\mathrm{r}} = \rho_{\mathrm{r}}V_{\mathrm{r}}, \quad V_{\mathrm{r}} = L_{\mathrm{r}}A_{\mathrm{r}}. \tag{11}$$

According to Figure 2, the positive direction of gas movement corresponds to the positive sign of the pressure difference Δp, therefore it should be $\Delta p = p_{\mathrm{c}} - p_{\mathrm{e}}$. Since the regenerator is a porous (mesh) structure made of thin metal wire [19, 20], then in the determination of the gas volume V_{r} in the general case, the porosity should be added as a factor. Porosity should also be taken into account in determining the coefficient ζ. Here it is assumed that the porosity is close to one.

4. Accounting for changes in the composition of the working gas

In volumes V_{c} and V_{e}, first-order chemical reactions occur at constant temperatures $T_{\mathrm{c}} = T_{\mathrm{min}}$ and $T_{\mathrm{e}} = T_{\mathrm{max}}$. In the first of them, the chemical transformation (reverse reaction) occurs according to the scheme B → A at a rate of k_{c}, and in the second (forward reaction) — according to the scheme A → B at a rate of k_{e}. At the same time, a mass of gas enters (or leaves) these volumes at a rate of m'_{r}. That is, in each of them there can be two sources of substances of types A and B. Each of them in an arbitrary volume has a mass of m_{A} and m_{B}, their sum is always equal to the total mass of gas in this volume. Substances A and B are characterized by relative mass concentrations g_{A} and g_{B}, their sum is equal to

$$g_{\mathrm{A}} + g_{\mathrm{B}} = 1. \tag{12}$$

For simplicity, the chemical transformation inside the regenerator is not taken into account. The simple relationship (12) between the concentrations allows us to use the equations for only one of them, for example, g_{B}. The cooler and heater are spatially separated from each other; they differ in the composition of the gas in them. Therefore, the mass concentration g_{B} will be determined in different ways. Therefore, below g_{B} is supplemented with indices indicating its value in V_c and V_e, i.e. $g_{B,c}$ and $g_{B,e}$. With their help it is possible to determine the gas constants of the mixture in the cooler $R_{g,c}$ and the heater $R_{g,e}$ [23]:

$$R_{g,c}=R\left(\frac{g_{B,c}}{\mu_B}+\frac{1-g_{B,c}}{\mu_A}\right),\qquad R_{g,e}=R\left(\frac{g_{B,e}}{\mu_B}+\frac{1-g_{B,e}}{\mu_A}\right),\tag{13}$$

where R is the universal gas constant; μ_A, μ_B are the molar masses of substances A and B.

4.1. Chemical reaction in the regenerator

The simplest methods are used to model the chemical reaction in all parts of the engine [27]. In particular, in the volume of the regenerator, the rates of the forward and reverse chemical reactions are approximately equal. Since chemical transformation does not occur in the regenerator as a whole, then when calculating the mass of gas in the regenerator m_r, the gas constant in it $R_{g,r}$ is determined by the conditions:

if $m'_r \geq 0$, then $R_{g,r} = R_{g,c}$; if $m'_r < 0$, then $R_{g,r} = R_{g,e}$.

The mass m_r is found from the equation of state

$$m_r=\frac{p_rV_r}{R_{g,r}T_r}.\tag{14}$$

4.2. Chemical reaction in a cooler

Consider the volume V_c and the **1st case** $m'_r > 0$, then the substance B will decrease due to convective entrainment from this volume and due to the chemical reaction. A simple first-order reaction gives a conservation equation for the mass $m_{B,c}$,

$$\frac{dm_{B,c}}{dt}=-g_{B,c}m'_r-m_ck_cg_{B,c}.\tag{15}$$

By definition of relative mass concentration, $g_{B,c} = m_{B,c}/m_c$. Then, taking into account the first equality in (7), equation (15) can be written for $g_{B,c}$:

$$\frac{dg_{B,c}}{dt}=-k_cg_{B,c}.\tag{16}$$

In the **2nd case** $m'_r < 0$ and the content of gas of type B changes both due to the chemical reaction and due to convective transfer from the heater. In the volume V_e the reaction A → B occurs. There its concentration is designated $g_{B,e}$. Now the equation of conservation of mass will take the form

$$\frac{dm_{B,c}}{dt}=-g_{B,e}m'_r-m_ck_cg_{B,c}.$$

After moving here to the concentration $g_{B,c}$, we obtain

$$\frac{dg_{B,c}}{dt}=\frac{g_{B,c}-g_{B,e}}{m_c}m'_r-k_cg_{B,c}.\tag{17}$$

4.3. Chemical reaction in a heater

Here, the chemical reaction is also first order, but now the substance of type B is formed. The equations for concentration are derived in the same way as in the previous example. In the case of $m'_r > 0$, the equation for mass $m_{B,e}$ is obtained

$$\frac{dm_{B,e}}{dt}=g_{B,c}m'_r+m_ek_e(1-g_{B,e}).$$

To move to the equation for the concentration $g_{B,e}$, we use the second equality in (7) and the definition $g_{B,e} = m_{B,e}/m_e$, as a result this gives

$$\frac{dg_{B,e}}{dt}=\frac{g_{B,c}-g_{B,e}}{m_e}m'_r+k_e(1-g_{B,e}).\tag{18}$$

In case $m'_r < 0$, the concentration $g_{B,e}$ is determined from the equation

$$\frac{dg_{\mathrm{B,e}}}{dt} = k_{\mathrm{e}}(1 - g_{\mathrm{B,e}})\,. \tag{19}$$

5. Simulation results

Equations (3), (4), (7), (10) and (16)–(19) are the main ones. To them are added auxiliary equalities (5), (6), (8), (9), (11)–(14) and formulas for calculating the areas A_{p}, A_{d}, A_{rod}, the initial volumes $V_{\mathrm{c},0}$, $V_{\mathrm{e},0}$ and the initial coordinate of the displacer $x_{\mathrm{d},0}$. The choice of initial conditions for the differential equations can be arbitrary, but they should not be physically contradictory. For example, the concentrations $g_{\mathrm{B,e}}$ and $g_{\mathrm{B,c}}$ can only be within the interval from 0 to 1. The initial masses m_{e}, m_{c} and m_{r} are determined using the equation of state of the gas at a pressure p_0. The initial conditions for the piston and the displacer are

$$x_{\mathrm{p}}(t=0) = \left.\frac{dx_{\mathrm{p}}}{dt}\right|_{t=0} = 0; \quad x_{\mathrm{d}}(t=0) = x_{\mathrm{d},0}, \quad \left.\frac{dx_{\mathrm{d}}}{dt}\right|_{t=0} = 1 \text{ m/s}.$$

The initial velocity for the displacer of 1 m/s is necessary to “start” the engine.

The reversible reaction of formation of nitrogen tetroxide $2NO_2 \leftrightarrow N_2O_4$ is considered [24, 25]. At atmospheric pressure and a temperature of about 150 °C, the working gas consists almost entirely of NO_2, which is brown in color. At a temperature of about 0 °C, the working gas acquires a light-yellow color and consists mainly of N_2O_4. It is assumed here that substance A is nitrogen tetroxide N_2O_4 with a molar mass of $\mu_{\mathrm{A}} = 0.092$ kg·mol^{-1}; substance B is nitrogen oxide NO_2 with a molar mass of $\mu_{\mathrm{B}} = 0.046$ kg·mol^{-1}.

At a low temperature T_{c}, the predominant (exothermic) reaction of formation of nitrogen tetroxide occurs according to the scheme

$$\mathrm{B} \overset{k_{\mathrm{c}}}{\rightarrow} \mathrm{A}\,.$$

Its thermal effect is 57 kJ/mol. At high temperature T_{e}, the (endothermic) reaction of formation of nitrogen dioxide occurs according to the scheme

$$\mathrm{A} \overset{k_{\mathrm{e}}}{\rightarrow} \mathrm{B}\,.$$

The efficiency of the equilibrium Stirling cycle with a reversible chemical reaction can be greater than or equal to the efficiency of the equilibrium Carnot cycle with a chemically inert working gas [2]. Cycles with a reversible chemical reaction and having a high efficiency cannot exist at all temperatures of the heater $T_{\max}$ and cooler $T_{\min}$. If we combine the condition for the existence of the cycle and for its efficiency to be higher than that of the Carnot cycle for a chemically inert gas, then a restriction on the ratio follows $\Theta = T_{\max}/T_{\min}$,

$$\alpha_{\mathrm{St}} - (\gamma_{\mathrm{A}} - 1)G_1 \le \Theta \le \alpha_{\mathrm{St}}\,, \tag{20}$$

$$\alpha_{\mathrm{St}} = \frac{\mu_{\mathrm{B}}(\gamma_{\mathrm{B}} - 1)}{\mu_{\mathrm{A}}(\gamma_{\mathrm{A}} - 1)}, \qquad G_1 = \left(1 - \frac{\mu_{\mathrm{A}} - \mu_{\mathrm{B}}}{\mu_{\mathrm{A}}}\frac{\omega}{\omega - 1}\right)\ln\omega\,.$$

Inequalities (20) contain the adiabatic indices γ_{A} and γ_{B}, as well as the ratio of the volumes $\omega > 1$ of the initial and final states at temperature $T_{\max}$. Since in practice we are limited in the possibilities of choosing substances, the smaller the temperature ratio Θ, the easier it is to create heat engines with an efficiency exceeding that of Carnot engines with a chemically inert working gas.

The heat capacity of NO_2 dioxide at constant pressure is $c_{\mathrm{p,B}} = 797$ J·kg^{-1}·K^{-1}(substance B), and that of N_2O_4 tetroxide — $c_{p,\mathrm{A}} = 860$ J·kg^{-1}·K^{-1} (substance A) [26]. The adiabatic indices for these gases can be calculated using the formula [22]

$$\gamma = \left(1 - \frac{R}{c_{\mathrm{p}}\mu}\right)^{-1}.$$

Then the adiabatic index of nitrogen dioxide $\gamma_{\mathrm{B}} = 1.294$, nitrogen tetroxide $\gamma_{\mathrm{A}} = 1.118$. Accordingly, the parameter $\alpha_{\mathrm{St}} = 1.256 > 1$, which satisfies the condition for obtaining high efficiency [2]. The numerical solution of the equations was carried out by the Runge–Kutta method [27] with the second order of accuracy and with different time steps Δt to check the correctness of the obtained results. The data below were obtained with a step $\Delta t = 10^{-4}$ s.

The engine efficiency was determined as follows: first, the mechanical work powers in the cooler $P_{\mathrm{mech,c}}$ and the heater $P_{\mathrm{mech,e}}$ are found using the formulas

$$P_{\mathrm{mech,c}} = (p_{\mathrm{c}} - p_0)A_{\mathrm{p}}\left(\frac{dx_{\mathrm{d}}}{dt} - \frac{dx_{\mathrm{p}}}{dt}\right), \qquad P_{\mathrm{mech,e}} = (p_{\mathrm{e}} - p_0)A_{\mathrm{d}}\frac{dx_{\mathrm{d}}}{dt}.$$

These are alternating quantities, but the useful electrical power is produced regardless of the sign of the powers, so their absolute values are used. Therefore, the total power of the mechanical work of the engine P_{mech} is determined by the equation

$$P_{\mathrm{mech}} = \left|P_{\mathrm{mech,c}}\right| + \left|P_{\mathrm{mech,e}}\right|.$$

The electrical power P_{el} is equal to

$$P_{\mathrm{el}} = D_{\mathrm{p}}\left(\frac{dx_{\mathrm{p}}}{dt}\right)^2.$$

Then, averaging over time (this time is equal to several periods of piston oscillations) is performed for P_{mech} and P_{el}, and the ratio is taken as the engine efficiency η_{eng}

$$\eta_{\mathrm{eng}} = \frac{\langle P_{\mathrm{el}}\rangle}{\langle P_{\mathrm{mech}}\rangle},$$

where angle brackets denote time averages.

Inequality (20) is obtained under the assumption that in the section 1→2 (Fig. 1) the concentration g_{A} exactly reaches the value 1, and the value 0 in the section 3→4. However, this is not observed in the simulation, since the heater and cooler constantly exchange mass, and they have finite dimensions. These factors prevent g_{A} from reaching the extreme values 1 and 0. In addition, the Stirling engine cycle differs from the ideal cycle in Fig. 1, b [12], so the conditions for achieving high efficiency η_{eng} may change and not correspond to the predictions [2]. Figures 3–5 are constructed for the following input parameters (Table 1):

Table 1. Parameters of heater, cooler and regenerator.

Heater	Regenerator	Cooler	Buffer space
$m_{\mathrm{d}} = 4.0$ kg; $k_{\mathrm{d}} = 550$ N·m^{-1}; $D_{\mathrm{d}} = 0.94$ kg·s^{-1}; $d_1 = 0.8$ m; $d_2 = 1.1$ m; $L_{\mathrm{e}} = 0.7$ m; $k_{\mathrm{e}} = 9.0$ s^{-1}; $T_{\mathrm{max}} = 383$ K; $x_{\mathrm{d,0}} = 2.73$ m	$d_{\mathrm{r}} = 0.15$ m; $L_{\mathrm{r}} = 1.75$ m; $K_{\mathrm{r}} = 0.05$; $\zeta = 0.06$	$m_{\mathrm{p}} = 3.0$ kg; $D_{\mathrm{p}} = 230$ kg·s^{-1}; $d_{\mathrm{rod}} = 0.05$ m; $L_{\mathrm{c,1}} = 2.0$ m; $L_{\mathrm{c,2}} = 0.85$ m; $k_{\mathrm{c}} = 8.0$ s^{-1}; $T_{\mathrm{min}} = 273$ K	$p_0 = 10^5$ Pa; $\gamma = 1.37$

The buffer volume $V_{\mathrm{b,0}} = 10^5$ m^3, i.e. it is much larger than the volumes of the cooler and heater, so it has virtually no effect on engine operation. The reaction rates k_{c} and k_{e} are selected so that the concentrations of NO_2 and N_2O_4 approximately correspond to the experimental data [25]. The steady-state average powers and efficiencies obtained in the simulation are $\langle P_{\mathrm{el}}\rangle = 13.15$, $\langle P_{\mathrm{mech}}\rangle = 36.28$ kW; $\eta_{\mathrm{eng}} = 0.365$. The oscillation clock frequency $f = 1.56$ Hz.

The average concentration of NO_2 in the cooler $g_{\mathrm{B,c}} = 0.12$, in the heater $g_{\mathrm{B,e}} = 0.67$. The initial changes in concentration over 20 seconds are shown in Fig. 3. If the process in the engine occurred according to the Carnot cycle, the efficiency would be equal to $\eta_{\mathrm{C}} = 1 - T_{\mathrm{min}}/T_{\mathrm{max}} = 1 - 273/383 = 0.287 < \eta_{\mathrm{eng}}$. This result agrees with the conclusion of work [2]. The initial period of engine operation is unstable, the amplitudes of piston and displacer oscillations quickly increase over 12 seconds, but then tend to constant values. But their speeds of movement change greatly in the initial 0.84 seconds, when the working piston shifts to the average position of 0.74 m. The displacer practically remains in the initial position.

Fig. 4 shows the powers P_{mech} and P_{el} only during periods of stable engine operation. Below, the words "stable mode" are applied to large periods of time, when any significant influence of the initial conditions on subsequent engine operation is excluded. Since the pressure p_c differs little from the initial value p_0, the thermodynamic cycle in the cooler is shown in Fig. 5 in coordinates (V_c; $p_c - p_0$).

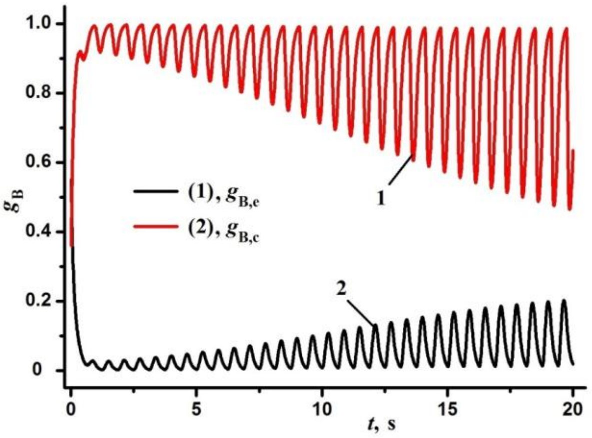

Fig. 3. Changes in the concentration of $g_{B,c}$ and $g_{B,e}$ for 20 s after "launch".

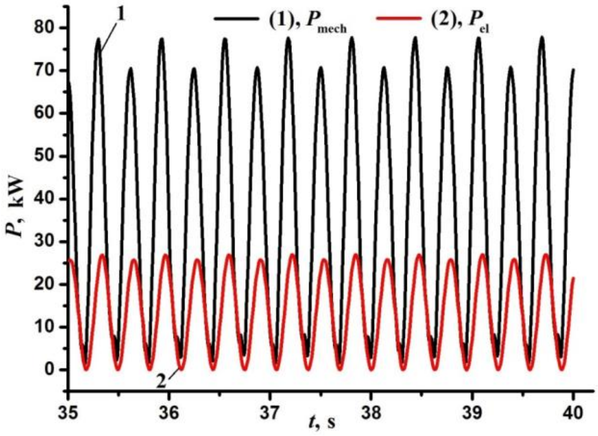

Fig. 4. Changes in powers P_{el} and P_{mech} during averaging time from 35 to 40 s.

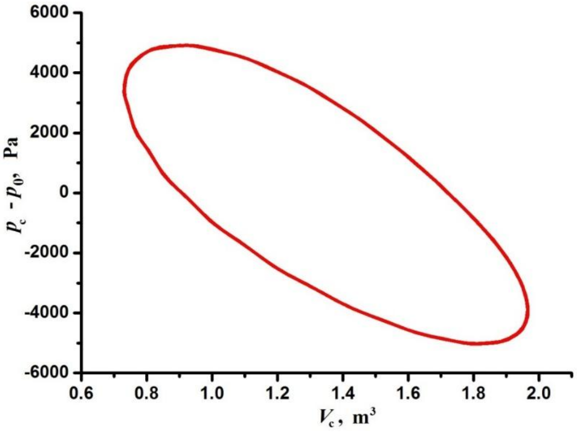

Fig. 5. Representation of the thermodynamic cycle in a Stirling engine with a free working piston. Weak wave-like distortions on the curve are introduced by errors in rounding off the numerical data.

5.1. Operation of a Stirling engine with a chemically inert working gas

Let us consider the operation of the engine without a chemical reaction in the working substance. For this, it is sufficient to take $\mu_A = \mu_B = 0.046$ kg·mol^{-1} in the model; now the working substance consists of one relatively light gas with the same molar mass as nitrogen dioxide gas. Formally, the chemical reaction remains in the model, but it does not lead to physical changes and does not affect the operation of the engine.

Now, stable operation at long times is possible with a lower friction coefficient $D_d = 0.52$ kg·s^{-1} (with the previous $D_p = 230$ kg·s^{-1}). The absence of a change in the molecular weight of the working gas reduced the produced electrical power and efficiency: $\langle P_{el} \rangle = 5.1$, $\langle P_{mech} \rangle = 31.4$ W; $\eta'_{eng} = 0.162$. In addition to the efficiency drop, there was also a strong reduction in the engine's output power; electrical power decreased by 2580 times, mechanical power by 1160 times. Now $\eta_C > \eta'_{eng}$, this result is consistent with the thermodynamics of cycles without a reversible chemical reaction.

5.2. Effect of temperature on the electrical efficiency of the engine

It makes sense to consider noticeable changes in the composition of the working gas in the temperature range from 0 to 170 °C, this is due not only to the peculiarity of the chemical reaction $2NO_2 \leftrightarrow N_2O_4$, but also to the phase state of the working gas [25]. At temperatures below 0 °C, the N_2O_4 gas passes into a liquid state and crystallizes at −11 °C. Therefore, it makes sense to consider the issue of the effect of temperature on the electrical efficiency of the engine with a small change in temperature $T_{\max}$ (Table 2).

Together with the temperature $T_{\max}$, the total mechanical power $<P_{\text{mech}}>$ also increases, which means greater heat consumption from its source. But the rate of growth of the electrical power $<P_{\text{el}}>$ outpaces it, which is evident from the increase in the efficiency η_{eng}. With the increase in temperature, the amplitude of the oscillations of the displacer and the working piston also increases.

Table 2. Results of the dependence of the main engine parameters on the heater temperature $T_{\max}$ at $D_p = 230$ kg·s^{-1}.

№	$T_{\max}$, K ($T_{\max}$, °C)	$<P_{\text{el}}>$, kW	$<P_{\text{mech}}>$, kW	η_{eng}
1	363 (90)	10.78	31.29	0.345
2	373 (100)	12.10	33.90	0.357
3	383 (110)	13.15	36.28	0.365
4	393 (120)	14.46	38.71	0.373
5	403 (130)	17.00	44.41	0.383

Therefore, to simulate the operation of the engine at higher temperatures, it is necessary to increase its length to give more freedom of movement to the moving parts of the engine.

6. Production of negative entropy

Erwin Schrödinger [29] explained the ability of biological objects to perform mechanical work as the consumption of negative entropy. However, Schrödinger's position is based only on physical intuition; he did not provide specific examples or models to prove the correctness of his views. In [1, 2], attention is drawn to the similarity between heat engines with a reversible chemical reaction and biological objects. There were two reasons for this: 1) such machines can have very high efficiency with a small difference in temperatures between the heater and the refrigerator; 2) they can exist only in a relatively narrow temperature range. It will be shown below that this analogy is deeper. If the working substance of a heat engine changes its properties as a result of a chemical reaction, then the first law of thermodynamics is written taking into account the chemical work w_{ch} [30]. For example, for the reaction A ↔ C involving substances A and C with constant heat capacities $c_{\upsilon,\text{A}}$ and $c_{\upsilon,\text{C}}$ this law can be written as [1]

$$c_{\upsilon} dT + dw_{\text{ch}} + dw = dq\,,$$

$$dw = -p d\upsilon, \quad dw_{\text{ch}} = (c_{\upsilon,\text{A}} - c_{\upsilon,\text{C}}) T dg_{\text{A}}\,, \quad c_{\upsilon} = (c_{\upsilon,\text{A}} - c_{\upsilon,\text{C}}) g_{\text{A}} + c_{\upsilon,\text{C}}\,.$$

Now the exergy will contain the sum of mechanical w and chemical work w_{ch}, i.e. $q_{\text{ex}} = w + w_{\text{ch}}$. The change in chemical work dw_{ch} is determined mainly by the change in the relative mass concentration g_{A} of substance A. This is sufficient, since the mass concentration g_{C} of substance C is easily determined through g_{A}: $g_{\text{C}} = 1 - g_{\text{A}}$. Let us apply Schrödinger's explanation of life to heat engines and thermodynamic cycles. If we consider a biological object as a heat engine, then in an ideal and equilibrium process the entropy q_{in} entering the machine together with heat

$$ds_{\text{in}} = \frac{dq_{\text{in}}}{T}$$

at temperature T it is partially converted into entropy of exergy

$$ds_{\text{ex}} = \frac{dq_{\text{ex}}}{T} = \frac{dw}{T} + \frac{dw_{\text{ch}}}{T}\,,$$

and the rest

$$d_e s = \frac{dq_{\text{out}}}{T}\,,$$

together with heat q_{out} is emitted into the environment. The processes occurring in an ideal heat engine from the point of view of entropy production can be represented by the equality

$$ds_{\text{in}} = ds_{\text{ex}} + d_e s\,, \quad \text{or,} \quad \frac{dq_{\text{in}}}{T} = \frac{dq_{\text{ex}}}{T} + \frac{dq_{\text{in}}}{T}\,.$$

Integrating over the entire cycle gives

$$\oint \frac{dq_{\text{in}}}{T} = \oint \frac{dq_{\text{ex}}}{T} + \oint \frac{dq_{\text{out}}}{T}\,. \tag{21}$$

The application of equation (21) for the Carnot cycle (Fig. 6) and with a reversible chemical reaction can be written as an equality

$$\frac{q_{\text{in}}}{T_{\max}} = \Delta s_{\text{ex}} + \frac{q_{\text{out}}}{T_{\min}}\,, \quad \Delta s_{\text{ex}} = \oint \frac{dq_{\text{ex}}}{T}\,, \tag{22}$$

где $T_{\min}$ и $T_{\max}$ – минимальная (охладителя) и максимальная (нагревателя) температура.

The Carnot cycle with a reversible chemical reaction is represented in a three-dimensional space of variables s, T and g_A (Fig. 6, *a*). In this way it differs fundamentally from the known cycle with a chemically inert working substance.

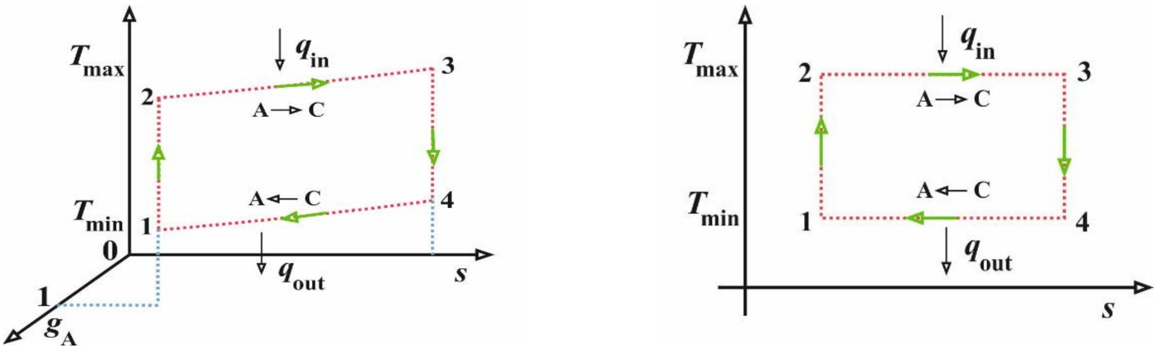

a) *b*)

Fig. 6. Carnot cycle with a reversible chemical reaction in the working substance in s-T-g_A coordinates (a) and its projection in s-T coordinates (b).

In (22) $\Delta s_{\text{ex}} = 0$ for a chemically inert working substance, but in the general case equality to zero may not be fulfilled. From (22) the removed heat is determined

$$q_{\text{out}} = \frac{T_{\min}}{T_{\max}} q_{\text{in}} - T_{\min} \Delta s_{\text{ex}}\,.$$

Using this result for the efficiency of the Carnot cycle η_C, the following expressions are obtained

$$\eta_{\tilde{N}} = 1 - \frac{T_{\min}}{T_{\max}} + \frac{T_{\min}}{q_{\text{in}}} \Delta s_{\text{ex}}\,, \tag{23}$$

$$\Delta s_{\text{ex}} = \frac{q_{\text{in}}}{T_{\min}} \left(\eta_{\tilde{N}} - \eta_0 \right).$$

Here, for the efficiency of the Carnot cycle with a chemically inert working substance, a separate designation η_0 is introduced,

$$\eta_0 = 1 - \frac{T_{\min}}{T_{\max}}\,. \tag{24}$$

Thus, in (23), the new cycle is compared with a cycle running on a chemically inert working substance. This is not necessary; any known cycle can be taken as a "reference point". But the use of such a Carnot cycle with the efficiency (24) turns out to be the most convenient for interpreting subsequent results. Since the exergies of different cycles differ, the index "ex" is not used below, but is replaced by an index indicating a specific cycle. But this does not mean that the entropy under consideration is not related to the exergy. In addition, in order to preserve Schrödinger's interpretation of the high efficiency of biological objects as a result of consuming negative entropy, the change in entropy taken with a negative sign is further used. For example, for the Carnot cycle $\Delta s_{\mathrm{C}} = -\Delta s_{\mathrm{ex}}$. The efficiency of an ideal Stirling cycle with a reversible chemical reaction η_{St} is determined by the formulas [2]

$$\eta_{\mathrm{St}} = 1 - \frac{T_{\min}}{T_{\max}} G(\omega), \tag{25}$$

$$G(\omega) = \frac{G_{0,1} + G_1}{G_{0,2} + G_1}, \qquad G_1 = \left(1 + \frac{\mu_{\mathrm{C}} - \mu_{\mathrm{A}}}{\mu_{\mathrm{A}}} \frac{\omega}{\omega - 1}\right) \ln \omega,$$

$$G_{0,1} = \frac{1}{\gamma_{\mathrm{C}} - 1} \frac{T_{\max}}{T_{\min}} - \frac{\mu_{\mathrm{C}}}{\mu_{\mathrm{A}}(\gamma_{\mathrm{A}} - 1)}, \qquad G_{0,2} = \frac{1}{\gamma_{\mathrm{C}} - 1} - \frac{\mu_{\mathrm{C}}}{\mu_{\mathrm{A}}(\gamma_{\mathrm{A}} - 1)} \frac{T_{\min}}{T_{\max}}.$$

Here, for the expansion coefficients ω_2 and compression coefficients ω_1, their equality is accepted: $\omega_2 = \omega_1 = \omega$. For the change in entropy in the Stirling cycle Δs_{St}, the equality is satisfied

$$\Delta s_{\mathrm{St}} = \frac{q_{\mathrm{in}}}{T_{\min}} \left(\eta_0 - \eta_{\mathrm{St}}\right). \tag{26}$$

The supplied q_{in} and removed q_{out} heat are defined as [2]

$$q_{\mathrm{in}} = -\frac{R}{\mu_{\mathrm{C}}} T_{\max} (G_{0,2} + G_1), \qquad q_{\mathrm{out}} = -\frac{R}{\mu_{\mathrm{C}}} T_{\min} (G_{0,1} + G_1), \tag{27}$$

$R = 8.31\ \mathrm{J \cdot kg^{-1} \cdot K^{-1}}$.

The results in Figures 7 (*a*, *b*) based on (25)–(27) were obtained for the expansion coefficient $\omega = 1.1$ and this is a realistic value. At $T_{\max} > 340$ K the inequality $\eta_{\mathrm{St}} > \eta_0$ is satisfied and at the same time the change in entropy Δs_{St} becomes negative.

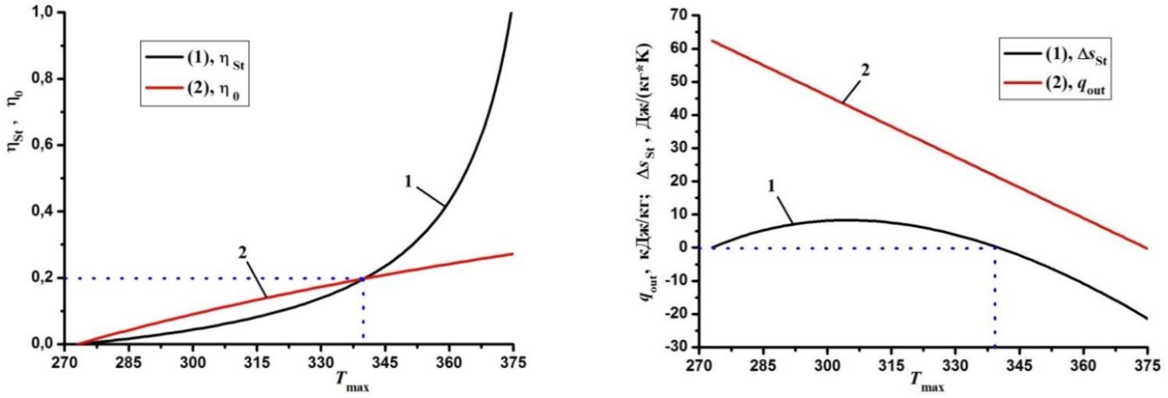

a) *b*)

Fig. 7. Efficiency of the Stirling cycle η_{St} and Carnot η_0 (*a*), as well as changes in entropy Δs_{St} and removed heat q_{in} (*b*) depending on the heater temperature $T_{\max}$.

If we take $\omega = 1.3$, then the inequalities $\eta_{\mathrm{St}} > \eta_0$ and $\Delta s_{\mathrm{St}} < 0$ are satisfied at the maximum temperature $T_{\max}$ of about 330 K. Since the effective flow of the direct reaction $N_2O_4 \rightarrow 2NO_2$ is assumed when obtaining theoretical results (25)–(27), this is possible at pressures below atmospheric. For such pressures, the low-temperature regions in Fig. 7 have a physical meaning. Formula (25) gives overestimated values of the efficiency η_{St} (Fig. 7, a) compared to the simulation data (Table 1). And this difference increases significantly with increasing temperature $T_{\max}$. Most likely, this is due to the influence of friction forces (equations (10) and (11)), as well as the effect of the electrical load, which has a dissipative effect with a coefficient D_{d}.

7. Conclusion

The conducted modeling showed a higher efficiency of the Stirling engine with a reversible chemical reaction $2NO_2 \leftrightarrow N_2O_4$ compared to the same engine, but with a chemically inert working gas. Moreover, the increase in power when switching from a chemically inert gas to a chemically reacting gas is approximately more than a thousand times, and the efficiency increases by 2.25 times. The obtained modeling results confirm the conclusions made in [1, 2].

A Stirling engine with a free working piston has the property of instability of the initial state; this is evident from the need to give an initial impulse to start it. After this, the oscillations that arise in the engine develop with increasing amplitude until the internal friction forces stop this process. If, in modeling, the friction force is taken as a linear dependence on the speed with a friction coefficient D_d, then its numerical value sometimes has to be selected to obtain a stable engine operating mode.

An increase in power and efficiency is also observed with an increase in the heater temperature. At the same time, due to the increase in the amplitude of oscillations of the working piston, it is necessary to lengthen the engine to obtain higher power and efficiency.

A similar study to the one given above was previously conducted in [27], but where the reaction of methanol formation $CO + 2H_2 \leftrightarrow CH_3OH$ was considered. In this case, the engine power was about 1–1.5 kW with close geometric parameters and temperatures. Thus, the use of the reaction $2NO_2 \leftrightarrow N_2O_4$ is more economically advantageous. Engines with a reversible chemical reaction are similar to biological objects [1, 2], but this conclusion was previously made based on their ability to have high efficiency with a small difference in temperature between the heater and cooler. The ability of such engines to produce negative entropy of E. Schrödinger further confirms the conclusions of [1, 2].

Using the isothermal approximation in the presented model can introduce significant changes to the results obtained above. This can primarily be due to large temperature fluctuations in the heater and cooler. Intensive mass and heat exchange can occur between them due to the regenerator. This can lead to a decrease in the average temperature difference between the heater and cooler. However, this can be minimized by increasing their volumes.

Conflict of interest statement

The authors declare that they have no conflict of interest in relation to this research, whether financial, personal, authorship or otherwise, that could affect the research and its results presented in this paper.

CRediT author statement

Sabdenov K.O.: Conceptualization, Methodology, Writing-Review & Editing; **Konysbekova G.K.**: Original Draft, Visualization, Software. The final manuscript was read and approved by all authors;

References

1 Sabdenov K. O. (2021) The thermodynamic Brayton cycle with a reversible chemical reaction. *Tech. Phys.*, 66, 1275–1283. https://doi.org/10.1134/S1063784221090164

2 Sabdenov K. (2023) The Thermodynamics Cycles with a Reversible Chemical Reaction. *Americ. Journ. Modern Phys.*, 12 (2), 14–20. https://doi.org/10.11648/j.ajmp.20231202.11

3 Vialaron A. (1981) Chemical Storage and Pumping of Solar Energy. In: den Ouden, C. (eds) Thermal Storage of Solar Energy. Springer, Dordrecht., 295–307. https://doi.org/10.1007/978-94-009-8302-1_29

4 Williams O. M. (1980) A comparison of reversible chemical reactions for solar thermochemical power generation. *Revue Phys. Appl.*, 15 (3), 453. https://doi.org/10.1051/rphysap:01980001503045300

5 Egenolf-Jonkmanns B., Bruzzano St., Deerberg G. (2012) Low temperature chemical reaction systems for thermal storage. *Energy Procedia*, 30, 235. https://doi.org/10.1016/j.egypro.2012.11.028

6 Jun Li, T. Zeng, N. (2019) Kobayashi, et all. Lithium Hydroxide Reaction for Low Temperature Chemical Heat Storage: Hydration and Dehydration Reaction. *Energies*, 12(19), 3741. https://doi.org/10.3390/en12193741

7 Chen R, Deng S, Xu W, Zhao L. (2019) A graphic analysis method of electrochemical systems for low-grade heat harvesting from a perspective of thermodynamic cycles. *Energy,* 191, 116547, https://doi.org/10.1016/j.energy.2019.116547

8 Ruihua Chen, Weicong Xu, Shuai Deng, Ruikai Zha, Siyoung Q. Choi, Li Zhao. (2023) Towards the Carnot efficiency with a novel electrochemical heat engine based on the Carnot cycle: Thermodynamic considerations. *Energy*, 284, 128577. https://doi.org/10.1016/j.energy.2023.128577

9 Scot T. Martin. (2025) Molar Heat Capacity for Graphical Pedagogy Applied to Heat Engines, Refrigerators, and Heat Pumps Driven by Chemical Change. *Journal of Physical Chemistry A.*, 129 (46), 10762-10770. https://doi.org/10.1021/acs.jpca.5c04285

10 Kovtun I. M., Naumov A. N., Nesterenko V. B. (1967) Stirling cycle on dissociating gas. *Bulletin of the Academy of Sciences of the BSSR, Series of physical and technical sciences* [in Russian]. 1, 52–57.

11 Metwally M.M., Walker G. (1977) Stirling engines with a chemically reactive working fluid — some thermodynamic effects. *Journal Eng. Power,* 99 (2), 284–287. https://doi.org/10.1115/1.3446287

12 Langlois, Justin L. R. (2006) Dynamic computer model of a Stirling space nuclear power system. *Trident Scholar project report no. 345*. – Annapolis: US Naval Academy, https://citeseerx.ist.psu.edu/document?repid=rep1&type=pdf&doi=cd482348cc9b1fe3d06ae79d3e5e64f9e78ca0b7

13 Wong H.M, Goh S.Y. (2020) Experimental comparison of sinusoidal motion and non-sinusoidal motion of rise-dwell-fall-dwell in a Stirling engine. *Journ. Mech. Eng., Sci.,* (JMES)., 14 (3), 6971–6981.

14 Snyman H., Harms T., and Strauss J. (2008) Design analysis methods for Stirling engines. *Journal of Energy in Southern Africa*, 19 (13), 4–19. https://doi.org/10.17159/2413-3051/2008/v19i3a3329

15 Salem Ghozzi, R. Boukhanouf. (2015) Computer Modeling of a Novel Mechanical Arrangement of a Free-Piston Stirling Engine. *Journ. Clean Ener. Techn*., 3 (2), 140–144. https://doi:10.7763/JOCET.2015.V3.184

16 Sutapat Kwankaomeng, Banterng Silpsakoolsook, Pongnarin Savangvong. (2014) Investigation on Stability and Performance of a Free-Piston Stirling Engine. *Energy Procedia*., 52, 598–609.

17 Farid Z. M., Faiz R. M., Rosli A. B. and Kumaran K. (2018) Thermodynamic performance prediction of rhombic-drive beta-configuration Stirling engine. *1st International Postgraduate Conference on Mechanical Engineering* (IPCME 2018). https://doi:10.1088/1757-899X/469/1/012048

18 Dovgyallo A. I., Nekrasova S. O., Sarmin D. V., Pulkina A. Yu. (2020) Free piston pulse tube engine: a numerical and experimental power generation estimation. *Journal of Physics: Conference Series*, 1565 (1):012100. https://doi.org/10.1088/1742-6596/1565/1/012100

19 Zhiwen Dai, Chenglong Wang, Dalin Zhang, Wenxi Tian, Suizheng Qiu, G.H. Su. (2021) Design and analysis of a free-piston Stirling engine for space nuclear power reactor. *Nucl. Eng. Techn*., 53 (2), 637–646. https://doi.org/10.1016/j.net.2020.07.011

20 Fr. Catapano, C. Perozziello, B. M. Vaglieco. (2021) Heat transfer of a Stirling engine for waste heat recovery application from internal combustion engines. *Appl. Therm. Eng*., 198, 117492. https://doi.org/10.1016/j.applthermaleng.2021.117492

21 Sabdenov K.O. (2024) A simple model of a Stirling machine (engine) with a free working piston. *Journ. Engin. Phys. Thermoph*, 97 (4), 1034–1041. https://doi.org/10.1007/s10891-024-02974-3

22 Sabdenov K. O., Erzada M., Zholdybaeva G. T. (2024) Simulation of conductions for achieving high electrical power and efficiency in a Stirling engine with a free piston. *Euras. Phys. Techn. Journ.*, 21(4), 49–60. https://doi.org/10.31489/2024No4/49-60

23 Çengel Y. A., Boles M. A., Kanoglu M. (2024) Thermodynamics: An Engineering Approach.10th ed. New York: McGraw-Hill, 948. https://u.eruditor.one/file/3945201/

24 Jones K. (2013) *The Chemistry of Nitrogen: Pergamon Texts in Inorganic Chemistry*. Oxford: Pergamon Press (Elsevier). 242. https://doi.org/10.1016/c2013-0-05694-0

25 Kirk-Othmer. (2005) *Encyclopedia of Chemical Technology*. John Wiley & Sons. 10, 898. Available at: https://www.abebooks.fr/edition-originale/Encyclopedia-Chemical-Technology-Kirk-othmer-John-Wiley/31582420860/bd

26 Bruce E. Poling, John M. Prausnitz, John P. O'Connell. (2001) *The Properties of gases and liquids. Fifth Edition*. McGraw-Hill Companies., 792. Available at: https://www.ebooks.com/en-us/book/300463/the-properties-of-gases-and-liquids-5e/bruce-e-poling/

27 Sabdenov K. O., Smagulov Zh. K., Erzada M., Zhakataev T. A. (2025) Simulation of a Stirling Engine with a Reversible Reaction CO + 2H2 ↔ CH3OH. *Bulletin of the Karaganda University*: «*Physics Series*», 29(2), 55–66. https://doi.org/10.31489/2025ph2/55-66

28 Kalitkin N. N. (2013) *Numerical methods*. Moscow, Academia, 298. [in Russian] Available at: https://search.rsl.ru/ru/record/01006711380

29 Rob Phillips, Jane Kondev, Julie Theriot, Hernan Garcia. (2012) *Physical Biology of the Cell*. Garland Science. New York. 1088. https://doi.org/10.1201/9781134111589

30 Reid, Charles E. (1990) *Chemical Thermodynamics*. McGraw-Hill College. 332. Available at: https://www.amazon.com/Chemical-Thermodynamics-Charles-Reid/dp/007051769X

AUTHORS' INFORMATION

Sabdenov, Kanysh – Doctor of Phys.-Math. Sciences, Professor, Electrical Engineering Department, Transport and Energy Faculty, L.N. Gumilyov Eurasian National University, Astana, Kazakhstan; https://orcid.org/0009-0008-4733-6667; sabdenovko@yandex.kz

Konysbekova, Gulbarshyn – Master of Technical Sciences, PhD student, Thermal Engineering Department, Transport and Energy Faculty, L.N.Gumilyov Eurasian National University, Astana, Kazakhstan; https://orcid.org/0000-0003-2204-4672 , gulbarshyn_1991@mail.ru

EURASIAN PHYSICAL TECHNICAL JOURNAL

2026, Volume 23, No. 1(55)

https://doi.org/10.31489/2026N1/48-59

Received: 18/11/2025 Revised: 29/01/2026 Accepted: 19/03/2026

Research Article

UDC 53.662

OPTIMIZATION OF THERMAL PROCESSES IN SOLAR BIOGAS PLANT

Sharipov M.Z.[1*], Majitov J.A.[2], Imomov Sh.J.[3], Kovalev I.V.[4], Narzullayev M.N.[5],
Negmatillayev B.[2], Ziyoyev D.A[2]

[1] Bukhara State University, Bukhara, Uzbekistan
[2] Bukhara State Technical University, Bukhara, Uzbekistan
[3] Tashkent Institute of Irrigation and Agricultural Mechanization Engineers "National Research University", Tashkent, Uzbekistan
[4] Siberian Federal University, Krasnoyarsk, Russia
[5] Bukhara State Pedagogical Institute, Bukhara, Uzbekistan

*Corresponding author: m.z.sharipov@rambler.ru

Abstract. *This article presents the results of research devoted to improving the thermal regime of a small-scale biogas plant operating under the conditions of Uzbekistan and utilizing solar energy. The study optimized the constructive and energetic parameters of a cylindrical solar-heated biogas plant. The main part of the plant is a bioreactor equipped with a solar heating system, designed for anaerobic fermentation of organic materials to produce biogas and organic fertilizer (humus). During the research, the amount of solar radiation, daily variations of ambient and bioreactor temperatures, and the dynamics of biogas production were analyzed. The results showed a stable increase in biogas production, which demonstrates the efficiency of using solar energy and highlights the importance of maintaining the optimal thermal regime of the bioreactor. Changes in the composition of biogas under mesophilic and psychrophilic regimes were also studied. The final conclusion emphasizes that temperature plays a key role in ensuring the stability of the fermentation process in small-capacity biogas plants, and that mathematical modeling of thermal processes is essential.*

Keywords: *solar energy, mesophilic, psychrophilic, biogas, fertilizer, reactor, absorber, heat accumulator, thermal insulation, thermostat, plastic pipe, spiral, collector.*

1. Introduction

Solar-assisted anaerobic digestion systems are thermo-physical systems whose efficiency is determined by the stability of the reactor temperature under mesophilic conditions (36–37 °C) [1-6]. For small-capacity cylindrical reactors, maintaining this temperature requires compensation of conductive and convective heat losses through the reactor walls. The paper by Perrigault et al. [7] presents a time-dependent thermal model of a digester using climatic input parameters (solar radiation, wind speed, ambient temperature) and reactor geometry. It was shown that environmental conditions significantly influence internal temperature distribution and heat losses. However, the study was focused on transient simulation and did not address structural optimization of reactor walls or insulation thickness as an energy-efficiency problem. A related parametric analysis of thermal-technical and geometric characteristics of a small-scale biogas plant was presented in [8], where substitution of structural parameters was investigated. It was shown that reactor dimensions significantly affect thermal performance. However, the quantitative role of multilayer wall resistance and insulation thickness under real solar loading conditions was not fully evaluated. Numerical modeling of heat exchange processes in individual bioenergy installations was also reported in [9], confirming the sensitivity of temperature stabilization to external climatic conditions. Nevertheless, the coupled problem of optimizing collector performance and cylindrical wall heat resistance remains insufficiently resolved.

The utility model patent "Solar biogas plant" [10] proposes a constructive solution integrating a solar collector and phase-change thermal storage. Experimental solar thermal systems of combined type are described in [11], demonstrating the practical feasibility of solar heat supply for decentralized installations. However, neither [10] nor [11] provides a thermo-physical justification of insulation parameters, equivalent thermal resistance of the cylindrical wall, or a quantitative analysis of heat-loss minimization. As a result, the energy-saving effect of the proposed structures remains insufficiently quantified. The difficulty of optimizing energy-saving structures in small-scale systems is associated with the coupled influence of geometry, surface-to-volume ratio, convective boundary conditions, and multilayer conductive resistance. Excessive insulation increases construction cost, while insufficient insulation leads to thermal instability and additional collector load. In addition, maintaining stable microbial activity under mesophilic conditions requires controlled thermal regimes, as noted in studies of bioenergy system stability [12]. A systematic heat-transfer analysis of the reactor as a multilayer cylindrical body is therefore required.

In this work, the reactor is considered as a multilayer cylindrical heat-transfer system with solar heat input and external convective boundary conditions. The scientific novelty of the study consists in: quantitative evaluation of the equivalent thermal resistance of the reactor wall as a function of insulation thickness; determination of rational insulation parameters ensuring stable mesophilic temperature under real climatic conditions; experimental validation of the calculated heat-loss characteristics for a small-capacity solar collector biogas plant; and assessment of the interaction between solar heat supply and phase-change thermal accumulation in maintaining thermal stability. The relevance of the proposed approach is consistent with modern developments in renewable agrotechnological systems [13], where analytical optimization of thermal regimes is considered a key factor of decentralized energy efficiency.

Thus, the study aims to justify energy-saving structural parameters of a small-capacity solar biogas reactor based on a combined analytical and experimental heat-transfer analysis.

2. Main Part

2.1. Object of Research

The object of research is a small-capacity solar-assisted biogas plant operating under mesophilic conditions (36–37 °C). From a thermo-physical viewpoint, the system is considered as a multilayer cylindrical reactor subjected to solar heat input and external convective heat losses.

The structural configuration of the experimental device is presented in Fig. 1. The central element of the system is a cylindrical fermentation reactor (1) containing the biomass (9). The reactor is placed inside an external cylindrical vessel forming a water jacket (2, 4). A spiral heat exchanger (3) is installed in the jacket and connected to flat-plate solar collectors (5). Phase-change thermal storage material (19) is arranged around the heat exchanger to accumulate excess solar energy during peak radiation periods. The system also includes external thermal insulation (18), a mixing device (10), gas outlet and purification elements (11-14), biomass loading and discharge units (7, 8, 15), and temperature control components (16, 17).

This configuration allows the reactor to be analyzed as a multilayer cylindrical heat-transfer system consisting of biomass, metallic wall, water jacket, insulation layer, and external convective boundary. The key performance parameter of the system is the ability to maintain a stable internal temperature within the mesophilic range under real climatic conditions.

Prepared biomass intended for fermentation of organic waste is introduced into the reactor through a hatch installed on its side, ensuring that the volume of biomass inside the reactor equals two-thirds of the reactor's total capacity. To reduce heat loss to the external environment, the outer cylindrical vessel is completely covered with thermal insulation [5-8]. To ensure that the fermentation process inside the reactor proceeds uniformly and that biogas is released at a steady rate, a finned mixing device is installed in the center of the reactor, designed for manual operation. For this device, an optimal mixing frequency of 4–5 times per day has been determined, which prevents the formation of a dense layer on the biomass surface that could hinder gas release. The operating principle of the biogas plant is as follows: in the morning, when the sun rises, solar radiation falls on the transparent surface of the solar collectors, passes through it, and is absorbed by a flat metal plate acting as the absorber.

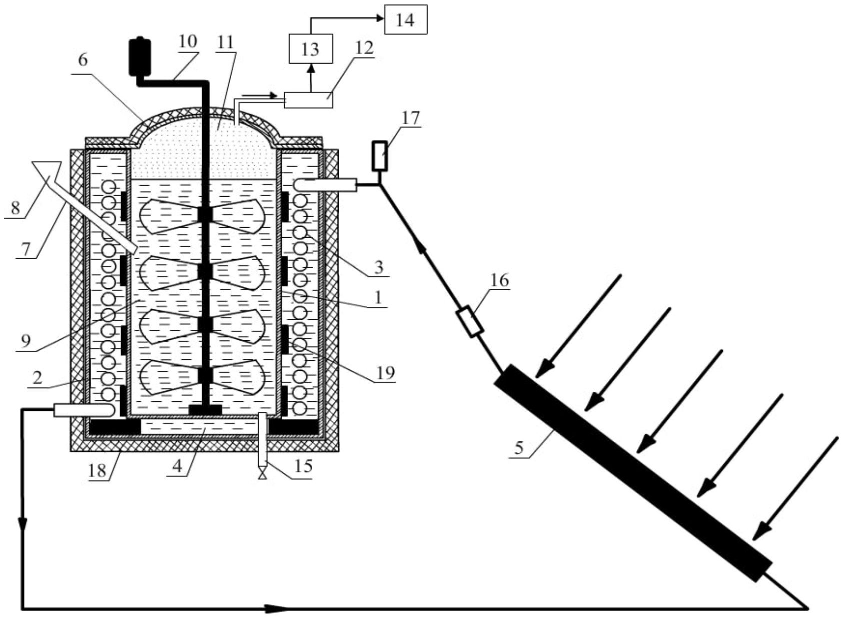

Fig. 1. Schematic diagram of a solar biogas plant. (FAP 2440 19.03.2024): 1 - reactor of biogas device; 2 - water reservoir; 3 - helical heat exchanger made of plastic tube; 4 - water in Reservoir jacket; 5-solar water heater collectors; 6 - reservoir and reactor top seal; 7 and 8 - reactor ready biomass injector Hatch and its throat; 9-biomass in reactor; 10 - mixer device; 11 - formed biogas; 12 - throttle; 13 - gas filter 14 - gas kraynik; 15 - humus release lug; 16 - thermoregulator; 17 - expansion tank; 18 - external thermal insulation; 19 - phase variable heat-collecting material

The absorbed radiation is converted into heat, which warms the water-filled metal fins attached to the plate, thereby heating the water inside the collectors. The heated water in the collectors circulates convectively and passes through a spiral-shaped heat exchanger installed in the water jacket of the external vessel containing the reactor. In doing so, it transfers its thermal potential to the water in the jacket and to the phase-change heat storage materials placed there. After releasing its heat, the water flows back through the lower pipe of the spiral heat exchanger to the solar collectors. The repetition of this process throughout the day ensures uniform heating of the water surrounding the reactor, the heat accumulator, and ultimately the biomass inside the reactor [14].

As phase-change heat accumulators around the spiral heat exchanger, materials are selected whose melting temperatures correspond to the optimal isothermal mesophilic regime. Thus, part of the solar energy received during the day is stored in the phase-change heat accumulator. In the evening or when solar radiation decreases, this stored heat maintains the optimal isothermal process inside the reactor. One of the most important aspects of the ongoing research on this device is the study of the constructive and thermal-energetic characteristics of the solar water-heating collectors and the spiral-shaped heat exchanger connected to them.

2.2. Materials and Methods

The experimental prototype has a total reactor volume of 1.7407 m^3. The working biomass occupies 70% of the total volume (1219 kg at initial loading). Thermophysical parameters used in calculations include: biomass density: 1030 kg/m^3; specific heat capacity: 3.2-3.5 $kJ/(kg\cdot{}^0C)$; operating temperature range: 36–37 ^0C; annual global solar radiation (Bukhara region): 1766 kWh/m^2; solar collector area: 0.745 m^2; collector efficiency: 42.6%.

Solar radiation was measured using a calibrated pyranometer (measurement error ±0.01 W/m^2). Ambient temperature and wind speed were recorded to determine external convective heat-transfer coefficients. Temperature measurements inside the collector loop and reactor were performed using thermocouples connected to a data acquisition system.

The investigation combines analytical modeling and experimental validation of the solar collector–bioreactor thermal system. The methodological framework is based on solving an energy balance problem for a flat-plate solar collector coupled with a multilayer cylindrical bioreactor. The investigation combines analytical modeling and experimental validation.

Analytical Modeling of the Solar Collector

The useful heat gain of the flat-plate solar collector is determined from the steady-state energy balance between absorbed solar radiation and thermal losses to the environment:

$$Q_u = \tau\alpha I_T A_c - U_L A_c\left(T_{pm} - T_a\right) \tag{1}$$

or in compact form:

$$Q_u = A_c\left[\tau\alpha I_T - U_L\left(T_{pm} - T_a\right)\right] \tag{2}$$

where: Q_u - useful heat gain (W); A_c - collector area (m^2); τ - glass cover transmittance; α - absorber absorptance; I_T - incident solar radiation (W/m^2); U_L - overall heat loss coefficient (W/(m^2 ^{0}C)); T_p - mean absorber plate temperature (^{0}C); T_a - ambient temperature (^{0}C).

The instantaneous thermal efficiency of the collector is defined as:

$$\eta_c = \frac{Q_u}{A_c I_T} \tag{3}$$

Substituting Eq. (2) into Eq. (3):

$$\eta_c = \tau\alpha - \frac{U_L\left(T_{pm} - T_a\right)}{I_T} \tag{4}$$

The useful heat transferred to the working fluid is also determined experimentally from:

$$Q_u = \dot{m} C_{pf}\left(T_{fo} - T_{fi}\right) \tag{5}$$

where $\dot{m}$ is the mass flow rate of the fluid (kg/s), C_{pf} is its specific heat capacity (J/(kg·^{0}C)), T_{fo} and T_{fi} are outlet and inlet fluid temperatures (^{0}C).

For the stagnation condition ($\dot{m}$=0), the useful heat gain becomes zero:

$$0 = \tau\alpha I_T A_c - U_L A_c\left(T_s - T_a\right) \tag{6}$$

which yields the stagnation temperature:

$$T_{st} = T_a + \frac{\tau\alpha I_T}{U_L} \tag{7}$$

These relations provide the basis for determining collector performance parameters under varying climatic conditions.

Modeling of Heat Losses from the Bioreactor

Heat losses from the bioreactor are evaluated by modeling the reactor wall as a multilayer cylindrical system. Radial heat transfer through the wall and insulation layers is described using the equivalent thermal resistance approach. For steady-state radial conduction, the heat flow rate is:

$$Q = \frac{2\pi L\left(T_{pm} - T_a\right)}{\sum_j \frac{\left(r_{j+1}/r_j\right)}{\lambda_j} + \frac{1}{h_{ext} r_{ext}}}$$

where: L - reactor height (m); T_i - internal biomass temperature (^{0}C); r_j - inner radius of layer j; λ_j - thermal conductivity of layer j (W/(m·^{0}C)); h_{ext} - external convective heat transfer coefficient (W/(m^2·^{0}C)); r_{ext} - external radius of the insulated reactor (m).

This formulation allows determination of: the dependence of total heat loss on insulation thickness, the reduction in overall heat transfer coefficient U_L, the influence of external convective conditions (wind speed), and the stabilization effect on biomass temperature.

Assumptions and Applicability of the Thermal Model

The proposed thermal model is based on the following assumptions:

1. Heat transfer is considered quasi-steady during the analyzed time intervals; transient thermal inertia effects are neglected.
2. Radial one-dimensional heat transfer is assumed for the multilayer cylindrical reactor wall; axial gradients are neglected.
3. Thermophysical properties of materials are taken as constant within the mesophilic temperature range (33–40 ^{0}C).
4. Solar radiation is assumed uniformly distributed over the collector surface.

5. The biomass temperature inside the reactor is treated as spatially uniform due to mixing.

The model is applicable under moderate climatic conditions (solar radiation up to 800 W/m^2 and wind speeds up to 5 m/s). For strongly transient regimes or extreme environmental conditions, a time-dependent distributed model would be required.

Experimental measurements included: solar radiation intensity; ambient temperature and wind speed; inlet and outlet temperatures of the heat-transfer fluid; biomass temperature inside the reactor; daily biogas production and methane content. Experimental temperature profiles were compared with analytical predictions to validate the heat-transfer model and to determine rational insulation parameters ensuring thermal stability.

To ensure reliability and reproducibility, experimental measurements were carried out in accordance with internationally recognized standards and recommendations for thermal and biogas systems.

The composition of biogas (CH_4, CO_2 and trace gases) was determined using gas chromatography in accordance with ISO 6976:2016 (Natural gas - Calculation of calorific values, density and Wobbe index) and methodological recommendations for biogas analysis described in VDI 4630 (2016). Methane concentration was calculated as the volumetric fraction (%) based on chromatographic peak area normalization. Calibration of the analyzer was performed using certified reference gas mixtures. Measurement uncertainty of methane content did not exceed ±1.5%.

Temperature measurements were performed using calibrated thermocouples (type K) installed at the inlet and outlet of the collector circuit. The measurement procedure followed the requirements of ISO 9488:1999 (Solar energy - Vocabulary) and recommendations for performance testing of solar collectors according to ISO 9806:2017 (Solar energy - Solar thermal collectors - Test methods). Temperature data were recorded with a time resolution of 5 minutes. The expanded measurement uncertainty of temperature did not exceed ±0.5 ^{0}C.

Global solar radiation was measured using a calibrated pyranometer installed on a horizontal surface without shading, in accordance with ISO 9060:2018 (Solar energy - Specification and classification of instruments for measuring hemispherical solar radiation) and WMO Guide to Meteorological Instruments and Methods of Observation (WMO-No. 8). Data were logged continuously and averaged over 10-minute intervals. The instrumental error of radiation measurements was ±0.01 W/m^2.

Processing of experimental data was performed using standard methods of statistical analysis: arithmetic mean values were calculated for daily temperature and radiation profiles; standard deviation was used to estimate dispersion; relative measurement error was determined using propagation of uncertainty; correlation analysis was applied to evaluate the relationship between biomass temperature and methane production rate. All reported results correspond to averaged values with indicated measurement uncertainties.

3. Results and Discussion

3.1. Analysis of Insulation Thickness and Heat-Loss Reduction

In the experiments, to measure the solar radiation falling on the experimental device, the pyranometer was installed on a horizontal surface without any obstacles. The output data from the pyranometer were recorded in a data log, and these records were then used to calculate the total amount of solar radiation received over a certain period of time. In the research site in Bukhara city during the summer months, the maximum average value of global solar radiation is approximately 800 W/m^2, which occurs at midday, while the minimum value is about 200 W/m^2, occurring around sunrise and sunset. This graph (Figure 2) shows the daily variation of temperature in the Bukhara region during the summer months of 2025. The temperatures, measured in Celsius, are plotted against time, labeled as “Time” on the axis. Starting from 7:12 in the morning, the temperature gradually rises from slightly above 30 ^{0}C and reaches over 40 ^{0}C in the afternoon, indicating the intense heat characteristic of the region. In the evening, a gradual decrease in temperature is observed.

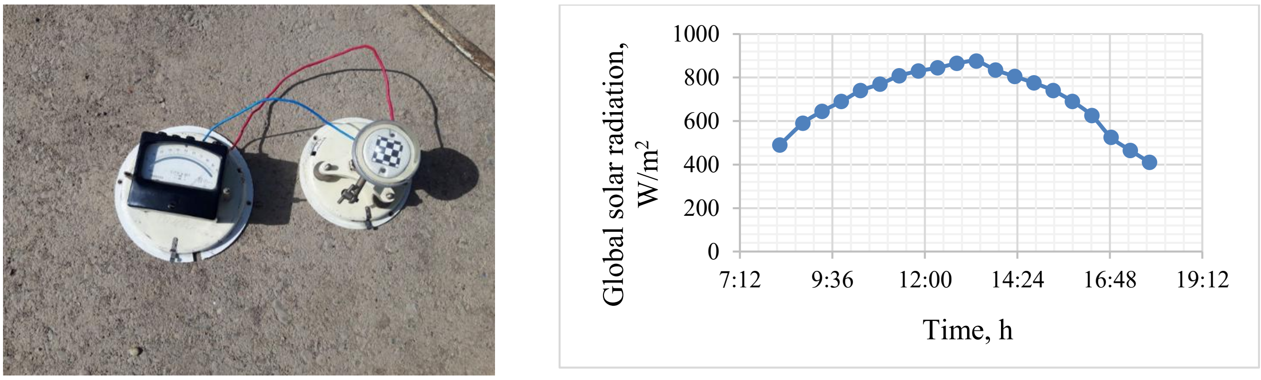

a) b)

Fig. 1. Pyranometer for measuring solar radiation (a) and daily solar radiation variation in studies (b).

These data illustrate the typical temperature variation of a hot day in Bukhara, which is important for understanding or planning around local climate changes, although the pattern becomes even clearer when compared with long-term historical temperature records. In some cases, temperature variations are also linked to wind direction and speed. In the analysis, the daily wind speed in the Bukhara region is plotted with time on the abscissa axis and wind speed on the ordinate axis (Figure 3), showing the average values of daily variation. The data reveal that the highest wind speeds reached around 4–5 m/s. Temperature gradients may be influenced by various factors such as geographical features and time of day.

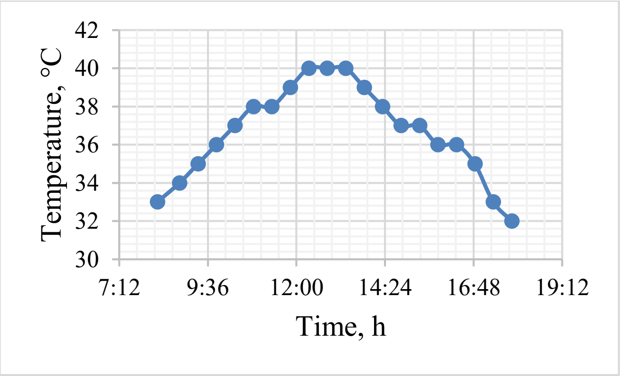

Fig. 2. Daily variation of ambient temperature

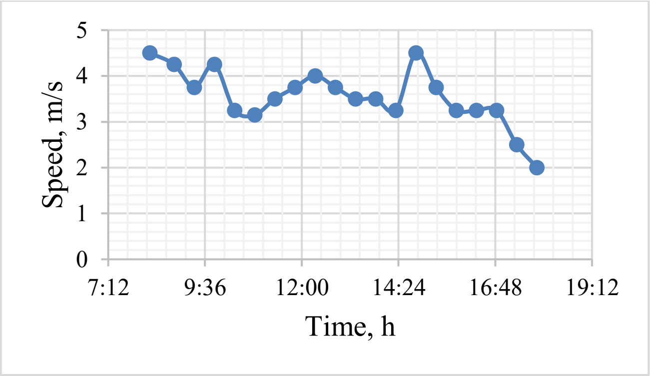

Fig. 3. Daily variation of wind speed

In our research, the daily dynamics of the inlet and outlet hot water temperatures in the experimental device were analyzed (Figure 4). The collector was connected to the reactor through pipes, through which hot water began to heat the water in the reactor tank. These values-the temperature of the water exiting the collector and heating the water in the reactor tank-were measured using a thermocouple. The average values of these measurements are presented in Figure 5.

The graph in Figure 5 illustrates the performance of the flat-plate solar collector, showing the dynamics of inlet (t_i) and outlet (t_o) temperatures at specific times of the day (from 7:12 to 19:12). The dashed line connected with red squares represents the outlet temperature, which rises rapidly in the morning, reaches close to 100 ^{0}C around midday, and then decreases again in the evening. In contrast, the inlet temperature of the heat-transfer fluid, shown with blue circles and a continuous line, remains stable and significantly lower, around 40 ^{0}C. During the daytime, the solar collector effectively absorbs solar energy, heating the heat-transfer fluid, which is then partially cooled when reintroduced into the biogas unit. Methane bacteria adapted to the operating temperature regime in bioreactors cannot function under sharply fluctuating temperatures [15-22]. From a physicochemical perspective, temperature stability is also critical for preventing degradation of thermally sensitive organic compounds and maintaining biochemical equilibrium. Experimental studies of thermally induced transformations in organic systems [23,24] confirm that even moderate temperature deviations may alter molecular stability and reaction kinetics. Therefore, maintaining controlled mesophilic conditions is not only a microbiological requirement but also a thermophysical constraint of the system.

Fig. 4. External appearance of the experimental setup

This graph shows the variation of biomass temperature in the bioreactor heated by a flat-plate solar collector throughout the day (from 7:12 to 19:12). The biomass temperature starts slightly above 30 ^{0}C, gradually rises to about 44 ^{0}C at midday, and then begins to decrease in the evening. These variation curves demonstrate the successful absorption of solar energy by the flat-plate solar collector and its transfer to the biomass. However, there is a need to stabilize this fluctuating temperature. To mitigate sharp changes, we used the daily loading dose intended for the bioreactor as a heating buffer [22]. This solar heating method highlights the direct correlation between the maximum accumulation of solar energy and the optimal temperature range for biomass, thereby increasing the likelihood of creating ideal conditions for metabolic processes [21,22]. During the day, solar radiation causes the temperature to rise, which enhances the metabolism responsible for biogas production. The differences between each measurement are relatively uniform, with no sharp increases or decreases, indicating stable conditions inside the bioreactor and a smooth process. The linear increase also suggests that, in the absence of additional feedstock, the substrate availability and microbial stability are maintained. Overall, the data reflect a healthy and stable biogas production process, dependent on the time of day, demonstrating both the efficiency of the solar collector and the influence of temperature on microbial activity within the bioreactor.

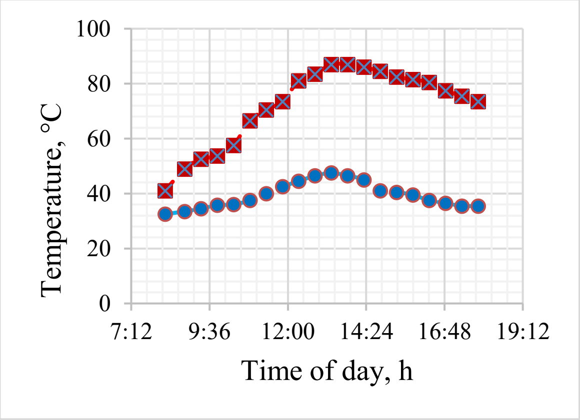

Fig. 5. Dynamics of inlet and outlet heat-carrying water temperature variation

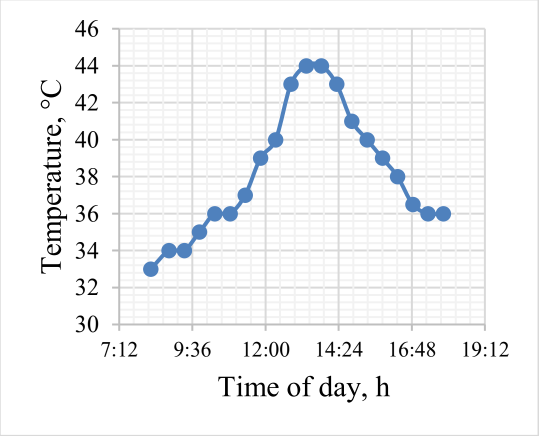

Fig. 6. Daily dynamics of temperature inside the bioreactor

In our research, the composition of biogas and the variation in methane content were analyzed. Biogas mainly consists of methane CH_4 and carbon dioxide (CO_2), along with about 2% trace gases (such as sulfur compounds, nitrogen oxides, S, NO). The primary economic indicator of this process is the methane content in the biogas, although in some cases, rapid processing of organic waste is also required.

Looking at the normalized data starting at 8:14, with subsequent times given in minutes, we observe a steady and gradual increase in biogas production. Biogas production starts at 0.1340 m^3 and continues until the end of the day, reaching 0.1570 m^3 from the baseline after 576 minutes (i.e., 9 hours and 36 minutes) from the start time. The stable growth in biogas production is linked to various factors, such as the rise in temperature inside the bioreactor, since the bioreactor was heated using a solar collector [22].

3.2 Variation of biogas composition under mesophilic and psychrophilic temperature regimes

In practice, to increase the methane content of biogas, valuable methanogens are additionally loaded into bioreactors [15,16,25]. Introducing methanogens as simulators into small-capacity biogas units limits their use only to solving ecological problems [16-19]. In our research, the practical influencing factors on small-capacity biogas bioreactors are analyzed. Table 1: Standard and threshold indicators of biogas.

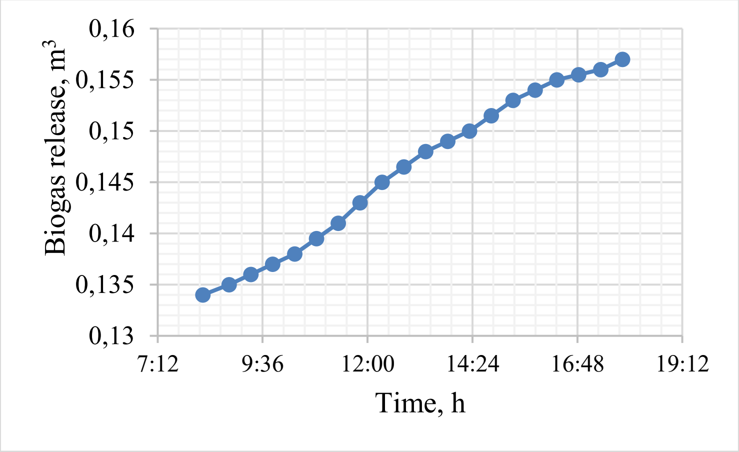

Fig. 7. Daily dynamics of temperature inside the bioreactor

In this context, the pH level is considered one of the main indicators of the anaerobic process occurring in small-capacity bioreactors. For biogas production, the required pH range is between 6.8 and 7.4. In many cases, when organic waste with high pH values (such as pigsty and poultry waste) is used, it is necessary to pass the units through a metabolic adaptation stage before operation [20-22]. The experimental study examines the composition of organic waste loaded into small-capacity units and their standard indicators (Table 1).

Table 1. Composition and standard indicators of the biomass loaded into the bioreactor.

Indicators	Standard values	Limit values
pH	6/8 – 7.4	6.4 – 7.8
Volatile fatty acids content (as CH_3COOH)	50 – 500 mg/l	200 mg/l
Total alkalinity (as $CaCO_3$)	500 – 1500 mg/l	1000 – 3000
Composition of produced gas	60 – 72% metan, 28 – 40% Carbon dioxide and other gases	
Salts		
NH_4 (as N)		300 mg/l.
Na		3500 – 5500 mg/l.
K		2500 – 4500 mg/l.
Ca		2500 – 4500 mg/l.
Temperature, °C	33 – 37	
Biogas production	0.3 – 0.52 m^3/kg based on dry organic matter	

The amount of volatile fatty acids should range from 50 to 500 mg/l. The threshold indicator is set at 200 mg/l [25]. In bioreactors, the total alkalinity of the organic waste load is required to be between 500 and 1500 mg/l. However, these specified conditions cannot be considered strict, since alkalinity in wastewater is highly variable, and levels ranging from 1000 to 3000 mg/l are also observed.

The salts most frequently and unsuccessfully involved in waste composition (NH_4, Na, K, and Ca) are required to remain within certain limits. The methane (CH_4) content in biogas obtained from different types of organic waste is shown in Table 2. As mentioned above, for anaerobic treatment of organic waste to produce biogas, the ideal temperature should be around 38 ± 2^0C. It is necessary to select a regime suitable for the temperature to which methanogens have adapted. This table presents the types of organic waste, the amount of biogas obtained, and its composition. It is known that from cattle manure, 0.340 to 0.500 m^3 of biogas can be obtained per kilogram of dry matter (taking into account the duration of processing). The methane (CH_4) content of the resulting biogas is approximately 68%.

Table 2. Biogas yield and methane content from different types of organic waste

Animal manure	1 kg gas yield from dry matter, m^3	Methane storage, %
Cattle manure		
Pig manure	0.340 – 0.500	65.0
Poultry droppings	0.340 – 0.580	65 – 70
Fattening calf manure	0.310 – 0.620	60.0
Breeding calf manure	0.200 – 0.300	56 – 60
Organic waste from farms	0.300 – 0.620	70.0
Wastewater		
Vegetable residues	0.310 – 0.740	70
Potato residues	0.330 – 0.500	50 – 70
Beet residues	0.280 – 0.490	60 – 75
Plant waste	0.400 – 0.500	85
Straw		
Hay	0.200 – 0.300	50 – 60
Barley straw	0.200 – 0.300	59
Corn stalks	0.290 – 0.310	59
Flax	0.380 – 0.460	59
Beet pulp	0.360	59
Sunflower waste	0.165	59
Alfalfa	0.300	59
Other types	0.430 – 0.490	59
Green grasses		
Fallen leaves	0,280 – 0,630	70
Animal manure	0,210 – 0,290	58

Table 3 provides detailed information about the components of biogas and their properties: biogas composition and specific characteristics. The volumetric share of methane (CH_4) gas can range from 55 to 61% (in mixed organic waste), and from 62 to 72% (in single-type organic waste under warm climate conditions). The volumetric calorific value can reach 35.8 MJ/m^3 or higher. In our research, in order to increase the methane content, the biogas exiting the bioreactors was passed through a water filter (see Table 3).

Table 3. General specific characteristics of the average biogas obtained

Characteristics	Components of biogas				Biogas mixture (60%CH_4+40%CO_2)
	CH_4	CO_2	H_2	H_2S	
Volumetric fraction, %	55...70	27...44	<1	<3	10
Volumetric calorific value, MJ/m^3	35.8	–	10.8	22.8	21.5
Flammability limit (concentration in air), %	5...15	–	4...80	4...45	6...12
Ignition temperature, ^{0}C	650...750	–	585	–	650...750
Critical pressure, MPa	4.7	7.5	1.3	8.9	7.5...8.9
Critical temperature, ^{0}C	– 82.5	31.0	–	100	– 2.5
Normal density, g/l	0.72	1.93	0.09	1.54	1.2
Critical density, g/l	102	468	31	349	320
Density relative to air	0.55	2.5	0.7	1.2	0.83

3.3 Comparison with previous studies

The obtained experimental results were compared with published data on solar-assisted biogas systems and flat-plate solar collectors operating under mesophilic conditions [1-3, 15-25].

The measured solar collector efficiency (42–50%, average 42.6%) is consistent with values reported for conventional flat-plate collectors under high solar radiation levels (800 W/m^2), where efficiencies typically range from 35% to 55% depending on the heat-loss coefficient and operating temperature difference. The observed stagnation temperature behavior also agrees with analytical predictions reported in similar thermal studies. The biomass temperature in the reactor was maintained within 33 - 44 ^{0}C, corresponding to the mesophilic regime. Comparable systems described in the literature report temperature stabilization within 35-40 ^{0}C when external insulation and solar preheating are applied. The slightly wider temperature fluctuation observed in the present study is attributed to diurnal solar variability and wind-induced convective losses.

The annual biogas yield (932.535 m^3/year) and methane content (60-70%) are in agreement with reported values for cattle manure and mixed organic waste under mesophilic conditions, where specific yields typically range between 0.3 and 0.6 m^3/kg of dry organic matter. The methane fraction obtained after water filtration corresponds to published data on small-scale purification methods. Compared with previously reported small-capacity systems without enhanced insulation, the present configuration demonstrates reduced thermal losses and improved temperature stability, which directly contribute to sustained microbial activity and stable methane production.

4. Conclusion

Our research has shown that temperature plays a key role in maintaining the stability of the anaerobic fermentation process in small-scale biogas plants, and that the use of mathematical expressions for its calculation is important.

The results of studies conducted in rural conditions, using organic waste and small-scale biogas plants heated with solar energy, are presented. In the study, the design of the biogas plant was examined, including solar collectors, heat exchange elements, and thermal accumulators made of phase-change materials, which help maintain stable biomass temperature throughout the day.

During the experiments, solar radiation, ambient temperature, reactor temperature, and the daily dynamics of biogas production volume were analyzed. The results demonstrate that effective utilization of solar energy to ensure optimal temperature regimes in the bioreactor leads to stable growth in biogas production. The study also highlighted the influence of biomass type on the composition of the biogas produced. Temperature is the main factor for the stability of the anaerobic fermentation process, and its effective management emphasizes the importance of biomass processing efficiency.

Conflict of interest statement

The authors declare that they have no conflict of interest in relation to this research, whether financial, personal, authorship or otherwise, that could affect the research and its results presented in this paper.

CRediT author statement

Sharipov M.Z., Kovalev I.V. - Conceptualization, Methodology, Supervision; **Majitov J.A., Imomov Sh.J.:** Formal Analysis, Validation, Writing-Reviewing and Editing; **Narzullaev M.N., Negmatillayev B., Ziyoyev D.A. -** Investigation, Data curation, Writing - original draft. The final manuscript was read and approved by all authors.

References

1 Chen J. Heat-transfer Enhancement for Slurries from Biogas Plants- Properties, processes and thermal systems. *Diss…, Luleå: Luleå University of Technology*, 2022. https://www.researchgate.net/publication/389503732_Heat-transfer_Enhancement_for_Slurries_from_Biogas_Plants_-_Properties_processes_and_thermal_systems

2 Budhijanto W., Purnomo C.W. and Siregar N.C. (2012) Simplified Mathematical Model for Quantitative Analysis of Biogas Production Rate in a Continuous Digester. *Engineering Journal*, 16, 5, 167–176. https://doi.org/10.4186/ej.2012.16.5.167

3 Delgadillo Mirquez L., Machado Higuera M. and Hernández Sarabia M. (2018) Mathematical modelling and simulation for biogas production from organic waste. *International Journal of Engineering Systems Modelling and Simulation*, 10, 2, 97. https://doi.org/10.1504/IJESMS.2018.10013112.

4 Elsgaard L., Olsen A. B. and Petersen S. O. (2016) Temperature response of methane production in liquid manures and co-digestates. *Science of The Total Environment*, 539, 78–84. https://doi.org/10.1016/j.scitotenv.2015.07.145.

5 Bai Y., Yang M., Wang Z., Li X. and Chen L. (2019) Thermal stratification in a cylindrical tank due to heat losses while in standby mode. *Solar Energy*, 185, 222–234, https://doi.org/10.1016/j.solener.2018.12.063.

6 Ohk S.M. and Chung B.J. (2017) Natural convection heat transfer inside an open vertical pipe: Influences of length, diameter and Prandtl number. *International Journal of Thermal Sciences*, 115, 54–64, https://doi.org/10.1016/j.ijthermalsci.2017.01.014.

7 Perrigault T., Weatherford V., Martí-Herrero J. and Poggio D. (2012) Towards thermal design optimization of tubular digesters in cold climates: A heat transfer model. *Bioresour Technol*, 124, 259–268. https://doi.org/10.1016/j.biortech.2012.08.019.

8 Sharipov M., Majitov J., Ergashev S., Shodiyev E., Narzullayeva Z. (2025) Substitution Of Thermal-Technical and Geometric Parameters of A Small-Scale Biogas Plant. *Eurasian Physical Technical Journal*, 22(3-53), 84–90. https://doi.org/10.31489/2025N3/84-90

9 Sharipov L.A., Imomov S.J., Majitov J.A., Sharipov M.Z., Pulatova F., Abdisamatov O.S. (2020) Modeling of heat exchange processes in the Metanetka bioenergy plant for individual use. *Iop Conference Series Earth and Environmental Science,* 2020, 614(1), 012035. https://doi.org/10.1088/1755-1315/614/1/012035

10 Majitov J.A., Kamilov O.S., Yuliyev O.O. (2024) Solar biogas plant. Utility model patent No. FAP 2440. Published 19.03.2024. [in Uzbek] https://im.adliya.uz/document/check/e00d4d85-4e28-4988-917b-eb8f60e58fb7

11 Komilov O.S., Astanov S.Kh., Safarov O.F., Sharipov M.Z., Faizullaev A.R., Tillaev L. (2009) Combined solar drying unit. *Applied Solar Energy English Translation of Geliotekhnika*, 45(4), 262–265. https://doi.org/10.3103/S0003701X09040082

12 Mukhamadiev B.T., Sharipov M.Z. (2021) To the issue of organization of the communication system in microorganisms. *Iop Conference Series Earth and Environmental Science*, 848(1), 012224. https://doi.org/10.1088/1755-1315/848/1/012224

13 Mamatkarimov O, Ergashev O, Giyasidinov A, Sharipov M, Abrorov A, Khakimova N, Kovalev I. (2024) Overview of the IX International Conference on Advanced Agritechnologies, Environmental Engineering and Sustainable Development-AGRITECH-IX-2023, *E3S Web of Conferences.* 486, 00001. https://doi.org/10.1051/e3sconf/202448600001

14 Amon B. and C. A. Amon (2001) Emissions of NH_3, N_2O and CH_4 from dairy cows housed in a farmyard manure tying stall (housing, manure storage, manure spreading). Nutrient Cycling in Agroecosystems, 60(1):103-113. https://doi.org/10.1023/A:1012649028772

15 Talukdar D., Tsubokura M., (2022) Numerical study of natural-convection from horizontal cylinder at eccentric positions with change in aspect ratio of a cooled square enclosure. *Heat and Mass Transfer*, 58, 5, 849–871. https://doi.org/10.1007/s00231-021-03145-3.

16 Sebastian G., Shine S. R. (2015) Natural convection from horizontal heated cylinder with and without horizontal confinement. *Int J Heat Mass Transf*, 82, 325–334. https://doi.org/10.1016/j.ijheatmasstransfer.2014.11.063.

17 Fleming J.G. Novel simulation of anaerobic digestion using computational fluid dynamics. *North Carolina: North Carolina State University,* 2002. http://www.lib.ncsu.edu/resolver/1840.16/4158

18 Kalendar A., Alhendal Y., Hussain S., Karar S. and Oosthuizen P. (2021) Natural Convective Heat Transfer from Vertical Isothermal Polygonal Cylinders. *J. Thermophys Heat Trans*, 35, 4, 854–868, https://doi.org/10.2514/1.T6207.

19 Oosthuizen, P., Kalendar, A. (2014) Natural Convective Heat Transfer from Short Rectangular Cylinders Having Exposed Upper Surfaces and Mounted on Flat Adiabatic Bases. In: Natural Convective Heat Transfer from Short Inclined Cylinders. SpringerBriefs in Applied Sciences and Technology. Springer, Cham. https://doi.org/10.1007/978-3-319-02459-2_4

20 Kishor J., Goyal I. C., Sawhney R. L., Singh S. P., Sodha M. S. and Dayal M.(1988) Solar assisted biogas plants III: Energy balance of fixed dome biogas plants and enhancement of production in winters. *Int J Energy Res*, 12, 4, 711–737. https://doi.org/10.1002/er.4440120411.

21 Majitov J.A. (2020) Selection of design methodology for biogas facilities and assessment of economic efficiency. *Scientific and technical journal of the development of science and technology*, 7.129-134. [in Uzbek] https://journal.bmti.uz/?page_id=31

22 Majitov J.A. (2025) *Kichik quvvatli biogaz qurilmasining issiqlik-texnik parametrlarini asoslash. dis.PhD,* Qarshi. 71-74. https://library.ziyonet.uz/ru/book/135481

23 Astanov S., Sharipov M.Z., Faizullaev A.R., Kurtaliev E.N., Nizomov N. (2014) Thermal Destruction of Riboflavin in Different Aggregate States, *Journal of Applied Spectroscopy*, 81(1), 37-42. https://doi.org/10.1007/s10812-014-9883-z

24 Astanov S.K., Sharipov M.Z., Kasimova G.K. (2019) Hipochromic effect in riboflavin solutions, *Eurasian Physical Technical Journal,* 16(1), 12–17. https://doi.org/10.31489/2019no1/12-17

25 Rennie T. J., Baldé H., Gordon R. J., Smith W. N. and Vander Zaag A. C. (2017) A 3-D model to predict the temperature of liquid manure within storage tanks. *Biosyst Eng*, 163, 50–65. https://doi.org/10.1016/j.biosystemseng.2017.08.014.

AUTHORS' INFORMATION

Sharipov, Mirzo – Doctor of Physical and Mathematical Sciences, Professor, Head of Department of Physics, Bukhara State University, Bukhara, Uzbekistan; SCOPUS Author ID: 24177719300, https://orcid.org/0000-0003-0370-8066; m.z.sharipov@rambler.ru

Majitov, Jurabek – Doctor PhD, Associate professor, Physics Department Bukhara State Technical University, Bukhara, Uzbekistan; SCOPUS Author ID: 57221226030; https://orcid.org/0009-0005-9453-279X; majitov@mail.ru

Imomov, Shavkat – Doctor of Technical Sciences, Professor, National research university "Tashkent institute of irrigation and agricultural mechanization engineers" National research university, Tashkent, Uzbekistan; Scopus Author ID:57211805830, https://orcid.org/0009-0001-0191-7430; Researcher ID: T-3711-2018; Shavkat-imomov@rambler.ru

Kovalev, Igor - Doctor of Technical Sciences, Professor, Siberian Federal University, Krasnoyarsk, Russia; SCOPUS Author ID: 57360606900, https://orcid.org/0000-0003-2128-6661; kovalev.fsu@mail.ru

Narzullayev, Mukhiddin - Master, Senior Lecturer, Physics Department, Bukhara State Pedagogical Institute Bukhara; Uzbekistan; SCOPUS Author ID: 57221226030; https://orcid.org/0009-0000-5004-7315; muxiddin2024@mail.ru

Negmatillayev, Baxodir – Master, Senior Lecturer at the Department of Architecture, Bukhara State Technical University**,** Bukhara, Uzbekistan; https://orcid.org/0009-0000-9460-4478. bakhodir.negmatillayev@mail.ru

Ziyoyev, Dilshod – Master, Laboratory manager, Bukhara State Technical University, Bukhara, Uzbekistan; https://orcid.org/0009-0005-2202-6222; dilshodbek_ziyoyev@mail.ru

EURASIAN PHYSICAL TECHNICAL JOURNAL

2026, Volume 23, No. 1(55)

https://doi.org/10.31489/2026N1/60-67

Received: 28/11/2025 Revised: 29/01/2026 Accepted: 19/03/2026 Published online: 30/03/2026

Research Article

UDC 536.532; 621.311

STUDY TO ASSESS ELECTRICITY GENERATION IN A THERMAL POWER PLANT USING FAULT TREE ANALYSIS MODEL

Nygymanova A.*, Ongar B., Sarsenbayev Y.

K.I. Satbayev Kazakh National Research Technical University, Almaty, Kazakhstan

**Corresponding author:* a.nygymanova@satbayev.university

Abstract. *This paper presents the application of Fault Tree Analysis model for availability assessment of thermal power plant. Reliability analysis as well as availability evaluation is performed for performance evaluation of thermal power plant. Equipment maintenance data is collected from maintenance history for which the goodness of fit test viz Kolmogorov-Smirnov is conducted and parameters for the best distribution are determined. Further, reliability of subsystems at various time intervals is calculated. The Fault Tree Analysis models were developed for performance evaluation of thermal power plant. These models are employed for the subsystems of plant and furthermore availability indices are evaluated. The overall availability of 87.77% is evaluated using Fault Tree Analysis model. The comparative results are obtained from the study, which revealed that the Fault Tree Analysis model provides an availability index of the system closer to real-time data.*

Keywords: reliability analysis, availability analysis, thermal power plant, Fault Tree Analysis.

1. Introduction

In the context of increasing demands on the reliability and efficiency of electric power systems, the analysis of factors affecting the generation of electricity at thermal power plants (TPP) is of particular importance. Most of the existing thermal power plants are operated for a long time, which leads to wear of the main equipment, an increase in the number of failures and a decrease in installed and available capacity. As a result, there is an increased likelihood of under-generation of electricity, disruption of load schedules, and increased operating costs. Traditional methods of estimating electricity generation are usually based on statistical data and regulatory indicators of equipment reliability. However, such approaches do not always make it possible to identify cause-and-effect relationships between individual failures of technological circuit elements and the resulting decrease in plant output. This limits the ability to make informed management decisions in the field of equipment maintenance, repair, and modernization [1,3,4,7,8,10,13].

One of the promising tools for system analysis of reliability of complex technical facilities is the Fault Tree Analysis (FTA) method [11,12]. This method allows us to formalize the logical structure of the occurrence of emergency conditions, to establish the relationship between the primary failures of elements and the final undesirable event – a decrease or loss of electricity generation. The use of the fault tree model provides a visual representation of the mechanisms for generating power losses, and also makes it possible to quantify the contribution of each piece of equipment to the overall risk of underperformance. The purpose of this study is to develop and apply a fault tree analysis model to evaluate power generation at a thermal power plant, taking into account failures of the main and auxiliary equipment. As part of the work, the key technological subsystems of thermal power plants (boiler, turbine, generator, fuel supply, water treatment and electricity supply systems for their own needs) are considered, the fault tree structure is formed and the impact of failures on the level of actual electricity generation is assessed. Alternative reliability modelling approaches such as Markov models, Bayesian networks, and Petri nets are widely used in power system analysis. Markov models provide accurate state-transition representation but may become computationally complex for large-scale systems. Bayesian networks allow modelling of dependent failures but require extensive probabilistic information. Petri nets are suitable for dynamic systems but involve significant modelling effort. In the present study, FTA was selected due to its transparency, analytical simplicity, and suitability for real industrial operational data.

The practical significance of the study lies in the possibility of using the obtained model to increase the validity of decisions on managing the technical resource of equipment, optimizing repair impacts and reducing power losses. The proposed approach can be applied both in analysing the operation of a specific plant and in developing strategies to improve the reliability and efficiency of thermal power plants in general.

2. Plant description

A thermal power plant (TPP), is a complex multi-level energy facility designed for the simultaneous production of electrical and thermal energy based on the conversion of chemical fuel energy into mechanical and further into electrical energy. The main types of fuel used are coal, natural gas and fuel oil, the choice of which is determined by regional resources, economic and environmental factors. The functional block diagram of TPP presented in Figure 1. There are major equipment: a) turbine, b) generator, c) IDF (Induced Draft Fan), d) FDF (Forced Draft Fan), e) PAF (Primary Air Fan), f) BFP (Boiler Feed Pump), g) CWP (Circulating Water Pump), h) CEP (Condensate Extraction Pump), i) boiler, j) chimney, k) CM (Coal mill), l) condenser, m) HPH (High Pressure Heater), n) LPH (Low Pressure Heater), o) APH (Air Preheater), p) ESP (Electrostatic Precipitator). The boilers burn fuel and generate superheated steam with high parameters (pressure and temperature). The resulting steam is supplied to the turbine, where its thermal energy is converted into mechanical energy of rotation of the shaft connected to the electric generator. The generator, in turn, converts mechanical energy into electrical energy, which is supplied to the power grid [1,3,10].

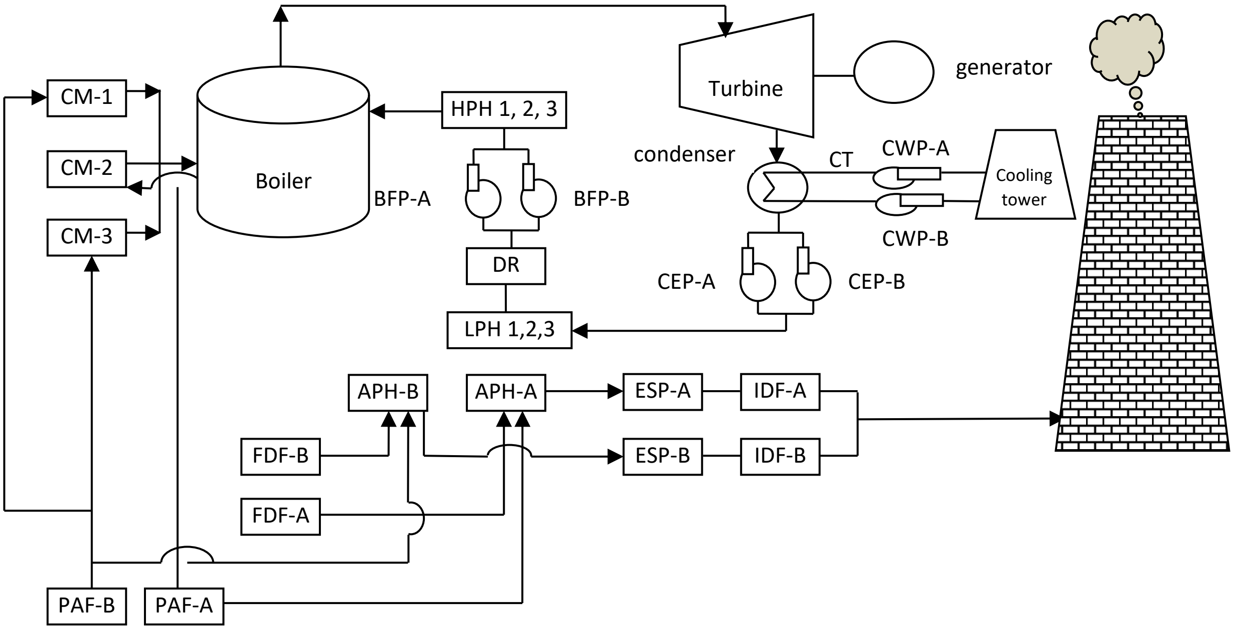

Fig. 1 Model of thermal power plant for electricity generation

The operation of thermal power plants is characterized by high complexity and interdependence of technological nodes. Malfunction of any element – boiler, turbine, generator, fuel supply system or automation can lead to a decrease in power, deterioration in the quality of electricity, or a complete shutdown of the unit. In conditions of equipment wear, variable load conditions and exposure to external factors, the probability of failures increases, which directly affects the volume of electricity generation and the reliability of energy supply. In this regard, the TPP is considered as a complex technical system with a hierarchical structure of failures. The use of the Fault Tree Analysis (FTA) model makes it possible to formalize the cause-and-effect relationships between failures of individual elements and the final event a decrease or loss of electricity generation. This approach ensures the identification of critical nodes, the assessment of the contribution of individual failures to the overall risk, and the formation of informed decisions to improve the reliability and efficiency of the plant.

2.1 Modelling the availability of thermal power plants

A thermal power plant belongs to the class of complex technical systems, the functioning of which is characterized by a multilevel structure and a significant number of interrelated elements. In this regard, the analysis of the availability of thermal power plants is a prerequisite not only for ensuring the operability of individual components, equipment and subsystems, but also for sound planning of maintenance and repair activities. Accessibility modelling is a systematic approach based on the step-by-step decomposition of a power plant into subsystems, equipment, and individual components. This approach allows us to take into account the impact of element failures, as well as the frequency and duration of restoration work on the integrated indicator of installation availability. The reliability and maintainability indicators of the elements directly determine the probability of finding a thermal power plant in working condition. For systems whose elements are connected in a sequential configuration, the assessment of overall availability is usually carried out using the analytical expression (1), which makes it possible to determine the contribution of each element to reducing the availability of the entire system [7,8,9,10,14].

$$Av = \prod_{i=1}^{n} Ai \tag{1}$$

where: A_v – overall availability of the Thermal Power Plant (TPP); Ai – availability of the i-th component (or subsystem) of the plant; n – total number of components (subsystems) included in the reliability model.

For the current work, availability of TPP is investigated and assessed by FTA method.

2.2 FTA modelling of TPP

The fault tree diagram allows you to obtain information about the unavailability of the system and thereby determine the degree of criticality of various pieces of power plant equipment. Within the framework of this study, the fault tree analysis (FTA) model for the station is formed using the logical elements "OR" and "AND", which is illustrated in Figure 2 [11,12,13].

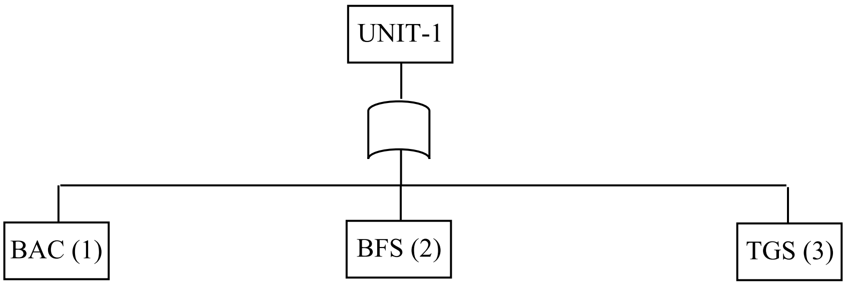

Fig. 2. FTA model of thermal power plant

After forming the FTA model at the subsystem level, the corresponding unavailability of the system is estimated using the cut-set method based on a probabilistic approach, the main provisions of which are summarized below.

$$q_{U-1} = 1 - \prod_{i=1}^{3} (1 - q_i) \tag{2}$$

where: $q_{(U-1)}$ – probability of failure (unavailability) of subsystem $U-1$ or the top event in the Fault Tree Analysis (FTA) model; q_i – probability of failure (basic event probability) of the i-th component.

In constructing the FTA model, several assumptions were adopted. It was assumed that failures of individual components are statistically independent and that failure rates remain constant within the considered operating period. Each element was modeled in a binary state (operational or failed). Common-cause failures and dynamic interactions between components were not explicitly considered. These assumptions correspond to classical FTA methodology and allow analytical estimation of subsystem and system unavailability.

3. Result and Discussion

To ensure the assessment of the availability of thermal power plants, maintenance data is collected based on the operational and repair logs of the power plant and used in further availability analysis. Due to the complexity of the TPP system under consideration, it is divided into three main subsystems for analytical evaluation, namely: the boiler air circulation system, the boiler furnace, and the turbo generator. The assessment of the availability and unavailability of TPP subsystems is based on the development of a fault tree analysis model (FTA). The summary values of the availability and unavailability of TPP subsystems obtained using the FTA model are presented in Table 1. The availability indices presented in Table 1 were obtained from a statistical analysis of operational data of the first power unit of the thermal power plant over an observation period of 17,520 hours (equivalent to two years of operation) [1,3]. Seasonal load variations and scheduled maintenance activities were observed during this period. These operational factors may influence failure frequency and recovery time, which in turn affect the calculated reliability and availability indicators.

Table 1. Summary of FTA model-based availability index

Subsystem	Unavailability	Availability
BAC (Boiler and Air Circuit)	0.000191	0.999809
BFS (Boiler Feedwater System)	0.053442	0.946558
TGS (Turbine–Generator System)	0.044167	0.955833

This expression corresponds to the inclusion–exclusion expansion presented in equation (2) and provides an exact solution for an OR-type top event under independence assumptions. The total unavailability of the first power unit of the plant, determined using the FTA model, is 0.122260.

$$q_{U-1} = 0.122260$$

Accordingly, the availability of the power unit is: $A_{U-1} = 1 - q_{U-1} = 0.877740\ (87.77\%)$

The total availability of the first power unit of the station, calculated using the FTA model, is 0.877740 (87.77%). The conducted research has shown that the FTA approach allows obtaining system availability values close to the indicators observed in real time. However, when using the FTA method, the effect of system redundancy is not taken into account. The results of the analysis confirmed that FTA is the most appropriate method for assessing station availability. In the future, a reliability analysis is performed for various time intervals of the station's operation, which is discussed in the following sections.

It should be noted that explicit modelling of equipment redundancy (e.g., standby pumps or parallel fans) was not incorporated into the present FTA structure. The subsystems were represented primarily in a series configuration at the analytical level. Therefore, the obtained availability value may represent a conservative estimate. Inclusion of redundancy mechanisms could potentially increase the calculated availability indices.

4. Reliability Analysis thermal power plant

Reliability analysis includes evaluating parameters, building models, and determining the likelihood that the system will function satisfactorily for a specified period of time [8,14]. For a normal distribution, the probability density function is estimated using equation (3), and reliability is estimated using equation (4). Similarly, in the case of the Weibull distribution, the reliability indicator is determined by equation (5).

$$F(t) = \frac{1}{\sigma\sqrt{2\pi}} e^{-\left(\frac{t-\mu}{\sigma}\right)^2} \tag{3}$$

$$R(t) = 1 - F(t) \tag{4}$$

$$R(t) = e^{-\left(\frac{t}{\theta}\right)^\beta} \tag{5}$$

where: *F(t)* – probability density function of the random variable t (for example, time to failure of equipment in a TPP); t – random variable (typically operating time or time to failure); μ – mean value (mathematical expectation) of *t*, represents the average operating time; σ – standard deviation, characterizes the dispersion of operating time around the mean value; π – mathematical constant (≈ 3.14159); e – base of the natural logarithm; *R(t)* – reliability function; θ – characteristic life of the component, it determines the time scale of the distribution.

As part of this study, data on previous thermal power plant failures is collected and systematized in the form of recovery time (TTR) and time between failures (TBF). To determine the most appropriate theoretical failure distribution, we consider the Weibull, lognormal, exponential, and normal distributions. The parameters are estimated using the maximum likelihood method, and the approximation quality is checked using the Kolmogorov–Smirnov criterion (K-S). The purpose of choosing the best distribution is to determine the statistical model that best describes the available data set. The K-S consent criterion allows us to assess the degree to which the data on TPP failures correspond to the selected distribution of the general population [5,6]. The various theoretical distributions for the TBF index of subsystems are presented in Tables 2 - 4.

Table 2. Best- fit distribution of BAC

Equipment	K-S test							Parameters
	Exp. 1P	Exp. 2P	Log. normal	Normal	Weibull 2P	Weibull 3P	Best fit distribution	
PA Fan	28.36	21.75	9.4083	0.0149	1.1328	0.0022	Normal	μ=12684.66 σ = 8462.17
FD Fan	95.56	76.06	1.8067	1.377	1.5740	12.06	Normal	μ=19322.12 σ=5859.22
APH	50.84	43.77	13.27	0.0007	0.8754	0.00019	Normal	μ=15445.70 σ=8928.90
ESP	95.56	76.06	1.8067	1.3777	1.5740	12.0619	Normal	μ=19322.12 σ=5859.22
ID Fan	56.99	57.94	76.028	15.115	55.1115	41.6604	Weibull 3P	β=0.35967 θ=12372.54 γ=10.78

Table 3. Best –fit distribution for BFS

Equipment	K-S test							Parameters
	Exp. 1P	Exp. 2P	Log-normal	Normal	Weibull 2P	Weibull 3P	Best fit distribution	
Boiler Drum	95.56	76.06	1.8067	1.377	1.574	12.06	Normal 2P	μ=19322.1 σ=5859.22
Boiler tubing	84.78	22.83	0.5787	0.316e-4	0.10e-4	0.55e-4	Weibull-2P	β=2.61432 θ=19371.3
Fuel firing system	95.56	76.06	1.8067	1.377	1.574	12.06	Normal 2P	μ=19322.1 σ=5859.22
Superheater	95.56	76.06	1.8067	1.377	1.574	12.06	Normal 2P	μ=19322.1 σ=5859.22
Economizer	95.56	76.06	1.8067	1.377	1.574	12.06	Normal 2P	μ=19322.1 σ=5859.22
Reheater	95.56	76.06	1.8067	1.377	1.574	12.06	Normal 2P	μ=19322.1 σ=5859.22

The choice of the most appropriate theoretical distribution for the time between failures (TBF) was carried out using the Kolmogorov–Smirnov (K–S) goodness-of-fit criterion**.** This method evaluates how well a theoretical distribution matches the observed (empirical) data. For each equipment item, empirical TBF data were first obtained from operational records. Then, several candidate distributions (exponential, lognormal, normal, and Weibull) were fitted to the data using the maximum likelihood method. The K–S statistic is defined as the maximum absolute difference between the empirical distribution function $F_n(x)$ and the theoretical cumulative distribution function *F(x):*

$$D = max|F_n(x) - F(x)|$$

The value *D* quantifies the deviation between the model and the actual data. The smaller the value of D, the better the agreement between the theoretical distribution and the observed data.

Table 4. Best-fit distribution of TGS

Equipment	K-S test							Parameters
	Exp. 1P	Exp. 2P	Log. normal	Normal	Weibull 2P	Weibull 3P	Best fit distribution	
Turbine Governing	95.56	76.06	1.8067	1.377	1.574	12.06	Normal 2P	μ=19322.1 σ=5859.22
Turbine Lubrication	75.51	66.54	26.2606	1.867	5.780	0.4821	Normal-2P	μ=17243.5 σ=7819.99
Generator Oil system	99.87	66.89	0.1805	11.52	13.8136	1.775	Lognormal-2P	μ=9.0955 σ=0.393221
Generator Gas	95.56	76.06	1.8067	1.377	1.5740	12.06	Normal 2P	μ=19322.1 σ=5859.22
Generator Exct.	95.56	76.06	1.8067	1.377	1.5740	12.06	Normal 2P	μ=19322.1 σ=5859.22

For each equipment unit, the K–S statistic was calculated for all candidate distributions, and the distribution with the minimum K–S value was selected as the best-fit model. This approach ensures that the chosen distribution most accurately reflects the statistical behavior of failures. In this work, the reliability of the TPP estimated on series arrangement of the subsystem via Equation (6).

$$Rs(t) = \prod_{i=1}^{n} Ri(t) \tag{6}$$

where: *Rs(t)* – reliability function of the system, it denotes the probability that the entire system operates without failure up to time *t*; *Ri(t)* – reliability function of the *i*-th component, it represents the probability that component *i* operates without failure up to time *t*; n – total number of components in the system. Now the overall reliability of TPP is given by Equation (7).

$$R_s(t) = R_{BAC}(t) \times R_{BFS}(t) \times R_{TGS}(t) \tag{7}$$

Rs(t) – overall reliability of the TPP; $R_{BAC}(t)$ – reliability of the Boiler and Air Circuit (BAC) subsystem; $R_{BFS}(t)$ – reliability of the Boiler Feedwater System (BFS); $R_{TGS}(t)$ – reliability of the Turbine–Generator System (TGS); *t* – operating time.

The reliability of the subsystem at different time levels is determined and presented from Figures 3-5. It follows from the graphs presented above that as the operating time increases from 0 to 17520 hours, the overall reliability of the installation decreases significantly. The probability of trouble-free operation of the ID fan, generator oil system, BFP for a period exceeding one year (8760 hours) is less than 50%.

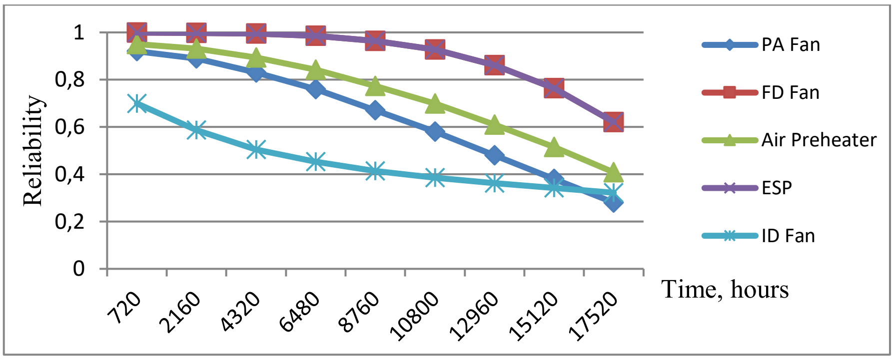

Fig. 3. Reliability Analysis of BAC

Based on the reliability analysis carried out, taking into account the performance of the equipment after one year of operation, the planning of maintenance of critical equipment should be carried out with increased priority. The maintenance schedule is determined by the level of criticality of each element, and information about the failure rate of the system contributes to a more efficient allocation of maintenance resources.

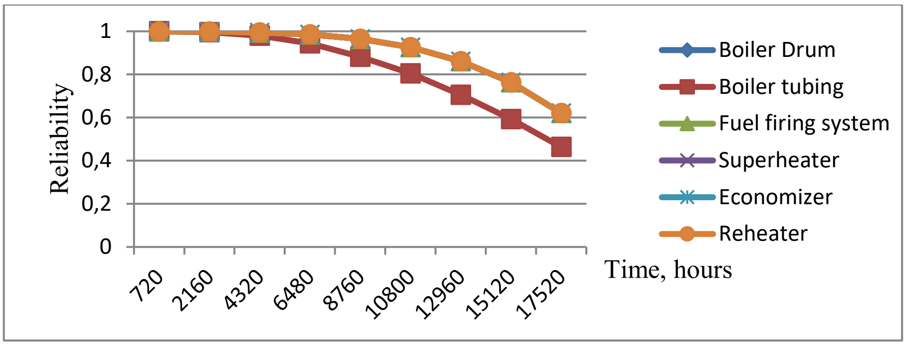

Fig. 4. Reliability analysis of BFS

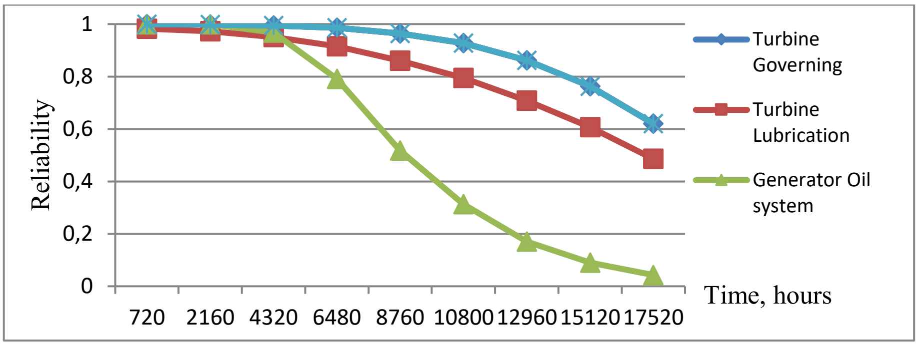

Fig. 5. Reliability analysis of TGS

The use of estimated reliability values makes it possible to determine the degree of criticality of equipment and systems. The results of the analysis show that individual systems are the most vulnerable in terms of operational readiness, which necessitates the urgent adoption of corrective measures. The findings made it possible to adjust maintenance schedules based on the actual operating conditions at the enterprise. In addition, the results of the reliability analysis serve as the basis for managerial decision-making, allowing you to plan maintenance activities by subsystem and rationally allocate resources.

5. Conclusion

As part of this study, an analysis of the reliability of thermal power plants was performed based on operational maintenance data obtained for various subsystems in real time. To assess the availability of the system, the FTA model was developed and applied, the results of which are presented in the paper. The study showed that using the FTA approach makes it possible to obtain availability values that are closest to real operational data, while the impact of system redundancy is not taken into account in this technique. In addition, an analysis of the reliability of TPP subsystems for various periods of operation was carried out, which revealed that the probability of trouble-free operation of the ID fan, generator oil system, BFP over the last year of operation is less than 50%. Failure of any of these subsystems can lead to the shutdown of thermal power plants, and therefore they are classified as critically important and require special monitoring [14, 15]. The obtained results and conclusions of the study can be used to improve the reliability of equipment and increase the volume of electricity generation at thermal power plants.

Conflict of interest statement

The authors declare that they have no conflict of interest in relation to this research, whether financial, personal, authorship or otherwise, that could affect the research and its results presented in this paper.

CRediT author statement

Nygymanova A.: Conceptualization, Methodology, Investigation, Data analysis, Writing – original draft; **Ongar B.:** Data curation, Statistical analysis, Validation, Writing – review & editing; **Sarsenbayev Y.:** Supervision, Scientific consultation, Methodology review, Writing – review & editing. The final manuscript was read and approved by all authors.

References

1 Adhikary D.D., Bose G.K., Chattopadhyay S., Bose D. and Mitra S. (2012) RAM investigation of coal-fired thermal power plants: A case study. *Int. J. Ind. Eng. Comput*. 3, 3, 423 – 424. https://doi.org/10.5267/j.ijiec.2011.12.003

2 Bisanovic S., Hajro M. and Samardzic M. (2013) Component Criticality Importance Measures in Thermal Power Plants Design. *Int. J. Electr. Comput. Energ. Electron. Commun. Eng.,* 7, 3, 213 – 218. Available at: https://www.academia.edu/112818866/Component_Criticality_Importance_Measures_in_Thermal_Power_Plants_Design

3 Pariaman H., Garniwa I., Surjandari I. and Sugiarto B. (2015) Availability improvement methodology in thermal power plant. *Sci. J. PPI-UKM,* 2, 1, 43 – 52. http://kemalapublisher.com/index.php/ppi-ukm/article/viewFile/44/pdf_7

4 Kumarappan N., Suresh K. (2015) Combined SA PSO method for transmission constrained maintenance scheduling using levelized risk method. *Int. J. Electr. Power Energy Syst.* 73, 1025 – 1034. https://doi.org/10.1016/j.ijepes.2015.06.026

5 Dong W., Zhang X., Dong Y., Lin Y. (2023) Equipment reliability assessment based on a two-parameter Weibull distribution. *Proceedings of the 2023 Intern. Conf. on Management Science and Software Engineering*. *Atlantis Press*, 538 – 544. https://doi.org/10.2991/978-94-6463-262-0_56

6 Hassani H., Silva E.S. (2015) A Kolmogorov–Smirnov based test for comparing predictive accuracy. *Econometrics*, 3(3), 590 – 609. https://doi.org/10.3390/econometrics3030590

7 Eti M.C., Ogaji S.O.T., Probert S.D. (2007) Integrating reliability, availability, maintainability and supportability with risk analysis for improved operation of the Afam thermal power-station. *Appl. Energy*, 84, 2, 202 – 221. https://doi.org/10.1016/j.apenergy.2006.05.001

8 Barabady J., Kumar U. (2007) Reliability characteristics-based maintenance scheduling: A case study of a crushing plant. *Int. J. Performability Eng.* 3, 3, 319 – 328. https://doi.org/10.23940/ijpe.07.3.p319.mag

9 Nygymanova A., Bekbayev A.B., Sarsenbayev E.A., Almuratova N.K. (2025) A method for determining the reliability indicators of equipment at electric power plants. *Bulletin of the Almaty University of Power Engineering and Telecommunication,* 71, 4, 6 – 19. https://doi.org/10.51775/2790-0886_2025_71_4_6

10 Carazas F.J.G., Salazar C.H., Souza G.F.M. (2011) Availability analysis of heat recovery steam generators used in thermal power plants. *Energy,* 36, 6, 3855 – 3870. https://doi.org/10.1016/j.energy.2011.04.007

11 Jung S., Yoo J., Lee Y.-J. (2020) A software fault tree analysis technique for formal requirement specifications of nuclear reactor protection systems. *Reliability Engineering & System Safety*, 202, 107064. https://doi.org/10.1016/j.ress.2020.107064

12 Nehal N., Lounis Z., Bouhadiba B., Lounis Z. (2023) Modelling of heating furnace fire scenarios using fault tree analysis, a bayesian network, and a thermal transfer method for system reliability analysis. *J. Loss Prev. Process Ind.,* 83. 104995. https://doi.org/10.1016/j.jlp.2023.104995

13 Zio E., Podofillini L. (2007) Importance measures and genetic algorithms for designing a risk-informed optimally balanced system. *Reliab. Eng. Syst. Saf.,* 92, 10, 1435 – 1447. https://doi.org/10.1016/j.ress.2006.09.011

14 Mandelli D., Wang C., Agarwal V., Lin L., Manjunatha K.A. (2024) Reliability modeling in a predictive maintenance context: A margin-based approac*h*, *Reliab. Eng. Syst. Saf.*, 243, 109861. https://doi.org/10.1016/j.ress.2023.109861

15 Akula S. K., & Salehfar H. (2026) Reliability Assessment of Power System Microgrid Using Fault Tree Analysis: Qualitative and Quantitative Analysis. *Electronics*, *15*(2), 433. https://doi.org/10.3390/electronics15020433

AUTHORS' INFORMATION

Nygymanova Ainur - PhD student, Master (Sci.), Kazakh National Research Technical University named after K.I.Satpayev, Almaty, Kazakhstan; https://orcid.org/0000-0002-1880-4969; a.nygymanova@satbayev.university,

Ongar Bulbul - Ph.D., Associate Professor, Kazakh National Research Technical University named after K.I.Satpayev, Almaty, Kazakhstan, SCOPUS ID: 57200992503; https://orcid.org/0000-0002-8333-8343; b.ongar@satbayev.university;

Sarsenbayev Yerlan - Ph.D., Associate Professor, Kazakh National Research Technical University named after K.I.Satpayev, Almaty, Kazakhstan, SCOPUS ID: 57979875600; https://orcid.org/0000-0002-8887-1171; y.sarsenbayev@satbayev.university

EURASIAN PHYSICAL TECHNICAL JOURNAL

2026, Volume 23, No.1 (55)

https://doi.org/10.31489/2026N1/68-77

Received: 15/01/2026 Revised: 13/02/2026 Accepted: 19/03/2026

Original Research Article

UDC 536.8; 621.43; 662.613; 519.6

COUPLED SPUTTERING AND COMBUSTION DYNAMICS OF DIVERSE FUEL TYPES

Bolegenova S., Askarova A., Ospanova Sh.*, Bolegenova S.,
Nurmukhanova A., Assilbekova Sh.

Department of Thermophysics and Technical Physics, Al-Farabi Kazakh National University, Almaty, Kazakhstan

*Corresponding author: Shynar.Ospanova@kaznu.edu.kz

Abstract. *This study presents a comprehensive computational investigation of the sputtering and combustion dynamics of biodiesel and fossil diesel fuel droplets in turbulent gas flows. Advanced computational modeling and the CHEMKIN chemical kinetics framework were employed to analyze the thermophysical and chemical processes of fuel atomization, ignition, and flame propagation under varying oxidizer temperatures. The results indicate that biodiesel droplets exhibit higher mobility, enhanced mixing with the oxidizer, and more uniform heating, resulting in near-complete combustion and higher local temperatures compared to fossil diesel fuel. Soot formation during biodiesel combustion was notably lower, while carbon monoxide emissions were significantly reduced, demonstrating more efficient and cleaner combustion. Analysis of the Sauter mean diameter (SMD) highlighted improved droplet dispersion and atomization quality for biodiesel, facilitating optimized injector design and fuel-air mixing. Heat flux visualization revealed stronger convective energy transfer in biodiesel flames, and flame front dynamics confirmed that biodiesel can be used in conventional internal combustion engines without modification. Overall, these findings highlight biodiesel as a sustainable, low-emission alternative to fossil diesel fuel, supporting the development of energy-efficient technologies and the transition toward cleaner, renewable fuels.*

Keywords: Bioenergetics, Biodiesel, Fossil Fuel, Fuel Sputtering, Turbulent Combustion, Computational Modeling, Advanced Fuel Injection System, Pollutant Emissions.

1. Introduction

Energy problems are growing every year and require both non-renewable natural energy resources and non-carbon forms of energy. Rising prices for traditional fuels and increasing environmental regulations necessitate a transition to alternative energy sources and the pursuit of biofuels derived from renewable resources. Alternative energy sources, in particular biofuels, have gained the status of a competitive energy source in both developed and developing countries. This was primarily due to the growing price competitiveness of technologies using renewable energy sources and biofuels, as well as political initiatives, the need to address energy and environmental security issues, the increasing demand for energy from developing and emerging economies worldwide, and the desire to make modern energy more accessible.

Global changes in the structure of energy production have led to the fact that today, the share of various types of biofuels in the total energy consumption, according to the World Bioenergy Association, is approximately 14% (. 1) [1]. The International Energy Agency (IEA) has set a target to use up to 80% of renewable energy sources by 2050 and halve CO_2 emissions as an indicator of the emission of harmful substances [2-4]. As for Kazakhstan, several state laws and regulations on environmental protection have been developed that provide for the reduction of air pollution. In densely populated Kazakh cities with large traffic flows, the problem of gas pollution from the exhaust gases of internal combustion engines of vehicles is acute. According to the energy agency, more than 40% of pollutant emissions in Central Asia are generated by Kazakhstan [5, 6]. Biodiesel fuel is an alternative to fossil diesel fuel and can be used in diesel internal combustion engines (ICE), both in pure form and as a blend component. It has a slightly higher cetane number and better lubricity, which, when blended with traditional diesel fuel, ensures more stable engine operation. Biofuels contain virtually no sulfur and aromatic compounds, which significantly reduces the formation of harmful sulfur oxides and soot during their combustion.

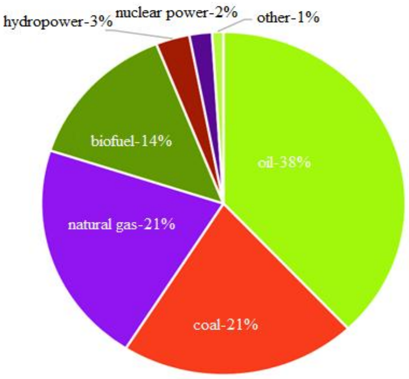

Fig.1. World energy consumption structure today

Most of the CO_2 generated during the combustion of biofuels is absorbed during the growth of plants used as raw materials, which ultimately reduces carbon dioxide emissions into the atmosphere by up to 80% compared to the use of fossil fuels [7, 8]. The technology for producing biodiesel fuel is theoretically simpler and less energy-consuming than the technology for producing traditional diesel fuel.

Problems related to global energy and environmental security require not only obtaining alternative energy sources but also the rational organization of their combustion. It is necessary to develop energy conversion systems that have higher efficiency and lower emissions of harmful substances. The efficiency of fuel consumption, productivity, and environmental friendliness of a power plant depend on the optimization of fuel combustion processes, which is associated with its preparation, method of supply, and proper combustion [9].

The above indicates the relevance of the identified problem and the need for a comprehensive study of heat and mass transfer processes during fuel combustion in energy devices. In this regard, this article is devoted to the use of the latest information technologies to study the combustion processes of liquid fuels (traditional fossil diesel fuel and biodiesel) in internal combustion engines.

In this work, for the first time, the processes of sputtering and combustion of biofuel droplets (biodiesel) were studied using information technologies and new 3D modeling software packages, to identify their advantages over fossil diesel fuel, with a subsequent assessment of the harmful emissions and greenhouse gases released during their combustion. The results of such research will contribute to the introduction of resource-saving energy technologies that meet modern environmental requirements.

2. Computational and spatial models of the problem

The mathematical model of the problem of atomization, combustion, and evaporation of liquid fuel droplets consists of equations of continuity, momentum, internal energy, and concentration of the reacting components of a two-phase flow [10-13]. The continuity equation of the fuel-air mixture is written as follows:

$$\frac{\partial \rho}{\partial t} + \mathrm{div}\left(\rho \mathbf{u}\right) = S_{mass}, \tag{1}$$

where u is the fluid velocity, S_{mass} is the local change in gas density due to evaporation or condensation.

The mixture momentum equation has the form:

$$\rho\frac{\partial u}{\partial t}+\rho\left(\text{grad}\mathbf{u}\right)\mathbf{u}=\text{div}\boldsymbol{\xi}+\rho\mathbf{g}+S_{mom}, \tag{2}$$

where S_{mom} is the local rate of change in momentum of the gas phase due to the movement of droplets.

The conservation equation for internal energy has the following form:

$$\rho\frac{\partial E}{\partial t}=\boldsymbol{\tau}:\mathbf{D}-\rho\text{div}\mathbf{u}-\text{div}\mathbf{q}+S_{energy}, \tag{3}$$

where q is the specific heat flux expressed by Fourier's law, and S_{energy} denotes the contribution to the change in internal energy due to the presence of the atomized liquid phase.

The conservation equation for the concentration of component m has the form:

$$\frac{\partial\left(\rho c_m\right)}{\partial t}=-\frac{\partial\left(\rho c_m u_i\right)}{\partial x_i}+\frac{\partial}{\partial x_i}\left(\rho D_{c_m}\frac{\partial c_m}{\partial x_i}\right)+S_{mass}, \tag{4}$$

where ρ_m is the mass density of component m, ρ is the total mass density.

For the numerical calculation of complex turbulent flows, we used the RANS method, which is widely used due to its simplicity, saving of computational resources, and a sufficient degree of accuracy in predicting the properties of reacting flows with chemical transformations. This method works well at high Reynolds numbers and high degrees of flow turbulence [14]. In our simulation, we used a prototype direct injection engine, where a jet of liquid fuel is sprayed at high pressure from multiple holes. In such internal combustion engines, fuel at a pressure of 200 bar is injected in the form of combinations of liquid ligaments and fragments of various sizes, which form near the injector nozzle and break into droplets, moving downstream due to interaction with air, which contributes to the growth of instability at the surface of the liquid. Figure 2 shows a schematic model of a multi-hole injector used in DI engines. The L_i/D_i ratio is a crucial parameter for this type of injector, as it influences the internal flow formation at the nozzle exit and the development of the spray structure [15, 16].

In an internal combustion engine with multi-hole injection, an individual injector is installed in the inlet pipe of each cylinder, supplying fuel directly to the intake valve, where the fuel mixture is prepared immediately before entering the combustion chamber. Therefore, the fuel-air mixture in multi-hole injection is uniform in composition and quality of flow for each of the cylinders, which has a beneficial effect on the power and efficiency of the engine, as well as on the toxicity of exhaust gases.

Figure 3 presents a perspective view of an unstructured computational grid composed of control volumes. This grid was generated using a set of specialized subroutines, allowing for the incorporation of various predefined initial parameters to accurately represent the computational domain.

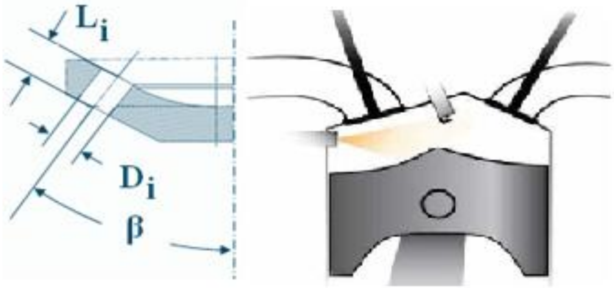

Fig.2. Schematic model of a direct injection: L_i –nozzle opening length; β – injection angle directed from the central axis of the injector; D_i – nozzle hole diameter.

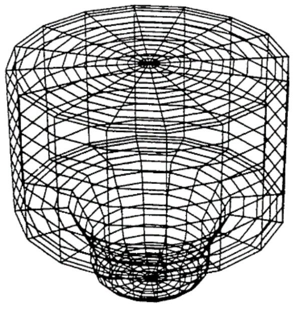

Fig.3. Perspective view of the used computational grid.

The highlighted region at the bottom of the grid, which contains several distinct subdomains, is filled with liquid fuel, providing the initial conditions necessary for simulating fuel injection, sputtering, and subsequent combustion processes. This visualization emphasizes the spatial distribution and connectivity of control volumes, which play a crucial role in capturing the detailed physical phenomena within the computational domain.

3. Computational modeling results and analysis

In this study, pure rapeseed biodiesel, specifically Biofuel RME B100, was employed as the biofuel. This fuel consists of a mixture of fatty acid methyl esters (FAME) derived from rapeseed oil. The predominant component is methyl oleate ($C_{19}H_{36}O_2$), a monounsaturated ester, which constitutes approximately 90% of the total composition, accompanied by smaller amounts of saturated and polyunsaturated esters. The application of RME is particularly suitable under Kazakhstani conditions due to its enhanced cold-flow properties, which are crucial for the northern regions of the country. Furthermore, Kazakhstan's agroclimatic conditions are well-suited for rapeseed cultivation, rendering the production of RME both sustainable and economically viable on a national scale.

The equations for the complete combustion of fossil diesel fuel and biodiesel under internal combustion engine conditions with the participation of air are presented as follows:

$$C_{12}H_{26}+18.5O_2+69.56N_2=12CO_2+13H_2O+69.56N_2,$$
$$C_{19}H_{36}O_2+27O_2+101{,}52N_2=19CO_2+18H_2O+101{,}52N_2.$$

In the engine, biodiesel undergoes combustion, producing carbon dioxide (CO_2) and water (H_2O), and releasing enough thermal energy to sustain engine operation. However, its energy content is slightly lower than that of conventional petroleum diesel fuel.

The chemical kinetics of biodiesel combustion, as well as its comparison with fossil diesel fuel, were simulated using the CHEMKIN code. This tool enables the development of detailed reaction mechanisms that comprehensively describe the thermodynamic and kinetic characteristics of fuel oxidation, including interactions between the fuel and the oxidizer [17]. The modeling framework incorporates critical parameters such as temperature, pressure, and flow velocity, providing a robust platform for accurately predicting the dynamics of combustion for both biodiesel and conventional diesel fuels. Importantly, this approach allows for the evaluation of pollutant formation while also assessing overall combustion efficiency. By integrating these factors, CHEMKIN facilitates a thorough understanding of the complex chemical and physical processes occurring during the combustion of different fuel types, offering valuable insights for optimizing engine performance and reducing harmful emissions.

In this study, computational experiments were conducted to investigate the sputtering and combustion dynamics of biofuel (biodiesel) droplets, as well as fossil petroleum diesel, in a turbulent gas flow. The effects of the initial oxidizer temperature on the sputtering, distribution, and combustion of both biodiesel and diesel fuel droplets within a model combustion chamber were systematically examined. This approach allowed for a detailed analysis of how temperature variations influence droplet dynamics, flame development, and the overall efficiency of the combustion process.

The dependence of the maximum fuel combustion temperature on the initial temperature of the oxidizer in the combustion chamber was determined for two types of liquid fuels. It has been established that combustion is not observed at an oxidizer temperature of less than 900 K. If the gas in the combustion chamber is heated to temperatures above 900 K, then in this case, there is combustion of liquid fuel with high heat release and heating of the chamber to 3000 K (Fig.4).

Figure 4 shows the dependence of the maximum fuel combustion temperature on the initial gas temperature. The maximum temperature during biodiesel combustion reaches about 3100 K, which is an indicator of combustion efficiency and the high heat capacity of biofuel. The initial gas temperature has the greatest influence on biodiesel combustion, as a 100 K increase in initial temperature results in a 1600 K increase in the maximum temperature in the combustion chamber.

Since modern diesel engines are designed to reduce harmful emissions and be gentle on the environment, they have higher injection pressures than previous-generation diesel engines [18]. This means that the internal surfaces of engines are more likely to be subject to abrasion from soot and other contaminants.

Figure 5 shows the results of a comparative analysis of soot formation obtained using the global Shell model of chemical reactions [19]. The highest concentration of soot is formed during the combustion of petroleum diesel (9.8 g/m^3). When biodiesel burns, significantly less soot is released (7.5 g/m^3), which is a favorable reason for increasing engine efficiency and reducing fuel consumption and carbon dioxide emissions in the exhaust gases. The use of biodiesel as a fuel leads to a substantial reduction in carbon monoxide (CO) emissions compared to conventional petroleum diesel. While CO is inevitably formed during the combustion process, the amount released is considerably lower due to the higher oxygen content and more complete combustion of biodiesel droplets. This improved combustion behavior limits the formation of incomplete combustion products, making biodiesel a cleaner alternative in terms of CO output. The reduction in CO emissions not only mitigates local air pollution but also contributes to lower health risks associated with carbon monoxide exposure.

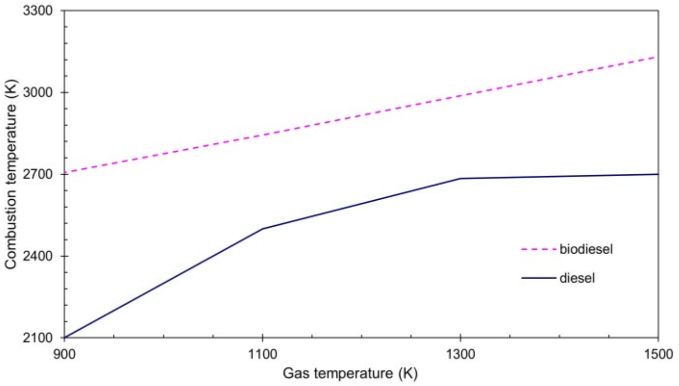

Fig.4. Temperature profiles during combustion of fossil diesel fuel and biodiesel depending on the initial gas temperature

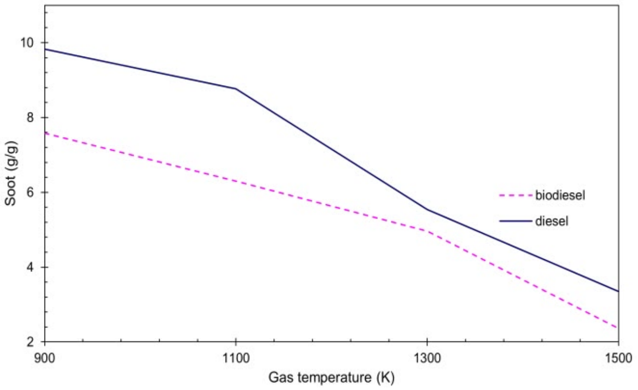

Fig.5. Soot formation during combustion of fossil diesel fuel and biodiesel depending on the initial gas temperature

The computational results indicate that, under the same operating conditions, engines fueled with biodiesel release significantly less CO than those running on traditional diesel, highlighting the environmental advantages of biodiesel in urban and industrial settings (Fig.6). Based on the analysis of the influence of gas temperature on the combustion processes and distribution of biodiesel and petroleum diesel droplets, a 3D visualization of the thermophysical characteristics of the reacting flow was obtained.

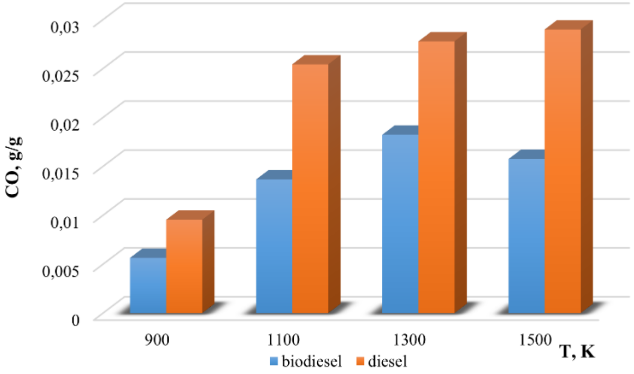

Fig.6. Carbon monoxide formation during combustion of biodiesel and diesel at different gas temperatures

Figure 7 shows graphs of droplet temperature distribution at 3 ms. The turbulent motion of the gas flow imparts additional kinetic energy to the droplets of both biodiesel and conventional diesel, accelerating them toward the exit of the combustion chamber. As a result of this rapid movement, the droplet temperature rises to over 600 K, promoting active chemical reactions.

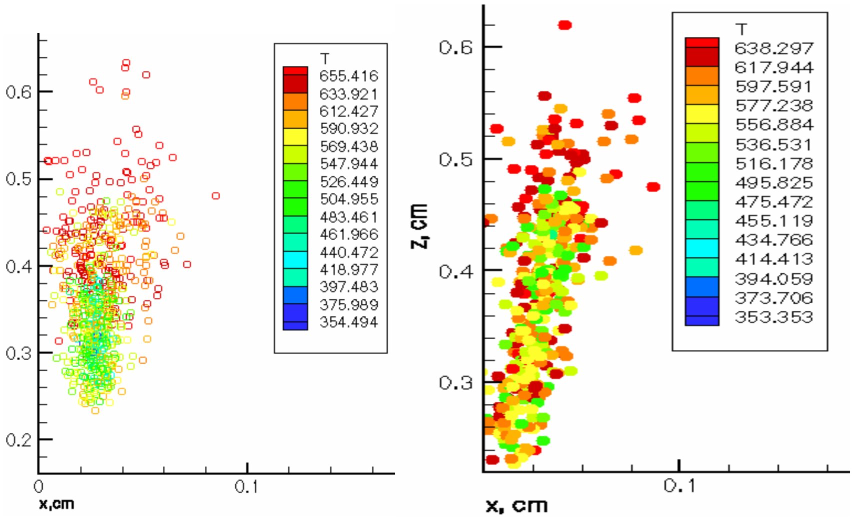

a) biodiesel b) diesel

Fig.7. Temperature distribution of diesel and biodiesel droplets along the height of the combustion chamber at t=3 ms

Biodiesel droplets, in particular, exhibit higher mobility and respond more readily to the turbulent eddies within the chamber, leading to enhanced mixing with the surrounding oxidizer. This intensified interaction improves the local combustion environment, facilitates more uniform heating, and promotes near-complete combustion of the fuel droplets. Consequently, the dynamic behavior of biodiesel under turbulent conditions contributes to more efficient energy release and a reduction in unburned fuel residues, highlighting its advantages over conventional diesel in terms of combustion performance. In the case of combustion of a fuel-oxidizer premixed system, the temporal evolution of the biodiesel flame front is illustrated in Figure 8. The figure clearly demonstrates that both the shape and the size of the flame are strongly influenced by the degree of mixing between the fuel and the oxidizer. At 3 ms after ignition, the flame core extends from approximately 0.6 cm to 1.25 cm along the vertical axis of the combustion chamber. This elongation is attributed to elevated temperatures, which cause the boundary between the flame core and the ignition zone to expand, enhancing the propagation of the combustion front.

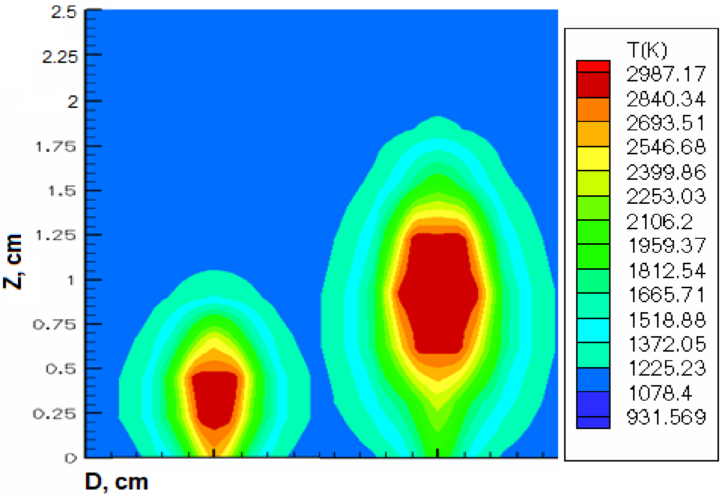

a) t=2 ms b) t=3 ms

Fig.8. Variation of the biodiesel flame front over time

The flame morphology is inherently dependent on the properties of the flammable mixture and the characteristics of the injection system employed. Importantly, the combustion behavior of biodiesel indicates that it can be utilized in conventional internal combustion engine units without requiring modifications to the fuel delivery or injection system.

Beyond combustion performance, biodiesel exhibits a significant tribological benefit: its inherent lubricating properties reduce engine wear by approximately 60%, thereby extending the operational lifespan of critical engine components, including the fuel injection system, combustion chamber, and exhaust assembly. This combination of favorable flame dynamics and mechanical advantages underscores biodiesel's potential as a sustainable and efficient alternative to conventional petroleum diesel in automotive applications.

Figure 9 illustrates the distribution of heat flux in both biodiesel and diesel fuel mixtures reacting with an oxidizer. The visualization corresponds to the early stages of the ignition process, at a moment when the fuel has not yet fully reacted with the oxidizer. At this initial stage, the Nusselt number ranges between 1 and 2, reflecting the early development of convective heat transfer. Higher Nusselt numbers, in contrast, indicate regions of intense convective heat flux, which are characteristic of turbulent flow conditions.

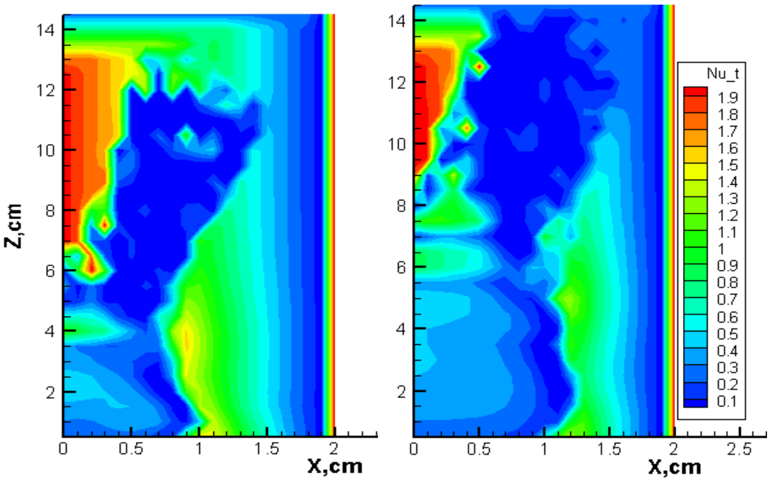

a) biodiesel b) diesel

Fig.9. Visualization of heat flow intensity in a reacting mixture of biodiesel and oxidizer

As shown in Figure 9, the axis of the combustion chamber exhibits pronounced mixing of the fuel and oxidizer, driven by the temperature gradients within the flame core. For both biodiesel and diesel, this mixing plays a critical role in determining flame structure and combustion efficiency. However, due to differences in droplet mobility and fuel properties, biodiesel demonstrates more rapid and uniform mixing compared to conventional diesel, promoting earlier and more complete combustion. Additionally, the curvature of the flame front, previously observed in Figure 8, disrupts the formation of a flat, laminar combustion zone, leading to the development of a fully turbulent flame. This effect is more pronounced for biodiesel, where enhanced droplet dispersion and higher reactivity accelerate the transition from laminar to turbulent combustion, improving heat release rates and overall energy conversion.

Figure 10 illustrates the results of computational simulations tracking the temporal evolution of the Sauter mean diameter (SMD) of biodiesel droplets as a function of distance from the injector. These results are further compared with experimental data for conventional diesel fuel reported by [20], allowing for a direct evaluation of differences in atomization behavior between the two fuels. The Sauter mean diameter represents a key volumetric-surface parameter that characterizes the size distribution and atomization quality of liquid fuel droplets. Consequently, analysis of SMD provides critical information for the selection of injector design, optimization of fuel injection pressure, and determination of effective fuel flow rates necessary to achieve uniform droplet sizes throughout the combustion chamber. Such detailed characterization ensures improved fuel-air mixing and more efficient combustion, which is particularly important for enhancing engine performance and minimizing pollutant formation.

Analysis of Figure 10 indicates that the computational simulation results are generally in good agreement with the experimental data, with the exception of the region located approximately 10 mm from the injector nozzle at 0.5 ms. In this zone, the calculated Sauter mean diameter (SMD) of biodiesel droplets reaches a peak value of 136 μm, whereas the experimental measurements report a maximum SMD of 110 μm.

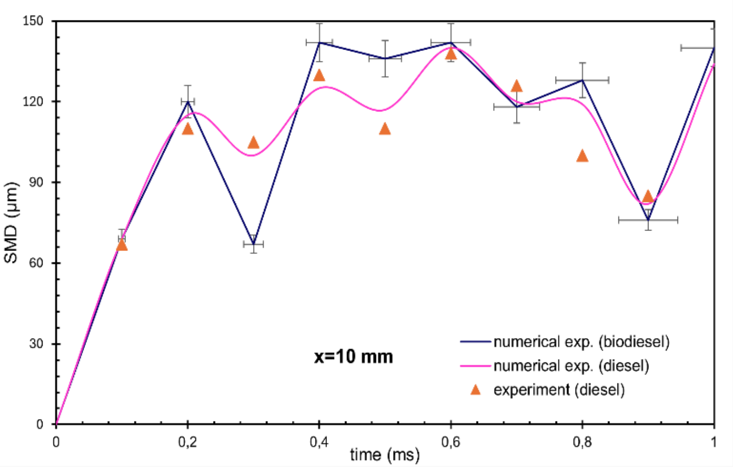

Fig.10. Comparison of time distributions of the Sauter mean diameter of droplets of diesel and biodiesel fuels at a distance of 10 mm from the injector nozzle

The observed discrepancies can be attributed to the proximity of the droplets to the injector, where end effects and localized flow disturbances are most pronounced. These phenomena inherently lead to deviations between the idealized conditions of numerical simulations and the complex dynamics captured in experimental observations, particularly in the near-nozzle region.

4. Conclusions

From the results of the computational experiments of biodiesel and fossil diesel fuel droplets sputtering and combustion, the key findings regarding combustion efficiency, emissions, and droplet dynamics can be summarized as follows:

1. Biodiesel, specifically rapeseed methyl ester (RME B100), demonstrates significant potential as an alternative to conventional petroleum diesel. Its higher oxygen content, lower sulfur and aromatic compounds, and better lubricity contribute to more complete combustion, reduced emissions of soot and carbon monoxide (CO), and decreased engine wear. Computational results confirm that CO emissions from biodiesel are substantially lower than from fossil diesel fuel under identical operating conditions, highlighting its environmental and health advantages;
2. The combustion of biodiesel droplets in a turbulent gas flow shows enhanced mobility, improved mixing with the oxidizer, and more uniform heating compared to diesel droplets. This leads to near-complete combustion, higher local temperatures (up to ~3100 K), and accelerated transition from laminar to turbulent flames. The shape and size of the flame front depend on fuel-oxidizer mixing and injection system characteristics, yet biodiesel can be utilized in standard diesel engines without modifications;
3. Visualization of heat flux indicates that biodiesel achieves more efficient convective heat transfer in the combustion chamber due to enhanced droplet dispersion and higher reactivity. Turbulent mixing promotes rapid flame propagation and effective energy release, contributing to higher combustion efficiency compared to fossil diesel fuel;
4. Analysis of the Sauter mean diameter (SMD) of fuel droplets shows that biodiesel exhibits slightly larger droplets near the injector due to end effects, but overall droplet dispersion and atomization are favorable. SMD analysis provides critical guidance for injector design, fuel injection pressure optimization, and uniform droplet formation, ensuring better fuel-air mixing and efficient combustion for both biodiesel and diesel;
5. The combined results of computational simulations and experimental comparisons indicate that biodiesel offers both environmental and operational advantages. Its use can reduce harmful emissions, improve engine lifespan due to natural lubrication, and provide a sustainable alternative in regions suitable for rapeseed cultivation, such as Kazakhstan. These findings support the broader adoption of biodiesel in internal combustion engines as part of a strategy to transition toward cleaner and renewable energy sources.

Conflict of interest statement

The authors declare that they have no conflict of interest in relation to this research, whether financial, personal, authorship or otherwise, that could affect the research and its results presented in this paper.

CRediT author statement

Bolegenova S.: Supervision; **Askarova A.:** Conceptualization, Funding acquisition; **Ospanova Sh.:** Investigation, Writing-Original draft preparation, Writing Reviewing and Editing; **Bolegenova S.:** Resources, Software; **Nurmukhanova A.:** Data curation, Methodology, Investigation; **Assilbekova S:** Visualization, Validation.

The final manuscript was read and approved by all authors.

Funding

This work was supported by the Science Committee of the Science and Higher Education Ministry of the Republic of Kazakhstan (No 26105185).

References

1. The Global Bioenergy Statistics (GBS) report. WBA Global Bioenergy Statistics (2023). Available at: https://www.worldbioenergy.org/news/763/47/WBA-publishes-the-Global-Bioenergy-Statistics-2023-report/

2. AlKheder Sh., AlDousari A., AlOtaibi M. (2024) A simplified system dynamics model to investigate the effects of urban transportation management policies on reducing CO_2 and greenhouse gas emissions, *Phys. Chem. Earth*., 135, 103623. https://doi.org/10.1016/j.pce.2024.103623

3. Pradhan R.P., Nair M.S., Hall J.H., Bennett S.E. (2024) Planetary health issues in the developing world: Dynamics between transportation systems, sustainable economic development, and CO2 emissions, *J. Clean. Prod.*, 449, 140842. https://doi.org/10.1016/j.jclepro.2024.140842

4. Comineti C.S.S., Pretel A.F., Schlindwein M.M. (2023) The type of development promoted by Brazilian National Biofuels Policy, *Renew. Sustain. Energy Rev.*, 182, 113368. https://doi.org/10.1016/j.rser.2023.113368

5. Report of the IEA: IEA CO_2 Emissions from Fuel Combustion Statistics: Greenhouse Gas Emissions from Energy (2023). Available at: https://www.iea.org/reports/co2-emissions-in-2023

6. Askarova A., Bolegenova S., Ospanova S., Maxutkhanova A., Bolegenova K., Baidullayeva G. (2025) Study of thermophysical dynamics in biofuel droplet atomization and combustion, *Eurasian phys. tech. j.*, 22, 60–69. https://doi.org/10.31489/2025N2/60-69

7. Kiselev A., Magaril E., Karaeva A. (2024) Environmental and economic efficiency assessment of biogas energy projects in terms of greenhouse gas emissions, *Energ. Ecol. Environ.,* 9, 68–83. https://doi.org/10.1007/s40974-023-00305-5

8. EdwinGeo V., Fol G., Aloui F. et al (2021) Experimental analysis to reduce CO_2 and other emissions of CRDI CI engine using low viscous biofuels, *Fuel*, 283, 118829. https://doi.org/10.1016/j.fuel.2020.118829

9. Askarova A., Bolegenova S., Ospanova Sh., Slavinskaya N., Aldiyarova A., Ungarova N. (2021) Simulation of non-isothermal liquid sprays under large-scale turbulence, *Phys. Sci. Technol*., 8, 28-40. https://doi.org/10.26577/phst.2021.v8.i2.04

10. Oruganti S.K., Gorokhovski M.A. (2024) Stochastic models in the under-resolved simulations of spray formation during high-speed liquid injection, *Phys. Fluids,* 36, 052105. https://doi.org/10.1063/5.0206826

11. Gorokhovski M.A., Oruganti S.K. (2022) Stochastic models for the droplet motion and evaporation in under-resolved turbulent flows at a large Reynolds number, *J. Fluid Mech*., 932, 18. https://doi.org/10.1017/jfm.2021.916

12. Askarova A., Bolegenova S., Ospanova S., Bolegenova K., Nurmukhanova A. (2025) Energetic efficiency of turbulent biofuel combustion for advanced bioenergy technologies, *Int. J. Math. Phys*., 16 (1), 20–28. https://doi.org/10.26577/ijmph.20251612

13. Zhong W., Xin Z., Wang L., Liu H. (2024) Investigations on High-Speed Flash Boiling Atomization of Fuel Based on Numerical Simulations, *Comput. Model. Eng. Sci.*, 139, 1427-1453. https://doi.org/10.32604/cmes.2023.031271

14. Guo H., Li Y., Wang B., Zhang H., Xu H. (2019) Numerical investigation on flashing jet behaviors of single-hole GDI injector, *Int. J. Heat Mass Transf.,* 130, 50-59. https://doi.org/10.1016/j.ijheatmasstransfer.2018.10.088

15. Chang M., Kim H., Zhou B., Park S. (2023) Spray collapse resistance of GDI injectors with different hole structures under flash boiling conditions, Energy, 268, 126689. https://doi.org/10.1016/j.energy.2023.126689

16. Geissler C.H., Ryu J., Maravelias Ch.T. (2024) The future of biofuels in the United States transportation sector, *Renew. Sustain. Energy Rev.,* 192, 114276. https://doi.org/10.1016/j.rser.2023.114276

17. Ra Y., Reitz R.D. (2008) A reduced chemical kinetic model for IC engine combustion simulations with primary reference fuels, *Combust. Flame*, 155, 713–738. https://doi.org/10.1016/j.combustflame.2008.05.002

18. Yin Z., Liu S., Tan D., Zhang Z., Wang Z., Wang B. (2023) A review of the development and application of soot modelling for modern diesel engines and the soot modelling for different fuels, *Process. Saf. Environ. Prot.,* 178, 836-859. https://doi.org/10.1016/j.psep.2023.08.075

19. Cui M., Zhang W., Fu J., Luo X., Hung D.L.S., Xu M., Li X. (2024) Impact of flash boiling spray on soot generation of a rich fuel–air mixture under various ambient pressures, *Combust. Flame,* 263, 113388. https://doi.org/10.1016/j.combustflame.2024.113388

20. Arcoumanis C, Gavaises M, French B (1997) Effect of fuel injection processes on the structure of diesel sprays. *SAE Technical Paper*, 970799. https://doi.org/10.4271/970799

AUTHORS' INFORMATION

Bolegenova, Saltanat Alikhanovna – Doctor of Phys. and Math. Sciences, Professor, Head of the Department of Thermophysics and Technical Physics, Al-Farabi Kazakh National University, Almaty, Kazakhstan; SCOPUS Author ID: 57192917040; https://orcid.org/0000-0001-5001-7773; Saltanat.Bolegenova@kaznu.edu.kz

Askarova, Aliya Sandybayevna – Doctor of Phys. and Math. Sciences, Professor, Department of Thermophysics and Technical Physics, Al-Farabi Kazakh National University, Almaty, Kazakhstan; SCOPUS Author ID: 6603209318; ORCID: https://orcid.org/0000-0003-1797-1463; Aliya.Askarova@kaznu.edu.kz

Ospanova, Shynar Sabitovna – PhD, Senior Lecturer, Department of Thermophysics and Technical Physics, Al-Farabi Kazakh National University, Almaty, Kazakhstan; Scopus Author ID: 55988678700; ORCID ID: 0000-0001-6902-7154; Shynar.Ospanova@kaznu.edu.kz

Bolegenova, Symbat Alikhanovna – PhD, Associate Professor, Department of Thermophysics and Technical Physics, Al-Farabi Kazakh National University, Almaty, Kazakhstan, Scopus Author ID: 57195694754; ORCID: 0000-0003-1061-6733; Bolegenova.Symbat@kaznu.edu.kz

Nurmukhanova, Alfiya Zeinullovna – Candidate of Tech. Sciences, Department of Thermophysics and Technical Physics, Al-Farabi Kazakh National University, Almaty, Kazakhstan, Scopus Author ID: 57217224044; ORCID: 0000-0002-0289-3610; alfiyanurmukhanova7@gmail.com

Assilbekova, Shira Kultubayevna – PhD student, Department of Thermophysics and Technical Physics, Al-Farabi Kazakh National University, Almaty, Kazakhstan, ORCID: 0009-0000-2246-1033; Asilbekovashira6@gmail.com

EURASIAN PHYSICAL TECHNICAL JOURNAL

2026, Volume 23, No.1 (55)

https://doi.org/10.31489/2026N1/78-86

Received: 13/12/2025 Revised: 13/022026 Accepted: 19/03/2026 Published online: 30/03/2026

Original Research Article

UDC 53.043

EVALUATION OF THE EFFECTIVENESS OF THE NON-KILNED ASH-SLAG GRAVEL STRUCTURE UNDER THERMAL IMPACT

Atyaksheva A.V.*, Seitova Zh. A., Issataeva A. K., Ryasnov D. Yu., Khamitova Ye.M.

Energy Institute of S. Seifullin, Kazakh Agrotechnical Research University, Astana, Kazakhstan
**Corresponding author:* sahsa77@mail.ru

Abstract. *The article presents an analysis of the stress-deformed state results for gravels based on ash-slag mixtures, with the same specified composition, but different in structure and density under the thermal impact with temperature 500 ℃. The evaluation of the gravels structure was carried out in a numerical simulation of the thermostatic structural analysis process. According to the results, the two – component gravel structure shows greater thermal stability. Separation into two component structure leads to a more even distribution of iso Surfaces, which in turn eliminates the possibility of stress surges leading to sharp changes in the structural characteristics of materials accompanied by degradation processes. In two component structure, there is a reduction of a stress intensity resulting from sudden stresses surges and leading to the formation of material failure points. The maximum stress intensity of two component gravel for about*$1.8 \cdot 10^6$ *Pa in compare of single component for about* $2.1 \cdot 10^7$ *Pa. The higher thermal viability of two-component gravel is demonstrated by thermal deformation due to a reduction in shear stress, which is (max)* $9.03 \cdot 10^5$ *Pa, in compare of single component (max)* $1.11 \cdot 10^7$ *Pa. Such conditions of the stress-deformed state indicate a greater reserve of thermal resistance for two – component gravel in compare of single component gravel and the possibility of its use as a heat protection in the composition of heat-resistant panels or independently in the temperature range up to 500 ℃.*

Keywords: gravel, structural, ash-slag mix, cement, thermal, deformation, strain, stress.

1. Introduction

The range of materials that can withstand high temperatures today is wide enough. There are lot of materials are available for use in different temperature ranges and operating conditions. However, materials that can withstand high temperatures are usually based on natural components, such as basalt, asbestos, different kinds of clay and so on. Moreover, such materials are usually subjected to high temperature technologies such as roasting, fusion and other (ceramic, pottery, etc.) At the same time, the trend of increasing environmental and economic attractiveness of heat-resistant materials technologies dictates conditions for the need to use production wastes, especially non-utilized waste, reducing costs and minimizing the technological burden on the environment through recycling. One of the most promising areas is related to the specific application of techno-genic waste from energy generation, especially, waste ash-slag mixes, having in its composition both active and inert components. Ash-slag waste is currently widely used for structural lightweight concrete, road construction and as a filler with enhanced thermal insulation properties [1-3]. Today kilned and non-kilned ash-slag gravels are successfully used as fillers. Kilned ash-slag gravel, at bulk density not more than 600 kg/ m^3 can successfully solve the problems of providing heat protection functions, including heat resistance. However, the manufacture of kiln materials generally requires a significant amount of energy in kilns at a temperature not less than 1150 °C – 1200 °C [4]. In this regard, the proportion of kilned materials today is being reduced intensively when replaced by non-kilned materials [5,6]. Non-kilned gravel in uniform density based on ash and slag waste is intensively used as a heat insulation material in construction production and in many works is noted as a material with the use of various complex additives and unconventional thermal treatment as heat resistant material [7,8]. However, the use of superplasticizers, binding fibrous materials, wave heat treatment or other significantly increase the cost of non-burning gravel, which defines it as uncompetitive compared to the numerous varieties of thermal insulation materials based on natural components of the same ranges of heat and heat resistance. Of particular interest for use in heat-resistant materials is non-calcined gravel based on ash-slag wastes from the combustion of coals with mechanical viscosity (Coal Mv) under condition of structuring, in which the strength and heat functions are divided according to the perception of the gravity of the power and heat engineering functions [9,10]. Furthermore, application of ash-slag mixtures, which include refractory ash that has a melting temperature range from 1600 °C to 1800°C and high elastic- plastic properties [11,12], complements thermostable qualities and further determines the ability to produce a material capable of withstanding significant thermal loads.

Thus, the study is aimed at determining the possibility of using a non-kilned ash-slag gravel with a two-component structure in which the strong shell, which is ash-slag cement mix shell, accepts the deformation load, and the inner area, performs thermal functions. Results obtained for thermal stress and high-temperature deformation of stationary convective heat exchange (T – 500° C) was possible to evaluate the possibility of using non-kilned, two-component gravel as a filler in heat-resistant materials and as a stand-alone material for use in low temperature furnaces for heating, drying and heat treatment.

2. Material and Methods

The object of the study is a thermal stress-deformation parameters of the non-kilned gravel structure. The aim of the study is to evaluate the efficiency of a structure of non-kilned gravel, based on an ash-slag mixture under temperature impact in conditions of stationary heating in the temperature range from 22 °C to 500 °C. To achieve this, the following objectives are being solved:

- to analyze the equivalent stress and stress intensity during the thermal impact process on single and two component structure ash slag gravel;
- to analyze the total deformation and shear stress of non-kilned gravel with single and two-component structure that occurs during thermal action.

Materials, which are used as samples of non-kilned ash-slag gravels of a single-component structure with uniform density, 2000 kg/ m^3 and a two-component structure with density 2500 kg/ m^3 and a thickness of shell not no more than 2 mm (first component) and the inner volume of a mixture consisting of ash-slag mixture with density 1800 kg/m^3 (second component). Samples of gravels represented on the Fig. 1. For the production of both samples of gravels, a ash-slag mixture from the combustion of Ekibastuz coal containing refractory ash and Karaganda Slag Portland-cement were used (SPC) quality Class 400.

a) b)

Fig.1. Non-kilned ash-slag gravels: a) – single component structure; b) two component structure.

In this case, the double-layer gravel shell has a closed, evenly distributed porosity at relatively small grain size, optimal for operating conditions of strength and thermal porosity [13,14]. The evaluation of the efficiency of structured non-kilned gravels under thermal impact was carried out on the basis of numerical simulation of thermal heating in conditions of stationary convective heat exchange with heating up to a temperature of 500°C at specified input parameters of cement and ash mixture properties in Ansys CFX (Computational Fluid Dynamics) software environment. For simulation were used Thermal Static and Static Structural modules. Modelling is based on the finite element method in ANSYS APDL (ANSYS Parametric Design Language). The simulation was carried out on physical models of non-kilned gravels in equal volumes of single-component gravel 33510 mm^3 (s1), and two-component gravel when dividing functions of volumes (s2) into the volume of the shell is equal 19373 mm^3 and internal cavity, filled with 14137 mm^3 of ash-slag loose mixture. The physical models of gravel samples are shown on the Fig.2. Numerical simulation was carried out over 3600 seconds in 36-second increments under stress and strain control.

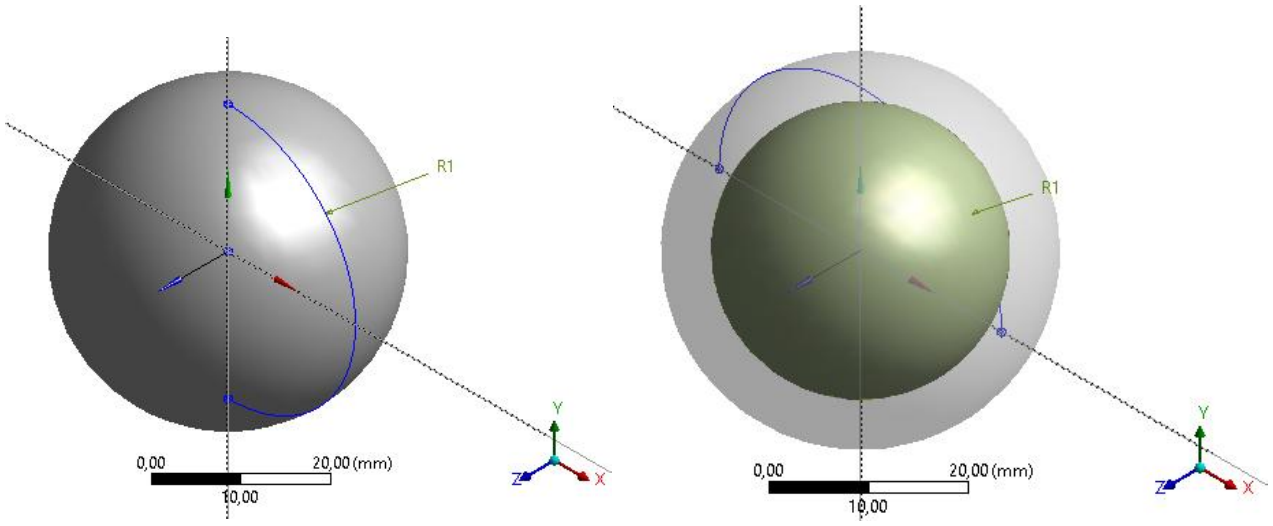

a) b)

Fig.2. Physical models of non-kilned ash-slag gravels:
a) – single component structure; b) two component structure.

Engineering data for numerical simulation of the test models s1 and s2 materials presented in tables 1 and 2.

Table 1. Physical properties

N	Density, kg/m^3	Coefficient of thermal expansion, °C^{-1}	Isotropic thermal conductivity, W/m°C	Specific heat, J/kg°C
Ash slag mix	2000	6e-06	0.2	840
Slag Portland-cement	2500	5e-06	1.2	800

Table 2. Elastic – plastic properties

N	Young's Modulus, MPa	Poisson's Ratio, Pa	Bulk Modulus, GPa	Shear Modulus, GPa
Ash slag mix	6000	0.17	3.030	4.564
Slag Portland-cement	2500	0.133	7.356	7.149

During the experiment, a thermal load was applied, approximated to the real conditions when controlling the thermal and stress-deformation parameters of the condition of non-kilned gravel. Heating was carried out for one hour, with parameter control increments of 1 second for 36 seconds after reaching the granule surface at 500 °C.

3. Results and discussion

3.1 Analysis results of the equivalent stress and stress intensity evaluation during the thermal impact process on single and two component structure ash slag gravels

The heat load creates an equivalent stress in the body of gravel of different intensity. Equivalent stress is a value representing the stress arising in different directions and calculated on the basis of three main stresses allowing to estimate, in case of thermal imp act, the resistance of the gravels when split due to temperature action [15].

$$\varepsilon_x = \frac{1}{E}\left[\sigma_x - \mu\left(\sigma_y + \sigma_z\right)\right] + \alpha\Delta T, \tag{1}$$

$$\varepsilon_y = \frac{1}{E}\left[\sigma_y - \mu\left(\sigma_x + \sigma_z\right)\right] + \alpha\Delta T, \tag{2}$$

$$\varepsilon_z = \frac{1}{E}\left[\sigma_z - \mu\left(\sigma_x + \sigma_y\right)\right] + \alpha\Delta T, \tag{3}$$

where ($\sigma_{x,}$ $\sigma_{y,}$ $\sigma_{z,}$) is principal thermal stresses in direction x, y, z; μ is Poisont's ratio; E is Bulk modulus; α is a thermal expansion factor; ΔT – temperature difference at the moment of thermal impact and ambient temperature.

According to Figure 3 the equivalent stress of the two-component structure gravel is less than stress of single component gravel and it consist at temperature 500 °C approximately 1.8106 Pa. Volumetric change of the total stress of a single-component gravel shows the change in structural characteristics with simultaneous thermal degradation of the gravel at the moment of reaching the stress value ≈ $2.1 \cdot 10^7$ Pa (formation both on the surface of gravel and inside isothermal surfaces with uncharacteristic density and energy). At the same time Iso Surfaces of two-component gravel are distributed more evenly without inclusions of uncharacteristic dimensional surfaces. Such conditions of development of tensions indicate the possible beginning of formation of cracks in the body of one-component gravel.

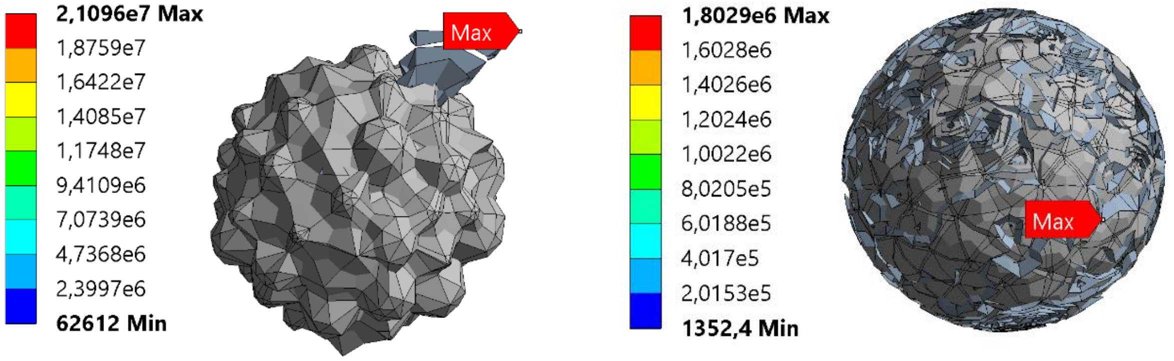

a) b)

Fig 3. Iso Surfaces of the equivalent stress (Pa) of the single and two component ash slag gravels during the 500°C thermal impact: a – single component structure; b – two-component structure.

The Stress intensity factor, as a measure of tension characterizing the potential for crack formation and development that experiences gravel with different structure and density under thermal heating, has been investigated to confirm the assumption of possible crack formation on the surface of gravel. Figure 4 shows the distribution of the intensity of the tension in ash-slag gravels with different structure [16].

According to Figure 4, the maximum stress intensity at 500 °C has a single component gravel for about $1.80 \cdot 10^6$ Pa in compare of single component $2.27 \cdot 10^7$ Pa. The minimum stress intensity factor of single component gravel is also greater than two-component gravel and it consist of $6.2\ 10^4$ Pa in compare of two component stress intensity factor $1.5\ 10^3$ Pa.

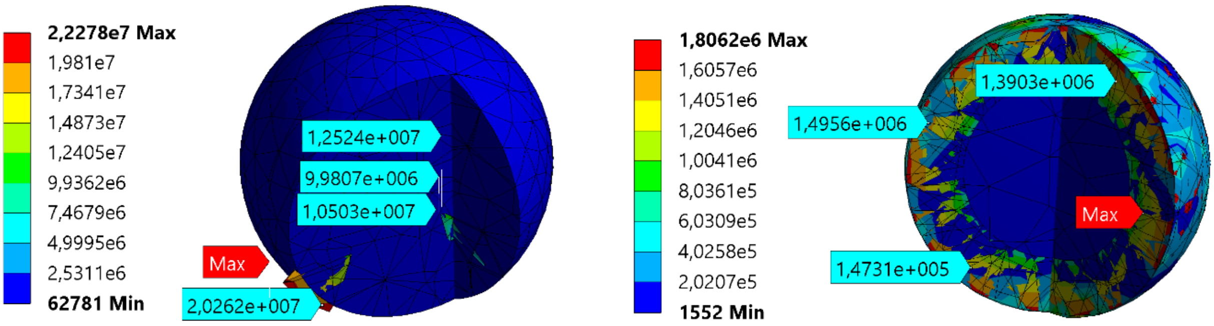

a) b)

Fig 4. Stress intensity (Pa) of the single and two component ash slag gravels during the 500 ° C thermal impact: a – single component structure; b – two component structure.

In addition, two-component gravel has a more even stress intensity distribution pattern, which is also positive for even load distribution. On the other hand, in single component gravel there are zones with a sharp increase in the intensity of stresses, which indicates a greater probability of cracks formation and possibility flow of processes of destruction. In order to identify the nature of the stress-deformed state of gravels with different structure, a dependence of the stress intensity and equivalent stress on the temperature in the range of their occurrence was identified.

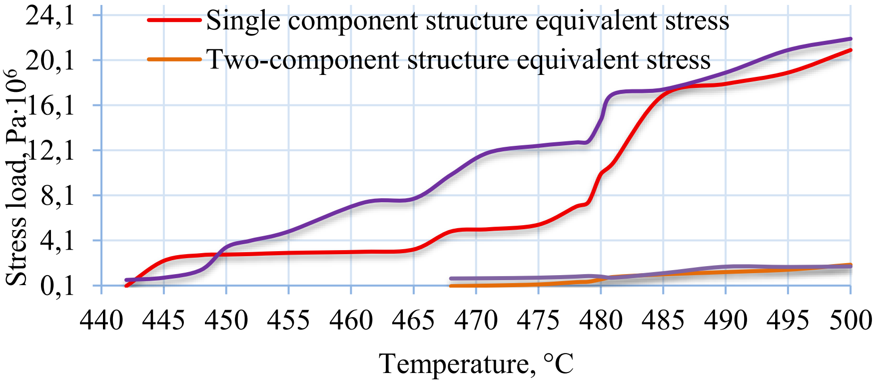

Fig 5. Dependence Stress load (equivalent and stress intensity) of single and two-component ash-slag structure gravel on temperature.

Fig. 5 shows that single component gravel has a greater maximum stress equivalent value of 22 MPA, proportional to the intensity of the stresses of 21 MPA. However, the minimum value of these values for both gravel materials is approximately at the same level and is 0.06 MPA equivalent stress and stress intensity 0.6 MPa and 0.05 MPA equivalent stress and stress intensity 0.1 MPa respectively. But at the same time, the area of occurrence of equivalent stress of two-component gravel is shifted towards higher temperatures and its occurrence begins at a temperature of 468 °C, in contrast to the single component where stresses arise earlier at a temperature of 442 °C. This picture of the stressed state of the granules under thermal impact is directly determined by the plasticity and strength of the gravel, which depends on the structure and speed of the thermal action.

3.2 Analysis results of the total deformation and shear stress evaluation during the thermal impact process on single and two component structure ash slag gravels

Evaluation of deformation state and shear stress of different structure gravels is necessary to determine conditions of occurrence of irreversible degradation processes in the body of gravel material. Irreversible degradation processes usually start when plastic deformation occurs. The beginning of the plastic deformation is the maximum shear stress, showing the points of failure of the material from elastic deformation, in which there is the greatest concentration of stresses and determined by the [17]:

$$\tau^{b}_{\max} = \frac{1}{2}\left[\sigma_{\max\, prstress} - \sigma_{\min\, prstress}\right], \qquad (4)$$

where $\sigma_{\max,\min\, prstress}$ are principal thermal stresses for gravel.

Studies have shown that the maximum concentration of stresses occurring in the points of a single-component gravel can be significantly greater than in a two-component gravel body. The maximum shear stress of deformation under thermal static action for single-component gravel is more than 11 MPA, which exceeds tensile strength for this kind of gravels according to patent author data [18] consist no more than 2,4 MPa. The mean value of the maximum shear stress in single component gravel also has a higher value. For two-component gravel, the maximum shear stress of deformation is almost 12 times less and consist for about 0.9 MPa, as shown by the numerical experiments in Fig. 6. However, a single-component gravel has a zones of reaction to the thermal impact, which is expressed as complete material rejection according to figure 6 (a). This leads to sharp in Equivalent stress (von Mises stress) (figure 3(a)), the increase of which indicates rapid plastic deformation with non-reversible loss of material properties at the point.

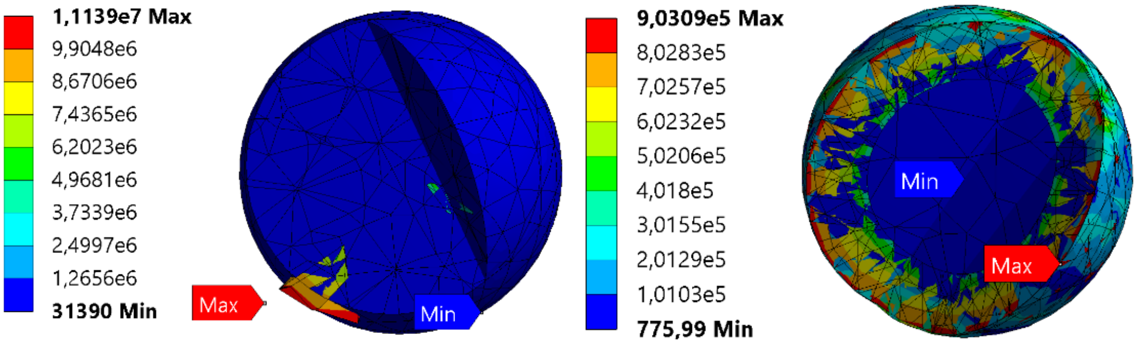

e

a) b)

Fig 6. Maximum shear stress (Pa) of the single and two component ash slag gravels at the temperature 500 ° C: a – single component structure; b – two-component structure.

To predict the reaction of gravel to shear stresses caused by thermal action, with the possibility of predicting failure points, a dependence was defined for maximum shear stress from temperature with account of total deformation, represented on the Fig. 7 [19].

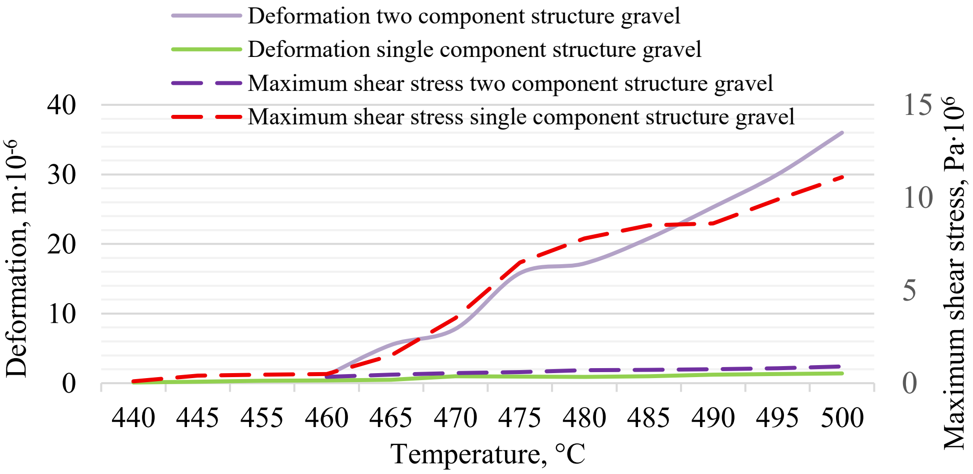

Fig.7. Maximum shear stress (Pa) with account total deformation of the single and two component ash slag gravels at the temperature 500 ° C: a – single component; b – two-component.

According to the fig.7 for single component gravel full deformation during thermal heating is less than for two-component gravel ($1.4\cdot10^{-6}$m and $36\cdot10^{-6}$m respectively). But at the same time, the maximum shear stress of single component gravel is much higher than the shear stress of two-component gravel under the same conditions of thermal action. ($0.9\cdot10^{6}$ Pa и $11.1\cdot10^{6}$ Pa respectively). This is determined by the physical-chemical properties of the material, primarily by the coefficient of thermal expansion, which causes a shift due to the uneven size and density of the particles, leading to splitting during thermal heating. In addition, in two-component gravel there is thermal contact resistance at the joint of solid phases (4) caused by violations of the boundaries of the mortar and cement, which reduce the heat flux to the center of the gravel at the mean absolute temperature of the conditional boundary layer during the phase separation of the cement-ash-slag mixture [20, 21]:

$$R_{ashc}{}^{c} = \frac{T_{c}^{abs} - T_{ash}^{abs}}{Q}, \tag{4}$$

$$T_{c}^{abs} = 273.2 + \frac{1}{2}(t_{ambient} + t_{c}), \tag{5}$$

$$T_{ash}^{abs} = 273.2 + \frac{1}{2}(t_{ash} + t_{c}), \tag{6}$$

where $R_{ashc}{}^{c}$ is contact thermal resistance between cement and ash slag layers; T_{c}^{abs} is absolute temperature of the cement- ambient relative layer, K; T_{ash}^{abs} is absolute temperature of the cement- ash slag relative layer, K; Q is heat flux, W/m^2; $t_{ambient}$, t_{ash}, t_c are the temperatures ambient, ash-slag mix and cement accordingly, °C.

Such conditions reduce the heat flow rate inwards to the center of the gravel and consequently reduce the thermal stress state. As a result, stress-deformed state of gravel, according to the theory of maximum shear stress (theory Tresk) [22], indicate that the strength margin determined by thermal action for single component gravel is lower than for two-component gravel, that reacts to thermal load with the prediction of less damage to the failure material. Thus, with less deformation of single-component gravel, its structure has material fault zones in which the gravels are already breaking down at 465°C.

To confirm the scientific novelty of the studies, model results were compared with experimental data on the stress-deformed state of single-component gravel. For the research, Ust-Kamenogorsk PC, Karaganda SPC and ash-slag mixture of CHP - 2 Astana were used. Research was conducted at the Eurasian University named by L.N. Gumilyov in the development of a fundamentally new ash-slag gravel and were selected in his thesis for the degree of candidate of technical sciences Atiaksheva A.V. "Research and development of non-kilned gravel based on the ash-slag mixture, removed by hydraulic means." 05.23.05 "Building materials and constructions". The thermal stress depends on the modulus of elasticity, the coefficient of thermal expansion and is a value less than or equal to the time resistance at tensile strength. Table 3 presents the results of experimental data on time resistance to gravel strain with different diameters.

Table 3. Tensile strength of the ash-slag two-component gravel.

№	Characteristic	Cement								
		Ust-Kamenogorsk PC				Karaganda SPC				The investigated two-component gravel
		gravel diameter								
		5	10	20	40	5	10	20	40	40
1	Tensile strength, MPa	3.8	3.6	3.0	3.6	3.1	3.0	2.6	2.0	2.4
2	Young's Modulus, MPa$\cdot 10^4$	1.82	1.65	1.47	1.28	1.67	1.43	1.25	1.0	0.6

Experimental data confirm simulation studies and scientific novel of the thermal strength of two-component gravel, its use as a heat protection in the composition of heat-resistant panels or independently in the temperature range up to 500 °C.

4. Conclusion

Evaluation of the effectiveness of the non-kilned as-slag gravel structure under thermal impact in conditions of stationary heating in the temperature range from 22 °C to 500 °C shows on the following results:

1) results of the equivalent stress and stress intensity evaluation during the thermal impact process show, that the two-component gravel has a greater viability in conditions of stationary thermal action at a temperature of 500 °C, as it experiences equivalent stress significantly less ($0.78 \cdot 10^6$ Pa in compare of single component $10.9 \cdot 10^6$ Pa). The two-component gravel also shows a lower stress intensity value ($1.12 \cdot 10^6$ Pa in compare of single component stress intensity value $15.58 \cdot 10^6$ Pa), determining the material's instability and limit of fragility at the moment of thermal exposure.

2) results of the total deformation total deformation and shear stress evaluation during the thermal impact process confirm the assumption of higher thermal stability of gravel two-component structure. Under conditions of less deformation, the appearance of more shear stress indicates that two-component gravel has a greater margin of thermal strength in the temperature range from 460°C to 500°C ($19.94 \cdot 10^{-6}$ m), because its maximum shear stress ($1.14 \cdot 10^6$ Pa) caused by thermal expansion is at a level below the maximum shear stress of single component gravel ($7.23 \cdot 10^6$ Pa) taking into account the deformation of single component gravel having less ($1.21 \cdot 10^{-6}$ m) in the same temperature range and under the same thermal conditions.

Consideration of results of the equivalent stress, stress intensity, total deformation and shear stress for a given size of gravel allows to think that, the two-component structure of ash-slag gravel better accepts the thermal effect in the temperature range from 22 to 500 C. This makes it possible to use two-component gravel in the composition of thermal panels, fine thermal blocks and bricks for thermal protection of low-temperature furnaces and other industrial equipment.

Conflict of interest statement

The authors declare that they have no conflict of interest in relation to this research, whether financial, personal, authorship or otherwise, that could affect the research and its results presented in this paper.

CRediT author statement

Atyaksheva A.V.: Conceptualization, Data Curation; **Seitova Zh. A., Issataeva A. K.:** Writing Original Draft; Methodology. **Ryasnov D.Yu., Khamitova Ye.M.:** Investigation, Software, Writing Review & Editing, Supervision. The final manuscript was read and approved by all authors.

Acknowledgements

This work was carried out with the support of the center "Energy saving and dissemination of knowledge" of the NCJSC «S.Seifullin Kazakh Agrotechnical Research University»

References

1 Pogorelov S. N., Kramar L.Y., Kostiunina I.L. (2022) The physical and chemical composition of fly ash from Troitsk state district power plant (GRES) and its potential use in the construction industry. *IOP Conf. Series: Earth and Environmental Science*, 1061, 1, 012038). https://doi.org/10.1088/1755-1315/1061/1/012038

2 Abdrakhimov V.Z. (2023) Influence of ash and slag on the characteristics of heat insulation based on metallurgical waste. *Coke and Chemistry*, *66*(6), 310-315. https://doi.org/10.3103/S1068364X23700874

3 Duan X., Jiang Y., Yang K., Cui R., Xue Q. (2025) Utilization of Ferronickel Slag in Heat-Resistant Concrete: Performance Evaluation and Mechanism Analysis. *Journal of Building Engineering*, 113914. https://doi.org/10.1016/j.jobe.2025.113914

4 Cherif A., González-Corrochano B., Moussi B., Jamoussi F., Alonso-Azcárate J. (2023) Influence of kiln type on the production of lightweight aggregates. *Materials and Structures*, 56(8), 154. https://doi.org/10.1617/s11527-023-02237-2

5 Makarova M., Vigovskaya A., & Bazhenov Y. (2018) Application of ash and slag wastes in the production of building materials. *IOP Conf. Series: Materials Science and Engineering*, 365, 3, 032040. https://doi:10.1088/ 1757-899X/365/3/032040

6 Anastasov M. S., Alexandrov S. P., Shestov A. V., & Ryabova Y. S. (2021) Ash and Slag Waste–Secondary Raw Materials with Benefits for the Environment. *2021 Intelligent Technologies and Electronic Devices in Vehicle and Road Transport Complex (TIRVED),* IEEE, 1-7. https://doi.org/10.1109/TIRVED53476.2021.9639197

7 Paunescu L., Axinte S. M., & Dragoescu M.F. (2022) Cellular gravel of slag and coal ash made by an unconventional heat treatment method. *Academic Journal of Manufacturing Engineering*, 20(1). https://www.ajme.ro/PDF_AJME_2022_1/L4.pdf

8 Paunescu L., Axinte S. M., & Fiti A. (2023) Cellular are gravel produced from residual alumino-silicate materials (fly ash, metacajlin, slag and alkalineearth alumino-silicate glass) by nonconventional techniques. *Nonconventional Technologies Review/Revista de Tehnologii Neconventionale*, *27*(2). https://www.revtn.ro/index.php/revtn/article/view/417

9 Atyaksheva A., Niyazbekova R., Sarsikeyev Y., Konkanov M., & Atyaksheva A. (2018) On the Issue of an Ash Microsphere Application as a Framework Forming Filler in Composite Materials. *Key Engineering Materials*, 781, 176-181. https://doi.org/10.4028/www.scientific.net/KEM.781.176

10 Atyaksheva A., Sarsikeyev Y., Atyaksheva A., Galtseva O., & Rogachev A. (2021) The Study of the Dependence of Optimal Structure of Composite Materials Containing Hollow Aluminosilicate Microspheres on Humidity. *Micro and Nanosystems*, *13*(4), 385-392. https://doi.org/10.2174/1876402912999201109204218

11 Shaimerdenova K., Sakipov K., Abdirova N., & Suleimenova S. (2024) Improving the quality of Ekibastuz coal using the dry enrichment method. *Eurasian Physical Technical Journal*, *21*(1(47), 67–73. https://doi.org/10.31489/2024No1/67-73

12 Atyaksheva A., Dashevskaya A., Mergalimova A., Ybray S., Aitmagambetova M., Umirzakov R., & Sultanbek Z. (2025) Evaluating of the sudden heat impact on the volatile gases release during the gasification process of weakly grade metamorphized coal. *Eastern-European Journal of Enterprise Technologies*, 135(6). https://doi.org/10.15587/1729-4061.2025.331223

13 Isagulov A. Z., Ibatov M. K., Kwon S. S., Kovaleva T. V., Arinova, S. K., & Dostayeva, A. M. (2019). Impact of porosity on the strength of refractory products. *iPolytech Journal*, *23*(3 (146)), 594-601. http://dx.doi.org/10.21285/1814-3520-2019-3-594-601

14 Yun F., Du Y., Liu D., Wu X., Tang M., Yan Q., & Xu H. (2025) Numerical Analysis of Thermal–Structural Coupling for Subsea Dual-Channel Connector. *Journal of Marine Science and Engineering*, *13*(10), 1867. https://doi.org/10.3390/jmse13101867

15 Shin G.H., & Hur J. W. (2022) A new finite element analysis model to estimate contact stress in ball screw. *Applied Sciences*, *12*(9), 4713. https://doi.org/10.3390/app12094713

16 16. Lunev A. A., & Sirotyuk V. V. (2019) Stress distribution in ash and slag mixtures. *Magazine of Civil Engineering*, 2 (86), 72 – 82. https://doi.org/10.18720/MCE.86.7

17 Zhao J., Guo Y., Chen P., Hu L., & Wang J. (2025) True triaxial shear strength and failure mechanism of sandstone under real-time high-temperature conditions. *Rock Mechanics and Rock Engineering*, 1-21. https://link.springer.com/article/10.1007/s00603-025-04471-2

18 Ganjara V.I, Atiaksheva A.V., Zhakishev B.A. Pre-patent of the Republic of Kazakhstan 14317 (2004) Method of manufacturing artificial gravel**.** https://kz.patents.su/0-pp14317-sposob-izgotovleniya-iskusstvennogo-graviya.html

19 Atyaksheva A., Rozhkova O., Sarsikeyev Y., Atyaksheva A., Yermekov M., Smagulov A., & Ryvkina N. (2022) Determination of rational parameters for heat treatment of concrete mixture based on a hollow aluminosilicate microsphere. *Eastern-European Journal of Enterprise Technologies*, *1*(6), 115. https://doi.org/10.15587/1729-4061.2022.251004

20 Sebastian Bryson L., Mahmoodabadi M., & Adu-Gyamfi K. (2017) Prediction of consolidation and shear behavior of fly ash–soil mixtures using mixture theory. *Journal of Materials in Civil Engineering*, *29*(11), 04017222. https://doi.org/10.1061/(ASCE)MT.1943-5533.0002077

21 Zhang B. (2023) Repair of ordinary concrete using alkali activated slag/fly ash: High temperature resistance and micro structure evolution of adhesive interface. *Construction and Building Materials*, 386, 131559. https://doi.org/10.1016/j.conbuildmat.2023.131559

22 Ren H., Cai X., Wu Y., Jing P., & Guo W. (2023) A study of strength parameter evolution and a statistical damage constitutive model of cemented sand and gravel. *Materials*, 16(2), 542. https://doi.org/10.3390/ma16020542

AUTHORS' INFORMATION

Atyaksheva, Alexandra Vladimirovna - PhD(Eng.), Associate Professor, Energy Institute, S. Seifullin Kazakh Agrotechnical Research University, Astana, Scopus Author ID: 57204188485; https://orcid.org/0000-0003-2523-3890; sahsa77@mail.ru

Seitova Zhadra Adilbekovna - PhD (Eng.), Senior lecturer, Energy Institute, S. Seifullin Kazakh Agrotechnical Research University, Astana, Scopus Author ID: 59156439300; https://orcid.org/0000-0001-7812-2540

Issataeva, Akmaral Kiyalovna — Master (Eng.), Senior lecturer, Department of Thermal Power Engineering, Energy Institute, S. Seifullin Kazakh Agrotechnical Research University, Scopus ID: 58925932700; https://orcid.org/0009-0000-6544-1921; akmadani@mail.ru

Ryasnov, Dmitry - Master student, Energy Institute, S.Seifullin Kazakh Agrotechnical Research University, Astana, https://orcid.org/0009-0009-7534-651X; 1_4_9844@mail.ru

Khamitova, Yeldana – Master student, Energy Institute, S.Seifullin Kazakh Agrotechnical Research University, Astana, https://orcid.org/0009-0008-6684-3488; yeldanakhamitova73@gmail.com

EURASIAN PHYSICAL TECHNICAL JOURNAL

2026, Volume 23, No.1 (55)

https://doi.org/10.31489/2026N1/87-92

Received: 30/10/2025 Revised: 02/03/2026 Accepted: 19/03/2026

Original Research Article

UDC 53.097; 537-77

STUDY OF THE INFLUENCE OF ELECTROHYDRAULIC DRILLING PARAMETERS ON THE EFFICIENCY OF HARD SOILS DESTRUCTION

Shaimerdenova K.M.[1], Nussupbekov B.R.[2], Schrager E.R.[3], Akhmadiyev B.A.[1],
Nakipova S.Zh.[1]*, Rakhmankyzy A.[1]

[1] Buketov Karaganda National Research University, Karaganda, Kazakhstan
[2] Abylkas Saginov Karaganda Technical Research University, Karaganda, Kazakhstan
[3] National Research Tomsk State University, Tomsk, Russia
*Corresponding author: sn88.06@mail.ru

Abstract. *This article examines several aspects of the electrohydraulic drilling method. It presents the results of an experimental study examining the influence of electrohydraulic drilling modes on the efficiency of breaking stone. A brief description and diagram of the experimental setup are provided. Quantitative relationships between the electrical parameters of the optimal mode of electrohydraulic drilling technology for breaking hard soils samples of varying thicknesses are determined. The experimental data confirm the feasibility of achieving significantly higher drilling speeds for vertical wells in hard soil compared to traditional methods.*

Keywords: electrohydraulic drilling, hydraulic pressure, pulse capacitor, well.

1. Introduction

Traditional methods still form the basis of the drilling industry due to the well-established nature of their equipment and technological processes [1-4]. Rotary, auger, core, and other drilling technologies remain effective and reliable under certain studied geological conditions; they are economically viable for drilling simple wells. New technologies, such as managed pressure drilling (MPD), are successfully used for drilling complex wells, allowing for consideration of soil rheological properties or changes in borehole geometry [1]. To improve efficiency, alternative methods are proposed, such as centrifugal drilling or combined technologies with additional automation, which provide more precise drilling and minimize harmful environmental impacts [2, 3]. Indeed, the current development of the petrochemical, energy, and geothermal industries requires the implementation of efficient and reliable well drilling methods in a variety of geological conditions. Traditional mechanical drilling methods encounter challenges when working in hard soil or heterogeneous formations. High mechanical loads, rapid wear of drilling tools, and significant energy consumption reduce the efficiency of traditional drilling technologies and increase operating costs.

Analysis of the current state of drilling technologies and the formulation of recommendations in the context of changing economic and environmental realities necessitates the integration of new technologies and scientific research to achieve a sustainable future in the energy sector [4]. In recent years, significant progress has been made in the development of electric pulse and hydropulse drilling technologies for the destruction of hard soils masses and deep geothermal formations. High-voltage pulsed electrical discharges are capable of generating powerful shock waves and plasma channels within the material structure, leading to the effective propagation of cracks and the destruction of crystalline formations such as granite and basalt. These technologies ensure selective destruction of rock mass with significantly less mechanical wear compared to traditional drilling methods and have high potential for application in geothermal energy, mining, processing industries, and other industries [5–9]. Electrohydraulic drilling is a fundamentally new drilling method that has not yet been widely adopted in industrial practice; therefore, the study of its potential and practical application remains a pressing scientific challenge. One of the key advantages of this technology is the ability to use it in spatially confined environments, such as buildings, basements, and other confined spaces, where the use of traditional drilling equipment is often difficult due to the significant dimensions and complexity of classic drilling rigs. In addition, electrohydraulic drilling systems ensure long-term and reliable operation due to the absence of constant mechanical contact and friction between the system elements. Ease of maintenance and operation is achieved through the use of an accessible cable as the active element, which functions as a consumable electrode [10–12].

The electro-hydro-pulse (EHP) method is based on the use of high-voltage pulsed electrical discharges, the discharge of which in a liquid medium is accompanied by the formation of shock waves, cavitation phenomena, and high pulsed hydraulic pressures. These physical processes lead to the initiation and propagation of microcracks, change the properties and structure of solid stone, and lead to their destruction [13-18]. However, despite the promising characteristics of this technology, its practical implementation in drilling processes remains limited. One of the main reasons is the insufficient understanding of the optimal electrophysical parameters required for effective rock fracture. Furthermore, the response of geological materials to electrohydraulic pulses depends significantly on their physical and structural properties, such as density, mineral composition, electrical strength, and the presence of internal fracture systems. Therefore, experimental study of the interaction of high-voltage electrical discharges with various types of hard rock is essential for improving the efficiency of electrohydraulic drilling technologies.

This paper presents the results of an experimental study of the influence of electrophysical parameters of the discharge circuit on the efficiency of hard soil fracture during electrohydraulic drilling.

2. Experimental unit and measurement techniques

Compared with traditional drilling methods, electrohydraulic technology provides a more efficient and rapid destruction of hard soil formations encountered during the drilling of boreholes for the installation of heat exchangers. This is achieved by generating high-intensity shock waves in a liquid medium [7-9]. The electrohydraulic effect is the occurrence of a high-voltage electric discharge in a liquid medium. During the formation of an electric discharge channel in the liquid, a significant amount of energy is released in an extremely short time. A high-voltage pulse with a steep rise front initiates a number of physical phenomena, including the formation of ultra-high pulsed hydraulic pressure, electromagnetic radiation in a wide frequency range, which may include X-ray radiation, and cavitation processes [11-13].

The samples used in the experiments were solid fossilized soil fragments (of the hard soils) collected from the experimental site in the Karaganda region. Before the experiments, the samples were sorted by size and, if necessary, subjected to minor mechanical processing to achieve the required thickness. Electrohydraulic pulse phenomena, which underlie various electro pulse technologies, have been investigated in previous works by the authors [14]. Experimental studies were carried out using an electrohydraulic pulse setup, the diagram of which is shown in Fig. 1. From a design point of view, the electrohydraulic pulse system includes several functional units, including a control panel, a capacitor unit equipped with a protection system, and a pulse current generator connected to a switchboard.

The capacitor is connected to the positive (+) and negative (−) terminals, which are connected in parallel with the transformer. The alternating voltage passes through the series resistance of the transformer's primary winding, generating a high voltage in the secondary winding. This voltage is then rectified by a rectifier, and the resulting direct current is fed to the capacitor. As a result, the voltage on the capacitor gradually increases to a certain level, at which point the accumulated energy is transferred through the forming gap (FI) to the working zone of the electrohydraulic pulse drill (ED), where a high-voltage electrical discharge occurs in the liquid medium. This process is repeated at a specific frequency determined by the operating parameters of the electrical circuit. The pulse frequency depends on the transformer output voltage, the capacitor capacitance, and the distance between the electrodes in the forming gap.

The experiments involved natural stone samples, that is, a material with diverse structures formed from various natural minerals.

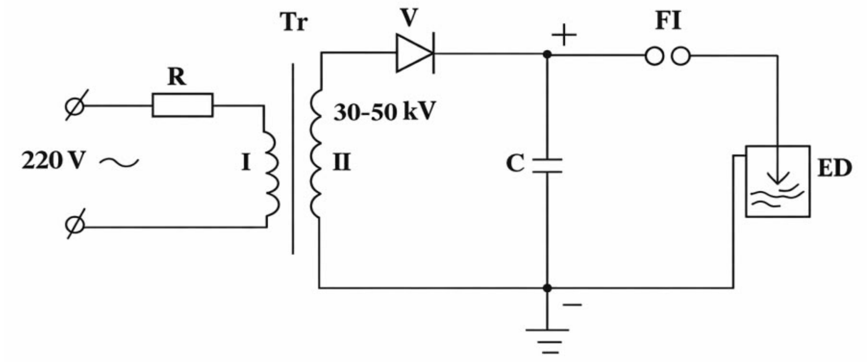

Fig. 1. Electrical diagram of the electrohydraulic pulse unit:
R — discharge resistor; Tr — high-voltage transformer; V — rectifier; C — pulse capacitor;
FI — forming gap (spark gap); ED — electrohydraulic pulse drilling machine.

There are involved samples of nature hard soils (stones) placed in a circular working cell; which the geometric parameters were determined by the design of an electrohydraulic drill. The working zone diameter for the drill's design was 115 mm. The working group height varied depending on the size of the samples being processed and was approximately 70–80 mm. The samples were placed in a working chamber filled with a liquid—ordinary process water—in which a production discharge was generated, generating shock waves. The experimental electrohydraulic drilling circuit is shown in Figure 2.

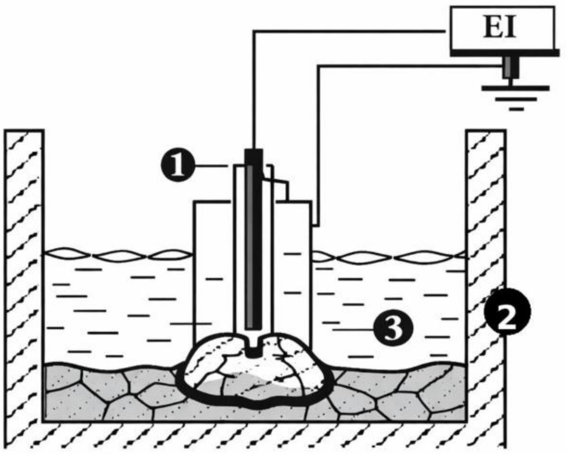

Fig. 2. Electrohydraulic drilling scheme:
1 — positive electrode; 2 — working chamber; 3 — hard soil particles.

This study examined hard rock samples from the Karaganda region of the Republic of Kazakhstan, as siltstone (a hard rock intermediate between clay and sandstone). The hardness of the natural rock samples subjected to high pressure testing was approximately 5-6 on the Mohs scale [13]. But in these experiments, no special methods were used to determine the structure and hardness of the soil samples. The destruction caused by the electro-hydro-pulse discharges, as well as the structure and density of the stones, were recorded visually, based on the actual destruction and crushing of the stones. During laboratory testing, it was necessary to ensure optimal drilling parameters at which the high pressure at the shock wave front leads to intensive destruction of the hard soil samples. The experiments were conducted at least three times under identical conditions. The average measurement error was 7-9%.

3. Results and discussions

Experiments were conducted on hard stone samples with varying structure and composition. The comparative graphs in Figure 3 (a, b) illustrate the relationship between the number of pulse discharges and the initial voltage U_0 at a constant capacitor bank capacitance for hard stone samples 60 mm (a) and 70 mm (b) thick. Based on the results of laboratory experiments, it can be concluded that the greatest efficiency in breaking natural stone using electric discharges is achieved with the following operating parameters of the high-voltage pulse generator discharge circuit: U0 = 35 kV, C = 3 μF, and an interelectrode distance of 12 mm.

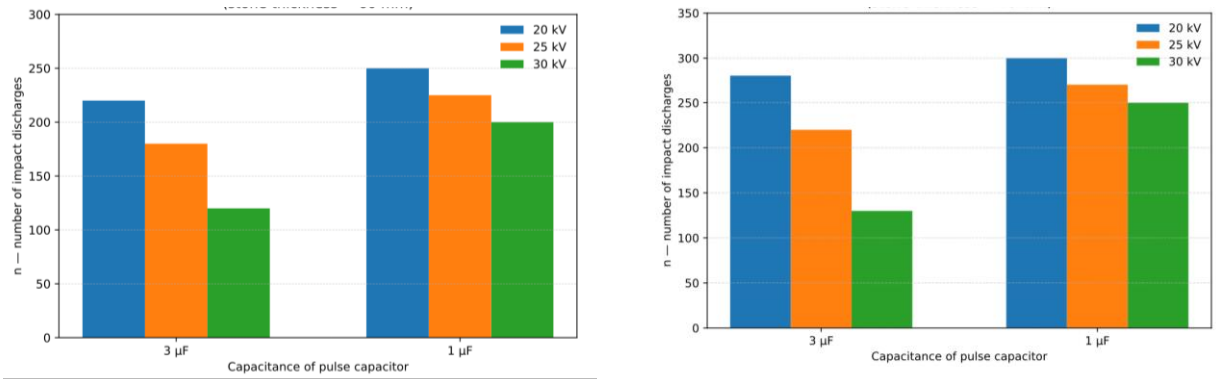

a) b)

Fig. 3. Comparative graph of the number of shock discharges for different capacitors; thickness of the hard stone sample: a) 60 mm; b) 70 mm.

It was found that the most effective breaking of hard stone in a borehole occurs with a discharge circuit voltage in the range of 20–35 kV, a capacitance of 1–3 μF, and an interelectrode distance of 7–12 mm. Under these conditions, electrohydraulic pulses generate shock waves with sufficient energy to initiate and propagate cracks in the stone structure. The experiments determined the voltage influence (20-35 kV) discharge circuit on mineral stones destruction, and number and frequency of spark discharges required for electrohydraulic drilling at a given thickness of the hard stone soil layer (Figure 4).

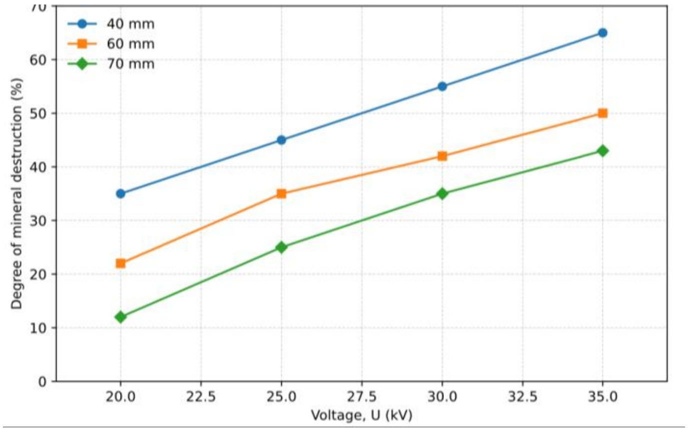

Fig. 4. Effect of discharge voltage on the degree of mineral destruction for different thicknesses of hard soil samples.

Based on the experiments, the range of electrophysical parameters at which intensive destruction of hard soil, particularly natural stone, begins was determined. The optimal energy required to destroy stone is in the range of 0.3–0.6 kJ. With an increase in discharge energy to approximately 612 J, complete destruction of the stone samples is observed (Figure 5). Based on the results, the optimal range of electric discharge energy for the most effective destruction of natural materials was determined. The depth of hard soil mass destruction increases proportionally to the number of pulsed discharges, as each discharge generates a pressure pulse that propagates through the material and intensifies the destruction of the structure and surface of hard soil. As the discharge intensity increases, so does the generated pressure, which intensifies the destruction process and, consequently, leads to an increase in drilling depth. The obtained results confirm that the electrohydraulic effect provides an effective mechanism for the direct conversion of electrical energy into mechanical energy by generating high-energy shock waves and cavitation processes in a liquid medium. A comparison with traditional mechanical drilling technologies shows that the electrohydraulic method offers a number of significant technological advantages. In particular, the absence of constant mechanical contact between the drilling tool and the hard soil mass significantly reduces mechanical wear of the equipment and increases the operational reliability of the system.

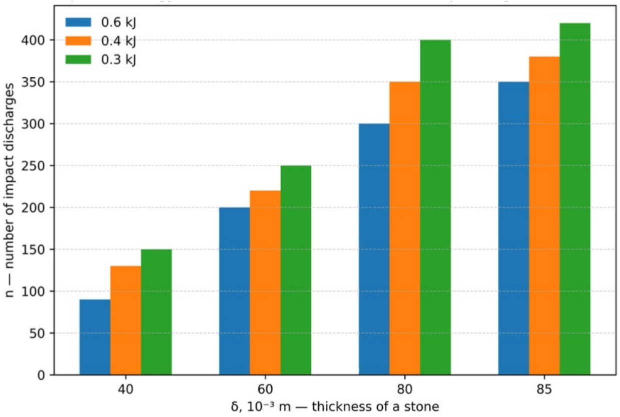

Fig. 5. Dependence energy level of hard soil destruction depending on the thickness of a stone.

Furthermore, electrohydraulic drilling rigs are characterized by a relatively simple design and compact dimensions, allowing their use in space-constrained environments where the use of traditional drilling equipment is difficult or impossible.

4. Conclusion

Based on the experimental studies, optimal electrophysical parameters were determined to initiate intensive destruction of hard soil using electrohydraulic pressure pulses. Test experiments demonstrated that hard soil sample destruction efficiency depends significantly on the electrical characteristics of the discharge circuit, including the initial voltage, the capacitance of the pulse capacitor, and the distance between the electrodes. The highest efficiency of hard soil destruction in the experiments was achieved with parameters of the order of U0 = 35 kV, C = 3 μF, and an interelectrode distance of 12 mm, which ensures the generation of powerful shock waves.

Electrohydraulic drilling technology provides high destruction efficiency, reduces specific energy consumption, minimizes wear on drilling tools, and enables efficient operation in hard, heterogeneous soils. Unlike traditional mechanical drilling methods, electrohydraulic technology ensures more efficient destruction of hard soils by converting electrical energy into shock wave energy, which reduces mechanical wear on equipment and lowers specific energy consumption. The novelty of this study lies in establishing the optimal parameters for electrohydraulic pulse action and identifying patterns of fracture in hard soils. The practical significance of these results lies in the potential application of this technology for shallow well drilling for ground heat exchangers in complex geological conditions, including hard soils. The presented experimental data can serve as a basis for further optimization of electrohydraulic drilling systems in future.

CRediT author statement
Shaimerdenova K.M.: Supervision, Methodology, Writing – review & editing; **Nussupbekov B.R.:** Conceptualization, methodology; **Schrager E.R.:** Data curation, Validation; **Akhmadiyev B.A.**: Investigation,Visualization; **Nakipova S.Zh.:** Investigation, Writing – original draft; **Rakhmankyzy A.**: Formal analysis, Data curation.
The final manuscript was read and approved by all authors.

References

1 Arbuzov E.S. (2014) Efficiency of managed pressure drilling with MPD technology. *Proceeding of the All-Russian scientific and technical conf. " Problems of scientific and technological progress in well drilling*", Tomsk, 295-296. https://earchive.tpu.ru/bitstream/11683/65620/1/conference_tpu-2014-C11-V2_p295-296.pdf [in Russian]

2 Bakhshaliyev S. (2024) Innovations in drilling technologies and their impact on business performance. *Competitiveness in a global world: economics, science, technology,* 10, 99–102. https://doi.org/10.5281/ZENODO.14090851

3 Tunkiel A.T., Sui D., Wiktorski T. (2021) Training-while-drilling approach to inclination prediction in directional drilling utilizing recurrent neural networks. *Journal of Petroleum Science and Engineering*, 196:108128 https://doi.org/10.1016/j.petrol.2020.108128

4 Nurmakova Zh.I., Meramgalieva R.S., Mitrofanov O.P. (2025) New drilling technologies and their impact on the efficiency of hydrocarbon production – a study of trends in the field of horizontal drilling and hydraulic fracturing. *Oil and gas technologies and environmental safety*, (3), 49-55. https://doi.org/10.24143/1812-9498-2025-3-49-55

5 Schiegg H. O., Rødland A., Zhu G., & Yuen D. A. (2022) Advances in electro-pulse drilling technology for deep geothermal energy extraction. *Geothermal Energy, 10*, 15. https://doi.org/10.1186/s40517-022-00213-4

6 Li C., Zhang Y., Xu J., & Zuo Z. (2021) Mechanisms of granite fragmentation by high-voltage electro-pulse boring for geothermal drilling. *Renewable Energy, 172*, 1176–1186. https://doi.org/10.1016/j.renene.2021.03.082

7 Andres U., Timoshkin I., Jirestig J., & Stallknecht H. (2021). Pulsed power application for rock fragmentation and drilling. *IEEE Transactions on Plasma Science,* 49, 2585–2592. https://doi.org/10.1109/TPS.2021.3099954

8 Zuo Z., Li C., Xu J., & Zhang Y. (2020) Experimental investigation of rock fragmentation using high-voltage electro-pulse boring technology. *Energies, 13*(9), 2296. https://doi.org/10.3390/en13092296

9 Sakipova S.E., Nussupbekov B.R., Ospanova D., Khassenov A., Sakipova Sh.E.(2015) Effect of electric pulse on physical and chemical properties of inorganic materials. *Proceeding of the IOP Conf. Ser.: Mater. Sci. Eng.,* 81, 01205, https://doi.org/10.1088/1757-899X/81/1/012051

10 Li C., Xu J., Zhang Y., & Li H. (2018) Influences on high-voltage electro-pulse boring in granite. *Energies, 11*(9), 2461. https://doi.org/10.3390/en11092461

11 Nussupbekov B., Sakipova S., Edris A., Khassenov A., Nussupbekov U., Bolatbekova M. (2022) Electro-hydraulic method for processing of the phosphorus containing sludges. *Eurasian Physical Technical Journal*, *19*(1(39), 99–104. https://doi.org/10.31489/2022No1/99-104.

12 Lehmann F., Reich M., Mezzetti M., Anders E., & Voigt M. (2017) The future of deep drilling – A drilling system based on electro impulse technology. *Oil & Gas European Magazine, 43*(4), 187–191.https://www.researchgate.net/publication/322445714_The_future_of_deep_drilling-A_drilling_system_based_on_electro_impulse_technology

13 Kussainov K., Nussupbekov B.R., Shuyushbaeva N.N., Tanasheva N.K., Shaimerdenova K.M., Khassenov A. On the method of electric pulse drilling of wells and destruction of solid bodies. *Journal of Technical Physics*, 87(6):852. https://doi.org/10.21883/JTF.2017.06.44506.1827 [in Russian]

14 Akhmadiyev B. A., Zhetimekova G., Duisenbayeva M., Sharzadin A., & Nussupbekov B. (2023) Prepa-ration of wells using an electrohydraulic drill and modeling of heat transfer processes in heat transfer elements of a heat pump. *Eastern-European Journal of Enterprise Technologies, 4*(1), 96–103. https://doi.org/10.15587/1729-4061.2023.285179

15 Zhang Q., Liu Y., Zhao Y., & Lin F. (2023) High-voltage electric pulse drilling: A study of variables through simulation and experimental tests. *Energies, 16*(3), 1174. https://doi.org/10.3390/en16031174

16 Zhu X., Zhang Y., Luo Y., & Liu W. (2024) Experimental investigation on high-voltage electric pulse drilling in sandstone under different voltage peaks and electrode structures. *Geoenergy Science and Engineering*, 242, 213274, https://doi.org/10.1016/j.geoen.2024.212706

17 Liu W., Zhang Y., Zhu X., & Luo Y. (2023) Influence of pore characteristics on rock fragmentation mechanism by high-voltage electric pulse. *Plasma Science and Technology, 25*(5), 055502. https://doi.org/10.1088/2058-6272/acab42

18 Wang S., Chen H., Li Y., & Zhao X. (2024) Physical simulation experiment on the rock-breaking mechanism induced by controllable shock waves generated by electric explosion. *Processes, 12*(1), 78. https://doi.org/10.3390/pr12010078

AUTHORS' INFORMATION

Shaymerdenova, Kulzhan Meiramovna – Candidate of Technical Sciences, Professor, Department of Engineering Thermophysics named after prof. Zh.S. Akylbaev, Buketov Karaganda National Research University, Karaganda, Kazakhstan; https://orcid.org/0000-0002-9588-4886; gulzhan.0106@mail.ru

Nussupbekov, Bekbolat Rakishovich– Candidate of Technical Sciences, Professor, Vice Rector for Academic Affairs, Karaganda Technical University named after Abylkas Saginov, Karaganda, Kazakhstan; Scopus Author ID: 56289675900, https://orcid.org/0000-0003-2907-3900, bek_nr1963@mail.ru

Schrager, Ernst Rafailovich - Doctor of Physical and Mathematical Sciences, Professor, National Research Tomsk StateUniversity, Tomsk, Russia; Scopus Author ID: 55956811200; https://orcid.org/0000-0002-7178-4071,sher@mail.tsu.ru

Akhmadiyev,BektursynAitzhanovich – SeniorLecturer,Department of Engineering Thermophysics named after prof. Zh.S. Akylbaev, Buketov Karaganda National Research University, Karaganda, Kazakhstan; Scopus Author ID: 57009117600, https://orcid.org/0000-0002-4813-6367, akhmadiyev_bektursyn@mail.ru

Nakipova, Sayazhan Zhetkenovna – PhD student, Buketov Karaganda National Research University, Karaganda, Kazakhstan; https://orcid.org/0009-0005-4999-8662; *sn88.06@mail.ru*

Rakhmankyzy, Akerke – Master (Eng.), Teacher, Department of Engineering Thermophysics named after prof. Zh.S. Akylbaev, Buketov Karaganda National Research University, Karaganda, Kazakhstan; https://orcid.org/0000-0002-6410-4111

EURASIAN PHYSICAL TECHNICAL JOURNAL

2026, Volume 23, No. 1(55)

https://doi.org/10.31489/2026N1/93-100

Received: 23/12/2025 Revised: 25/02/2026 Accepted: 19/03/2026

Research Article

UDC 532.517:532.135

TURBULENT FLOW OF VISCOELASTIC FLUID BASED ON THE REYNOLDS STRESS MODEL

Zhapbasbayev U.K.[1], Pakhomov M.A.[2], Ramazanova G.I.[1], Sattinova Z.K.[3,*]

[1] Satbayev University, Almaty, Kazakhstan
[2] Kutateladze Institute of Thermophysics SB RAS, Novosibirsk, Russia
[3] L.N. Gumilyov Eurasian National University, Astana, Kazakhstan

**Corresponding author:* sattinova.kz@gmail.com

Abstract. *This article presents the results of applying a turbulent stress model to the simulation of high-viscosity viscoelastic fluid flow in a pipe. The model is used to numerically determine averaged velocity and stress fields within the Navier–Stokes equations. The proposed model takes into account the influence of the Sisko fluid rheology on turbulent momentum transfer, providing a physically sound description of the interaction between turbulence and non-Newtonian effects. Calculations for a Newtonian fluid are performed as a baseline for evaluating the effectiveness of the proposed approach. It is shown that for Sisko fluid, the averaged velocity profile in universal coordinates is systematically shifted upward compared to the Newtonian case, indicating weakening of turbulent momentum transfer and a decrease in hydrodynamic drag. It is established that the level of axial velocity fluctuations exceeds the Newtonian value, while radial fluctuations are lower, indicating pronounced anisotropy of turbulent stresses. The viscoelastic properties of the fluid lead to a reduction in turbulent friction due to the suppression of small-scale vortex structures and, as a consequence, to a reduction in the hydraulic resistance of the pipe.*

Keywords: highly viscous elastic fluid, Sisco rheological model, turbulent stresses, non-Newtonian effects.

1. Introduction

The phenomenon of drag reduction (DR), present in turbulent viscoelastic flows, has been studied for decades [1-7]. It is well known that the addition of polymer particles to a Newtonian fluid in turbulent flow can achieve a reduction in transfer energy of up to 80% by reducing turbulent friction [1-9]. Another effect is the reduction in heat transfer. Both phenomena provide significant benefits in terms of energy savings for transporting fluids over long distances, and for this reason, researchers are focusing their efforts on its use in engineering systems. Since the discovery of the drag reduction phenomenon, numerous studies have been conducted to understand the origin of drag reduction in turbulent flows, and several theories have been proposed to describe this complex mechanism, but a definitive consensus has not been reached.

The two preferred theories are Lumley's theory [3, 4], known as the viscous idea, and Tabor and De Gennes's theory [8], known as the elastic explanation. Lumley suggests that the phenomenon of drag reduction (DR) is a consequence of an increase in effective viscosity in the region beyond the viscous sublayer and in the buffer layer, caused by polymer stretching in turbulent flow. He also suggests that the onset of drag reduction occurs when the polymer time scale exceeds the flow time scale. Another suggestion by Tabor and De Gennes is that the elastic energy stored in the polymer becomes equivalent to the turbulent kinetic energy in the buffer layer, suppressing normal energy transfer and thickening the buffer layer where the viscoelastic length scale is greater than the Kolmogorov length scale.

It is known that DR is associated with an increase in the effective elongation viscosity of a dilute polymer solution, which leads to a decrease in vortex dynamic activity, according to Lumley's theory [3, 4]. Later, Lvov et al. [10] quantitatively described the viscous scenario, showing that the additional effective viscosity increases linearly with distance from the wall in the buffer layer. They also proposed direct numerical simulations (DNS) of Newtonian turbulent flows, including artificial viscosity, to validate their theory [11]. This was followed by De Angelis et al. [11], who obtained the same drag reduction properties as the equivalent viscoelastic simulation [12].

However, the DNS results between the two scenarios showed some inconsistencies when considering the high and maximum drag reduction regimes. Recently, Dallas et al. [13] demonstrated that high drag reduction can be achieved without a complete helix-to-stretch transition of polymer molecules, which is contrary to viscous theories. This supports the explanation of Mina et al. [14], in which polymers in the near-wall region extract energy from the flow due to mean-shear-induced unwinding and release some of the stored elastic energy back into the flow by compressing as they move away from the wall.

Although DNS is a powerful tool, it is not applicable to most engineering applications involving turbulent viscoelastic flows. It is significantly more computationally intensive and memory-intensive due to the larger number of primary variables. An alternative approach is to use Reynolds-averaged Navier–Stokes (RANS) models, which are less computationally intensive. Therefore, they have gained increased interest in recent decades. Engineering calculations require turbulence models that accurately describe the average fields and large-scale pulsations of swirling currents. The work of Horvath and Dressel (2012) presents the results of numerical simulation of RANS for a generalized configuration - a single subchannel with lateral periodicity. The authors tested vortex viscosity models and stress transfer models using standard wall functions. The first attempt to incorporate the elastic effect into turbulence models was undertaken by Pinho [15] and Cruz et al. [16].

They developed a (k-ε)-model of low-Reynolds-number turbulence using the generalized Newtonian fluid (GNF) equation of state. They also developed an anisotropic version that incorporates enhanced Reynolds stress anisotropy (Resende et al., [17]), which is capable of satisfactorily predicting drag reduction. This model is designed to describe the viscoelastic effects responsible for the Toms effect (reduction of hydrodynamic resistance) during turbulent flow in pipelines. Modification of the Launder–Sharma (k–ε) model by taking into account the rheology of viscoelastic media and using the Cruz – Pinho damping function made it possible to adapt it to calculate dilute non-Newtonian solutions. In this case, the viscoelastic properties are described using a modified generalized Newtonian fluid model (GNF). The authors [16-17] performed a direct numerical simulation corresponding to a statistically converging turbulent fluid flow in the GN channel with a low Reynolds number of friction.

The variable viscosity is taken into account using the Carro model, while the data for the Newtonian case are compared with the results of modeling media exhibiting dilatance and pseudoplasticity properties. The study confirms that variable viscosity affects the internal structure of the flow, where shear thinning dampens wall vortices and banded structures. This inhibits the development of turbulence and leads to the effect of reducing drag.

The main changes in the flow structure include an increase in the longitudinal and suppression of the transverse turbulence intensity, as well as a decrease in the Reynolds shear stresses. In addition, the energy exchange between the components of the stress tensor slows down through the correlation of pressure and velocity, which leads to an increase in the anisotropy of turbulence on small and large scales. In the center of the channel, shear liquefaction enhances the manifestation of specific turbulent structures, which are usually observed at low Reynolds numbers.

In this paper, the RSM model is used to describe the anisotropy of the pulsating velocity components and the reduction of the Reynolds stress.

2. Model mass transfer

2.1 Basic equations

The equations governing the flow are presented in vector symbols, although they are solved for axisymmetric flow in cylindrical coordinates. The system of stationary axisymmetric RANS equations of continuity, momentum in the axial and radial directions of a turbulent incompressible generalized Newtonian fluid has the form [18-20]:

$$\nabla \cdot (\rho U) = 0 \tag{1}$$

$$\nabla \cdot (\rho U U) = -\nabla P + \nabla \cdot \left(2\mu_{eff} S\right) + \nabla \cdot (-\rho \langle u' u' \rangle) + \nabla \cdot \langle 2\mu_{eff}^{/} S^{/} \rangle \tag{2}$$

Here ρ, μ_{eff} expressions of density, effective molecular viscosity of a fluid, respectively. $\mathbf{U} \equiv \left(u_x,\ u_r\right)$ expresses the velocity vector with components ($u_x = U$, $u_r = V$) fluids in axial (x) and radial (r) coordinates, respectively; P express pressure; $-\rho\left\langle \mathbf{u}^{/}\mathbf{u}^{/}\right\rangle$ express the Reynolds friction stresses. Expression $\nabla \cdot \left\langle 2\mu_{eff}^{/}\mathbf{S}^{/}\right\rangle$ in equation (2) is found according to the representation [18,20]. Turbulent Reynolds stresses $-\rho\left\langle \mathbf{u}^{/}\mathbf{u}^{/}\right\rangle = -\rho\left\langle u_i u_j\right\rangle$ were found according to the Boussinesq hypothesis [21]. Turbulent viscosity μ_T is determined by using the RSM turbulent stress model [22, 23].

2.2 The RSM Turbulence model

The elliptical relaxation model of turbulent stresses RSM [22] takes into account the anisotropy of complex turbulent flows and is computationally more complex than the known (k-ε) - turbulence model. The RSM model shows better results than (k-ε) isotropic turbulence model. The Reynolds stress components are derived from a system of partial differential equations, and the system of governing equations of the second moment closure model [23] is given below:

$$\frac{\partial}{\partial x_j}\left(\rho U_j \left\langle u_i^{/} u_j^{/}\right\rangle\right) = \rho\left(P_{ij} + \phi_{ij} - \varepsilon_{ij}\right) + \frac{\partial}{\partial x_l}\left[\rho \nu_{eff}\delta_{lm} + \rho\frac{C_\mu T_T}{\sigma_k}\left\langle u_l^{/} u_m^{/}\right\rangle\right]\frac{\partial}{\partial x_m}\left\langle u_i^{/} u_j^{/}\right\rangle$$

$$\frac{\partial}{\partial x_j}\left(\rho U_j \varepsilon\right) = \frac{1}{T_T}\left(C_{\varepsilon 1}\tilde{P} - C_{\varepsilon 2}\varepsilon\right) + \frac{\partial}{\partial x_l}\left[\rho \nu_{eff}\delta_{lm} + \rho\frac{C_\mu T_T}{\sigma_\varepsilon}\left\langle u_l^{/} u_m^{/}\right\rangle\right]\frac{\partial \varepsilon}{\partial x_m}$$

$$\chi - L_T^2 \nabla^2 \chi = 1. \tag{3}$$

Here, P_{ij} and $\tilde{P} = 0.5\tilde{P}_{kk}$ are intensity of the energy transfer from the average velocity to the fluctuating motion (stress production terms), ϕ_{ij} is redistribution term [23], $L_T = \max\left(\frac{k^{3/2}}{\varepsilon},\ C_\eta \frac{\nu^{3/4}}{\varepsilon^{1/4}}\right)$ and $T_T = \max\left(\frac{k}{\varepsilon},\ C_T\sqrt{\frac{\nu}{\varepsilon}}\right)$ are turbulent time and length macroscales, where $2k = \left\langle u_i^{'} u_i^{'}\right\rangle$ is the turbulent kinetic energy, ε_{ij} is viscous dissipation rate tensor of turbulent stresses, $\varepsilon = 0.5\varepsilon_{kk}$, and χ is a blending coefficient, and it changes from zero at the wall to unity far from the wall [23]. The constants and model functions of the system of equations (3) are given in [23]. The effect of the rate of dissipation of the turbulent kinetic energy is ignored in this model. This term can dominate over the mean flow viscous dissipation in a developing turbulent flow. The NF at the inlet is fully developed and this effect can be neglected.

2.3 Boundary conditions

The flow diagram is shown in Fig. 1.

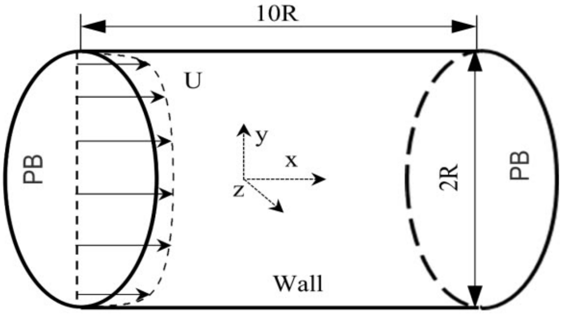

Fig.1. Computational domain for flow in a pipe.

On the wall surface, the conditions of no slip for the velocity are specified [23]:

$$r = R;\ U = V = \overline{u_i u_j} = 0;\ \varepsilon = 2\nu_W \frac{k}{y^2}\ ;\chi = 0 \tag{4}$$

Symmetry conditions for all variables are specified on the pipe axis.

$$r = 0;\ \frac{\partial U}{\partial r} = V = 0;\ \frac{\partial \overline{u_i u_j}}{\partial r} = \frac{\partial \varepsilon}{\partial r} = \frac{\partial \chi}{\partial r} = 0 \tag{5}$$

At the inlet section (x = 0), distributions of all variables across the pipe cross-section are specified, corresponding to developed turbulent flow in the pipe. At the outlet edge (x = L), soft boundary conditions are specified for all variables. Numerical modeling of the system of equations (1)-(3) under boundary conditions (4), (5) is presented in [21, 24].

3. Discussion of calculated data

An isothermal turbulent flow of a 0.2% XG xanthan gum solution in a pipe with an internal diameter (ID) D = 2R = 0.15 m and a length L = 3 m is considered. The average mass velocity of the liquid flow at the inlet of the pipe was U_{m1} = 4,0 m/s. Fluid flow density at the inlet section ρ_1 = 998 kg/m^3.

The Reynolds number of the flow, determined from the flow parameters at the inlet, Re = $U_{m1}D_1/\nu_{W1}$ = 8300. The axial velocity profile at the pipe inlet corresponds to a developed flow, and other characteristics of a turbulent flow correspond to this. The Sisco model for a viscoelastic fluid (shear-thinning fluid) [25] viscosity is determined by the formula for 0.2% XG:

$$\mu_{eff} = \mu_{ref}\left(\lambda_S \dot{\gamma}\right)^{n-1} + \mu_0 \tag{6}$$

In equation (6) μ_{ref} and λ_S – viscosity and time constant in the Sisco model, μ_0 – shear viscosity in the Sisco model, $\dot{\gamma} = \sqrt{2S_{ij}S_{ij}} = S$ – shear rate tensor (Table 1), $S_{ij} = 0.5\left(\frac{\partial U_i}{\partial x_j} + \frac{\partial U_j}{\partial x_i}\right)$ – strain rate tensor.

Table 1. Properties of viscoelastic fluid according to [24].

μ_{ref}, Pa·s	λ_S, s	μ_0, Pa·s	n
58.1	1900	0.0016	0.34

Here $u_* = \sqrt{\tau_W / \rho}$ – friction speed, $y^+ = yu_* / \nu_W$, $y = R - r$ – distance from the pipe wall along the normal, τ_W – shear stress, ν_W and ρ – kinematic viscosity determined from the parameters on the wall and the density of the medium.

Figure 2, a shows the averaged axial velocity profiles in universal coordinates for a Newtonian fluid (NF) and a non-Newtonian, viscoelastic fluid (NNF). The standard logarithmic law-of-the-wall profile of turbulent flow in a pipe at high Reynolds numbers (Re) for the Newtonian fluid is also plotted. At Reynolds number Re = 8300, the averaged axial velocity profile for the Newtonian fluid in the laminar sublayer has the same law-of-the-wall distribution.

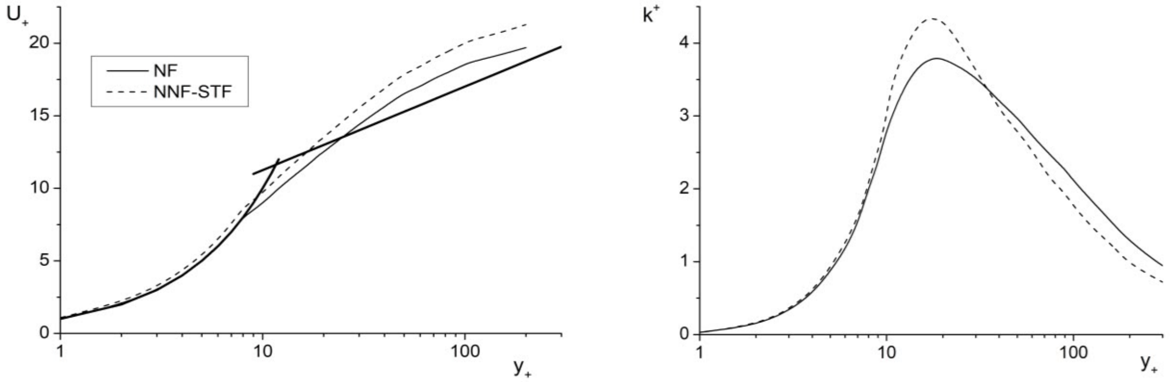

a) b)

Fig.2. Averaged axial velocity profiles $U^+ = U / u_*$ (a), kinetic energy of turbulence $k^+ = k / u_*^2$ (b) in universal coordinates.

In the core of the current $y^+ = yu_* / \nu_W > 50$ the average axial velocity (NF) profile lies above the linear logarithmic profile, which corresponds to the laws of turbulent flow in a pipe at low Re numbers. The averaged axial velocity profile for a non-Newtonian viscoelastic fluid (NNF) lies even higher than the profile of a Newtonian fluid (NF) in the turbulent core of the flow (see Fig. 2, a). This is explained by the fact that vortices in the viscoelastic fluid accelerate the flow, causing the profile to stretch in the core of the flow.

The distribution of turbulent kinetic energy of a viscoelastic fluid shows an increase in the value in the buffer zone of the flow compared to the distribution of a Newtonian fluid (see Fig. 2,b). As can be seen from Fig. 2,b, the maximum value of turbulent kinetic energy is reached at a value of $y^+ = yu_* / \nu_W = 20$. Turbulent kinetic energy in both Newtonian and viscoelastic fluids reaches its maximum value in the buffer zone (see Fig. 2, b).

Figure 3 shows the profiles axial $u^{'+} = u^{'} / u_*$ (a) and radial $v^{'+} = v^{'} / u_*$ (b fluctuations and Reynolds stresses $\langle uv \rangle^+ = \langle u'v' \rangle / u_*^2$ (c) in universal coordinates. The turbulent stress model (RSM) describes the anisotropic property of turbulent flow in a pipe. As can be seen from Figure 3, the profiles axial $u^{'+} = u^{'} / u_*$ (a) and radial $v^{'+} = v^{'} / u_*$ (b) fluctuations have different distribution patterns. If the axial fluctuation profile $u^{'+} = u^{'} / u_*$ reaches its maximum value at $y^+ = yu_* / \nu_W < 20$, then, as radial fluctuation profile $v^{'+} = v^{'} / u_*$ reaches its maximum value at $y^+ = yu_* / \nu_W < 80$, i.e. at a significantly greater distance from the pipe wall (see Fig. 3). It should be noted that the maximum value of the axial fluctuation profile $u^{'+} = u^{'} / u_*$ viscoelastic fluid is greater than Newtonian fluid (see Fig. 3, a). Then, as the maximum value of the radial fluctuation profile $v^{'+} = v^{'} / u_*$ less than Newtonian fluid (see Fig. 3, b).

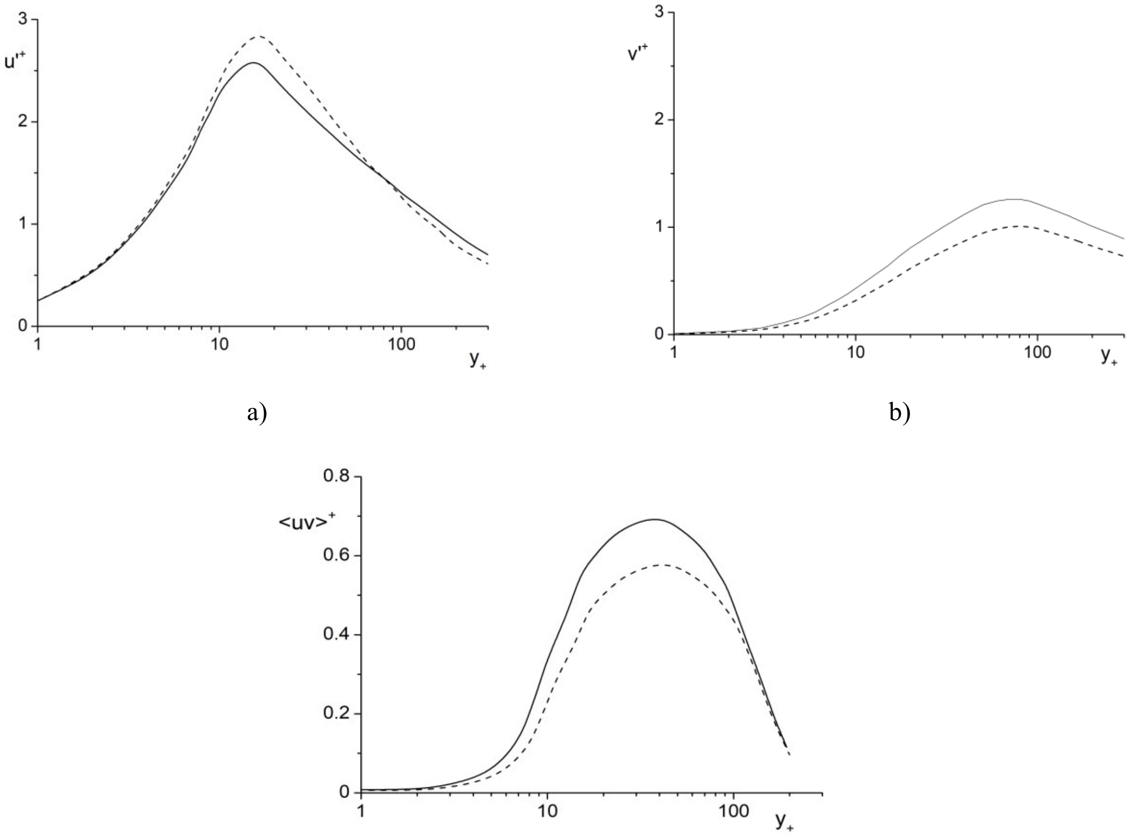

a) b)

c)

Fig.3. Axial $u'^{+}=u'/u_*$ (a) and radial $v'^{+}=v'/u_*$ (b) profiles fluctuations and Reynolds stress $\langle uv\rangle^{+}=\langle u'v'\rangle/u_*^2$ (c) in universal coordinates.

Varied distribution of profiles axial $u'^{+}=u'/u_*$ and radial $v'^{+}=v'/u_*$ fluctuation leads to the form of Reynolds stress $\langle uv\rangle^{+}=\langle u'v'\rangle/u_*^2$ in universal coordinates (see Fig. 3,c). Reynolds stress distribution $\langle uv\rangle^{+}=\langle u'v'\rangle/u_*^2$ viscoelastic fluid (dashed line) passes below the Reynolds stress distribution $\langle uv\rangle^{+}=\langle u'v'\rangle/u_*^2$ Newtonian fluid (see Fig. 3, c). Turbulent flow friction determined by the Reynolds stress $\langle uv\rangle^{+}=\langle u'v'\rangle/u_*^2$, decreases in viscoelastic fluid compared to a Newtonian one.

Thus, the viscoelastic property of the fluid causes a decrease in turbulent friction and hydraulic resistance of the flow.

4. Conclusion

The paper demonstrates that the use of a turbulent stress model allows one to accurately describe the turbulent flow characteristics of a non-Newtonian viscoelastic fluid in a pipe without directly resolving all turbulence scales. A comparison with the Newtonian case allowed us to quantify the contribution of non-Newtonian effects due to the rheology of Sisko fluid to the formation of velocity and turbulent stress profiles. It was found that the averaged velocity profile in universal wall-layer coordinates for Sisko fluid lies above the corresponding profile for a Newtonian fluid, which is due to a decrease in effective viscosity with increasing shear rate. It was shown that the turbulent kinetic energy profile for Sisko fluid is more elongated compared to the Newtonian case, indicating weakening of local turbulent energy dissipation. Significant differences between the axial and radial fluctuation velocity profiles indicate pronounced anisotropy of turbulent stresses and confirm the model's ability to adequately reproduce this flow property. The obtained effect of reducing hydrodynamic resistance confirms the correctness of taking into account the viscoelastic properties of the fluid in the proposed model of turbulent stresses.

Conflict of interest statement

The authors declare that they have no conflict of interest in relation to this research, whether financial, personal, authorship or otherwise, that could affect the research and its results presented in this paper.

CRediT author statement

Zhapbasbayev U.K.: Conceptualization, Funding acquisition, Supervision; **Pakhomov M.A.**: Investigation, Methodology, Validation; **Ramazanova G.I.**: Formal analysis, Writing – original draft; **Sattinova Z.K.:** Data curation, Writing Reviewing and Editing. The final manuscript was read and approved by all authors.

Funding

This work was supported by the Science Committee of the Ministry of Science and Higher Education of the Republic of Kazakhstan (Grant No's. AP23486543 for 2024-2026)

References

1 Toms B.A. (1948) Some observations on the flow of linear polymer solutions through straight tubes at large Reynolds numbers. *Proc. Int. Cong. Rheol.*, 2, 135–141. https://ci.nii.ac.jp/naid/10004666161

2 Bayode E.Owolabi, David J.C.Dennis & Robert J.Poole (2017) Turbulent drag reduction by polymer additives in parallel shear flows. *J. of fluid Mechanics*, 827. https://doi.org/10.1017/jfm.2017.544

3 Sellin R.H. J., Hoyt J.W.& Scrivener O. (1982) The effect of Drag-Reducing Additives on fluid flows and their industrial applications. *J. of Hydraulic Research*, 20(1), 29–68. https://doi.org/10.1080/00221688209499499

4 Berman N.S. (1989) Polymer contributions to transport equations. In Drag reduction in fluid flows. *Techniques for Friction Control*, 21. https://link.springer.com/chapter/10.1007/978-3-7091-2574-8_10

5 Keizo Watanabe, Satoshi Ogata. (2023) Drag Reduction by Complex Mixtures in Turbulent Pipe Flows. *Flow, Turbulence and Combustion*, 113, 41-49. https://doi.org/10.1007/s10494-023-00448-9

6 Zhapbasbayev U.K., Bossinov D.Zh., Pahomov M.A., Sattinova Z. (2025) Modeling of Turbulent Non-Isothermal Flow in a Heating Network Pipe. *Bulletin of The Karaganda University. Physics Series,* 30, 2(118), 67-74. https://doi.org/10.31489/2025ph2/67-74

7 Thais L., Gatski T.B. & Mompean G. (2012) Some dynamical features of the turbulent flow of a viscoelastic fluid for reduced drag. *J. Turbul.* 13, N19. https://doi.org/10.1080/14685248.2012.685522

8 Tabor M. & De Gennes P.G. (1986) A cascade theory of drag reduction. EPL. *Europhys. Lett.,* 2 (7), 519. https://doi.org/10.1209/0295-5075/2/7/005

9 Ptasinski P.K., Boersma B.J., Nieuwstadt F.T.M., Hulsen M.A., Van der Brule B.H.A.A., & Hunt J.C.R. (2003) Turbulent channel flow near maximum drag reduction: simulations, experiments and mechanisms. *J. Fluid Mech.*, 490, 251-291. https://doi.org/10.1017/S0022112003005305

10 L'vov V.S., Pomyalov A., Procaccia I. &Tiberkevich V. (2004) Drag reduction by polymers in wall bounded turbulence. *Phys. Rev. Lett.*, 92, 244503. https://doi.org/10.1103/PhysRevLett.92.244503

11 De Angelis E.; Casciola C.M.; L'vov V.S.; Pomyalov A.; Procaccia I.; & Tiberkevich V. (2004) Drag reduction by a linear viscosity profile. *Phys. Rev. E.*, 70, 055301(R). https://doi.org/10.1103/PhysRevE.70.055301

12 Sureshkumar R.; Beris A.N.; & Handler R.A. (1997) Direct numerical simulation of the turbulent channel flow of a polymer solution. *Phys. Fluids*, 9, 743–755. https://doi.org/10.1063/1.869229

13 Dallas V., Vassilicos J.C.; & Hewitt G.F. (2010) Strong polymer-turbulence interactions in viscoelastic turbulent channel flow. *Phys. Rev. E*, 82, 066303. https://doi.org/10.1103/PhysRevE.82.066303

14 Min T., Yoo J.Y., Choi H., Joseph D.D. (2003) Drag reduction by polymer additives in a turbulent channel flow. *J. Fluid Mech.*, 486, 213–238. https://doi.org/10.1017/S0022112003004610

15 Pinho F. A. (2003) GNF framework for turbulent flow models of drag reducing fluids and proposal for a $k-\varepsilon$ type closure. *J. Non-Newton. Fluid Mech.*, 114, 149–184. https://doi.org/10.1016/S0377-0257(03)00120-4

16 Cruz D.; Pinho F.; & Resende P. (2004) Modelling the new stress for improved drag reduction predictions of viscoelastic pipe flow. *J. Non-Newton. Fluid Mech.*, 121, 127–141. https://doi.org/10.1016/j.jnnfm.2004.05.004

17 Resende P.; Escudier M.; Presti F.; Pinho F.; & Cruz D. (2006) Numerical predictions and measurements of Reynolds normal stresses in turbulent pipe flow of polymers. *Int. J. Heat Fluid Flow*, 27, 204 – 219. https://doi.org/10.1016/j.ijheatfluidflow.2005.08.002

18 Gavrilov A.A., & Rudyak, V.Y. (2016). Reynolds-averaged modeling of turbulent flows of power-law fluids, *J. Non-Newton. Fluid Mech.*, 227, 45–55. https://doi.org/10.1016/j.jnnfm.2015.11.006

19 Sakipova S.E., Shaimerdenova K.M., Nussupbekov, Ospanova D.A., Kutum B.B. (2023) Modeling the dynamics of heat and mass transfer processes in a tubular heat exchanger under pulsed influences. *Eurasian Physical Technical Journal*, 20, 1(43), 51-55. https://doi.org/10.31489/2023No1/51-55

20 Lovato S., Keetels G.H., Toxopeus S.L. & Settels J.W. (2022) An eddy-viscosity model for turbulent flows of Herschel–Bulkley fluids. *J. Non-Newtonian Fluid Mech*., 301 104729. https://doi.org/10.1016/j.jnnfm.2021.104729

21 Pakhomov M.A., & Zhapbasbayev U.K. (2024) Comparative predictions of turbulent non-isothermal flow of a viscoplastic fluid with a yield stress. *Heliyon*, 10e24062. https://doi.org/10.1016/j.heliyon.2024.e24062

22 Manceau R. & Hanjalic K. (2002) Elliptic blending model: a new near-wall Reynolds-stress turbulence closure. *Phys. Fluids*, 14(2) 744–754. https://doi.org/10.1063/1.1432693

23 Fadai-Ghotbi A., Manceau R. & Boree J. (2006) Revisiting URANS computations of the backward-facing step flow using second moment closures. Influence of the numerics. *Flow, Turbulence and Combust*., 81(3) 395–410. https://doi.org/10.1007/978-3-540-92779-2_79

24 Pakhomov M.A. & Zhapbasbayev U.K. (2024) RANS Predictions of Turbulent Non-Isothermal Viscoplastic Fluid in Pipe with Sudden Expansion. *Journal of Non-Newtonian Fluid Mechanics*, 334, 105329, https://doi.org/10.1016/j.jnnfm.2024.105329

25 Pereira A.S., & Pinho F.T. (2000) Turbulent characteristics of shear-thinning fluids in recirculating flows. *Exp. Fluids,* 28, 266–278. https://doi.org/10.1007/s003480050387

AUTHORS' INFORMATION

Zhapbasbayev Uzak Kairbekovich – Doctor of Technical Sciences, Professor, Head of the Research and Production Laboratory "Modeling in Energy", Satbayev University, Almaty, Kazakhstan; Scopus ID: 6508298888; https://orcid.org/0000-0001-5973-5149, uzak.zh@mail.ru,

Pakhomov Maksim Aleksandrovich – Doctor of Physical and Mathematical Sciences, Major Research Worker, Kutateladze Institute of Thermophysics SB RAS, Novosibirsk, Russian Federation. Scopus ID: 6602734341; https://orcid.org/0000-0002-8127-3638, Pakhomov@itp.nsc.ru

Ramazanova Gaukhar Izbasarovna – Candidate of Physical and Mathematical Sciences, Deputy Head of "Modeling in Energy", Satbayev University, Almaty, Kazakhstan; Scopus ID: 6506885857; ORCID: https://orcid.org/0000-0002-8689-9293, gaukhar.ri@gmail.com

Sattinova Zamira Kanaevna - Candidate of physical and mathematical sciences, Acting Professor, L.N. Gumilyov Eurasian National University, Astana, Kazakhstan; Scopus ID: 54400166600; https://orcid.org/0000-0002-2990-6581; sattinova.kz@gmail.com

EURASIAN PHYSICAL TECHNICAL JOURNAL

2026, Volume 23, No. 1(55)

https://doi.org/10.31489/2026N1/101-112

Received: 22/01/2026 Revised: 05/02/2026 Accepted: 19/03/2026

Research Article

UDC 536.24, 004.94

MODELING OF HEAT TRANSFER AND HYDRODYNAMICS OF WATER-OIL HEAT CARRIERS IN HEAT EXCHANGERS

Zhumanbayeva A.S.[1], Volkov K.N.[2]*, Jaichibekov N.Zh.[1], Kurmanova D.E.[1]

[1] L.N. Gumilyov Eurasian National University, Astana, Kazakhstan
[2] Kingston University, London SW15 3DW, UK
Correspondence: jas968@mail.ru

Abstract. *Increased energy efficiency in the extraction and transportation of highly viscous oil is achieved by reducing its viscosity through heating. Numerical modeling is a powerful tool for developing and analyzing methods to improve heat transfer efficiency and optimize the design of heat exchange devices in the oil and gas industry. To solve this problem, the study uses Reynolds-averaged Navier-Stokes equations supplemented with turbulence models (k–ε, k–ω SST, and Transition SST) capable of accounting for the transition from laminar flow to turbulent flow with variable viscosity. The results of calculations of smooth and spiral pipes are compared, as well as an assessment of the reliability and performance of turbulence models used to simulate the operation of heat exchangers with direct and reverse heat flow. The dependences of the numbers Nu and Re of the oil flow in a washed by water pipe for all three turbulence models are shown in comparison with the corresponding experimental result, indicating the qualitative agreement of the numerical calculation results with the experiment. The results of the comparative analysis showed that the kw SST model most effectively describes the flow movement in the inter-tube space. The Computational Fluid Dynamics calculation data obtained is of practical importance for the design and optimization of heat exchanger structures.*

Keywords: heat exchanger, heat exchange, turbulence, modeling, intensification, helicoid tube, oil, hydrodynamics, laminar-turbulent transition, viscosity

1. Introduction

The efficiency of high-speed heat exchangers is achieved due to the intensification of heat exchange, which is provided by swirling the coolant flows. This vortex movement radically changes the hydrodynamics of currents: it increases their kinetic energy, causes severe turbulence and intense mixing of layers, which together significantly improves heat transfer performance. In addition, the vortex motion reduces the hydraulic resistance of the device and promotes self-cleaning of heating surfaces from hardened deposits. The twisting of the medium in the intertubular space is provided by the spiral seams of the housing, which, in addition to their main function, also act as stiffeners. This method of reinforcing the structure is innovative, since traditionally, the thickness of their walls is increased to increase the strength of heat exchangers.

In [1, 2] modeling and calculation of the hydrodynamics of heat carriers (water, oil) flowing through smooth pipes were carried out. In these works, empirical formulas were used for heat transfer from [3]. The information gathered during numerical modeling is used to determine the best approaches for heat transfer intensification [4, 5]. Research indicates that the viscosity of oil has less of an impact on the pipeline's hydraulic properties when it is transported in highly turbulent conditions.

The curvature of the pipe has a significant effect on heat transfer and flow hydrodynamics [6]. In [7], the characteristics of a helicoid tube's movement and heat exchange in heat exchangers of various shapes with straight-tube heat exchangers under different operating conditions were compared. A wide range of studies on increasing the heat transfer rate and reducing the size and cost of shell-and-tube heat exchangers is presented in [8]. Artificial roughness using a corrugated surface improves heat transfer characteristics by destroying and destabilizing the thermal boundary layer.

The coefficient of convective heat transfer in both helicoid and direct tubular heat exchangers under turbulent flow conditions was experimentally determined in [9]. The overall heat transfer coefficient in helicoid heat exchangers is much higher than in straight tube heat exchangers. Helical fins provide higher heat transfer speeds and efficiency than straight pipes due to the development of secondary flow inside the helicoid tube [10]. In [11], an analysis of a spiral-wound heat exchanger was carried out taking into account various boundary conditions. Setting the boundary conditions of constant temperature or constant heat flow for a real heat exchanger does not lead to agreement between the calculated and experimental data. To improve the accuracy of calculations, it is necessary to take into account the coupled heat transfer. Studies of the characteristics of a spiral tubular heat exchanger with different inner tube geometries have been devoted to [12, 13]. [14] presents a numerical study of the characteristics of heat transfer and pressure losses in a vortex cooling pipe with five tangential inlet nozzles and recesses on the inner surface of the pipe. The recesses on the inner surface of the pipe lead to an intensification of heat transfer (the heat transfer coefficient increases by 7.2%) due to the increased heat transfer area and the interaction between the swirling flow and the wall with recesses. A numerical study of heat transfer and entropy generation during laminar flow in screw tubes of various cross-sections is considered in [15].

By facilitating and sealing the tube bundle in support elements made of polymer materials, the maximum possible heat exchange surface is achieved in high-speed heat exchangers [16, 17]. The dynamics of fluid flow in the inter-tube space of heat exchangers is characterized by a high degree of complexity and is influenced by many factors. Heating of oil and petroleum products is a widely used method to reduce energy losses during their transportation [18]. Numerical modeling of heat exchange processes in heat exchange devices with various designs is presented in [19]. The results of the conducted studies indicate a decrease in the influence of the viscosity of the pumped oil on the hydraulic characteristics of the pipeline system under developed flow turbulence conditions. The movement of liquid in the inter-tube space of heat exchangers is highly complex and is due to a number of factors. Heating of oil and petroleum products is actively used to minimize energy losses during their transportation [18]. Numerical modeling of heat exchange processes in apparatuses of different configurations is considered in the source [19]. The data obtained indicate that with the developed turbulence of the flow, the influence of the viscosity of the transported oil on the hydraulic parameters of the pipeline is significantly weakened. A comparative analysis of the accuracy of various turbulence models used to solve the Reynolds equations, the dynamics of heat and mass transfer processes is the object of research in the works [20-26]. In computational practice the three turbulent models are typically employed. A sufficient agreement between the outcomes of numerical modeling and the data collected during industrial tests can be achieved through calculations carried out utilizing these models [2].

The present study presents the results of numerical modeling analyzing the flow and heat transfer in helicoid-shaped pipes. These data are compared with similar indicators for smooth pipes. During the calculations, parameters such as the degree of pipe twist, flow rate, and initial oil temperature were varied. Special attention is paid to how the geometry of a spiral tube affects hydrodynamics and heat transfer, in particular, flow turbulence and its role in increasing heat transfer efficiency. Various approaches have been used to model turbulence, including the *k–ε*, *k–ω SST*, and Transition *SST* models (which take into account the laminar-turbulent transition). Comparing the results of these models with data from physical experiments and semi-empirical calculations allows us to determine the most suitable turbulence model for designing direct-flow and countercurrent heat exchangers.

2. Model and calculation method

Method of modeling and computation The Navier-Stokes equations modified by Reynolds (RANS) are used for numerical simulation of hydrodynamics and thermal transfer of an incompressible fluid with changing viscosity. The three turbulence models, which takes the luminaire-turbulent transition into account, are used to close the Reynolds equations.

2.1. Basic equations

The equations describing the flow have the following form:

- the equation of continuity

$$\frac{\partial \vartheta_j}{\partial x_j} = 0;$$

- the momentum equation

$$\vartheta_j \frac{\partial \vartheta_i}{\partial x_j} = -\frac{1}{\rho}\frac{\partial p}{\partial x_i} + \frac{\partial}{\partial x_j}\left[(\nu + \nu_t)\frac{\partial \vartheta_i}{\partial x_j}\right];$$

- the energy equation

$$\vartheta_j \frac{\partial T}{\partial x_j} = \frac{\partial}{\partial x_j}\left[\left(\frac{\nu}{\mathrm{Pr}} + \frac{\nu_t}{\mathrm{Pr}_t}\right)\frac{\partial T}{\partial x_j}\right].$$

In this equation, ρ stands for density, ϑ_i for velocity components in the direction of coordinates x_i, p for pressure, T for temperature, ν for the liquid's kinematic viscosity, ν_t for turbulent viscosity, and Pr, Pr_t for the Prandtl number for laminar and turbulent flow regimes. The subsequent equations, which pertain to the turbulence models, are sourced from [26]. For the turbulence model *k*–ε, the dissipation of the turbulent energy ε and the cinematic energy of the turbulence k are determined using the following set of equations:

$$\frac{\partial}{\partial x_i}(\rho k \vartheta_i) = \frac{\partial}{\partial x_j}\left[(\mu + \frac{\mu_t}{\sigma_k})\frac{\partial k}{\partial x_j}\right] + G_k + G_b - \rho\varepsilon - Y_M + S_k$$

$$\frac{\partial}{\partial x_i}(\rho \varepsilon \vartheta_i) = \frac{\partial}{\partial x_j}\left[(\mu + \frac{\mu_t}{\sigma_\varepsilon})\frac{\partial \varepsilon}{\partial x_j}\right] + C_{1\varepsilon}\frac{\varepsilon}{k}(G_k + C_{3\varepsilon}G_b) - C_{2\varepsilon}\rho\frac{\varepsilon^2}{k} + S_\varepsilon.$$

Here ϑ_i is the component of velocity in the corresponding direction, μ is the dynamic viscosity, μ_t is the turbulent viscosity, Y_M is the total dissipation velocity, $G_k, G_b, C_{1\varepsilon}, C_{2\varepsilon}$ are constants, S_k, S_ε are user–defined initial terms.

$$\mu_t = \rho C_\mu \frac{k^2}{\varepsilon}.$$

Additional transfer equations for the k–ω SST model have the form

$$\vartheta_j \frac{\partial Re_{\theta t}}{\partial x_j} = P_{\theta t} + \frac{\partial}{\partial x_j}\left[\sigma_{\theta t}(\nu + \nu_t)\frac{\partial Re_{\theta t}}{\partial x_j}\right];$$

$$\vartheta_j \frac{\partial \gamma}{\partial x_j} = P_\gamma - E_\gamma + \frac{\partial}{\partial x_j}\left[\left(\nu + \frac{\nu_t}{\sigma_\gamma}\right)\frac{\partial \gamma}{\partial x_j}\right];$$

Here $P_{\theta t}$ is a derivative of the Reynolds number in terms of the thickness of the pulse loss; P_γ and E_γ are the conditions for the formation and dissipation of intermittency; $\sigma_{\theta t}$ and σ_γ are the constants of the model, γ is the intermittency parameter.

The traffic sources are defined as follows:

$$P_{\gamma 1} = F_{length} c_{a1} \rho S [\gamma F_{onset}]^{c_{\gamma 3}} (1 - c_{e1}\gamma),$$

where S is the strain rate magnitude; F_{length} is an empirical relation that controls the length of the transition area; F_{onset} is the location of the beginning of the transition, $c_{a1}, c_{e1}, c_{\gamma 3}$ are the constants for the intermittency equation.

The source of destruction/relamination is defined as follows:

$$E_\gamma = c_{a2} \rho \Omega \gamma F_{turb} (c_{e2}\gamma - 1)$$

where Ω is the amount of vorticity, c_{a2}, c_{e2} are constants for the intermittency equation, F_{turb} the function that determines the fracture coefficient outside the laminar boundary layer.

For the Transition SST model, instead of the second equation of the above system, the equation is written

$$\frac{\partial(\rho\vartheta_j\gamma)}{\partial x_j} = P_{\gamma 1} - E_{\gamma 1} + P_{\gamma 2} - E_{\gamma 2} + \frac{\partial}{\partial x_j}\left[(\mu + \frac{\mu_t}{\sigma_\gamma})\frac{\partial\gamma}{\partial x_j}\right].$$

The definitions for $P_{\gamma 1}$, $P_{\gamma 2}$ representing sources of transition, and $E_{\gamma 1}, E_{\gamma 2}$ representing sources of destruction or relamination, are provided below

$$P_{\gamma 1} = c_{a1} F_{length} \rho S [\gamma F_{onset}]^{c_{\gamma 3}}, \; P_{\gamma 2} = c_{a2} \rho \Omega \gamma F_{turb}$$

$$E_{\gamma 1} = c_{e1} P_{\gamma 1} \gamma, \; E_{\gamma 2} = c_{e2} P_{\gamma 2} \gamma$$

2.2. Dependence of viscosity on temperature

Unacceptable strains on the pipe walls, "solidification" of the oil, and a halt to pumping can result from a rise in viscosity and the appearance of non-Newtonian qualities with a drop in the temperature of oil pumping. The Walter formula is used in the oil business to determine temperature-dependent kinematic viscosity [3].

$$lg[lg(\nu_1 + \mathrm{c})] = a + blgT$$

where a, b and c are the empirical coefficients characterizing the oil under study, which are located at three experimental points. In this case, for the possibility of applying the Walter formula based on two experimental points, $\mathrm{c} = 0.8$ is often assumed.

The coefficients *a* and *b* in the above formula are from the relations

$$a = \lg[\lg(\nu_1 + 0.8)] - b\lg T$$

$$b = \frac{\lg[\lg(\nu_1 + 0.8)] - \lg[\lg(\nu_2 + 0.8)]}{\lg T_1 - \lg T_2}$$

Here ν_1 and ν_2 are the values of the kinematic viscosity of the liquid at temperatures T_1 and T_2.

2.3. Computational procedure

The values obtained using the logarithmic average temperature pressure method are compared with the results obtained using numerical methods of hydrodynamics. The conditions of stationary and axisymmetric flow are accepted. In calculations, oil is assumed to be a Newtonian liquid with constant density and varying thermophysical parameters. The modeling and calculations were done using the Ansys Fluent program. This is supported, by the consistency and dependability of the flow, which considers mathematical models of physical processes, the discretization of space in CFD, which splits continuous real space and the computational domain into a discrete set of cells that are constant fields and medium properties.

The finite volume method, which enables working with grids of different complexity (unstructured), and the SIMPLE algorithm, which is intended for pressure correction, are the two primary techniques used to discretize the equations. Viscous fluxes are calculated using a centered second-order scheme, whereas inviscid flux components are calculated using the MUSCL scheme. By linking centered second-order finite differences with a dissipative term, the MUSCL scheme, which was founded on conservation principles, ensures the monotonicity of the solution and enhances its spatial accuracy. A flow limiter based on characteristic variables is used to accomplish the alternation between these elements. The resulting system of discrete equations is solved using an effective geometric multigrid approach.

2.4. Coefficients of friction and heat transfer

For the laminar flow regime at Reynolds numbers up to 2320, the coefficient of friction λ was determined by the Poiseuille formula.

$$\lambda = \frac{64}{Re}.$$

Since both laminar and turbulent regimes are possible in the Reynolds number range of 2320 to 4000, no comparison was done in this range. There are no well recognized analytical calculation formulas in the literature, and the experimental points vary significantly. Within the Blasius formula was used to calculate a turbulent flow regime with Reynolds values ranging from 4×10^3 to 10^5.

$$\lambda = \frac{0.31644}{Re^{0.25}}.$$

The Nusselt number is determined by a semi-empirical formula

$$Nu = 0.023\, Re^{0.8}\, Pr^{0.43}.$$

3. Geometry of the tube and heat exchanger

When considering a heat exchanger with a continuously varying temperature of the heat carriers, direct-flow and counter-flow devices are distinguished (Fig.1). Cold oil passes through the central pipe, and the surrounding outer pipe is filled with hot water. The heat exchange process is carried out in such a way that oil moves inside the system through a narrow channel, and a stream of hot water flows around it from the outside, providing the necessary temperature regime. The external surface of the heat exchanger is thermally insulated. In a direct-flow type heat exchanger, hot and cold heat carriers flow in the same direction parallel to each other. In a countercurrent type heat exchanger, two heat carriers flow parallel to each other, but in the opposite direction.

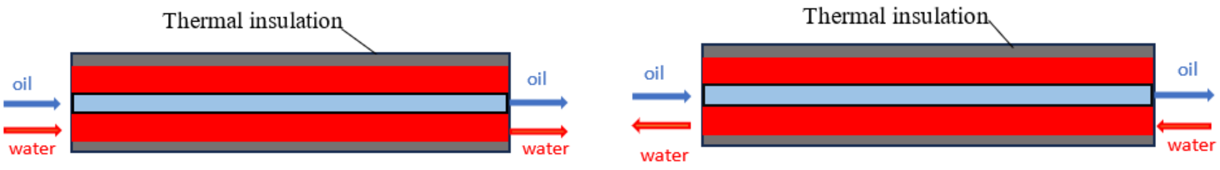

a) b)

Fig. 1. Schemes of direct-flow (a) and counter-flow (b) types of heat exchange devices.

Figure 6 shows the dependences of the Nu number on the Reynolds number (Re) for the cases of smooth and helicode tubes. It can be seen from the figure that for Re numbers up to 2.0×10^4, the heat transfer intensity is higher in the case of a smooth tube than for a helicoid tube. And at values of the Re number above 2.0×10^4, the heat transfer intensity is higher for the helicoid tube. This can be explained by the fact that with this Reynolds number, a laminar-turbulent transition occurs in the flow and it is pronounced precisely in the case of a helicoid tube. The inner diameter of the cold coolant pipe is 12 mm, the outer diameter is 14 mm. The diameter of the pipe through which the hot coolant passes is 20 mm. The temperatures of the heat carriers at the inlet are: cold — 303 K, hot — 423 K. The mass flow rates both of the heat carriers are 0,3814 kg/s and 0,6386 kg/s, respectively, at an inlet flow rate of 4 m/s in each case.

Applying the method of variable viscosity for a cold coolant and offering an improved geometry of the inner tube, in order to comprehensively apply various turbulence models in direct-flow and countercurrent devices, as well as in heat exchangers with a helicoid surface, heat transfer and flow dynamics of coolants are studied taking into account the laminar-turbulent transition. The inner tube of the heat exchanger with a smooth surface is shown in Fig.2a, and a helicoid tube with coils and a design grid is shown in Fig.2b. The number of coils on the surface of the tube is determined by the number of twists N, which in calculations take values from 5 to 40 with an interval of 5 twists.

As part of this task, it is assumed that oil fields are located at a depth of 0.9 to 2.4 km. The density of oil is 844-874 kg/m3, viscosity is 3.4–8.15 MPa·s, sulfur content is 0.16–2%, paraffins are 16-22%, resins are 8-20%. These parameters correspond to the characteristics of the Uzen oil and gas field located in Kazakhstan. These parameters make it possible to accept Uzen oil in the form of a Newtonian fluid [26]. Velocity and temperature profiles corresponding to laminar flow in a circular tube are set as boundary conditions in the inlet section. On the walls of the pipe, sticking conditions are used for speed. In the outlet section of the pipe, mild boundary conditions are applied (zero gradients of the desired functions). Boundary conditions of the second kind are used as boundary conditions for surface temperature.

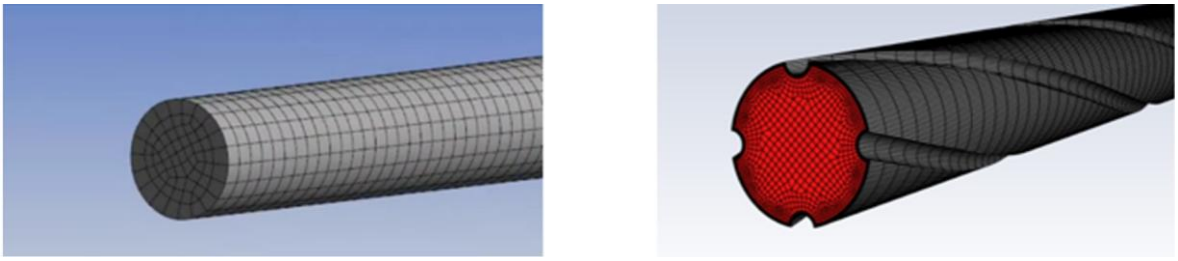

Fig. 2. View of smooth (a) and helicoid (b) design tubes.

The calculated grid contains 705,795 nodes and 657,696 elements. When y^+ is the dimensionless wall coordinate, the mesh cells are compressed close to the pipe walls so that $y^+<2$. The following initial parameters of the problem were also used for calculation: the radius of the unicode pipe is $R=0.006$ m, the radius of the groove is $r=0.001$ m, the flow velocity $\vartheta =4$ m/s, the temperature at the pipe inlet $T=303$ K, the heat transfer coefficient $\alpha=16685$ W/(m^2·K). The associated problem of heat exchange and hydrodynamics is solved for the heat exchanger. Boundary conditions of the 3rd kind are used on the walls of pipes. The temperature profiles of water and oil (cold and hot coolants) along the heat exchanger's length were produced using the widely recognized average-logarithmic temperature difference (LMTD) approach, as shown in [26], in order to validate the computation findings.

4. Discussion of the modeling results of flow in the helicoid tube

Based on the calculation results, distributions of hydrodynamic and thermal parameters for smooth and helicoid pipes are obtained. Figure 3a shows a graph of the dependence of the average mass temperature of oil at the outlet of a pipe with a length of 1 m on the number of coils. With an increase in the number of swirls, the oil outlet temperature increases, i.e., heat exchange between the heat carriers intensifies. With a tube length of 1 m, the maximum change in oil outlet temperature is approximately 3 degrees. Data analysis in Fig. 3b demonstrates that the heat flow through the surface of the pipe in contact with the washing liquid increases in proportion to the number of twists. This indicates that a larger number of twists contributes to increased heat transfer.

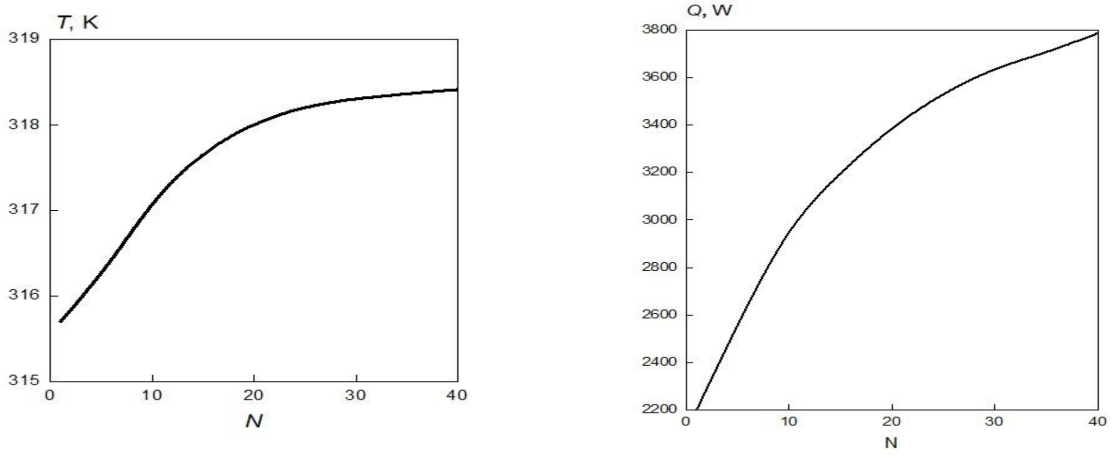

a) b)

Fig. 3. Dependence of the average mass temperature of oil at the outlet of the pipe (a) and heat flow (b) on the number of twists with a pipe length of 1 m.

The observed increase in the average oil temperature at the pipe's output (Fig. 3a) and a rise in heat flow with an increase in the number of twists in the pipe are due to the turbulence of the flow caused by the twisting process itself. The turbulence of the flow enhances the diffusion of liquid particles and, as a result, the intensification of heat exchange between them. The efficiency of this process is directly proportional to the number of twists in the pipe. In further calculations of oil parameters for smooth and helicoid surfaces, the pipe length was assumed to be 4 m, and the number of coils was 40. The data for a smooth pipe are taken from previous studies [26]. For a helicoid tube, heat exchange occurs more intensively, which is associated with an increase in the surface area of the heat exchange (in the presence of coils), and there is also an increase in heat exchange due to the diffusion process.

Figure 4 shows the dependence of the overpressure along the entire length of the tube. In the case of a helicoid pipe (line 2), a more drastic pressure drop is observed than in the case of a pipe with smooth walls. Additional flow resistance in the helicoid tube is associated with the development of vortex structures and increased friction caused by a violation of the linearity of the flow. Such effects are a consequence of the curved geometry and are accompanied by an increase in hydraulic losses. The coefficient of friction along the pipe was illustrated in Figure 5. It can be seen that the helicoid tube (line 2) exhibits a higher average coefficient of friction than the smooth tube (line 1). The flow and heat exchange in a pipe with spiral grooves are characterized by a number of distinctive features compared to smooth pipes. The presence of spiral grooves on the inner surface of the pipe induces a swirling flow movement, which leads to the formation of stable secondary vortex structures.

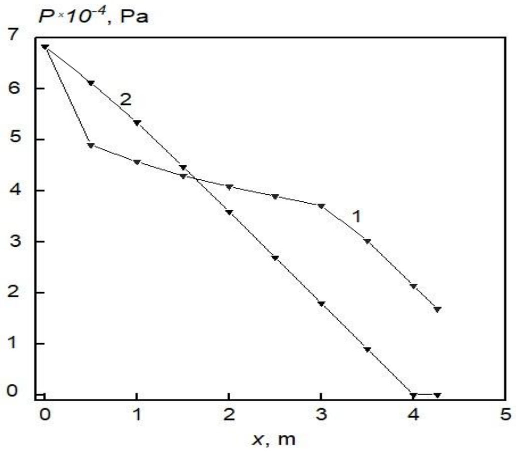

Fig. 4. Changes in oil overpressure along the length of a pipe with a smooth (line 1) and a helicoid (line 2) surface.

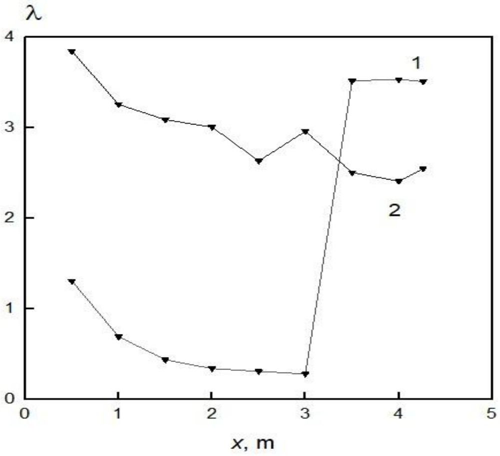

Fig 5. Changes in the coefficient of friction of oil along the length of a pipe with a smooth (line 1) and a helicoid (line 2) surface.

These vortices disrupt the laminar flow structure and contribute to a more uniform temperature distribution across the pipe section. An increase in the level of turbulence is already observed at relatively small values of the Reynolds number, which provides an increase in the intensity of heat transfer between the pipe surface and the moving medium. The grooves create the effect of pseudo-vortex mixtures, enhancing heat transfer and destroying the thermal boundary layer. The flow and heat exchange in a pipe with spiral grooves are characterized by a number of distinctive features compared to smooth pipes. The presence of spiral grooves on the inner surface of the pipe induces a swirling flow movement, which leads to the formation of stable secondary vortex structures. These vortices disrupt the laminar flow structure and contribute to a more uniform temperature distribution across the pipe section. As a result, turbulence increases significantly, even at relatively low values of the Reynolds number, which contributes to the intensification of heat exchange between the pipe wall and the flowing medium. The grooves create the effect of pseudo-vortex mixtures, enhancing heat transfer and destroying the thermal boundary layer. However, along with the increase in heat transfer, there is an increase in hydraulic resistance due to increased friction and vortex formation losses. Thus, the use of pipes with spiral grooves requires optimal design of the geometry of the grooves (depth, pitch, angle of inclination) in order to achieve maximum efficiency with acceptable energy consumption.

Figure 6 shows the dependences of the Nusselt number on the Reynolds number (Re) for the cases of smooth and helicode tubes. It can be seen from the figure that for Re numbers up to 2.0×10^4, the heat transfer intensity is higher in the case of a smooth tube than for a helicoid tube. And at values of the Re number above 2.0×10^4, the heat transfer intensity is higher for the helicoid tube. This can be explained by the fact that with this Reynolds number, a laminar-turbulent transition occurs in the flow and it is pronounced precisely in the case of a helicoid tube.

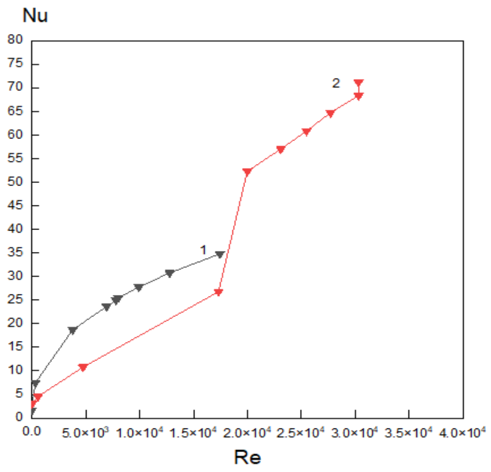

Fig 6. Dependence of the Nusselt number on the Reynolds number for the inner tube with oil.
1 - smooth tube, 2 - helicoid tube.

5. Comparison of the model and experimental analysis of the flow in the heat exchanger

Figures 7 and 8 show changes in the temperature of the heat carriers along the tubes. The graphs are constructed for three turbulence models, covering the forward and countercurrent flow patterns in smooth pipes. Triangular markers indicate calculations performed by the LMTD (Log-Mean Temperature Difference) method [26].

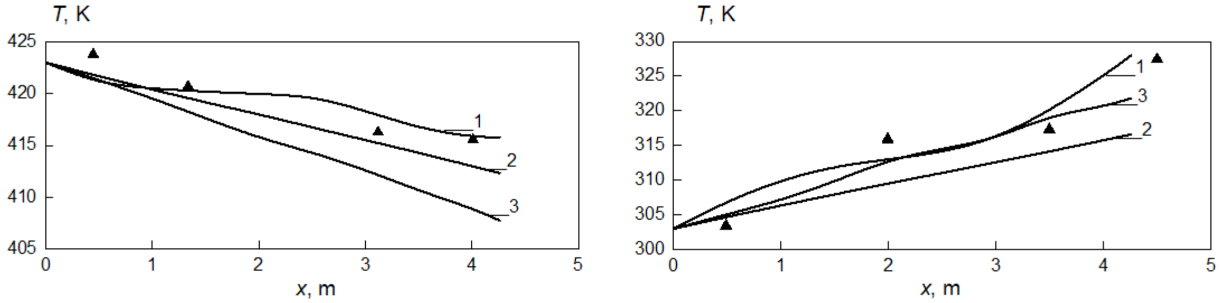

a) b)

Fig.7. Temperature changes of water (a) and oil (b) along the axial coordinate in a direct–flow heat exchanger for models k–ω SST (lines 1), k-ε (lines 2), Transition SST (lines 3).

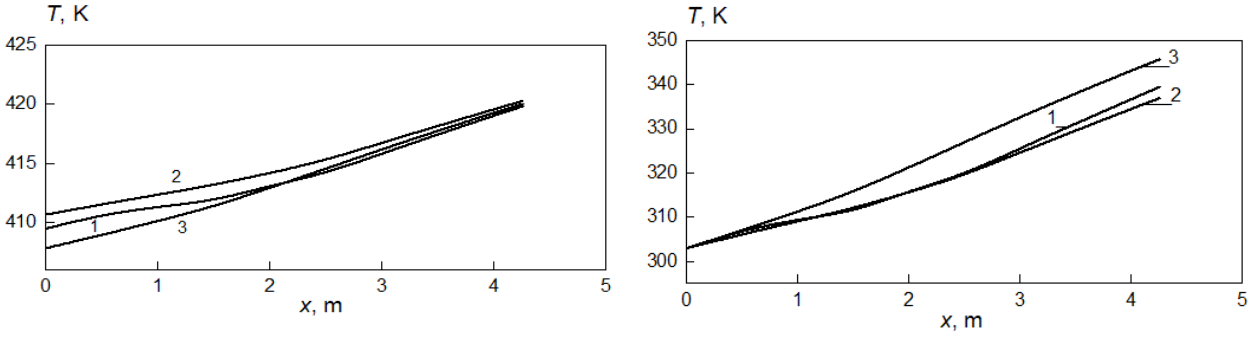

a) b)

Fig.8. Temperature change of water (a) and oil (b) along the axial coordinate in a countercurrent heat exchanger for models k–ω SST (lines 1), k–ε (lines 2), Transition SST (lines 3).

In the case of direct flow (Fig. 7), all three turbulence models demonstrate a similar pattern of temperature changes: the temperature of the hot coolant (water) decreases, and the temperature of the cold coolant (oil) increases in the axial direction. An analysis of the results shows that for all the turbulence models studied, the temperature differences between the heat carriers become more pronounced as they approach the outlet section. In particular, the k–ε model demonstrates a lower heating temperature of the cold coolant along the pipe compared to the other two models. On the other hand, the most intense cooling of the hot coolant is observed when using the Transition *SST* model. For the counterflow circuit (Fig. 8), the temperature of the cold coolant increases along the pipe in the direction from the inlet section to the outlet for all three turbulence models. However, stronger heating occurs for the Transition SST model compared to the direct-flow case. Unlike direct flow, the flow of hot coolant is directed from the outlet section of the heat exchanger towards its inlet section, therefore, cooling of this coolant occurs from the outlet section towards the inlet section. In this case, cooling occurs more slowly for the k–ε model, whereas for the direct current, such a change occurs for the SST model.

A comparison the cold coolants' (oil's) temperature variation for two instances of coolant flow shown in Figures 7 and 8 shows that for the considered turbulence models, the oil heating temperature is higher in the countercurrent case than in the direct-flow scheme with a relatively uniform cooling rate of the hot coolant.

The temperature field in a pipe with grooves is characterized by reduced unevenness compared to a smooth pipe. Due to the intensified mixing, a more efficient destruction of the thermal boundary layer is observed, which leads to a significant increase in the heat transfer coefficient. This effect is especially pronounced in laminar and transient flow regimes, where grooves play the role of an active element of heat exchanger. Figure 9 shows comparative graphs of the calculated and experimental dependences of the Nu number on the Re number for three cases of the turbulence model, namely the k–ω *SST*, k-ε and Transition *SST* models. The calculation results were compared with the experimental results in [27, 28]. This experimental work provides an analysis of the thermohydraulic characteristics and energy efficiency of shell-and-tube heat exchangers with a longitudinal flow in a counterflow.

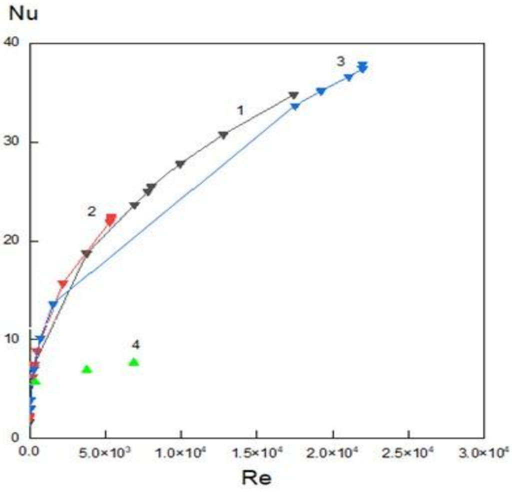

Fig.9. Comparative graphs of the dependences of the numbers Nu and Re in a tube with oil washed by water for all three models and experiment: 1- k-ω *SST*, 2 - k–ε model, 3 - Transition *SST* model, 4 - experimental data.

It can be seen from the figure that all three turbulence models give results close to each other, which are qualitatively consistent with the recalculated experimental results (due to different fluid densities). Naturally, one should not expect a quantitative coincidence of the results here, since the Nusselt tabular number for water is an order of magnitude higher than for oil. Nevertheless, the qualitative agreement of the calculated and experimental curves indicates an adequate description of the computational model used in this process.

Despite the physical differences between the cold coolants (water in one case and oil in the other), there is a qualitative agreement between the calculated curve and the experimental one. Naturally, one should not expect a quantitative coincidence of the results here, since the Nusselt table number for water is an order of magnitude higher than for oil. Nevertheless, the qualitative agreement of the calculated and experimental curves indicates an adequate description of the computational model used in this process.

Thus, the presence of spiral grooves makes it possible to significantly increase the efficiency of heat and mass transfer, however, this is accompanied by an increase in energy costs for overcoming resistance. Optimization of the geometry of the grooves (angle of inclination, pitch, depth) allows to achieve the best ratio between the intensification of heat exchange and pressure losses.

***Data Availability Statement*:** The data presented in this study are available upon request from the author.

6. Conclusion

Numerical studies of heat exchange and hydrodynamic characteristics in pipes of various geometries (smooth and helicoid) have revealed a number of fundamental features due to the shape of the channel. The use of a helicoid tube contributes to a significant intensification of heat exchange. The use of swirled tubes with coils leads to a noticeable increase in the oil outlet temperature and the local Nusselt number compared to a smooth pipe. The main reason for this is the turbulence of the oil flow caused by windings, which intensifies the heat exchange between the liquid layers through diffusion. In addition, a slight increase in the surface area of the tube due to the recesses also contributes to an increase in oil temperature, increasing the heat flow. These conclusions are confirmed by comparative graphs of the dependence of the oil outlet temperature for smooth and helical tubes with swirls.

The characteristic behavior of temperature curves is observed for the k–ε, k-ω *SST*, and Transition *SST* turbulence models: along the pipe's length, the hot coolant's temperature drops and the cold coolant's temperature rises of the pipe. In the countercurrent mode of movement of heat carriers, intensive heating of oil is observed compared to direct flow, which indicates a higher efficiency of the countercurrent circuit of the heat exchanger. The Transition *SST* model shows the greatest heating of the cold coolant in both modes, while the k–ε model demonstrates a smooth and linear behavior of the temperature profile.

In addition, the k-ω *SST* model most effectively identifies the laminar-turbulent transition that occurs in the range of 3-3.5 m from the inlet section and is confirmed by changes in key parameters such as the Reynolds number, heat transfer coefficient and coefficient of friction.

Conflict of interest statement
The authors declare that they have no conflict of interest in relation to this research, whether financial, personal, authorship or otherwise, that could affect the research and its results presented in this paper.

CRediT author statement
Volkov K.N.: Methodology, Conceptualization, Resources; **Jaichibekov N.Zh.:** Supervision, **Calculation** methods, Validation; **Zhumanbayeva A.S.:** Investigation, Data curation, Writing – review & editing; **Kurmanova D.E.:** Visualization, Formal analysis, Writing – original draft. The final manuscript was read and approved by all authors.

Acknowledgments
The authors express their sincere gratitude for the administrative and technical support provided during the implementation of this study: L.N. Gumilyov Eurasian National University and Kingston University (London, UK).

References

1 Kurmanova D.Y., Jaichibekov N.Zh., Karpenko A.G., Volkov K.N. (2023) Numerical modeling and calculation of heat transfer between heat carriers in heat exchangers. *Bulletin of Karaganda University. Physics Series,* 109(1), 59–70. https://doi.org/10.31489/2023ph1/59-70

2 Kurmanova D., Jaichibekov N., Karpenko A., Volkov K. (2023) Modelling and simulation of heat exchanger with strong dependence of oil viscosity on temperature. *Fluids,* 8(95), 1-18. https://doi.org/10.3390/fluids8030095

3 Barilovich V.A., Smirnov Yu.A. (2010) *Fundamentals of technical thermodynamics and theory of heat and mass transfer: a course of lectures*, St.Petersburg, Russia, 338. [in Russian] https://elib.spbstu.ru/dl/1976.pdf/view

4 Karar O., Emani S., Gounder S.M., Myo Thant M.M., Mukhtar H., Sharifpur M., & Sadeghzadeh M. (2021) Experimental and numerical investigation on convective heat transfer in actively heated bundle-pipe. *Engineering Applications of Computational Fluid Mechanics,* 15(1), 848-864. https://doi.org/10.1080/19942060.2021.1920466

5 Rana S., Zunaid M., Kumar R. (2022) CFD approach for the enhancement of thermal energy storage in phase change material charged heat exchanger. *Case Studies in Thermal Engineering*, 33, 101921. https://doi.org/10.1016/j.csite.2022.101921

6 Borse D., Bute J.V. (2018) A review on helical coil heat exchanger. *International Journal for Research in Applied Science and Engineering Technology,* 6, 492–497. https://doi.org/10.22214/ijraset.2018.2070

7 Inyang U., Uwa I. (2022) Heat transfer in helical coil heat exchanger. *Advances in Chemical Engineering and Science,* 12, 26–39. https://doi.org/10.4236/aces.2022.121003

8 Marzouk S.A., Al-Sood M.M., El-Said M.S., Younes M.M., & El Fakharany M.K. (2023) A comprehensive review of methods of heat transfer enhancement in shell and tube heat exchangers. *Journal of Thermal Analysis and Calorimetry,* 148, 7539–7578. https://doi.org/10.1007/s10973-023-12265-3

9 Coronel P, Sandeep K.P. (2008) Heat transfer coefficient in helical heat Exchangers under turbulent flow conditions. *International Journal of Food Engineering*, 4(1). https://doi.org/10.2202/1556-3758.1209

10 Inyang U., Uwa I. (2022) Heat transfer in helical coil heat exchanger. *Advances in Chemical Engineering and Science,* 12, 26–39. https://doi.org/10.4236/aces.2022.121003

11 Jayakumar J.S., Mahajani S.M., Mandal J.C., Vijayan P.K., & Bhoi R. (2008) Experimental and CFD estimation of heat transfer in helically coiled heat exchangers. *Chemical Engineering Research and Design*, 86(3), 221–232. https://doi.org/10.1016/j.applthermaleng.2016.04.037

12 Reddy N.S., Vishwanath K.C., Satheesha V., Thejaraju R., Raj K.N., Manoj M., Goutham H., & Manjunatha B.S. (2021) Study on heat transfer and pressure drop in tube-in-tube helical heat exchanger. *Journal of Applied Science and Engineering,* 24(4), 635–642. https://doi.org/10.6180/jase.202108_24(4).0019

13 Prabhanjan D.G., Raghavan G.S.V., Rennie T.J. (2002) Comparison of heat transfer rates between a straight tube heat exchanger and a helically coiled heat exchanger. *International Communications in Heat and Mass Transfer,* 29(2), 185–191. https://doi.org/10.1016/S0735-1933(02)00309-3

14 Liu Y., Rao Y., Weigand B. (2019) Heat transfer and pressure loss characteristics in a swirl cooling tube with dimples on the tube inner surface. *International Journal of Heat and Mass Transfer,* 128(2), 54–65. https://doi.org/10.1016/j.ijheatmasstransfer.2018.08.097

15 Kurnia J.C., Sasmito A.P., Shamim T., Mujumdar A.S. (2016) Numerical investigation of heat transfer and entropy generation of laminar flow in helical tubes with various cross sections. *Applied Thermal Engineering,* 102, 849–860. https://doi.org/10.1016/j.applthermaleng.2016.04.037

16 Eliseev V.V., Vetyukov Yu.M., Zinovieva T.V. (2011) Divergence of a helicoidal shell in a pipe with flowing liquid. *Journal of Applied Mechanics and Technical Physics,* 52, 450–458. https://doi.org/10.1134/S002189 4411030151

17 Morales R.E., Rosa E.S. (2007) Modeling of free surface flow in a helical channel with finite pitch. *Journal of the Brazilian Society of Mechanical Sciences and Engineering*, 29, 345–353. https://doi.org/10.1590/S167858782007000400002

18 Kelbaliev G.I., Rasulov S.R., Rzaev A.G., Mustafaeva G.R. (2017) Rheology of structured oils. *Journal of Engineering Physics and Thermophysics,* 90, 996–1002. https://doi.org/10.1007/s10891-017-1649-z

19 Yogesh S.S., Selvaraj A.S., Ravi D.K., Rajagopal T.K.R. (2018) Heat transfer and pressure drop characteristics of inclined elliptical fin tube heat exchanger of varying ellipticity ratio using CFD code. *International Journal of Heat and Mass Transfer,* 119, 26–39. https://doi.org/10.1016/j.ijheatmasstransfer.2017.11.094

20 Allouche,Y., Varga S., Bouden C., Oliveira A.C. (2016) Validation of a CFD model for the simulation of heat transfer in a tubes-in-tank PCM storage unit. *Renewable Energy,* 89, 371–379. https://doi.org/10.1016/j.renene.2015.12.038

21 Balaji D., Prakash L.S.S. (2016) CFD analysis of a pressure drop in a staggered tube bundle for a turbulent cross flow. *International Advanced Research Journal in Science, Engineering and Technology,* 3(2), 35–40. https://iarjset.com/upload/2016/february-16/IARJSET%209.pdf

22 Volkov K.N., Emelaynov V.N. (2012) *Computational technologies in problems of fluid and gas mechanics.* Moscow, 468. [in Russian] https://books.google.kz/books/about/%D0%92%D1%

23 Chen K., Mohammed H.I., Mahdi J.M., Rahbari A., Cairns A., & Talebizadehsardari P. (2022) Effects of non-uniform fin arrangement and size on the thermal response of a vertical latent heat triple-tube heat exchanger. *Journal of Energy Storage,* 45, 103723. https://doi.org/10.1016/j.est.2021.103723

24 Czarnota T., Wagner C. (2016) Turbulent convection and thermal radiation in a cuboidal Rayleigh–Binard cell with conductive plates. *International Journal of Heat and Fluid Flow,* 57, 150–172. https://doi.org/10.1016/j.ijheatfluidflow.2015.10.006

25 Mohanan A.K., Prasad B.V., Vengadesan S. (2020) Flow and heat transfer characteristics of a cross-flow heat exchanger with elliptical tubes. *Heat Transfer Engineering,* 42(21), 1–15. https://doi.org/10.1080/01457632.2020.1826742

26 Sakipova S.E., Shaimerdenova K.M., Nussupbekov B.R., Ospanova D.A., Kutum B.B. (2023) Modeling the dynamics of heat and mass transfer processes in a tubular heat exchanger under pulsed influences. *Eurasian Physical Technical Journal,* 1(43), 51-55. https://doi.org/10.31489/2023No1/51-55

27 Erik Dick, Slawomir Kubacki. (2017) Transition Models for Turbomachinery Boundary Layer Flows: A Review. *International Journal of Turbomachinery, Propulsion and Power,* 2(2), 1-45. https://doi.org/10.3390/ijtpp2020004

28 Niangi Li, Jian Chen, Tao Cheng, Jiří Jaromír Klemeš, Petar Sabev Varbanov, Qiuwang Wang, Weisheng Yang, Xia Liu, Min Zeng (2020) Analysing thermal-hydraulic performance and energy efficiency of shell-and-tube heat exchangers with longitudinal flow based on experiment and numerical simulation. *Energy,* 202, 117757. https://doi.org/10.1016/j.energy.2020.117757

AUTHORS' INFORMATION

Zhumanbayeva, Aizhan Serikovna – Doctoral graduate, Senior lecturer, Faculty of Mechanics and Mathematics, L.N. Gumilyov Eurasian National University, Astana, Kazakhstan; Scopus Author ID: 59328973500; https://orcid.org/0009-0007-2725-3672l; jas968@mail.ru

Volkov, Konstantin Nikolaevich – Doctor of Physical and Mathematical Sciences, Senior lecturer, Faculty of Science, Engineering and Computing, Kingston University, London, UK; Scopus Author ID: 8663950000; https://orcid.org/0000-0001-6055-2323; k.volkov@kingston.ac.uk

Jaichibekov Nurbulat Zhumabekovich – Doctor of Physical and Mathematical Sciences, Professor, Faculty of Mechanics and Mathematics, L.N. Gumilyov Eurasian National University, Astana, Kazakhstan; Scopus Author ID: 57195809348; WoS Researcher ID: A-2780-2015 ; https://orcid.org/0000-0002-3053-8288; jaich@mail.ru

Kurmanova Dinara Esentayevna – Ph.D, Senior lecturer, Faculty of Mechanics and Mathematics, L.N. Gumilyov Eurasian National University, Astana, Kazakhstan; Scopus Author ID: 58163166200; https://orcid.org/0009 0009-9787-7426; dikonya89_29@mail.ru

EURASIAN PHYSICAL TECHNICAL JOURNAL

2026, Volume 23, No. 1(55)

https://doi.org/10.31489/2026N1/113-120

Received: 25/11/2025 Revised: 06/03/2026 Accepted: 19/03/2026

Research Article

UDC 532.5

DYNAMIC MODELING AND SURFACE INTEGRITY OPTIMIZATION OF LOW-FREQUENCY HYDRAULIC IMPULSE SYSTEMS

Smakova N.[1], Pankov S.[2], Baisadykov B.[2], Zelenkov V.[2], Toibazarov D.[2], Karypov A.A.[3]

[1] Kazakh University of Technology and Business named after K. Kulazhanov, Astana, Kazakhstan
[2] National Defense University of the Republic of Kazakhstan, Astana, Kazakhstan
[3] LLP "Scientific and Technical Center Almaty Special Design Bureau «Alatau», Almaty, Kazakhstan
Corresponding author: nuri_5@mail.ru

Abstract. *This study investigates the dynamic behavior and surface integrity optimization of low-frequency hydraulic impulse systems operating under cyclic loading conditions. Particular attention is paid to the performance of the hydraulic module rod, which is subjected to repeated dynamic impacts during system operation. The influence of surface roughness, residual stresses, and microhardness on vibration stability and durability of friction pairs is analyzed. A dynamic mathematical model describing pressure variation, piston motion, and energy transfer within the hydraulic impulse chamber is developed. The model is implemented in the MATLAB/Simulink simulation environment for numerical analysis of transient processes. Experimental studies were conducted on cylindrical rod-type specimens made of 30KhGSA alloy steel processed using rotary multi-blade turning technology. The experimental results demonstrate that optimization of machining parameters significantly improves surface quality and reduces vibration amplitude of the hydraulic impulse system. The proposed modeling approach enables prediction of system dynamic behavior and provides a basis for improving operational stability. The obtained results confirm that the integration of advanced machining technologies with digital modeling tools can increase the reliability and efficiency of hydraulic impulse systems used in industrial applications.*

Keywords: Hydraulic impulse system, mechanical processing, surface roughness, dynamic load, mathematical modeling, system stability.

1. Introduction

Hydraulic impulse systems operate by converting the impulse energy of a working fluid into mechanical work within an extremely short period of time [1]. This conversion process is governed by the fundamental equations of hydrodynamics, including the momentum conservation equations, Bernoulli's law, and the equations of motion of an incompressible fluid. During operation, a sharp pressure gradient dp/dt is generated in the pulse chamber of the hydraulic system. The magnitude of this gradient c is determined by the inertial properties of the working fluid and the propagation velocity of the pressure wave

$$c = \sqrt{\frac{K}{\rho}}$$

where K is the bulk modulus of the fluid and ρ is its density.

According to [2], cyclic variable loads arising during hydraulic impacts lead to a complex stress state in the rod of the hydraulic vibration module. These stresses can be described using Hooke's law, Hertz contact theory, and σ–N fatigue diagrams. Repeated cyclic loading causes plastic deformation of the rod material, which significantly influences its durability and operational reliability.

The quality of machining, including surface roughness, microstructure of the surface layer, and residual stresses, plays an important role in the efficiency of energy transfer in hydraulic impulse systems. As shown in the work [3], rotational friction processing leads to the formation of local temperature fields described by Fourier's heat conduction equation. These thermal processes promote the formation of a strengthened surface layer with increased microhardness due to recrystallization phenomena.

In recent years, the development of hydraulic impulse systems has increasingly involved digital modeling approaches. The concept of a digital twin, introduced [4], and further developed in the work [5], links changes in dynamic system parameters with fundamental physical laws governing pressure, velocity, momentum, and temperature distributions in space and time. [6] proposed a mathematical model of a hydro-impulse mechanism based on the Navier–Stokes equations, taking into account viscosity effects, turbulence, and the rate of pressure change in the working chamber. In the [7], the elasticity of the chamber walls was considered, requiring the use of wave equations describing the interaction between solid bodies and fluids. Work [8] analyzed the dynamics of multi-mass impulse systems using Lagrange equations of the second kind, considering stability factors such as damping coefficients, stiffness parameters, and inertial characteristics of the system elements. [9] investigated optimization of hydraulic system parameters in construction machinery based on energy balance equations $W_p = p \cdot V$ and pressure loss relations losses $\Delta p = f(\lambda, L/D)$, where λ is the friction coefficient and L/D represents the geometric characteristics of the flow channel. These parameters significantly affect the amplitude and frequency of pressure pulses in hydraulic impulse systems. The physical mechanisms of surface strengthening during finishing operations are described in [10, 11]. Induction hardening is based on the interaction between high-frequency electromagnetic fields and the metal surface layer, where Foucault currents generate heat according to Joule–Lenz's law. Subsequent rapid cooling leads to martensitic transformations that improve the mechanical properties of the material.

Thermo-frictional processing methods investigated [12–14] were numerically modeled using the ANSYS Workbench software environment. These models describe the distribution of temperature fields, stresses, heat flows, and deformations using the Fourier–Kirchhoff heat conduction equations and the von Mises plasticity criterion. [15] demonstrated that the dynamic behavior of hydraulic impulse systems is determined by the laws of conservation of energy and momentum. In this context, the elastic properties of the working elements play an important role, influencing the natural frequency of the system ω according to the relation

$$\omega = \sqrt{\frac{k}{m}},$$

where k is the stiffness coefficient and m is the mass of interacting elements.

Despite the significant number of studies devoted to hydraulic impulse systems, several important aspects of their operation remain insufficiently explored. In particular, the relationship between the surface integrity of critical mechanical components and the dynamic stability of low-frequency hydraulic impulse mechanisms has not yet been fully clarified. Most existing studies focus either on hydrodynamic processes occurring in the working chamber or on the mechanical properties of individual structural elements. However, in real operating conditions these factors interact simultaneously and significantly influence the overall performance of the system. Surface quality parameters, including roughness, residual stresses, and microstructural changes formed during machining, may directly affect vibration behavior, friction conditions, and the efficiency of energy transfer within the hydraulic impulse chamber. Nevertheless, the combined influence of machining quality, dynamic loads, and hydraulic parameters on system stability has not been sufficiently investigated. At the same time, the rapid development of digital technologies creates new opportunities for advanced modeling and optimization of complex hydraulic systems. Modern simulation environments make it possible to analyze transient processes, predict system behavior under variable loads, and evaluate the influence of technological parameters on system performance.

Therefore, the objective of this research is to investigate the physical and mechanical factors affecting the operation of low-frequency hydraulic impulse systems and to develop a dynamic model for analyzing their operating parameters. Particular attention is paid to the influence of surface integrity and machining technologies on vibration stability and energy efficiency of hydraulic impulse mechanisms. The scientific substantiation of operating parameters for complex engineering systems is an important research problem in modern applied mechanics and instrumentation [16].

2. Methodology and experimental section

In order to investigate the dynamic behavior of the hydraulic impulse system and evaluate the influence of machining parameters on the operational stability of the mechanism, a combined experimental and numerical research methodology was applied. The methodological framework of the study includes experimental investigation of the surface integrity of the hydraulic module rod, development of a mathematical model describing the dynamic interaction of hydraulic and mechanical elements, and numerical simulation of transient processes in the working chamber. The experimental part of the research was aimed at determining the influence of machining parameters on surface roughness and mechanical properties of the processed components. At the same time, the mathematical model was developed to describe pressure variations, piston motion, and energy transfer processes occurring in the hydraulic impulse chamber during cyclic loading. Numerical simulations were performed to analyze the dynamic response of the system and to identify the optimal operating parameters ensuring stable operation of the hydraulic impulse mechanism.

Such an integrated methodological approach allows combining theoretical modeling with experimental validation, which significantly increases the reliability of the obtained results and provides a deeper understanding of the physical processes occurring in low-frequency hydraulic impulse systems.

2.1. Object and experimental equipment

The research was carried out on cylindrical *"rod-type"* specimens with a diameter of 60 mm and a length of 120 mm, made of alloy steel 30KhGSA, which provides high strength and heat resistance. Machining was performed using the multi-blade rotary turning method, which reduces the thermal load in the cutting zone and ensures uniform wear of the cutting edges [16]. The operating parameters were selected experimentally within the following ranges: $n = 600–900$ rpm, $S = 0.10–0.30$ mm/rev, $t = 0.50–1.00$ mm. The average surface roughness R_a is determined by the formula:

$$R_a = \frac{1}{L}\int_0^L |y(x)|dx,$$

where $y(x)$is the deviation of the surface profile from the mean line and L is the sampling length.

The obtained Ra values ranged from 0.63 to 1.25 μm, confirming the efficiency of rotary turning compared to classical longitudinal cutting [17-18]. To ensure reliability of the obtained experimental results, each measurement was repeated five times. The average values of the measured parameters were used for further analysis. Statistical processing of the experimental data was performed using standard deviation and confidence interval estimation methods.

2.2. Mathematical Model of the Hydraulic Impulse System

The system dynamics are described by a set of motion equations for the working piston, taking into account damping and the variable pressure in the chambers:

$$M\frac{d^2x}{dt^2} + C\frac{dx}{dt} + Kx = P_A(t) - P_B(t) - F_c,$$

where: M – equivalent mass of the moving elements; C – viscous damping coefficient; K – stiffness of the return spring; P_A(t), P_B(t) – pressures in the working and return chambers; F_c – friction and sealing losses. The chamber pressures are defined as:

$$P_A(t) = P_0 + \rho c\frac{dx}{dt}, P_B(t) = P_0 - \rho c\frac{dx}{dt},$$

where ρ is the fluid density and c is the speed of sound in the medium.

The energy of a single impact is given by:

$$E = \frac{1}{2}Mv^2,$$

where $v = \frac{dx}{dt}$ is the piston velocity at the moment of impact.

During optimization, the system aims to minimize the loss function:

$$J = min \int_0^T [(P_A - P_B)^2 + \alpha v^2]\, dt,$$

where α is a weighting coefficient representing energy losses.

2.3. Digital simulation

The model was implemented in MATLAB/Simulink and Python SciPy, using the fourth-order Runge–Kutta integration method to solve the system of differential equations numerically [19].

The boundary conditions were defined as:

$$x(0) = 0, v(0) = 0, P_A(0) = P_B(0) = P_0 = 10 \text{ MPa}.$$

Based on the results, dependencies of x(t), v(t), and P(t) were obtained, along with the dynamic force diagrams. Model verification was carried out by comparing the experimental vibration and pressure data with the calculated curves (see Fig. 3).

2.4. Parameter Optimization Algorithm

At the cognitive layer of the digital twin, a combination of Gradient Descent and Random Forest Regressor algorithms was applied to identify parameters that ensure minimum surface roughness under acceptable load conditions [19]. The optimization function was defined as:

$$\Phi = w_1 \frac{R_a}{R_{a,ref}} + w_2 \frac{P_{max}}{P_{ref}} + w_3 \frac{A_{vib}}{A_{ref}} \to min,$$

where $w_1, w_2, w_3$are the weighting coefficients for quality criteria; R_a is the surface roughness; $P_{max}$is the maximum pressure; and $A_{vib}$is the vibration amplitude.

The minimum of the objective function was reached at: $n = 860$ rpm, $S = 0.21$ mm/rev, $t = 0.70$ mm. Under these conditions, a balance is achieved between surface quality and hydraulic pulse stability.

2.5. Hardware–software Implementation

To synchronize the physical object with the virtual model, the MQTT protocol was employed, enabling real-time data exchange between sensors (pressure, temperature, vibration) and the simulation system. The data flow was visualized using the Node-RED Dashboard, while the computational results were automatically updated in MATLAB Live Script [20-21].

3 Results and discussion

The obtained results indicate that the dynamic stability of the hydraulic impulse system is significantly influenced not only by hydraulic parameters but also by the quality of mechanical processing of the working elements. In particular, the surface condition of the rod plays an important role in the formation of friction forces and vibration behavior of the system during cyclic loading. Improved surface integrity contributes to a more uniform distribution of stresses and reduces the probability of local stress concentration zones.

The experimental data confirm that optimization of machining parameters leads to a noticeable improvement in the operational characteristics of the hydraulic impulse mechanism. When the optimal cutting conditions were applied, the surface roughness decreased, which resulted in a reduction of friction losses and more stable piston motion in the hydraulic chamber. As a consequence, the energy transfer efficiency between the hydraulic and mechanical subsystems increased. The numerical simulation results also demonstrate that the proposed mathematical model adequately describes the transient processes occurring in the hydraulic impulse chamber. The calculated pressure fluctuations and piston displacement curves show good agreement with experimental observations. This confirms the applicability of the developed model for analyzing the dynamic behavior of similar hydraulic systems operating under cyclic impulse loading conditions.

In addition, the application of digital modeling tools makes it possible to analyze the influence of technological and operational parameters at the design stage of hydraulic equipment. This approach significantly reduces the need for expensive experimental testing and allows engineers to evaluate different operating scenarios before implementing the system in real industrial conditions. The research results confirmed the effectiveness of integrating a digital twin with a physical hydraulic pulse module. During the work, a three-level system structure was built (see Fig. 1), combining mechanical, hydraulic, and cognitive levels.

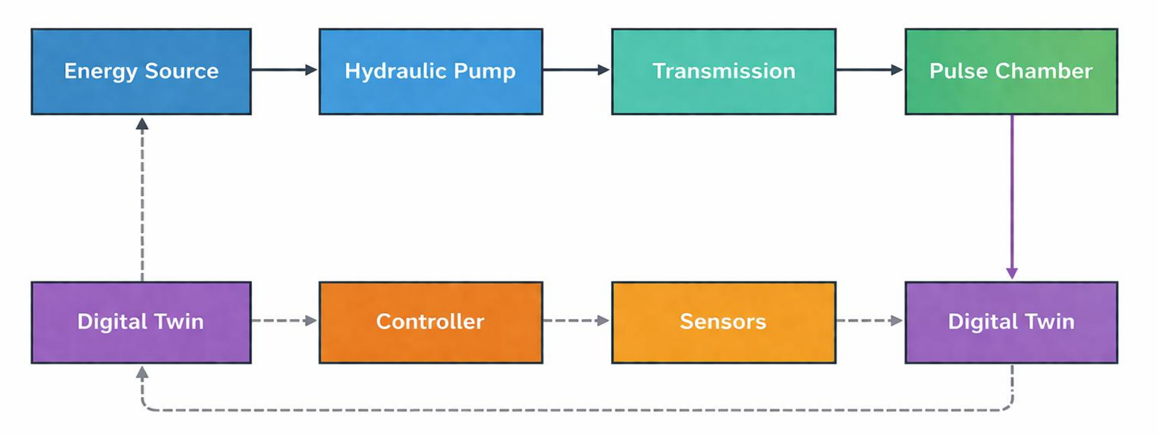

Fig. 1. Architecture of a hydraulic pulse module with a digital twin system (energy source – hydraulic pump – transmission – pulse chamber – sensors – controller – digital twin)

In the experimental part, the optimal parameters for rotary turning of the rod were determined (speed n = 870 rpm, feed S = 0.23 mm/rev, depth t = 0.75 mm). The obtained data were processed and visualized as a three-dimensional dependence of roughness on cutting parameters (Fig. 2).

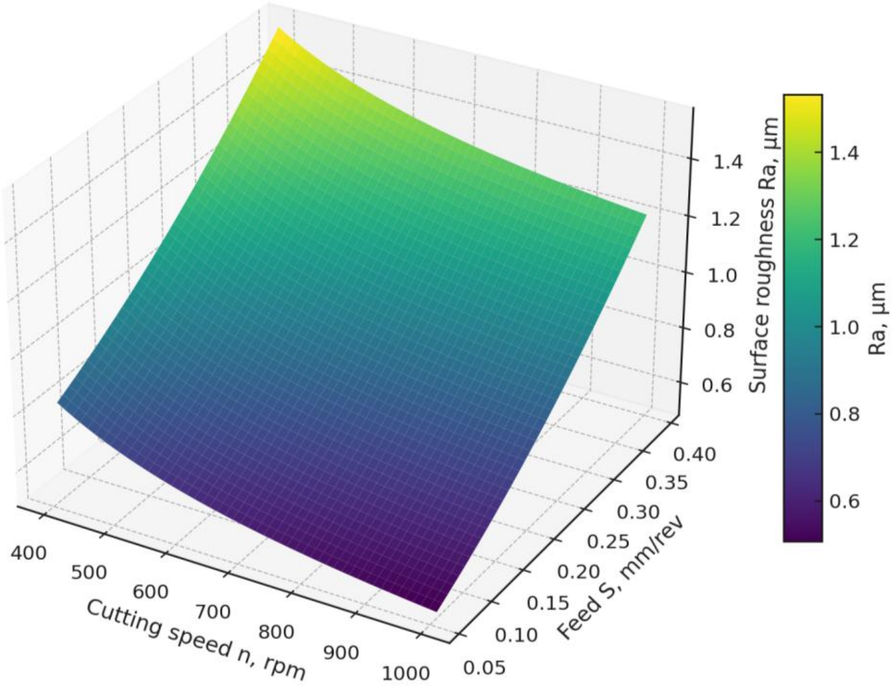

Fig. 2. Dependence of surface roughness Ra on speed n and feed S (the 3D graph shows the minimum Ra values in the range of high speeds and low feeds)

Numerical modeling has shown that the use of digital control significantly reduces pressure fluctuations in the working chamber (Fig. 3). The classic system exhibits increased pulsation, whereas when using a digital twin, the fluctuations stabilize with rapid attenuation [22].

Analysis of vibration activity showed that optimization of parameters led to a reduction in vibration amplitude by approximately 22% (Fig. 4). This reduces dynamic loads and extends the service life of the equipment.

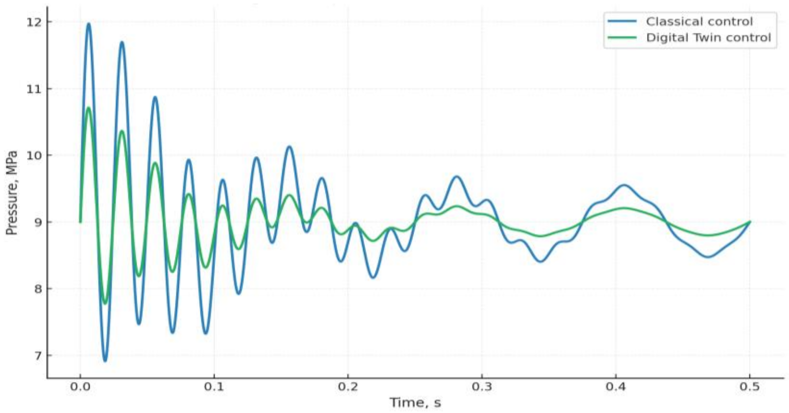

Fig. 3. Pressure changes in the pulse chamber over time (comparison of classic and digital control)

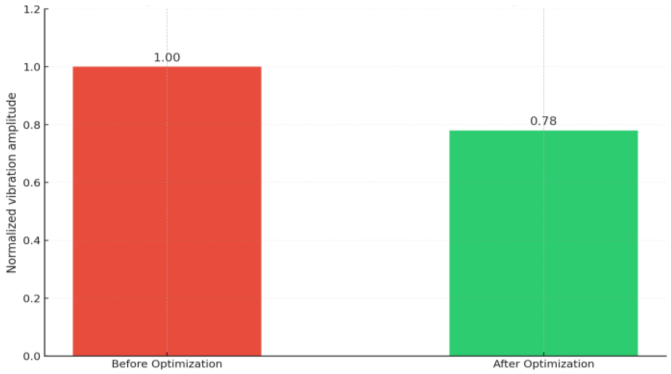

Fig. 4. Vibration amplitude before and after optimization (Digital Twin)
(After implementing the digital twin, the amplitude decreases from 1.00 to 0.78 units.)

To verify the strength of the structure, stress distribution along the rod was calculated (Fig. 5). The highest values are observed in the fastening area and transition sections, which corresponds to the results of calculations in ANSYS Workbench [23].

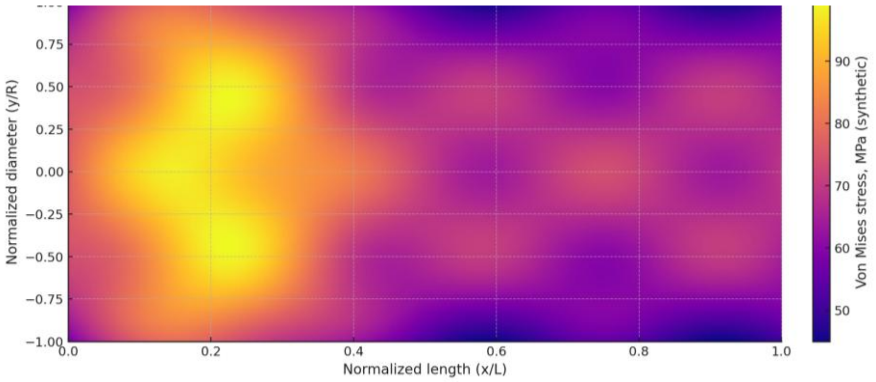

Fig. 5. Stress distribution along the rod (numerical simulation results)
(Red areas – zones of maximum stress, blue areas – zones of minimum stress)

Overall, the results showed that the use of a digital twin can reduce peak pressures by 15–18%, improve surface quality by ≈20%, reduce system vibration activity, and optimize the energy balance between hydraulic and mechanical elements. The developed model confirms the possibility of implementing intelligent control of hydraulic impulse systems with real-time parameter prediction [24-26].

4. Conclusion

This study presents a comprehensive approach to improving the performance and reliability of hydraulic impulse systems through the integration of intelligent digital twin technology and advanced machining optimization methods. The combination of rotary multi-blade turning and adaptive numerical modeling enabled achieving high surface quality (Ra = 0.63~μm) and uniform strengthening of working surfaces.

The developed mathematical and digital models accurately reproduced the system's transient dynamics, with less than 5 % deviation between experimental and simulated data. The results confirmed that real-time synchronization between the physical and virtual modules provides stable control of pressure and vibration parameters during operation. The adaptive correction algorithms embedded into the digital twin allowed continuous self-learning and optimization of system parameters under variable external loads. This approach ensured energy-efficient operation, reduced vibration amplitude by 22 %, and improved the service life of mechanical components. The obtained outcomes indicate that combining digital twin technologies, AI-based parameter optimization, and rotary machining can significantly enhance the operational stability of hydraulic impulse systems. The developed methodology can be further extended to other classes of dynamic hydraulic machines, including impact drilling and high-frequency vibration systems, supporting the transition toward intelligent, data-driven manufacturing environments. The obtained results demonstrate that the proposed approach can significantly improve the operational stability and efficiency of low-frequency hydraulic impulse systems and can be applied for further optimization and digital monitoring of hydraulic equipment in engineering practice.

Conflict of interest statement

The authors declare that they have no conflict of interest in relation to this research, whether financial, personal, authorship or otherwise, that could affect the research and its results presented in this paper.

CRediT author statement

Smakova N.: Conceptualization, Methodology, Writing – original draft, Supervision; **Pankov S.:** Investigation, Data curation; **Baisadykov B.:** Experimental validation; **Zelenkov V.:** Software, Modeling; **Toibazarov D.:** Visualization, Data analysis; **Karypov A.:** Resources, Technical support. The final manuscript was read and approved by all authors.

Funding:

This research was carried out within the framework of the scientific project IRN AR196079/0222 "Prospective appearance of the troop control system considering the creation of mobile command posts in accordance with the paradigm of network-centric warfare." The work was funded by the Science Committee of the Ministry of Science and Higher Education of the Republic of Kazakhstan.

References

1 Smirnov Y.M., Uraimov M., Smakova N.S. (2019) Mathematical model of hydraulic manipulators of impulse machines. *Proceedings of the University*, (1), 18–22 Available at: http://tu.kstu.kz/archive/issue/11 [in Russian]

2 Glotov, B.N., Kokenova, A.T., Smagina, V.S. (2015) Classification of hydraulic hand hammers. *Applied Research Journal*, (5), 385–388. Available at: https://s.applied-research.ru/pdf/2015/2015_05_3.pdf [in Russian]

3 Sherov K. T., Sikhimbayev M. R., Donenbayev B. S. (2017) Experimental research of rotational-and-frictional boring of big holes in large parts. *Journal of Theoretical and Applied Mechanics,* 47, 2, 67–74. https://doi.org/10.1515/jtam-2017-0018

4 Grieves M., Vickers J. (2017) Digital twin: Mitigating unpredictable, undesirable emergent behavior in complex systems. Springer https://doi.org/10.1007/978-3-319-38756-7_8

5 Lee J., Davari H., Singh J., Pandhare V. (2020) Industrial AI and digital twins for smart manufacturing. *Robotics and Computer-Integrated Manufacturing*, 61. https://doi.org/10.1016/j.rcim.2020.102095

6 Saruev, L.A., Ziyakaev, G.R., & Pashkov, E.N. (2011) Mathematical modeling of the hydro-impulse mechanism of drilling machines. *Mining Informational and Analytical Bulletin*. https://cyberleninka.ru/article/n/matematicheskoe-modelirovanie-gidroimpulsnogo-mehanizma-burilnyh-mashin [in Russian]

7 Gorodilov L.V. (2013) Analysis of the dynamics of two-way hydropercussion systems. II. Influence of design factors and their interaction with rocks. *Journal of Mining Science*, 49(3), 465–474. https://doi.org/10.1134/S1062739149030143

8 Shcherbakov, V.S., & Galdin, V.N. (2010) Modeling of hydraulic impulse systems. *Bulletin of VSTU*. Available at: https://cyberleninka.ru/article/n/modelirovanie-gidravlicheskih-impulsnyh-sistem [in Russian]

9 Galdin N.S., Galdin V.N., & Egorova N.N. (2013) Optimization synthesis of main parameters of hydraulic impulse systems of construction machines. *Bulletin of SibADI*. Available at: https://cyberleninka.ru/article/n/optimizatsionnyy-sintez-osnovnyh-parametrov-gidravlicheskih-impulsnyh-sistem-stroitelnyh-mashin [in Russian]

10 Skiba, V.Yu. (2021) Improving the efficiency of machine part processing by integrating abrasive grinding and induction hardening. *NSTUJ*. Available at: https://journals.nstu.ru/files/articles/ flash/27364/2/ [in Russian]

11 Skeeba V., Pushnin V., Erohin I. (2015) Numerical modeling of steel surface hardening by high-frequency currents. *Applied Mechanics and Materials*, 698, 288–292. https://doi.org/10.4028/www.scientific.net/AMM.698.288

12 Sherov K. T., Sikhimbayev M. R., Sherov A. K. (2017) Mathematical modeling of thermo-frictional milling using ANSYS Workbench. *Journal of Theoretical and Applied Mechanics*, 47(3), 34–42. https://doi.org/ 10.1515/jtam 2017-0008

13 Khodzhibergenov D.T., Esirkepov A., Sherov K.T. (2015) Rational milling of metals. *Russian Engineering Research*, 35, 15–19. https://doi.org/10.3103/S1068798X1501013X

14 Sherov K.T., Nasad T.G., Absadykov B.N. (2020) Reliability of cutting blades for thermo-frictional processing. *News of the National Academy of Sciences of the Republic of Kazakhstan.* https://doi.org/10.32014/2020.2518-170X.15 [in Russian]

15 Smakova N.S., Smirnov Y.M., Kenjin B.M., & Zhurunova M.A. (2020). Optimal control of operating modes of hydraulic impact actuators of mining machines. *Mining Informational and Analytical Bulletin*, (6), 95–104. https://doi.org/10.25018/0236-1493-2020-6-0-95-104

16 Geng H., Zhao J., Wang J. (2021) Digital twin-based real-time monitoring and fault diagnosis for hydraulic systems. *Chinese Journal of Mechanical Engineering*, 34. https://doi.org/10.1186/s10033-021-00640-8

17 Zhang Y., Zhou D., Li Z. (2023) Adaptive control of nonlinear hydraulic actuators using neural networks. *ISA Transactions*, 129, 362–375. https://doi.org/10.1016/j.isatra.2022.08.045

18 Wang X., Li Q., Chen L. (2023) Optimization of hydraulic impulse systems based on machine learning algorithms. *Mechanical Systems and Signal Processing*, 198.https://doi.org/10.1016/j.ymssp.2023.110520

19 Zhang H., Liu Y., Sun C. (2023) Simulation and experimental study of hydraulic impulse energy conversion. *Journal of Mechanical Science and Technology*, 37, 2, 891–903. https://doi.org/10.1007/s12206-023-0142-2

20 Zhao W., Chen J., Hu Y. (2023) Hybrid modeling and prediction of hydraulic cylinder performance using digital twin framework. *Applied Sciences*, 13, 4. https://doi.org/10.3390/app13042586

21 Li H., Yu X., Ren J. (2023) Research on energy-saving control of hydraulic systems based on digital twin technology. *Sensors*, 23, 1. https://doi.org/10.3390/s23010345

22 Liu P., Xie X., Zhang C. (2022) Machine learning-based optimization for hydraulic pump efficiency. *Energies*, 15, 19. https://doi.org/10.3390/en15197221

23 Xu H., Tian L., Sun W. (2023) Modeling and optimization of hydraulic impulse systems using MATLAB/Simulink. *Intern. J. of Dynamics and Control*, 11, 1152–1164. https://doi.org/10.1007/s40435-023-01231-8

24 Chen R., Gao D., Wu Z. (2023) Deep learning for fault prediction in hydraulic systems. *IEEE Access*, 11, 65903–65915. https://doi.org/10.1109/ACCESS.2023.3298765

25 Smakova N.S., Sherov K.T., Tusupova S.O., Buzauova T.M. (2020) The research of micro-hardness of side surfaces of teeth cylindrical wheels processed by “Shaver-Rolling Device”. *Journal of Theoretical and Applied Mechanics*, 50, 1, 50–56. https://doi.org/10.1515/jtam-2020-0006

26 Zhantlesov E.Zh., Gruzin V.V., Togusov A.K., Zhusupbekov T.Kh., Zhantlesov Zh.K. (2024) Scientific and technical substantiation of the parameters of the radiolocation device for the detection of prohibited items. *Eurasian phys. tech. j.*, 21, 3 (49), 93–98. https://doi.org/10.31489/2024No3/93-98

AUTHORS’ INFORMATION

Smakova, Nurgul Serikovna – PhD, Associate Professor, Kazakh University of Technology and Business named after K. Kulazhanov, Astana, Kazakhstan: https://orcid.org/0009-0002-5754-4001; nuri_5@mail.ru

Pankov, Sergey Vladimirovich – Candidate of Military Sciences, Professor, Leading researcher, National Defense University of the Republic of Kazakhstan, Astana, Kazakhstan; https://orcid.org/0000-0003-3764-3192; sergey.pankov@ndu.kz.

Baisadykov, Bahyt Zhumashevich – PhD, Teacher, National Defense University of the Republic of Kazakhstan, Astana, Kazakhstan; https://orcid.org/0000-0003-9234-5945; bahyt.baisadykov@ndu.kz.

Zelenkov, Valeriy Viktorovich – PhD, Department head, National Defense University of the Republic of Kazakhstan, Astana, Kazakhstan; https://orcid.org/0009-0005-4381-8384; valeriy.zelenkov@ndu.kz.

Toibazarov, Daulet Oralbekovich – PhD, Associate Professor, Senior researcher, National Defense University of the Republic of Kazakhstan, Astana, Kazakhstan; https://orcid.org/0009-0000-9135-7360; aldar-kose1@yandex.ru

Karypov, Andrey Andreevich – Candidate of Military Sciences, Chief Specialist, Scientific and Technical Center Almaty Special Design Bureau “Alatau” (LLP “STC ASDB Alatau”), Almaty, Kazakhstan; https://orcid.org/0009-0004-9404-8220; a_kar@bk.ru

EURASIAN PHYSICAL TECHNICAL JOURNAL

2026, Volume 23, No. 1(55)

https://doi.org/10.31489/2026N1/121-129

Received: 11/10/2025 Revised: 09/02/2026 Accepted: 19/03/2025

Research Article

UDC 539.14

INVESTIGATION OF ALPHA DECAY HALF-LIFE USING QUANTUM TUNNELING MODELS IN HEAVY NUCLEI

Kareem N.M.[1], Khalf Ya.S.[1], Khalaf, Saif Ali J.[2], Ahmed E.M.[3]

[1] College of Science, University of Mustansiryah, Baghdad, Iraq
[2] College of Science, University of Baghdad, Baghdad-Iraq
[3] College of Basic Education, Mustansiriyah University, Baghdad, Iraq

*Corresponding author: noor.m97@uomustansiriyah.edu.iq

Abstract. *Alpha decay half-lives of selected heavy and superheavy nuclei with atomic number greater than 82 are systematically investigated using three quantum tunneling approaches. The calculated half-lives are compared with evaluated experimental data compiled in international nuclear data libraries. The predictive performance of each approach is assessed using the root-mean-square deviation of the logarithm of half-life values. The analysis indicates that the model based on Coulomb interaction with nuclear surface proximity effects provides the closest overall agreement with experimental values, with a deviation of 0.46 in logarithmic units. The unified fission-type approach shows intermediate agreement with a deviation of 0.63, while the semiclassical tunneling approximation shows the largest deviation of 0.88. These results highlight the importance of including nuclear surface proximity effects in barrier penetration calculations for reliable prediction of alpha-decay lifetimes in heavy and superheavy nuclei.*

Keywords: Alpha decay, Quantum tunneling, Heavy nuclei, Coulomb and Proximity Potential Model, Wentzel–Kramers–Brillouin, Unified Fission Model.

1. Introduction

Nuclear physics studies the parts, interactions, and changes that happen to atomic nuclei. Nuclear decay is a very important part of nuclear physics. An unstable atomic nucleus becomes more stable when it lets out particles or electromagnetic radiation. Alpha (α), beta (β), and gamma (γ) decay are the three types of nuclear decay [1–3]. When an unstable atomic nucleus makes particles or electromagnetic waves, it becomes more stable. This is what happens when nuclear decay happens. This change could happen in a number of ways, such as through alpha (α), beta (β), or gamma (γ) decay [4–5]. It takes energy away from the nucleus.

Nuclear decay processes, particularly alpha decay in heavy nuclei ($Z > 82$), play a fundamental role in determining nuclear stability and guiding the synthesis of superheavy elements [1–2]. Alpha decay occurs when an unstable nucleus emits an alpha particle (^{4}He), reducing its atomic number by 2 and mass number by 4. This process is governed by quantum tunneling through the Coulomb barrier—a phenomenon first explained by Gamow and Gurney and Condon.

Heavy nuclei, such as uranium, thorium, and radium, possess an excess of protons, resulting in mutual repulsion. These nuclei really need alpha decay. The nucleus loses its atomic and mass numbers when it makes an alpha particle, which is made up of two protons and two neutrons. This makes the nucleus more stable [6–8]. Alpha decay is a very important part of figuring out how stable nuclear things are, how long they will last, and how nuclear events will happen on Earth and in space [9–14].

Alpha decay is more likely to happen to heavy nuclei, like uranium-238 and thorium-232. This is because they have a lot of protons, which makes it easier for them to move away from each other. There are two protons and two neutrons in an alpha particle. The atomic number (Z) goes down by 2, and the mass number (A) goes down by 4:

α-decay: $_Z^A X \rightarrow _{Z-2}^{A-4} Y + _2^4 He$

For comparison, other decay processes include:

β^--decay: $_Z^A X \rightarrow _{Z+1}^A Y + e^- + \bar{\nu}_e$
β^+-decay: $_Z^A X \rightarrow _{Z-1}^A Y + e^+ + \nu_e$
γ-decay: $_Z^A X^* \rightarrow _Z^A X + \gamma$

The half-life ($T_{1/2}$) is the time required for half of a given sample of nuclei to decay, and it is mathematically related to the decay constant (λ) by:

$T_{1/2} = \ln(2) / \lambda$

Quantum tunneling has a lot to do with alpha decay. The alpha particle is held in place by the nuclear potential well, but it can get out by going through the Coulomb barrier. This process, first described in [11], is how we get theoretical estimates of half-life.

Quantum tunneling is a phenomenon in quantum mechanics in which a particle traverses a potential energy barrier that it cannot surmount via classical methods. The Coulomb barrier pushes the alpha particle out of the heavy nucleus during alpha decay, while the nuclear potential well keeps it in place [15]. Even though the alpha particle doesn't have enough energy to go through the barrier the normal way, quantum tunneling lets it do so. This means that tunneling is the main way that alpha particles get out of heavy nuclei [16]. Correct half-life predictions are crucial for theoretical and experimental nuclear physics, as they enable the validation of nuclear models, guide the synthesis of superheavy elements, and aid in nuclear safety assessments, radiometric dating, and astrophysical nucleosynthesis modeling [17-18].

Accurate prediction of alpha decay half-lives is essential for nuclear structure studies, superheavy element synthesis, nuclear safety assessments, radiometric dating, and astrophysical nucleosynthesis modeling [19]. Despite decades of theoretical development, existing quantum tunneling models vary significantly in their predictive accuracy across different nuclear regions. Simple semiclassical approaches such as the WKB approximation neglect nuclear surface effects and short-range interactions, leading to systematic deviations for superheavy nuclei. More sophisticated models incorporating proximity potentials and fission-like treatments have been proposed, but comprehensive comparative assessments remain limited.

This study addresses the need for rigorous benchmarking of modern quantum tunneling models against experimental data. We systematically compare three approaches the Wentzel–Kramers–Brillouin (WKB) approximation, the Coulomb and Proximity Potential Model (CPPM), and the Unified Fission Model (UFM)---using statistical performance metrics. Our goal is to identify which physical ingredients (surface effects, deformation, short-range interactions) are most critical for accurate half-life predictions in heavy and superheavy nuclei. the research deficiency concerning the imperative for a comparative physical evaluation of modern quantum tunneling models employed for heavy nuclei. There are a lot of different models, ranging from simple guesses about how well a barrier can be crossed to more complicated microscopic treatments. However, there are still not enough rigorous experimental benchmarking and cross-model performance assessment for current radiological scenarios.

Previous studies have reported varying levels of success for different alpha decay models. The WKB approximation, while computationally simple, has been shown to systematically overestimate half-lives for superheavy nuclei ($Z \geq 114$) due to its neglect of nuclear surface diffuseness and proximity effects [20–22]. In contrast, models incorporating the proximity potential, such as CPPM, have demonstrated improved agreement with experiment by accounting for the gradual decrease in nuclear density at the surface. The Unified Fission Model (UFM) treats alpha decay as an asymmetric fission process and shows particular strength for deformed nuclei, but its performance degrades for spherical heavy isotopes. Discrepancies between models arise primarily from differences in barrier shape parameterization, treatment of nuclear surface effects, and inclusion (or omission) of deformation and pairing corrections. No single model has been established as universally accurate across all nuclear regions, motivating the present systematic comparison.

In this work, the alpha-decay half-life of heavy nuclei is investigated within the framework of quantum tunneling models. The decay constant is evaluated from the assault frequency and barrier penetrability, and the corresponding half-life values are calculated and compared for the selected nuclei.

2. Methodology

2.1. Selection of Nuclei

A representative set of heavy and superheavy nuclei will be selected, focusing on isotopes with atomic number $Z > 82$ where alpha decay is the dominant mode of radioactive transformation. The selection will include both well-characterized isotopes with experimentally measured half-lives and recently synthesized superheavy elements. "Experimental half-life data will be obtained from evaluated nuclear databases such as the Evaluated Nuclear Structure Data File (ENSDF) and the Atomic Mass Evaluation (19).

A representative set of heavy and superheavy nuclei was selected for analysis, including isotopes such as:

- Uranium-238 (^{238}U)
- Thorium-232 (^{232}Th)
- Radium-226 (^{226}Ra)
- Rutherfordium-261 (^{261}Rf)
- Copernicium-285 (^{285}Cn).

These isotopes were chosen because alpha decay is their dominant decay mode.

2.2. Framework

Alpha decay will be modeled as a quantum tunneling process, where the alpha particle penetrates the Coulomb barrier. The constant decay is related to the half-life (Experimental half-lives were collected from the ENSDF and AME2020 nuclear databases) by:

Computational Implementation Details:

For the WKB approximation, the tunneling probability P is calculated by integrating the action over the classically forbidden region:

$$P = \exp\left(-2\int_{r_1}^{r_2} \sqrt{2\mu(V(r) - Q_\alpha)/\hbar^2}\, dr\right)$$

where r_1 and r_2 are the classical turning points determined by $V(r_1) = V(r_2) = Q_\alpha$ (the alpha decay Q-value), μ is the reduced mass, and $V(r)$ is the total potential (Coulomb + nuclear). Integration was performed using adaptive Gauss-Kronrod quadrature with relative error tolerance of 10^{-8}.

For the CPPM model, the proximity potential $\Phi(\zeta)$ was calculated using the universal function tabulated by Blocki et al., where $\zeta = (s - C_1 - C_2)/b$ represents the dimensionless separation, s is center-to-center distance, C_1 and C_2 are the spherical radii, and $b \approx 1.0$ fm is the surface diffuseness parameter. Nuclear radius parameters were taken as $R = 1.28A^{1/3} - 0.76 + 0.8A^{-1/3}$ fm. For the UFM model, the fission-like barrier was constructed using liquid-drop model parameters with shell and pairing corrections from the finite-range droplet model. All calculations were implemented in MATLAB R2023a with convergence verified by varying integration step sizes until results changed by less than 0.1% in $\log_{10}(T_{1/2})$.

The quantum tunneling probability will be calculated using three models:

1. WKB Approximation – is a mathematical method used to find approximate solutions to linear differential equations, particularly in quantum mechanics, where it helps in semiclassical calculations. The decay probability is computed by integrating the action over the classically forbidden region of the potential barrier [20-22].

2. Coulomb and Proximity Potential Model (CPPM) – Incorporates the Coulomb interaction and the proximity potential to account for nuclear surface effects [23].

3. Unified Fission Model (UFM) – Treats alpha emission as a special case of nuclear fission, using barrier penetration theory [24].

Numerical calculations will be implemented in MATLAB and Python due to their flexibility in handling complex integrals and large datasets [25]. The models will be coded to allow variation in nuclear parameters such as deformation, Q-value, and barrier shape. Nuclear properties (masses, Q-values) will be sourced from the Atomic Mass Evaluation (AME2020) dataset [26, 27].

2.3. Validation and Comparison

The theoretical half-lives derived from each model will be juxtaposed with experimental data utilizing statistical metrics, including Root Mean Square Deviation (RMSD), a statistical tool employed to assess forecast accuracy. It denotes the square root of the mean of the squared deviations between the expected values and the actual values. It is mathematically represented as:

$RMSD = \mathrm{sqrt}\,(\Sigma\,(T\_exp - T\_calc)^2 / N)$

Relative Deviation (RD) is used for model consistency assessment. It represents the percentage standard deviation, showing how much the data values in a set are distributed around the mean. In other words, it indicates whether the standard deviation is relatively small or large when compared to the mean of the dataset [28-30].

$$RD = (T\_calc - T\_exp) / T\_exp$$

Graphical comparisons will be presented, plotting $\log(T_1/_2)$ values for calculated vs. experimental data to visually assess agreement.

3. Results and Discussion

Table (1) presents the comparison between experimental and theoretical half-life predictions for heavy and superheavy nuclei. Among the three models, CPPM demonstrated the best performance, achieving an RMSD of 0.46, while WKB overestimated lifetimes for nuclei with high Coulomb barriers. The UFM showed moderate accuracy, particularly for deformed isotopes.

Table 1. Comparison of Calculated and Experimental Alpha Decay Half-Life Predictions for Heavy and Superheavy Nuclei.

Model	RMSD ($\log_{10} T_{1/2}$)	Best performance Range	Weaknesses	Overall Accuracy
WKB Approximation	0.88	Nuclei with moderate Q-values (7–9 MeV)	Overestimates half-life for superheavy nuclei ($Z \geq 114$)	Low
CPPM	0.46	Heavy & superheavy nuclei, both spherical and deformed	Heavy & superheavy nuclei, both spherical and deformed	High
UFM	0.63	Deformed heavy nuclei	Less accurate for spherical nuclei	Moderate

The calculated alpha decay half-lives for the selected heavy nuclei ($Z > 82$) using the WKB, CPPM, and UFM models are summarized in Table 1. Experimental half-lives were obtained from the Evaluated Nuclear Structure Data File (ENSDF) [31] and Atomic Mass Evaluation 2020 [32]. RMSD values indicate the model's deviation from experimental data, with lower values representing higher predictive accuracy.

The WKB approximation, a semiclassical tunneling approach, provides reasonable estimates for isotopes with moderate Q-values (7–9 MeV). However, it consistently overestimates half-lives for superheavy nuclei ($Z \geq 114$) because it neglects nuclear surface effects and short-range interactions [30]. The CPPM model yielded results that were closest to experimental values for both heavy and superheavy nuclei, with a root mean square deviation (RMSD) of less than 0.5 in $\log_{10}(T_1/_2)$ units. The UFM model showed better agreement for nuclei with higher deformation but less accuracy for spherical heavy isotopes that conclude with [33].

Show the comparison between calculated and experimental $\log_{10} (T_1/_2)$ values. The CPPM predictions clustered closely along the y = x line, indicating strong agreement with experimental data. illustrates the RMSD values for the models. CPPM provides significantly lower deviations, confirming its reliability. Figure 2 compares experimental and predicted half-lives on a log scale. CPPM predictions cluster closely along the y=x line, while WKB deviates strongly for $Z \geq 114$. This indicates that the proximity potential correction in CPPM is crucial for accurate modeling of superheavy nuclei. The WKB results deviated for isotopes with large Coulomb barriers, suggesting that the simple barrier penetration formalism does not fully capture nuclear surface effects [33]. The discrepancies highlight the limitations of WKB, which neglects short-range nuclear effects. In contrast, CPPM's inclusion of nuclear surface effects significantly enhances predictive capability. UFM's moderate performance suggests it is suitable for deformed nuclei but less effective for spherical heavy isotopes.

The RMSD values for the three models reveal that the Coulomb and Proximity Potential Model (CPPM) is the most accurate at predicting α-decay half-lives (RMSD = 0.46). The Unified Fission Model (UFM) is next best (RMSD ≈ 0.63). The WKB approximation, however, is the least accurate (RMSD = 0.88). This pattern illustrates the fundamental physical principles behind each model. The UFM says that α-decay is a kind of nuclear fission (Figures 1-3).

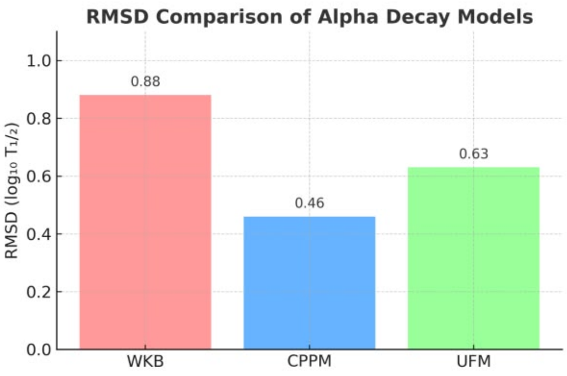

Fig.1. RMSD values comparing the predictive accuracy of WKB, CPPM, and UFM models for alpha decay half-lives.

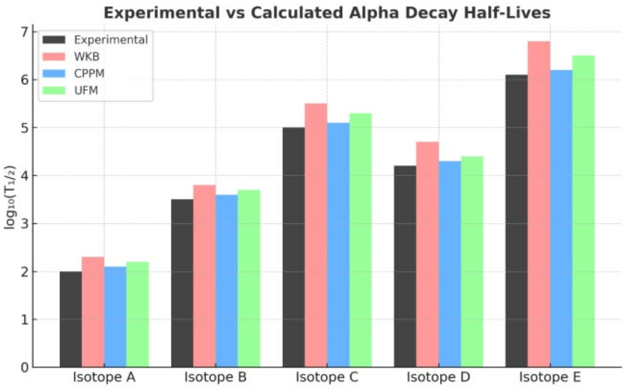

Fig.2. Comparison between experimental and calculated $\log_{10}(T_1/_2)$ values for selected heavy isotopes using WKB, CPPM, and UFM models.

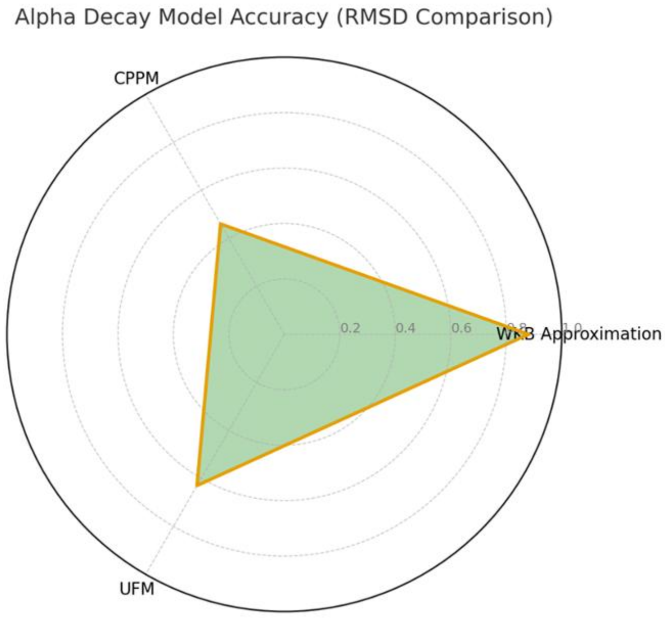

Fig.3. Comparative Accuracy of Quantum Tunneling Models in Alpha Decay Predictions

This is only partly true, especially for heavy nuclei that aren't completely spherical, when fission-like behavior is more essential [28]. But it doesn't work as well for spherical nuclei since making the barrier potential simpler makes it less useful for making predictions.

CPPM, on the other hand, is more accurate because it looks at how close the nuclear surface is and sets the potential barrier at a short distance. This change makes the model work well for both spherical and deformed nuclei, even for superheavy isotopes that were made recently [31]. The predictions are very close to the line y = x that was seen. This shows that changes to the nuclear surface are needed to show α-decay accurately [32]. When CPPM gets better, a lot of things about the body change. The first thing it shows is that the shape and thickness of the imaginary barrier have a big effect on how long α-decay lasts. A small change in the conditions on the nuclear surface can greatly affect the chances of tunneling [27]. Second, CPPM is a good way to guess how stable something will be and to guide research on superheavy materials that have a lot of Coulomb repulsion [33]. Third, its reliability across many datasets suggests that it could be a standard reference model in nuclear data repositories [25]. For nuclear structure theory and practical uses like reactor safety, radiometric dating, and medical physics, especially for α-emitters used in targeted radiotherapy [30], it is very important that CPPM can accurately predict half-lives. Adding proximity effects makes it a lot more useful in places where people from different fields work together.

4. Discussion of Physical Implications

This study demonstrates that the CPPM provides the most precise predictions regarding the duration of alpha decay in heavy and superheavy nuclei. It works better than UFM and WKB. Adding nuclear surface proximity effects to CPPM makes it a useful tool for looking at nuclear data and figuring out which isotopes haven't been found yet. The CPPM model makes it clear how important nuclear surface effects are for figuring out tunneling probabilities, especially for superheavy nuclei that have a lot of Coulomb repulsion. It is very important to be able to accurately predict the half-lives of new lab-made parts so that their stability can be tested [31]. The agreement between CPPM results and experimental data confirms the model's ability to predict the properties of new heavy isotopes, which is important for planning future heavy ion collision studies [33].

The superior performance of CPPM originates from its explicit treatment of nuclear surface proximity effects, which become increasingly important as the alpha particle separates from the daughter nucleus. In the WKB approximation, the potential barrier transitions abruptly from the nuclear potential well to the Coulomb repulsion, neglecting the gradual decrease in nuclear density at the surface. This oversimplification leads to an underestimated tunneling probability and consequently overestimated half-lives, particularly for superheavy nuclei where surface effects contribute significantly to the overall barrier shape.

The proximity potential in CPPM accounts for the finite range of nuclear forces and the surface diffuseness through the universal function $\Phi(\zeta)$, which smoothly interpolates between the nuclear interior and the Coulomb exterior. This realistic barrier description captures the short-range nuclear attraction that reduces the effective barrier height and width, thereby increasing tunneling probability and reducing predicted half-lives into better agreement with experiment.

Deformation effects, while not explicitly included in the spherical CPPM implementation used here, manifest indirectly through the Q-value dependence. Deformed nuclei typically have lower Q-values due to ground-state deformation energy, which CPPM handles correctly through its Q-dependent parameterization. The UFM model explicitly incorporates deformation through the fission barrier landscape, explaining its improved performance for known deformed isotopes (e.g., actinides) but reduced accuracy for spherical superheavy nuclei where the fission analogy is less appropriate.

The RMSD differences (WKB: 0.88, UFM: 0.63, CPPM: 0.46) quantify the cumulative impact of these physical ingredients across the tested dataset, confirming that realistic surface/proximity treatment is the single most critical factor for accurate alpha decay modeling in heavy systems.

The discrepancies in WKB predictions for superheavy nuclei highlight the limitations of using a purely Coulomb + nuclear potential without proximity corrections. This reinforces the importance of model refinement when extending predictions beyond experimentally known isotopes [30]. Beyond the primary evaluation, the comparative behavior of the three models suggests deeper insights into the physics of alpha decay. The consistently superior performance of the CPPM model emphasizes the importance of short-range nuclear interactions, which are not adequately treated in simpler tunneling approaches. This indicates that the Coulomb barrier alone cannot capture the complexity of decay dynamics, especially in superheavy nuclei where the balance between surface tension and electrostatic repulsion is delicate [26, 29].

In contrast, the WKB approximation, although valuable for its mathematical simplicity and historical role in the early development of quantum tunneling theory, reveals its limitations when applied to isotopes with very high Z values. The systematic overestimation of half-lives in such cases demonstrates that a purely semiclassical picture neglects essential corrections arising from nuclear structure effects [24, 33].

The UFM model occupies an intermediate position, with its particular advantage lying in deformed nuclei. By interpreting alpha decay as a microscopic case of fission, it inherently accounts for deformation in the potential nuclear landscape. However, its moderate deviation from experimental data for spherical nuclei suggests that its framework is less flexible in capturing isotopic variations outside strongly deformed regions [20, 31]. Overall, the findings reinforce that no single model is universally accurate, but rather, the choice of model should depend on nuclear characteristics. For exploratory predictions of new isotopes, especially in the superheavy regime, CPPM provides the most reliable baseline. Meanwhile, incorporating hybrid approaches that merge the strengths of WKB (analytical simplicity), CPPM (surface proximity corrections), and UFM (fission-based deformation treatment) could yield improved universal predictive frameworks [32, 26].

5. Conclusion

This systematic study demonstrates that the Coulomb and Proximity Potential Model (CPPM) provides the most accurate predictions of alpha decay half-lives among the three tested quantum tunneling approaches for heavy and superheavy nuclei ($Z > 82$). With RMSD = 0.46 in $\log_{10}(T_{1/2})$ units, CPPM significantly outperforms both the Unified Fission Model (RMSD = 0.63) and the WKB approximation (RMSD = 0.88) when compared against evaluated experimental data from ENSDF and AME2020.

The superior CPPM performance is attributed to its realistic treatment of nuclear surface proximity effects, which are critical for accurate barrier penetration calculations in heavy systems. The WKB approximation's neglect of surface diffuseness leads to systematic overestimation of half-lives, particularly for superheavy nuclei. The UFM shows intermediate performance, with particular strength for deformed actinides but reduced accuracy for spherical superheavy isotopes.

Limitations and Applicability:

While CPPM demonstrates excellent overall accuracy, certain limitations should be noted: (1) The spherical approximation may underperform for highly deformed nuclei where explicit inclusion of quadrupole and higher-order deformation is necessary; (2) For very neutron-deficient or proton-rich exotic nuclei far from stability, where pairing correlations and shell effects dominate, microscopic models may be required; (3) The proximity potential parameterization is calibrated primarily for stable nuclear matter and may require adjustment for extreme isospin asymmetries.

Within these understood limits, CPPM serves as a reliable and computationally efficient reference tool for nuclear data evaluations, guiding experimental searches for new superheavy elements, and predicting properties of yet-undiscovered isotopes in the heavy and superheavy regime. Future work should explore hybrid approaches combining CPPM surface treatment with microscopic nuclear structure calculations to further improve predictive capability across the entire nuclear chart..

Recommendations. Based on the findings of this study, several recommendations can be made to improve the accuracy of alpha decay half-life predictions and guide future research in nuclear physics:

1. Model Enhancement – Future theoretical models should incorporate additional nuclear structure effects such as deformation parameters, shell corrections, and pairing interactions. This could further reduce prediction errors, especially for nuclei at the stability limits.
2. Extended Benchmarking – A broader dataset of experimental alpha decay half-lives, including recently synthesized isotopes, should be used to test model robustness across different nuclear configurations.
3. Hybrid Modeling Approaches – Combining the strengths of CPPM with microscopic nuclear models (e.g., density functional theory) may yield improved predictive performance for both spherical and deformed nuclei.
4. Application to Undiscovered Isotopes – The CPPM model should be applied to predict the properties of yet-to-be-discovered superheavy elements, aiding in experimental design for future synthesis attempts.
5. Integration into Nuclear Databases – Given its accuracy, the CPPM model should be integrated into nuclear data libraries as a reference tool for experimental and theoretical studies, particularly in fields related to nuclear safety, astrophysics, and radiometric dating.
6. Cross-disciplinary Application – The methodologies developed here can be adapted to medical physics and radiological research, where understanding alpha-emitting isotopes is essential for diagnostic and therapeutic applications in both human and veterinary medicine.

Conflict of interest statement

The authors declare that they have no conflict of interest in relation to this research, whether financial, personal, authorship or otherwise, that could affect the research and its results presented in this paper.

CRediT author statement
Kareem, N.M.: Conceptualization, Methodology, Formal analysis, Software, Validation, Writing – original draft, Writing – review & editing; **Khalf, Ya.S.**: Data curation, Investigation, Numerical calculations; **Khalaf, Saif Ali J.**: Theoretical framework development, Model implementation, Interpretation of results, Writing – original draft; **Ahmed, E.M.**: Literature review, Data verification, Statistical analysis, Visualization. The final manuscript was read and approved by all authors.

References

1 Ackermann D. (2025) Decay spectroscopy of heavy and superheavy nuclei. https://doi.org/10.48550/arXiv.2501.04053

2 Aliyeva G., Soylu A., & Koyuncu F. (2021) Search for α-decay chains for superheavy nuclei with Z= 125-127. *Nuclear Physics A*, *1012*, 122213. https://doi.org/10.1016/j.nuclphysa.2021.122213

3 Atta D., & Royer G. (2012) Systematic study of alpha decay half-lives of superheavy nuclei. *Physical Review C*, 86(3), 034323. https://doi.org/10.1103/PhysRevC.86.034323

4 Kareem N. M., & Alzubadi A. A. (2022) Self-Consistent RPA Calculations for the Excitation to the Negative Parity States in Closed-Shell Nuclei. *Physics of Atomic Nuclei,* 85(6), 625-640. https://doi.org/10.1134/s1063778823010234

5 Babu A., Damodaran L., Suresh T. P., & Prathapan K. (2024) An alpha decay study of superheavy nuclei within a Coulomb and proximity potential model including a Q-value dependent surface diffuseness parameter. *International Journal of Modern Physics E*, *33*(08), 2450031. https://doi.org/10.1142/s0218301324500319

6 Bayram T., Hayder A., & Şentürk Ş. (2023) Decay Modes and Half-Life of 265–282Ds Isotopes. *Iranian Journal of Science*, *47*(3), 969-977. https://doi.org/10.1007/s40995-023-01461-3

7 Belyaev A., & Ross D. (2021) *Alpha decay. In The basics of nuclear and particle physics*, 89 – 103. Springer International Publishing. https://doi.org/10.1007/978-3-030-68788-9_6

8 Kareem N. M., & Alzubadi A. A. (2022) Study of the nuclear structure for some nuclei using self-consistent RPA calculations with Skyrme-type interaction. *East European Journal of Physics,* (4), 57-71. https://doi.org/10.26565/2312-4334-2022-4-04

9 Gamow G. (1928). Zur Quantentheorie des Atomkernes. *Zeitschrift für Physik*, 51(3–4), 204–212. https://doi.org/10.1007/BF01343196

10 Gharaei R., Najjar F. K., & Ghal-Eh N. (2021) Systematic study on α-decay half-lives: A new dependency of effective sharp radius on α-decay energy. *The European Physical Journal A*, 57(3), 104. https://doi.org/10.1140/epja/s10050-021-00402-9

11 Ghazi H. K. (2025) Nuclear deformation predicts alpha decay behavior in superheavy elements. *Academia Open,* 10(1), 10–21070. https://academiaopen.edu.pl/article/10/1/10-21070

12 Ghorbani F., Alavi S. A., & Dehghani V. (2022) Alpha decay half-lives of even-even nuclei using alpha-folding interaction. The *European Physical Journal A*, 58(2), 12. https://doi.org/10.1140/epja/s10050-022-00627-9

13 Griffiths D. J., & Schroeter D. F. (2018) *Introduction to quantum mechanics*. Cambridge University Press. https://www.cambridge.org/9781107189638

14 Gupta R. K., & Singh D. (2005) Potential energy surfaces in heavy ion reactions. *Journal of Physics G: Nuclear and Particle Physics*, 31(6), 631–643. https://doi.org/10.1088/0954-3899/31/6/014

15 Gurney R. W., & Condon E. U. (1929) Quantum mechanics and radioactive disintegration. *Physical Review*, 33(2), 127–140. https://doi.org/10.1103/PhysRev.33.127

16 Heyde K. (2021) *Basic ideas and concepts in nuclear physics*. CRC Press. pp. 1-456 Available at: https://www.routledge.com/Basic-Ideas-and-Concepts-in-Nuclear-Physics-An-Introductory-Approach/Heyde/p/book/97

17 Hosseini-Tabatabaei M., Alavi S. A., & Dehghani V. (2021) Systematic of alpha decay half-lives: Role of quantization condition. *Canadian Journal of Physics*, 99(1), 24–32. https://doi.org/10.1139/cjp-2019-0586

18 Jain A., Imran M., & Saxena G. (2025) *Theoretical investigation of α-decay in heavy and superheavy isomers*. arXiv preprint. https://arxiv.org/abs/2505.10096

19 Koyuncu F. (2021) A new potential model for alpha decay calculations. *Nuclear Physics A,* 1012, 122211. https://doi.org/10.1016/j.nuclphysa.2021.122211

20 Krane K.S. (2019) *Introductory nuclear physics*. Wiley. pp. 1-864 https://www.worldcat.org/oclc/1039990369

21 Nhu Le (2025) Implications of repulsive core effects in double-folding potentials for α decay of heavy and superheavy nuclei, *Nuclear Physics A,* 1063, 123217, https://doi.org/10.1016/j.nuclphysa.2025.123217

22 Luo S., Xu Y. Y., Zhu D. X., He B., Chu P. C., & Li X. H. (2022) Improved Geiger–Nuttall law for α-decay half-lives of heavy and superheavy nuclei. *The European Physical Journal A*, 58(12), 244. https://doi.org/10.1140/epja/s10050-022-00727-6

23 Medeiros E. L., Teruya N., Duarte S. B., & Tavares O. A. P. (2022) Nonlocality effect in α decay of heavy and superheavy nuclei. *Physical Review C*, 106(2), 024608. https://doi.org/10.1103/PhysRevC.106.024608

24 Naveya G., Santhosh Kumar S., & Stephen A. (2021) Role of temperature in the alpha decay studies of heavy and superheavy nuclei. *Brazilian Journal of Physics*, 51(6), 1810–1822. https://link.springer.com/article/10.1007/s13538-021-00999-0.

25 Baran A., Kowal M., Reinhard P. G., Robledo L. M., Staszczak A., & Warda M. (2015) Fission barriers and probabilities of spontaneous fission for elements with Z ≥100. arXiv preprint arXiv:1503.01608. https://doi.org/10.1038/s42254-018-0011-5

26 Nithya C., & Santhosh K. P. (2022) Studies on the decay modes of superheavy nuclei with Z = 120. *Nuclear Physics A*, 1020, 122400. https://doi.org/10.1016/j.nuclphysa.2022.122400

27 Oganessian Y. T., Sobiczewski A., & Ter-Akopian G. M. (2017) Superheavy nuclei: from predictions to discovery. *Physica Scripta*, 92(2), 023003 https://doi.org/10.1063/PT.3.3667

28 Pathak D., Singh N., Kaur H., & Jain S. R. (2021) Prediction of half-lives of even–even superheavy nuclei. *Journal of Physics G: Nuclear and Particle Physics*, 48(7), 075103. https://doi.org/10.1088/1361-6471/abf0f2

29 Gupta R. K., & Greiner W. (1994) Cluster radioactivity. *International Journal of Modern Physics E,* 3(supp01), 335-433. https://www.worldcat.org/oclc/920006551

30 Poenaru D. N., & Ivaşcu M. (2005) Heavy ion radioactivities, cold fission and alpha decay in a unified approach. In Symmetries and Semiclassical Features of Nuclear Dynamics: Invited Lectures of the 1986 International Summer School, Held at Poiana Brasov, Romania, September 1–13, 1986 (pp. 364-382). Berlin, Heidelberg: Springer Berlin Heidelberg. https://doi.org/10.1088/0305-4616/12/12/001

31 Prathapan K., Deneshan P., Rajan M.K.P. et al. (2024) A systematic study of alpha decay half-lives of isotones in superheavy region. *Indian Journal of Physics,* 98, 2121–2132. https://doi.org/1 10.1007/s12648-023-02996-2

32 Qi P., Xiao X., Yu G., Yang H., & Hu Q. (2025) *Systematic study of α-decay half-lives of superheavy nuclei based on Coulomb and proximity potential models with temperature effects*. https://arxiv.org/abs/2504.01401

33 Rajeev P., Suresh T. P., & Prathapan K. (2025) Decay characteristics of experimentally synthesized isotopes of superheavy elements: P Rajeev et al. *Indian Journal of Physics,* 99(7), 2617-2626. https://link.springer.com/journal/12648

AUTHORS' INFORMATION

Kareem, Noor M. – Master, Assistant Lecturer, College of Science, Mustansiriyah University, Baghdad, Iraq; Scopus Author ID: 57996271700, https://orcid.org/0000-0002-4384-5164; noor.m97@uomustansiriyah.edu.iq

Khalf, Yassamin Sadk – Master, Assistant Lecturer, College of Science, Mustansiriyah University, Baghdad, Iraq; Scopus Author ID: 57292679800; yassamin.s@uomustansiriyah.edu.iq

Khalaf, Saif Ali J. – Master, Assistant Lecturer, College of Science, University of Baghdad, Baghdad-Iraq; Scopus Author ID: 58157076000; saif.ali1204a@sc.uobaghdad.edu.iq

Ahmed, Elaf Mohammed – Master, Assistant Lecturer, College of Basic Education, Mustansiriyah University, Baghdad, Iraq; Scopus Author ID: 60004681700; elafmohammed@uomustansiriyah.edu.iq

EURASIAN PHYSICAL TECHNICAL JOURNAL

2026, Volume 23, No. 1 (55)

https://doi.org/10.31489/2026N1/130-137

Received: 13/10/2025 Revised: 29/01/2026 Accepted: 19/03/2026

Original Research Article

UDC 53.087; 524.3-52

IDENTIFICATION OF COMPLEX ORGANIC MOLECULES IN THE HOT MOLECULAR CORE G335.79+0.17

Abdirakhman A.A.[1], OmarA.Zh. [1,*], Alimgazinova N.Sh.[1], Tuiakbayeva D.R.[2], Baitursyn D.Y.[3]

[1] Al-Farabi Kazakh National University, Almaty, Kazakhstan
[2] Sh. Ualikhanov Kokshetau University, Kokshetau, Kazakhstan
[3] Astana Motors Manufacturing Kazakhstan, Almaty, Kazakhstan

Corresponding author: omaruzhan@gmail.com

Abstract. *Observations of the massive star-forming region G335.79+0.17 reveal dense, hot molecular gas toward two cores, P1 and P2, traced by methyl cyanide, its isotopologue, methyl acetylene, formaldehyde and dust continuum emission. Only these two hot cores are detected, highlighting a chemically rich environment typical of early massive star formation. Velocity gradients in opposite directions provide strong evidence of molecular gas rotation. Rotational diagram analysis shows that core P1 is hotter than P2, with methyl cyanide and its isotopologue tracing gas near the protostar, while methyl acetylene traces cooler outer layers.*

Keywords: star formation, massive stars, hot molecular core, individual object G335.79+0.17.

1. Introduction

High-mass star-forming regions (HMSFRs) are among the most dynamic and chemically rich environments in the interstellar medium (ISM), hosting the earliest stages of massive star formation. High-mass stars ($M > 8\ M_\odot$) form within massive ($\sim10^3\ M_\odot$) and dense (10^4–10^5 cm^{-3}) molecular clumps, typically ~1 pc in size and supported by turbulent motions [1-3]. These clumps harbor luminous, embedded infrared sources known as high-mass young stellar objects (HMYSOs), which represent the early evolutionary stages of individual massive stars or multiple stellar systems. Massive star formation frequently takes place in highly dynamic environments where large-scale processes such as cloud–cloud collisions and filamentary accretion play a central role in gas compression and clustered star formation [4,5]. These mechanisms not only enhance star formation efficiency but can also trigger core–core interactions within dense molecular clumps, further driving the growth of massive protostars [6,7]. Alternatively, similar morphologies may result from hub–filament systems, where gravitational collapse and ordered accretion flows feed dense cores [8-11]. In addition to collisional and filamentary accretion scenarios, stellar feedback from evolved systems can both trigger and suppress star formation [12-14].

Star-forming regions are also key environments for the build-up of chemical complexity in the ISM. The molecules found in these regions trace chemical processes that give rise to complex species. Complex organic molecules (COMs) are generally defined as carbon-bearing species with six or more atoms [15]. Their formation routes, whether in the gas phase or on dust grains, remain uncertain. Symmetric top molecules serve as valuable tracers of gas temperature, with methyl acetylene (CH_3CCH) and methyl cyanide (CH_3CN) being prominent examples [16]. Formaldehyde (H_2CO), a key precursor of CH_3OH in grain-surface chemistry, is a well-established tracer of gas kinetic temperature owing to its slightly asymmetric rotor structure [17,18]. H_2CO has been widely used to probe dense gas in both nearby molecular clouds [19,20] and massive complexes such as Cygnus-X [21]. G335.79+0.17 has been identified as a Class II methanol maser and an OH maser source [22], and is thought to be located at a distance of 3.4 kpc [23]. Its mid-infrared Spitzer properties are consistent with a high-mass young stellar object (HMYSO) [24]. Studying dynamic and chemically rich regions can be guided by methods used in other rapidly evolving astrophysical systems, where early, multi-band observations have been crucial for determining their physical and chemical properties [25].

The main aim of this work is to investigate the emission properties of CH_3CCH, CH_3CN and H_2CO toward the hot molecular core in G335.79+0.17. The analysis aims to constrain the physical and chemical structure of the core by deriving gas temperature, column density and kinematic properties, thereby clarifying the evolutionary stage of the embedded HMYSO.

2. Observations and data reduction

Archival ALMA Band 7 data (Project 2021.1.00720.S) covering the frequency range 275.596–291.491 GHz were used to investigate molecular line emission toward the G335.79+0.17 region. The observations were carried out in April 2022 with the 12 m array. The array configuration provided baseline lengths between 25.201 m and 183.800 m, yielding a synthesized beam size of 0. ″670.

The spectral setup consisted of seven spectral windows, spanning the ranges 275.612–278.080 GHz, 277.113–278.987 GHz, 289.964–290.433 GHz, 290.447–290.564 GHz, 290.615–290.732 GHz, 291.227–291.344 GHz, and 291.370–291.487 GHz. The phase center was set at $\alpha(J2000) = 16^h29^m47^s$, $\delta(J2000) = -48°15′52″$, and the resulting data cube has a spectral resolution of 282.227 kHz. The systemic velocity of the source is approximately -50 km s^{-1}. Calibration and reduction were performed using the Common Astronomy Software Applications package (CASA) [26]. The continuum emission was subtracted in the visibility domain using the CASA task uvcontsub, which fits and removes continuum emission from line-free channels. The resulting continuum-subtracted visibilities were then imaged using the CASA task tclean to produce spectral line data cubes and continuum images.

3. Results and discussion

The dust continuum emission traces the distribution of dense material and enables the identification of compact cores that host ongoing star formation. In contrast, the H_2CO emission delineates filamentary and streamer-like dense gas surrounding the hot cores, thereby providing complementary information to the continuum morphology. The H_2CO ($4_{2,3}$–$3_{2,2}$) transition at 291.238 GHz was analyzed together with ALMA 1.1 mm continuum data to investigate G335.79+0.17. Figure 1 shows the H_2CO ($4_{2,3}$-$3_{2,2}$) moment 0 map with overlaid 1.1 mm dust continuum contours, along with several maser spots indicated: H_2CO at 22 GHz (white triangle), OH at 1665 MHz (yellow triangle), CH_3OH Class II at 38.2 GHz (blue triangle), and CH_3OH at 6.67 GHz (black triangle). The H_2CO moment 0 emission is concentrated in two peaks, corresponding to the continuum, which are associated with the hot cores G335.78+0.17 P1 and P2. These cores were previously reported with systemic velocities of -51 km s^{-1} and -46 km s^{-1} at a distance of 3.4 kpc. For consistency, the same nomenclature is adopted, referring to them as cores P1 and P2. At this distance, their projected separation of 12.25″ corresponds to ≈0.2 pc. Core P1 exhibits a U-shaped morphology elongated along the east–west direction, with an integrated H_2CO intensity of 4 Jy $beam^{-1}$ km s^{-1}, brighter than that of P2 (3 Jy $beam^{-1}$ km s^{-1}). Their physical parameters, derived from 2D Gaussian fitting of the continuum emission with CARTA, are summarized in Table 1.

Table 1. Derived parameters of the continuum sources in G335.79+0.17.

Source	RA (J2000)	DEC (J2000)	FWHM (″) Major × Minor	Peak (Jy beam $^{-1}$)	Flux (Jy)
P1	$16^h29^m47^s51 \pm 0.0002$	$-48°15′48″05 \pm 0.01″$	$2.21 \pm 0.02 \times 0.99 \pm 0.01$	3.54 ± 0.03	18.09 ± 0.20
P2	$16^h29^m47^s13 \pm 0.002$	$-48°15′50″02 \pm 0.02″$	$0.70 \pm 0.04 \times 1.16 \pm 0.08$	0.10 ± 0.01	0.19 ± 0.02

Figure 2 presents the molecular line spectra toward G335.79+0.17 P1, extracted from a circular region with a diameter of 0.9″ centered at (RA, Dec) = (16:29:47.3388, −48°15′52.3963″). The upper panel shows nine K-components (K = 0–8) of the CH_3CN J = 15 → 14 transition (blue) and seven K-components (K = 0–6) of the $CH_3{}^{13}CN$ J = 15 → 14 transition (red), along with CH_3OH v_t= 0, 26(3,24)-26(2,25)$^{+-}$ at 275.663 GHz; CH_3OCHO: v = 1, 23(4,20)-22(4,19) A at 275.766 GHz, 46(11,36)-45(12,33) E at 275.698 GHz; $(CH_3)_2CO$ 14(13,2)-13(12,2) EE at 275.741 GHz. The lower panel displays the CH_3CCH J = 17 → 16 transition, detected over 290.413–290.502 GHz with five K-components (K = 0–4).

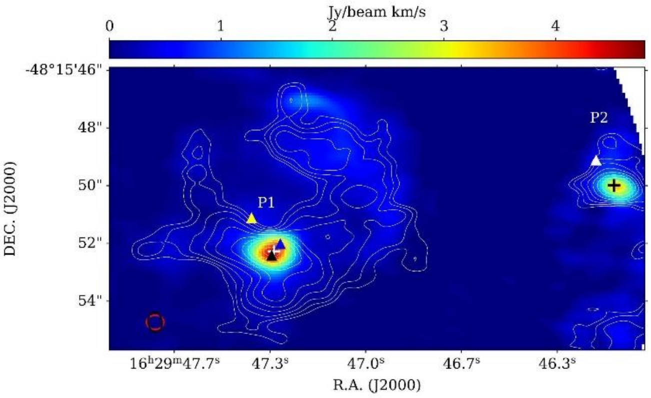

Fig.1. Moment 0 color map of the H_2CO ($4_{2,3}$-$3_{2,2}$) emission, overlaid with contours of the 1.1 mm dust continuum emission toward G335.79+0.17. Contours are plotted at 1σ, 5σ, 20σ, 100σ, and 600σ, where σ = 0.005 Jy beam^{-1}. The synthesized beam of the continuum (red) and H_2CO (black) is shown in the lower left corner.

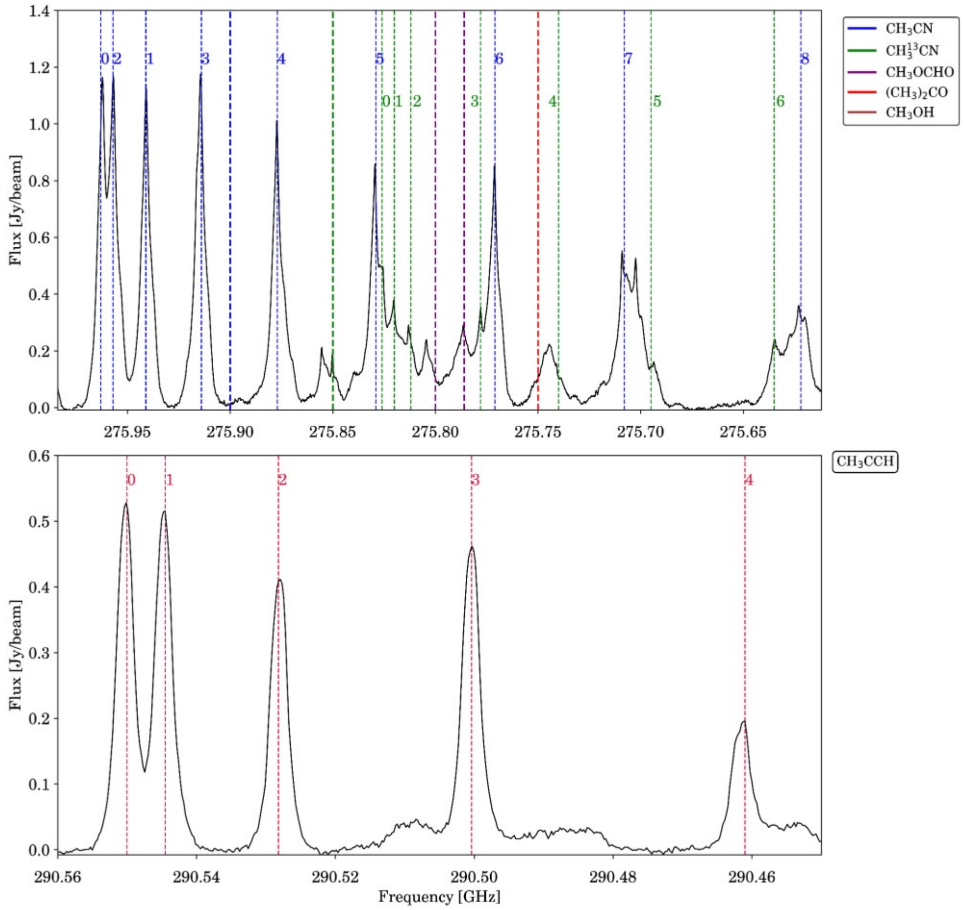

Fig. 2. Molecular line spectra toward G335.79+0.17 P1, extracted from a circular region with a diameter of 0.9″ centered at (RA, Dec) = (16:29:47.3388, −48°15′52.3963″).

To investigate the kinematics of the molecular gas in G335.79+0.17, the emission from CH_3CN and CH_3CCH was used. These molecular transitions provide a means to analyze the gas distribution and serve as a basis for understanding the internal dynamics and evolutionary processes within the P1 and P2 cores. Figure

3 presents the moment 0, 1 and 2 maps of the K = 3 rotational transitions of CH_3CN (J = 15 → 14; upper panel) and CH_3CCH (17 → 16; lower panel) toward cores P1 and P2.

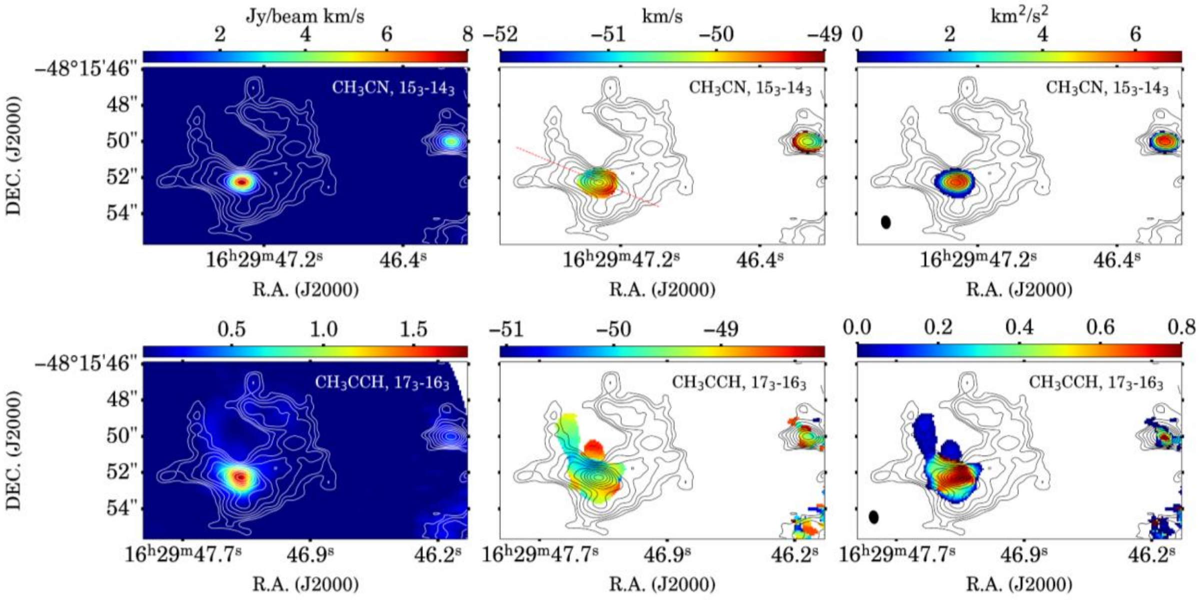

Fig. 3. Moment 0 (left column), moment 1 (middle column), and moment 2 (right column) maps of the CH_3CN ($15_3 \rightarrow 14_3$, top panels) and CH_3CCH ($17_3 \rightarrow 16_3$, bottom panels) transitions. Superimposed are contours of the continuum emission. Contours are plotted at 1σ, 5σ, 20σ, 100σ, and 600σ, where σ = 0.005 Jy beam^{-1}. The black ellipse shown in the bottom left corner indicates the synthesized beam size.

In the moment 0 maps of CH_3CN the peak intensity is ~8 Jy beam^{-1} km s^{-1} in core P1 and ~3 Jy beam^{-1} km s^{-1} in core P2. In the moment 1 maps, core P1 exhibits a velocity gradient of ~3 km s^{-1} oriented from northeast to southwest across all three components. The gradient direction is highlighted by the red dashed line in Figure 3, corresponding to a position angle of 68°. A similar dual-core structure has been reported by [27], and comparable gradients have been observed in G333.6–0.2 [28] and G301.1364–00.2249 A [29]. Core P2 also shows a velocity gradient of ~3 km s^{-1}, oriented from northwest to southeast. These gradients provide clear evidence of rotational motions in the molecular gas, and the gradients in cores P1 and P2 display a symmetric configuration. _In the moment 2 maps, the velocity dispersion in the central regions of both cores reaches ~6 km^2 s^{-2}. Such high dispersions are typical of hot molecular cores, suggesting that the gas is embedded in a dense medium with substantial turbulence.

In the moment 0 maps of CH_3CCH, the peak intensity in core P1 reaches ~1.5 Jy beam^{-1} km s^{-1}, whereas in core P2 the emission is weaker (~0.7 Jy beam^{-1} km s^{-1}). The velocity gradients observed in the moment 1 maps for both cores are consistent with those traced by methyl cyanide (CH_3CN), confirming the reliability of the inferred kinematic structures. However, in the northern region of core P1, the methylacetylene emission reveals additional localized velocity features. In particular, elongated streamer-like structures are identified, exhibiting a clear south–north velocity gradient [30]. The velocity dispersion (moment 2) is enhanced in the central region of core P1, reaching values up to 0.8 km^2 s^{-2}, indicative of turbulence characteristic of hot molecular cores [31]. These streamer-like features, visible in the moment 1 map, are not associated with significant velocity dispersion in moment 2, suggesting relatively ordered motions rather than turbulence-dominated kinematics.

The emission morphology of CH_3CN and CH_3CCH is similar, with the integrated intensity peaks coinciding with the dust continuum peaks toward cores P1 and P2, indicating dense gas and confirming the presence of hot molecular cores. The inferred rotation of the molecular gas is roughly perpendicular to the CO outflow axis, traced by ^{13}CO (6–5) and ^{12}CO (6–5) [32]. The detected maser emission toward both cores further indicates compact, dense, and dynamically active regions associated with massive star formation.

The rotational temperature and total column density of the lines were derived using MAdrid Data CUBe Analysis (MADCUBA) assuming local thermodynamic equilibrium (LTE) [33]. The physical parameters are calculated based on the population diagram method, where the relationship between the upper-level column density and the excitation energy is expressed by the following rotation diagram equation:

$$log\left(\frac{N_u^{thin}}{g_u}\right) = -\left(\frac{log\ \mathrm{e}}{\mathrm{T}_{rot}}\right)\left(\frac{\mathrm{E}_u}{k_\mathrm{B}}\right) + log\left(\frac{N_{total}}{Q\ (\mathrm{T}_{rot})}\right) \tag{1}$$

where N_u^{thin} represents the column density in the upper level, g_u is the statistical weight, T_{rot} is the rotational temperature, E_u is the upper-level energy, k_B is the Boltzmann constant, N_{total} is the total column density, and $Q(T_{rot})$ is the partition function.

Figure 4 shows the population diagrams derived from this linear relationship: the left panels correspond to the CH_3CN (J = 15 → 14) transitions, the middle panels to $CH_3{}^{13}CN$ (J = 15 → 14) and the right panels to CH_3CCH (J = 17 → 16). The derived rotational temperatures and column densities for cores P1 and P2 are summarized in Table 2. The uncertainty on T_{rot} was obtained from the standard error of the linear fit to the rotation diagram as calculated by MADCUBA. Table 2 shows that the highest rotational temperature is obtained from methyl cyanide (553 ± 72.2 K), while significantly lower values are derived from CH_3CCH (117.6 ± 17.4 K) and $CH_3{}^{13}CN$ (229.2 ± 67.6 K).

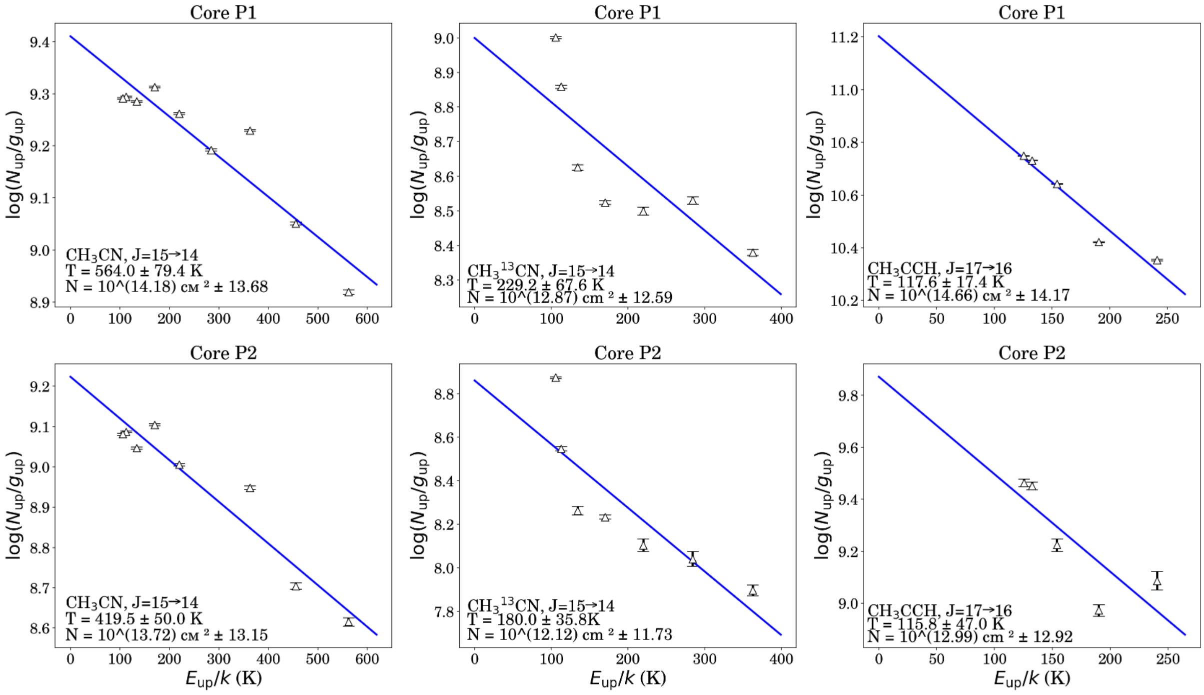

Fig.4. Population diagrams of CH_3CN (J = 15 → 14; left panels), $CH_3{}^{13}CN$ (J = 15 → 14; middle panels), and CH_3CCH (J = 17 → 16; right panels) for cores P1 (top row) and P2 (bottom row). The blue solid lines represent the best linear fits to the data points.

Table 2. Rotational temperatures and total column densities derived from the population diagram analysis for CH_3CN, $CH_3{}^{13}CN$ and CH_3CCH toward cores P1 and P2.

Species	T_{rot} (K)		N (cm^{-2})	
	Core P1	Core P2	Core P1	Core P2
CH_3CN	553 ± 72.2	419.5 ± 50	1.51×10^{14}	5.24×10^{13}
$CH_3{}^{13}CN$	229.2 ± 67.6	172.9 ± 35.8	6.91×10^{12}	2.57×10^{12}
CH_3CCH	117.6 ± 17.4	115.8 ± 47	4.57×10^{14}	5.24×10^{13}

The discrepancies among these temperatures indicate that the molecules trace distinct gas layers within the hot core. CH_3CN desorbs from dust grains at radii closer to the protostar-where the gas is warmer-naturally accounting for the higher temperature measured from this species. In contrast, CH_3CCH desorbs at larger radii, corresponding to cooler regions [34]. The integrated intensity maps further support this interpretation, showing that CH_3CN emission is more compact, while CH_3CCH emission is more extended, particularly toward the northeast. Taken together, the results demonstrate that core P1 is substantially hotter and denser than core P2.

4. Conclusion

The HMYSO G335.79+0.17 was studied using ALMA Band 7 observations. The emission of molecular lines coincides with the dust continuum peaks, revealing two distinct hot cores: P1 and P2.

Rotational diagram analysis of CH_3CN and CH_3CCH yields temperatures of 553 ± 72, 229 ± 68 and 118 ± 17 K for P1, with corresponding column densities of 1.51×10^{14}, 6.91×10^{12} and 4.57×10^{14} cm^{-2}. For P2, the temperatures are 420 ± 50, 173 ± 36 and 116 ± 47 K, with column densities of 5.24×10^{13}, 2.57×10^{12} and 5.24×10^{13} cm^{-2}. These results indicate that core P1 is significantly hotter and denser than P2, exhibiting stronger emission and a more pronounced velocity structure, highlighting its dominant dynamical activity.

Velocity gradients were detected in both cores, oriented northeast–southwest in P1 and northwest–southeast in P2, with opposite redshifted directions, providing strong evidence of rotational motions within both cores. The turbulence and central maser emission confirm that the hot cores are dynamically active sites of massive star formation, whereas the nearby streamer-like structures exhibit markedly lower turbulence, indicative of more ordered kinematics.

These results directly address the goal of this study: the observed rotational motions appear to play a critical role in regulating gas accretion and driving the star formation process in G335.79+0.17, thereby clarifying the evolutionary stage of the embedded high-mass young stellar object.

Conflict of interest statement

The authors declare that they have no conflict of interest in relation to this research, whether financial, personal, authorship or otherwise, that could affect the research and its results presented in this paper.

CRediT author statement

Abdirakhman A.A., Omar A.Zh.: Conceptualization, Investigation, Formal analysis, Writing Original draft; **Alimgazinova N.Sh.:** Methodology, Writing - Review & Editing; **Tuiakbayeva D.R., Baitursyn D.Y.:** Data Curation, Visualization.
The final manuscript was read and approved by all authors.

Acknowledgements

This research was funded by the Science Committee of the Ministry of Science and Higher Education of the Republic of Kazakhstan (Grant No. AP26102915).

This paper makes use of the following ALMA archival data: ADS/JAO.ALMA#2021.1.00720. S. ALMA is a partnership of ESO (representing its member states), NSF (USA), and NINS (Japan), together with NRC (Canada), MOST and ASIAA (Taiwan), and KASI (Republic of Korea), in cooperation with the Republic of Chile.
The Joint ALMA Observatory is operated by ESO, AUI/NRAO, and NAOJ.

References

1 Tan J. C., Beltrán M. T., Caselli P., Fontani F., Krumholz M. R., McKee C. F., & Stolte A. (2014) *Massive star formation* [arXiv preprint]. arXiv. https://doi.org/10.48550/arXiv.1402.0919

2 Berdikhan D., Esimbek J., Henkel C., Zhou J., Tang X., Liu T., Wu G., Li D., He Y., Komesh T., Tursun K., Zhou D., Imanaly E., & Jandaolet Q. (2024) Ammonia observations of Planck cold cores. *Astronomy & Astrophysics,* 684, A144. https://doi.org/10.1051/0004-6361/202348381

3 Sailanbek S., Esimbek J., Henkel C., Sobolev A. M., Ladeyschikov D. A., Berdikhan D., Wu G., Zhou J., Tang X., He Y., Li D., Tursun K., Zhou D., Ma Y., Komesh T., Ibraimov M., & Adilzhan K. (2025) Ammonia survey of the BGPS sources with the Nanshan 26-m telescope. *Monthly Notices of the Royal Astronomical Society*, 539, 2987–3012. https://doi.org/10.1093/mnras/staf564

4 Fukui Y., Habe A., Inoue T., Enokiya R., & Tachihara K. (2021) Cloud–cloud collisions and triggered star formation. *Publications of the Astronomical Society of Japan, 73* (Supplement_1), S1–S34. https://doi.org/10.1093/pasj/psaa103

5 Berdikhan D., Esimbek J., Henkel C., Xu Y., Zhou J., Liu D. J., Abdikamalov E., Ma Y., Komesh T., He Y., Zhang W., Tang X., Wu G., Li D., Zhou D., Tursun K., Shen H., Imanaly E., Jandaolet Q., & Tuiakbayeva D. (2025)

Cloud-cloud collision and star formation in G013.313+0.193. *Astronomy & Astrophysics*, 699, A137. https://doi.org/10.1051/0004-6361/202453285

6 Li D., Henkel C., Kraus A., Tang X., Baan W., Esimbek J., Wang K., Wu G., Liu T., Sobolev A. M., Zhou J., He Y., & Komesh T. (2025) Evidence for Core–Core Collision in Barnard 68. *The Astrophysical Journal*. 985, 230. https://doi.org/10.3847/1538-4357/add326

7 Ussipov N., Akhmetali A., Zaidyn M., Akniyazova A., Sakan A., Kalambay M., & Shukirgaliyev B. (2024) Fractal dimension of star clusters. *Eurasian Physical Technical Journal, 21*(3), 108–116. https://doi.org/10.31489/2024No3/108-116

8 Ma Y., Zhou J., Esimbek J., Baan W., Li D., Tang X., He Y., Ji W., Zhou D., Wu G., Tursun K., & Komesh T. (2023) Gravitational collapse and accretion flows in the hub filament system G323.46-0.08. *Astronomy & Astrophysics,* 676, A15. https://doi.org/10.1051/0004-6361/202346248

9 He Y. X., Liu H. L., Tang X. D., Qin S. L., Zhou J. J., Esimbek J., Pan S. R., Li D. L., Zhao M. K., Ji W. G., & Komesh T. (2023) Investigating the globally collapsing hub–filament cloud G326.611+0.811. *The Astrophysical Journal,* 957, 61. https://doi.org/10.3847/1538-4357/acf766

10 Zhang W., Zhou J., Esimbek J., Baan W., He Y., Tang X., Li D., Ji W., Wu G., Ma Y., Li J., Zhou D., Tursun K., & Komesh T. (2024) Kinematics and star formation of hub-filament systems in W49A. *Astronomy & Astrophysics,* 688, A99. https://doi.org/10.1051/0004-6361/202348580

11 Meng D., Esimbek J., Henkel C., Zhou J., Wu G., Tang X., Li D., He Y., Komesh T., Ma Y., Tursun K., Zhou D., Baan W., Sobolev A. M., Sailanbek S., & Jandaolet Q. (2025) A case investigation of an end-dominated collapse and hub-filament system, G53. *Astronomy & Astrophysics,* 701, A155. https://doi.org/10.1051/0004-6361/202453390

12 Li D., Esimbek J., Zhou J., Baan W., Wu G., Tang X., Ji W., Yuan Y., He Y., & Komesh T. (2016) KOSMA ^{12}CO (2–1) and (3–2) observations toward Infrared Dark Clouds. *Astrophysics and Space Science*, 361, 220. https://doi.org/10.1007/s10509-016-2807-z

13 Shen H., Esimbek J., Henkel C., Xu Y., Zhou J., Li D., He Y., Tang X., Wu G., Komes T., Tursun K., Zhou D., Imanaly E., & Berdikhan D. (2024) Extended CO (1–0) survey and ammonia measurements towards two bubble regions in W5: Feedback on molecular gas and clumps. *Astronomy & Astrophysics*, 689, A140. https://doi.org/10.1051/0004-6361/202347972

14 Shen H., Esimbek J., Henkel C., Li D., Zhou J., He Y., Tang X., Wu G., Komes T., Tursun K., Zhou D., Ma Y., Sailanbek S., & Berdikhan D. (2025) Triggered and dispersed under feedback of super HII region W4. *Astronomy & Astrophysics,* 693, A21. https://doi.org/10.1051/0004-6361/202450914

15 Herbst E., & Van Dishoeck,E. F. (2009).*Complex organic interstellar molecules. Annual Review of Astronomy and Astrophysics, 47*(1), 427–480. https://doi.org/10.1146/annurev-astro-082708-101654

16 Kalenskii S. V., Promislov V. G., Alakoz A., Winnberg A. V., & Johansson L. E. (2000) Probing the properties of methyl cyanide sources. *Astronomy and Astrophysics,* 354, 1036-1040. https://ui.adsabs.harvard.edu/abs/2000A&A...354.1036K

17 Komesh T., Esimbek J., Baan W., Zhou J., Li D., Wu G., He Y., Sailanbek S., Tang X., & Manapbayeva A. (2019) *H_2CO and H110α observations toward the Aquila Molecular Cloud. The Astrophysical Journal, 874*(2), 172. https://doi.org/10.3847/1538-4357/ab0ae3

18 Komesh T., Baan W., Esimbek J., Zhou J., Li D., Wu G., He Y., Rosli Z., & Ibraimov M. (2020) Studies of the distinct regions due to CO selective dissociation in the Aquila molecular cloud. *Astronomy & Astrophysics*, 644, A46. https://doi.org/10.1051/0004-6361/202038632

19 Mahmut U., Esimbek J., Baan W., Tang X., Zhou J., Li D., Yuxin H., Tursun K., Li J., Komesh T., & Sailanbek S. (2024) Formaldehyde observations of the Perseus Molecular Cloud. *Monthly Notices of the Royal Astronomical Society*, 528, 577–595. https://doi.org/10.1093/mnras/stad3959

20 Bu J., Esimbek J., Zhou J., Komesh T., Tang X., Li D., He Y., Tursun K., Zhou D., Imanaly E., & Sailanbek S. (2024) Calculating the Excitation Temperature for H_2CO Absorption Lines in Molecular Clouds. *Research in Astronomy and Astrophysics,* 24, 075022. https://doi.org/10.1088/1674-4527/ad5b36

21 Imanaly E., Esimbek J., Baan W., Wu G., Zhou J., Li D., Tang X., He Y., Komesh T., Zhou D., Tursun K., Ma Y., Berdikhan D., Sobolev A. M., & Jandaolet Q. (2025) Formaldehyde in the Cygnus-X region. *Monthly Notices of the Royal Astronomical Society,* 542, 2074–2086. https://doi.org/10.1093/mnras/staf1346

22 Smits D. P. (2003) *Monitoring of 6-cm excited OH masers—II. Monthly Notices of the Royal Astronomical Society,* 339(1), 1–11. https://doi.org/10.1046/j.1365-8711.2003.06096.x

23 Sakai T., Shiomura N., Sanhueza P., Furuya K., Olguin F. A., Tatematsu K. I., Aikawa Y., Taniguchi K., Chen H. R. V., Morii K., Nakamura F., Li S., Lu X., Zhang Q., Hirota T., Ishihara K., Ke H., Sakai N., & Yamamoto S. (2025) Digging Into the Interior of Hot Cores with ALMA (DIHCA). V. Deuterium Fractionation of Methanol. *The Astrophysical Journal,* 983, 37. https://doi.org/10.3847/1538-4357/adba5a

24 He Y. X., Zhou J. J., Esimbek J., Ji W. G., Wu G., Tang X. D., Yuan Y., & Baan W. A. (2015) Infall motions in massive star-forming regions: results from years 1 and 2 of the MALT90 survey. *Monthly Notices of the Royal Astronomical Society*, 450, 1926–1936. https://doi.org/10.1093/mnras/stv732

25 Abdullayev Z., Komesh T., Grossan B., Abdikamalov E., Maksut Z., Krugov M., Myrzakul S., & Tuiakbayeva D. (2025) Early-time optical spectral shape measurements of GRB 200925B. Revista Mexicana de Astronomía y Astrofísica (Serie de Conferencias), 59, 109–113. https://doi.org/10.22201/ia.14052059p.2025.59.20

26 McMullin J. P., Waters B. S. D. Y. W. G. K., Schiebel D., Young W., & Golap K. (2007). CASA architecture and applications. *In Astronomical data analysis software and systems XVI* (Vol. 376, p. 127). https://adsabs.harvard.edu/full/2007ASPC..376..127M

27 Komesh T., Omar A., Garay G., Assembay Z., Alimgazinova N., Zhumabay N., & Kyzgarina M. (2021) *ALMA observations of the environments of G333.0162+00.7615.* In T. Wong & W.-T. Kim (Eds.), *Proceedings of the International Astronomical Union* (Vol. 17, pp. 35–38). Cambridge University Press. https://doi.org/10.1017/S1743921323000121

28 Omar A., Abdirakhman A., Alimgazinova N., Kyzgarina M., Naurzbayeva A., Islyam Z., Turekhanova K., Demessinova A., & Manapbayeva A. (2025) ALMA Observations of G333.6-0.2: Molecular and Ionized Gas Environment. Galaxies. 13, 73. https://doi.org/10.3390/galaxies13040073

29 Assembay Z., Komesh T., Garay G., Omar A., Esimbek J., Alimgazinova N., Kyzgarina M., & Murat S. (2022) *ALMA observations of the environments of G301.1364-00.2249 A.* In T. Hirota, H. Imai, K. Menten, & Y. Pihlström (Eds.), *Proceedings of the International Astronomical Union* (Vol. 18, S380, pp. 204–206). Cambridge University Press. https://doi.org/10.1017/S1743921323002624

30 Hales A. S., Gupta A., Ruíz-Rodríguez D., Williams J. P., Pérez S., Cieza L., González-Ruilova C., Pineda J. E., Santamaría-Miranda A., Tobin J., Weber P., Zhu Z., & Zurlo A. (2024) Discovery of an accretion streamer and a slow wide-angle outflow around FU Orionis. *The Astrophysical Journal*, 966, 96. https://doi.org/10.3847/1538-4357/ad31a1

31 Komesh T., Garay G., Henkel C., Omar A., Estalella R., Assembay Z., Li D., Guzmán A., Esimbek J., Huang J., He Y., Alimgazinova N., Kyzgarina M., Bekdaulet S., Zhumabay N., & Manapbayeva A. (2024) Infall motions in the hot core associated with the hypercompact H II region G345.0061+01.794 B. *The Astrophysical Journal*, 967, 15. https://doi.org/10.3847/1538-4357/ad3e7b

32 Hoang T. D., Lee M. Y., Wyrowski F., Karska A., Navarete F., & Menten K. M. (2025) ATLASGAL-selected high-mass clumps in the inner Galaxy: XI. Morphology and kinematics of warm inner envelopes. *Astronomy & Astrophysics, 695,* A24. https://doi.org/10.1051/0004-6361/202452371

33 Martín S., Martín-Pintado J., Blanco-Sánchez C., Rivilla V. M., Rodríguez-Franco A., & Rico-Villas F. (2019) Spectral line identification and modelling (SLIM) in the MAdrid Data CUBe analysis (MADCUBA) package: Interactive software for data cube analysis. *Astronomy & Astrophysics, 631,* A159. https://doi.org/10.1051/0004-6361/201936144

34 Andron I., Gratier P., Majumdar L., Vidal T. H. G., Coutens A., Loison J.-C., & Wakelam V. (2018) Methyl cyanide (CH_3CN) and propyne (CH_3CCH) in the low-mass protostar IRAS 16293–2422. *Monthly Notices of the Royal Astronomical Society,* 481(4), 5651–5659. https://doi.org/10.1093/mnras/sty2680

AUTHORS' INFORMATION

Abdirakhman, Aidana A. — Master's student, Faculty of Physics and Technology, Al-Farabi Kazakh National University, Almaty, Kazakhstan; Scopus Author ID: 60077369400; https://orcid.org/0009-0002-0532-964; armiyaqyzyaidana@gmail.com.

Omar, Aruzhan Zh. — PhD, Senior lecturer, Faculty of Physics and Technology, Al Farabi Kazakh National University, Almaty, Kazakhstan; Scopus Author ID: 58420497300; https://orcid.org/0000-0002-5604-3742; omaruzhan@gmail.com.

Alimgazinova, Nazgul Zh. — Candidate of physical and mathematical sciences, Associate Professor, Faculty of Physics and Technology, al Farabi Kazakh National University, Almaty, Kazakhstan; Scopus Author ID: 35298349000; https://orcid.org/0000-0002-4596-1855; Nazgul.Alimgazinova@kaznu.kz.

Tuiakbayeva, Duriya R. — Master (Sci.), Sh. Ualikhanov Kokshetau University, Kokshetau, Kazakhstan; Scopus Author ID: 58829147000; https://orcid.org/0009-0003-8572-1850

Baitursyn, Darkhan Y. — Master (Eng.), Astana Motors Manufacturing Kazakhstan, Almaty, Kazakhstan; https://orcid.org/0009-0007-7398-4222; baitursyndarhan@gmail.com.

EURASIAN PHYSICAL TECHNICAL JOURNAL

2026, Volume 23, No. 1 (55)

https://doi.org/10.31489/2026N1/138-144

EURASIAN PHYSICAL TECHNICAL JOURNAL

Received: 06/11/2025 Revised: 13/03/2026 Accepted: 19/03/2026

Original Research Article

UDC 53.096; 524.354

PHONON DYNAMICS IN NEUTRON STAR CRUSTS AND THEIR CONNECTION TO PULSAR GLITCHES

Nasirova D.M.[1], Kurmangaliyeva V.O.[2] , Gazizova A.A.[1,*], Takibayev N.Zh.[2], Odsuren M.[3]

[1] Abai Kazakh National Pedagogical University, Almaty, Kazakhstan
[2] al-Farabi Kazakh National University, Almaty, Kazakhstan
[3] National University of Mongolia, Ulaanbaatar, Mongolia

* *Corresponding author:* askarkyzy_94@mail.ru

Abstract. *This paper investigates the role of phonon dynamics in the solid crust of neutron stars and their connection to large-scale structural instabilities. Electron capture reactions in the dense outer layers of compact stars generate excited nuclei, which may transfer their energy to the lattice in the form of phonons. These vibrational modes affect the elastic response of the crust, modifying its stress–strain behavior under extreme astrophysical conditions. Using fundamental parameters such as Young's modulus, density, and sound velocity, we estimate phonon frequencies, wave numbers, and lifetimes across different crustal layers. Numerical analysis indicates that phonon excitations are capable of storing elastic energy and may act as precursors of sudden stress release events. A special focus is given to pulsar glitches, with the Vela pulsar serving as a representative example. The comparison between calculated phonon energies and observed glitch energetics suggests that collective phonon processes could contribute to the mechanism of these abrupt rotational irregularities. By emphasizing the importance of lattice dynamics in neutron star models, this work provides the first quantitative estimates linking microscopic phonon excitations with macroscopic glitch energetics, thus contributing to a deeper understanding of how nuclear-scale transitions manifest as observable astrophysical signals. These findings can contribute to future models of neutron star crust dynamics and related astrophysical observations.*

Keywords: neutron stars, neutron star crust, phonons, electron capture, elastic properties, starquakes, pulsar glitches.

1. Introduction

Neutron stars are among the densest objects in the Universe. Their masses slightly exceed that of the Sun, yet they are compressed into a sphere only 10–15 km in radius [1]. They are the remnants of massive stellar collapses. They exhibit extremely high densities on the order of $\rho \geq 10^{12} - 10^{14}\ g/cm^3$ comparable to that of an atomic nucleus [2]. Their internal structure consists of ultra dense neutron matter, while the outer layers form a solid crystalline crust composed of heavy nuclei embedded in a degenerate electron background. The crust plays a crucial role in the star's dynamical processes, including the mechanisms of starquakes - sudden seismic-like events accompanied by the release of enormous amounts of energy [3].

One of the key processes governing the physical properties of the neutron star crust is electron capture [4], which occurs in its deeper layers. As density increases, electrons acquire sufficiently high energies to be captured by heavy nuclei, thereby transforming them into more neutron-rich isotopes. These reactions produce excited nuclear states that can transfer their energy to the crystal lattice in the form of phonons - quasiparticles responsible for elastic vibrations of the crystalline lattice [2, 5]. Such processes affect the elastic and transport properties of the crust [1, 6, 7].

The phonon dynamics within the neutron star crust determine the transport and dissipation of energy. They may also be associated with the emergence of macroscopic deformations that lead to starquakes. Investigating phonon spectra and their relation to the elastic properties of neutron star matter provides deeper insight into the mechanisms of stress accumulation and energy redistribution in the crust. These processes may play a fundamental role in the interpretation of observable astrophysical phenomena such as gravitational-wave events, sudden changes in pulsar rotation (glitches), and X-ray bursts [3, 8]. Glitches represent one of the few observable manifestations that provide direct information about the internal structure of neutron stars; thus, their study is essential for understanding the physics of dense matter. Pulsar glitches are thought to involve sudden release of crustal stresses [3, 9].

Therefore, the investigation of phonon dynamics induced by electron capture reactions constitutes an important direction in neutron star astrophysics, enabling a link between the microphysics of dense matter and its macroscopic astrophysical manifestations.

2. Methods and numerical experiment

The primary objective of this work is to investigate the phonon dynamics in the neutron star crust induced by electron capture reactions and their connection to the elastic properties of stellar matter. In particular, comparative estimates are provided for the mechanisms of phonon excitation resulting from nuclear transitions, as described in [4], their propagation within the crystalline structure of the crust, and their possible influence on global structural disturbances of the star, including starquakes. The investigation of phonon spectra and their relation to the elastic characteristics of neutron star matter provides valuable insights into the mechanisms of stress accumulation and energy redistribution within the crust.

During electron capture, excited nuclear states transfer energy to the lattice as phonons. In the crystalline crust of a neutron star, we consider longitudinal (acoustic) phonons whose dispersion in the long-wavelength limit is linear. In the present work we focus on longitudinal acoustic phonons as a first-order approximation, since they are directly associated with density perturbations in the crystalline lattice. The dispersion relation and the sound velocity are given by

$$V_s = \sqrt{\frac{E}{\rho}}, \omega_k = V_s k \tag{1}$$

where $E$is the Young's modulus of the crust, ρ is the mass density, V_s is the sound velocity, ω_k is the phonon frequency, and k is the wave number. Typical values used in our estimates are E = 10^{30}–10^{31} dyn/cm² for the Young's modulus and ρ ~ 10^{11}–10^{14} g/cm³ for the density, ranging from the outer to the inner crust [2, 10, 11]. These parameters determine the sound velocity and, in turn, the characteristic phonon frequencies. Detailed discussions of dense matter equations of state can be found in [2, 11]. For characteristic wave numbers $k \sim 10^8 - 10^{10} cm^{-1}$, the phonon frequencies lie in the range $\omega_k \sim 10^{20} - 10^{22} s^{-1}$ (see Table 1), consistent with possible interactions with excited nuclei [2, 6]. The characteristic wave number can be estimated as $k \approx \pi/L$, where L represents the typical spatial scale of stress redistribution in the neutron-star crust. Table 1 shows that phonon frequencies increase with density, reflecting the stiffer lattice in the inner crust. This analysis demonstrates how energy transfer from nuclear excitations is mediated by phonons in both outer and inner crust layers.

Table 1. Physical parameters of neutron star crust layers.

Region of crust	Density ρ (g/cm³)	Young's modulus E (dyn/cm²)	Sound velocity V_s (cm/s)	Wave vector k (cm^{-1})	Phonon frequency ω (Hz)
Outer crust	10^9-10^{11}	10^{30}-10^{31}	~10^8	10^{10}	~10^{18}-10^{19}
Inner crust	10^{12}-10^{14}	10^{31}-10^{32}	~10^9	10^{11}-10^{12}	~10^{20}-10^{22}

.

Phonons may decay due to scattering in interactions with neutrons as well as through other processes. For an order-of-magnitude estimate of the phonon lifetime τ, we write:

$$\tau \sim \frac{1}{\Gamma} \tag{2}$$

where Γ is the phonon damping width. For order-of-magnitude estimates we assume $\Gamma \sim 10^{8} - 10^{10} \mathrm{s}^{-1}$. Substituting these values gives phonon lifetimes in the range $\tau \sim 10^{-8} - 10^{-6}\mathrm{s}$ [1, 6].

This indicates that the excited phonons may exist long enough to participate in starquakes. Similar estimates of phonon damping in the neutron star crust are discussed by Chamel [1], where the dispersion and damping of collective excitations, including phonons, are studied. It is shown that, due to the strong mixing of drifting and elastic modes, both the phonon density of states and their propagation length are significantly modified. The aforementioned studies provide a detailed treatment of the methods for calculating phonon dispersions in the crystalline crust, taking into account the Young's modulus, matter density, and nuclear structure parameters in agreement with recent estimates of crustal elasticity [1, 6]. It is demonstrated that the range of permissible wave numbers is determined both by the intrinsic properties of the crust - such as lattice rigidity and density - and by external conditions, including temperature, magnetic field strength, and defect distribution. These effects have also been addressed in recent theoretical models. In particular, Baiko [12] points out that 10^{12} cm^{-1}, nonlinear effects in the dispersion relation begin to manifest, which may lead to local variations in propagation velocities and enhanced scattering. These results are of considerable importance for modeling the elastic properties of the crust and for predicting oscillation spectra under astrophysical perturbations.

The evaluation of phonon energy yields the following picture. We employ the expression

$$E = \hbar \cdot \omega_k. \tag{3}$$

Substituting $\hbar \approx 6{,}582 \times 10^{-22}\ \mathrm{MeV} \cdot \mathrm{s}$ and $\omega_k \approx 10^{19}\ \mathrm{s}^{-1}$, we obtain:

$$E \approx (6{,}582 \times 10^{-22}) \times (10^{19})\ \mathrm{MeV} \approx 6{,}58 \times 10^{-3}\ \mathrm{MeV} \approx 6{,}6 \times 10^{-3}\ \mathrm{MeV} \approx 6.6\ \mathrm{keV}. \tag{4}$$

This corresponds to approximately 6.6 keV. Energies of this order may interact with low-energy nuclear or lattice excitations in the neutron-star crust. Even when considering an ensemble of $N \approx 10^{30}$ such phonons, the total energy amounts to $E \approx 10^{26}\ \mathrm{eV} \approx 1{,}6 \times 10^{7}$ erg.

These estimates can be employed to discuss the potential role of phonons in starquakes, where they may excite elastic waves in the crust and contribute to the redistribution of the stored energy.

Consider the Vela pulsar (PSR J0835–4510), a relatively young object with a rotation period $P \approx 89$ ms and a distance of ~ 800 light years. It is known to exhibit sudden spin-up events (glitches) with a typical relative magnitude $\frac{\Delta\nu}{\nu} \approx 10^{-6}$ [3]. If a glitch is attributed to the sudden release of elastic energy stored in the crust, the corresponding change in the star's rotational energy can be estimated as

$$E \approx \frac{1}{2} I \cdot (\Delta\Omega)^2, \tag{5}$$

where $I \approx 10^{45}\ \mathrm{g} \cdot \mathrm{cm}^2$ — is the neutron-star moment of inertia, and $\Delta\Omega/\Omega \approx 10^{-6}$

$$E \approx 0{,}5 \times 10^{45} \times (10^{-6} \times \Omega)^2,$$

$$\Omega \approx 2\pi/P \approx 70{,}6\ \mathrm{rad/s} \rightarrow \Delta\Omega \approx 7{,}06 \times 10^{-5}\ \mathrm{rad/s},$$

$$E \approx 0{,}5 \times 10^{45} \times (4{,}98 \times 10^{-9}) \approx 2{,}49 \times 10^{36}\ \mathrm{erg}.$$

The comparison demonstrates that the energy of a typical glitch ($\sim 10^{36}$ erg) exceeds the energy stored in an ensemble of 10^{30} phonons ($\sim 10^{7}$ erg) by roughly 29 orders of magnitude. This indicates that, for phonons to contribute meaningfully to the glitch energy budget, either an enormously larger number of excitations must be involved or mechanisms of collective phonon interactions need to be invoked.

Our calculations, summarized in Table 1, indicate that phonon oscillations may span the frequency range $10^{19} - 10^{22}$ Hz. The energy of a single phonon is estimated as $E_{phonon} = 6$ keV, while the total energy associated with phonon processes can be evaluated in terms of the accumulated stresses within the crust. The connection between the calculated phonon oscillations and pulsar observations lies in the possibility that stresses may accumulate in the crust due to phonon excitations [8].

In this case, the energy released during structural oscillations should be comparable to the elastic energy stored in the crust [5]. A rough estimate of the accumulated elastic energy in the crust can be made as follows:

$$E_{elast.} \approx \frac{1}{2} E \varepsilon^2 V \tag{6}$$

where E is the Young's modulus, ε is the characteristic strain, and V is the volume of the crust.

Using the values of the Young's modulus from Table 1 and adopting typical parameters $\varepsilon \approx 10^{-4}$, $V \approx 10^{18} cm^3$ we obtain $E_{elast.} \approx 10^{41} erg = E_{glitch}$ - which is of the same order as the energy released during a glitch. This indicates that the elastic stresses accumulated in the crust can, in principle, account for the observed energetics of pulsar glitches. The accumulation of elastic stresses occurs over long-time scales (months to years), whereas phonon perturbations propagate on much shorter time scales determined by the sound velocity. Figure 1 shows the time evolution of the total elastic energy stored in the crust under constant stress. The linear increase suggests that stress accumulation may contribute to starquakes associated with pulsar glitches.

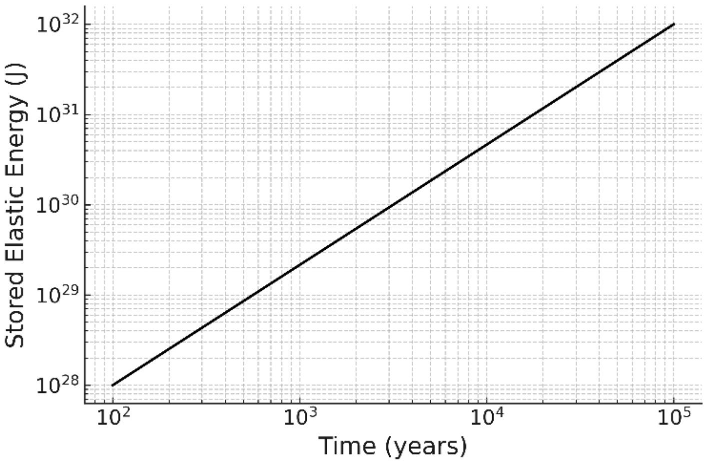

Fig.1. Energy accumulation in the crust of a neutron star.

Accumulation of elastic energy in the neutron-star crust over time under constant average stress, showing potential for triggering starquakes (glitches). This model is based on the expression for the elastic strain energy density. The accumulated energy over $10^4 - 10^6$ years can reach values of $10^{39} - 10^{41}$ erg – which is comparable to the energy released during glitches. This provides quantitative evidence that stress accumulation processes in the neutron star crust may serve as a source of starquakes (glitches), provided that a sudden release of energy occurs. The plot demonstrates the growth of accumulated elastic energy in the crystalline crust of a neutron star as a function of time, under the assumption of constant average stress. The model is derived from the relation for elastic energy density.

$$u = \frac{1}{2} \sigma \varepsilon \tag{7}$$

where σ is the mechanical stress and ε is the elastic strain.

By integrating this quantity over the crust volume, one obtains a linear dependence of the total accumulated energy on time under the assumption of a constant strain rate. Moreover, the modeling results are consistent with estimates derived from observational data on frequency glitches in pulsars such as PSR J0835–4510 (Vela), reinforcing the hypothesis that elastic processes in the crust play a key role in the glitch mechanism. Fig. 2 shows phonon frequency spectrum in the neutron-star crust, showing a peak at $\sim 10^{19}$ Hz corresponding to lattice oscillations in ultra-dense matter. Although these frequencies are much higher than

.

typical macroscopic observables such as pulsar glitches, the cumulative effect of phonon processes may contribute to energy transport and stress redistribution within the crust.

Figure 3 shows the modeled phonon density of states compared with astrophysical scales. The comparison demonstrates that phonon frequencies in the crust span a wide range ($10^{19} - 10^{22}$ Hz) and may contribute to the accumulation of elastic energy.

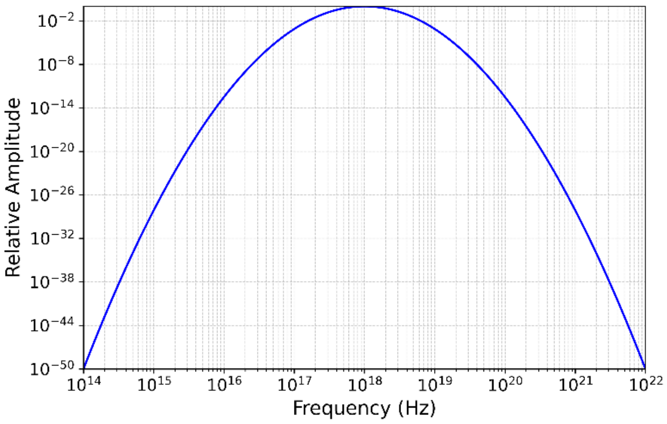

Fig. 2. Phonon frequency spectrum in the neutron star crust.

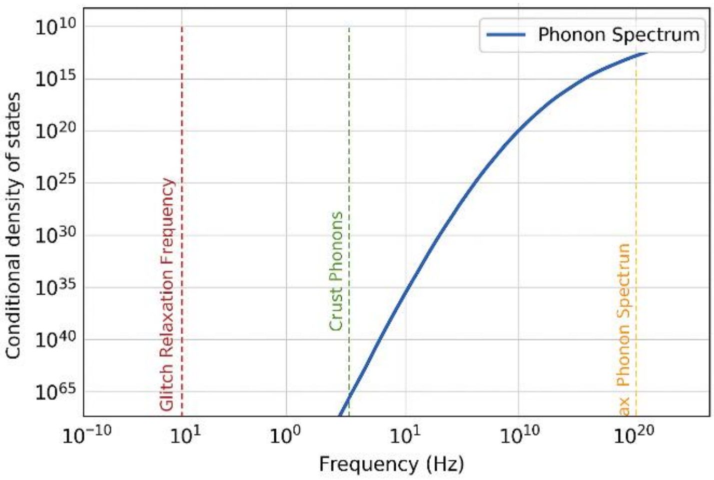

Fig. 3. Model phonon density of states compared with astrophysical scales.

The presented illustrations are based on the theory of elasticity, phonon dispersion, and available astrophysical observations, and are constructed using physically motivated scaling relations applicable to dense matter in the crust of neutron stars. While the adopted models are necessarily simplified, they reproduce the principal dependencies between density, elastic properties, and vibrational modes. Therefore, the obtained results should be regarded primarily as order-of-magnitude estimates rather than precise quantitative predictions.

3. Results and discussion

Our estimates for phonon energies and lifetimes are consistent with recent microphysical studies of lattice excitations in neutron star crusts [1, 2, 6]. Using typical lattice parameters, the energy of a single phonon in the inner crust is on the order of 10^{-4} $-$MeV, while lifetimes can reach 10^{-8}–10^{-6}s [1, 6]. These results confirm that phonons can strongly interact with both nuclear clusters and superfluid components, leading to complex dispersion relations and damping mechanisms.

Compared to previous studies, our work extends the analysis by evaluating the potential energetic contribution of collective phonon excitations to pulsar glitches. Although a single phonon carries negligible energy relative to a typical glitch ($\sim 10^{36}$ erg), the cumulative effect of coherent phonon modes over the entire crust volume ($V \sim 10^{18} cm^3$) can contribute up to 10^{41}erg, comparable to observed glitch energetics [3, 5].

This suggests that microscopic lattice dynamics may act as a trigger for macroscopic structural failures, bridging nuclear microphysics and observable pulsar phenomena [9, 13, 14].

Our findings align with [5], who highlighted the role of superfluid elasticity in storing and releasing energy, and with [4], who modeled electron capture reactions as sources of phonon excitations. These results are also consistent with studies of shear properties and seismic activity in neutron star crusts [15].

Moreover, comparison with observational glitch statistics [3, 8] indicates that phonon-mediated stress accumulation may partially account for the frequency and magnitude of glitch events.

The limitations of our model include a simplified treatment of lattice parameters, neglect of magnetic field effects, lattice defects, and coupling with superfluid components. Future work should incorporate these factors and examine whether collective phonon processes can reliably provide the energy required for glitch events, potentially through numerical simulations and more detailed microscopic modeling.

4. Conclusion

In this study, we investigated the phonon dynamics in the crust of neutron stars and their possible contribution to structural instabilities induced by electron-capture reactions. Our results demonstrate that nuclei in excited states can induce collective phonon oscillations, with their frequencies corresponding to nuclear-scale transitions. The calculated lifetimes suggest that phonons can persist long enough to participate in stress accumulation processes.

Although the energy of a single phonon is extremely small compared with the energy released during observed glitches, their collective action and the associated accumulation of elastic stresses in the crust may contribute significantly to the total energy budget. This result highlights the importance of including lattice dynamics in neutron star models and suggests that microscopic nuclear processes may leave observable imprints on macroscopic astrophysical phenomena such as starquakes, glitches, and possibly gravitational-wave or X-ray bursts.

Future investigations should incorporate the effects of magnetic fields, superfluid coupling, and realistic crust-failure scenarios. This will help to determine whether phonon processes can indeed connect microscopic excitations with macroscopic astrophysical signals.

Conflict of interest statement

The authors declare that they have no conflict of interest in relation to this research, whether financial, personal, authorship or otherwise, that could affect the research and its results presented in this paper.

CRediT author statement

Nasirova D.M.: Writing-Original draft preparation, Methodology, Writing - Review & Editing. **Gazizova A.**: Visualization, Formal Analys; **Takibayev N.Zh.**: Conceptualization, Methodology; **Kurmangaliyeva V.O., Odsuren M.**: Data Curation, Investigation. The final manuscript was read and approved by all authors.

Acknowledgments

The authors acknowledge the support from Abai Kazakh National Pedagogical University, Order No. 05-04/250 dated 3 April 2025.

References

1 Chamel N. (2013) Collective modes in the inner crust of neutron stars. *Physical Review C,* 87, 035803. https://doi.org/10.1103/PhysRevC.87.035803

2 Haensel P., Potekhin A. Y., & Yakovlev D. G. (2007) Neutron stars 1: Equation of state and structure (Astrophysics and Space Science Library, Vol. 326). Springer. https://doi.org/10.1007/978-0-387-47301-0

3 Espinoza C. M., Lyne A. G., Stappers B. W., & Kramer M. (2011) A study of 315 glitches in the rotation of 102 pulsars. *Monthly Notices of the Royal Astronomical Society*, 414, 1679–1704. https://doi.org/10.1111/j.1365-2966.2011.18503.x

4 Takibayev N., Nasirova D., Kato K., & Kurmangaliyeva V. (2018) Electron capture reactions in neutron star crusts. *Journal of Physics: Conference Series*, 940(1), 012058. https://doi.org/10.1088/1742-6596/940/1/012058

5 Chamel N., & Carter B. (2025) Superfluid elasticity in neutron star matter. *Physical Review C*, 111, 045801. https://doi.org/10.1103/PhysRevC.111.045801

6 Baiko D. A. (2024) Elastic properties and lattice dynamics of the neutron star crust. *Monthly Notices of the Royal Astronomical Society*, 528, 408. https://doi.org/10.1093/mnras/stad3109

7 Kobyakov D., & Pethick C. (2013) Elastic properties of dense matter in neutron star crusts. *Physical Review C,* 87, 055803. https://doi.org/10.1103/PhysRevC.87.055803

8 Yu M., Manchester R. N., Hobbs G., & Johnston S. (2013) The Parkes pulsar timing array: Glitch statistics. *Monthly Notices of the Royal Astronomical Society*, 429, 688–700. https://doi.org/10.1093/mnras/stt1522

9 Sotani H., & Takiwaki T. (2025) Elastic and magnetohydrodynamic instabilities in neutron star crusts. *Physical Review D,* 111, 103019. https://doi.org/10.1103/PhysRevD.111.103019

10 Shapiro S. L., & Teukolsky S. A. (1983) Black holes, white dwarfs, and neutron stars: The physics of compact objects. Wiley VCH. https://doi.org/10.1002/9783527617668

11 Yakovlev D. G. (2016) Equation of state and nuclear models of dense matter. *International Journal of Modern Physics A*, 31, 1641017. https://doi.org/10.1142/S0217751X16410177

12 Baiko D. A. (2024) Collective oscillations in dense stellar matter. *Communications in Theoretical Physics* (in press). Advance online publication. https://doi.org/10.1088/0253-6102/xx/xxx

13 Sotani H. (2023) Crustal oscillations and magnetic effects in neutron stars. *Physical Review D,* 107, 123025. https://doi.org/10.1103/PhysRevD.107.123025

14 Sotani H. (2024) Shear modes and magnetic coupling in neutron star crusts. *Physical Review D,* 109, 023030. https://doi.org/10.1103/PhysRevD.109.023030

15 Zemlyakov N. A., & Chugunov A. I. (2025) Shear properties and seismic activity of neutron star crusts. *Physical Review D,* 112, 043032. https://doi.org/10.1103/PhysRevD.112.043032

AUTHORS' INFORMATION

Nasirova, Diana – PhD, Associate professor, Department of Physics, Faculty of Mathematics, Physics and Informatics, Abay Kazakh National Pedagogical University, Almaty, Kazakhstan; SCOPUS ID: 55559630500, https://orcid.org/0000-0002-3349-0128, diana-nasirova@mail.ru

Kurmangaliyeva, Venera – Candidate of Physical and Mathematical Sciences, Associate professor, Department of Theoretical and Nuclear Physics, Faculty of Physics and Technology, Al-Farabi Kazakh National University, Almaty, Kazakhstan; SCOPUS ID: 57200796046, https://orcid.org/0000-0001-8046-8508, venera_baggi@mail.ru

Takibayev, Nurgali – Doctor of Physical and Mathematical Sciences, Professor, Department of Theoretical and Nuclear Physics, Faculty of Physics and Technology, Al-Farabi Kazakh National University, Almaty, Kazakhstan; SCOPUS ID: 24077239000; https://orcid.org/0000-0002-2604-6838, takibayev@gmail.com

Gazizova, Aisholpan – PhD student, Department of Physics, Faculty of Mathematics, Physics and Informatics, Abay Kazakh National Pedagogical University, Almaty, Kazakhstan; https://orcid.org/0009-0004-4849-5118, askarkyzy_94@mail.ru

Odsuren, Myagmarjav – PhD, Associate professor, School of Engineering and Applied Sciences, National University of Mongolia, Ulaanbaatar, Mongolia; SCOPUS ID: 26536315600; https://orcid.org/0000-0002-8863-9487, odsurenn@gmail.com

EURASIAN PHYSICAL TECHNICAL JOURNAL

2026, Volume 23, No. 1 (55)

https://doi.org/10.31489/2026N1/145-153

Received: 21/11/2025 Revised: 18/02/2026 Accepted: 19/03/2026

Original Research Article

UDC 53.01:524.3-52

KINEMATIC ANALYSIS OF THE MASSIVE STAR-FORMING REGION G328.2551-0.5321 VIA ALMA MOLECULAR LINE OBSERVATIONS

Islyam Zh.B.[1], Nodyarov A.S.[1], Demessinova A.M.[1,*], Manapbayeva A.B.[1,2],
Kyzgarina M.T.[1], Zhumabay N.[3]

[1] Al-Farabi Kazakh National University, Almaty, Kazakhstan
[2] Kazakh National Women's Teacher Training University, Almaty, Kazakhstan
[3] Abai Kazakh National Pedagogical University, Almaty, Kazakhstan
*Corresponding author: aizat.dem@gmail.com

Abstract. *This study reports on high-angular-resolution observations of the massive star-forming region G328.2551−0.5321 obtained with the Atacama Large Millimeter/submillimeter Array at a wavelength of 0.89 mm. The innermost core structure is investigated by targeting high-excitation transitions of methanol, sulfur dioxide, and its sulfur-34 isotopologue. Analysis of the molecular emission reveals a compact and dense methanol component located at the continuum peak, which is surrounded by more extended emission from sulfur-bearing molecules. Kinematic analysis demonstrates a coherent velocity gradient along the major axis of the system. Position–velocity diagrams exhibit a characteristic butterfly morphology, which is consistent with the presence of a Keplerian rotation. Numerical model fitting provides dynamical mass estimates of approximately twenty solar masses for the central object, confirming the existence of a massive, rotating disk-like structure. Rotational diagram analysis of methanol transitions yields a rotational temperature of 187.9 ± 23.7 Kelvin and a total column density of* 4.27×10^{16} *cm*$^{-2}$*, indicating the presence of a hot molecular core. These findings suggest that a high-mass protostar is actively accreting within a compact disk-envelope system embedded in a hot core environment. The results contribute to the understanding of the physical conditions and gas dynamics in the early stages of massive star formation.*

Keywords: star formation, ALMA millimeter/submillimeter interferometry, hot molecular core, individual object G328.2551–0.5321.

1. Introduction

Understanding the earliest stages of massive star formation is essential for constraining how these objects shape the physical, chemical, and dynamical evolution of their natal environments. Massive stars profoundly influence their surroundings through radiative, mechanical, and chemical feedback, yet the physical conditions and internal kinematics of the dense gas from which they form remain incompletely understood [1].

Observational studies using a wide range of molecular tracers have significantly advanced our knowledge of massive star-forming regions. Species such as NH_3 [2-4] and H_2CO [5,6] are widely used to diagnose gas temperature and density. Other molecules, including HNCO, SiO, and HC_3N, trace shocks, outflows, and chemical enrichment associated with massive protostellar activity [7]. These studies highlight that molecular lines provide a powerful means of probing the physical conditions and energetics in dense molecular clouds.

Kinematic studies play a central role in revealing the dynamical processes governing massive star formation. Infall motions, rotation, and large-scale accretion flows are key indicators of early gravitational collapse [8]. Many massive star-forming regions exhibit complex hub–filament networks, where converging flows feed material into central dense cores [9-11]. Signatures of bipolar outflows, traced by molecules such as SiO or CO, further demonstrate the dynamic nature of these systems. Feedback from nearby massive stars, including expanding H II regions, may additionally trigger or regulate subsequent star formation. Cloud–cloud or core–core collisions have also been proposed as mechanisms for generating dense massive cores [12,13]. Additionally, the study of high-energy phenomena such as gamma-ray bursts, including early-time optical spectral measurements of events like GRB 200925B, provides further insights into the late-stage evolution and explosive feedback of the most massive stars [14].

Despite this progress, the initial conditions of massive protostellar evolution – particularly in *mid-infrared-quiescent*, deeply embedded clumps – remain poorly constrained. In such early phases, hot molecular cores may already be forming, but the heating, chemistry, and kinematics at <1000 AU scales are still largely unknown [15]. Probing these regions requires molecular lines that selectively trace warm, dense gas close to the protostar. High-excitation transitions of SO_2, CH_3OH, and ^{34}SO are particularly well suited for this purpose, as they originate in hot cores and are sensitive to rotational motions and disk-like structures.

The target of this study, G328.2551−0.5321, provides an excellent laboratory for examining these processes. It is the only massive object embedded within the infrared dark cloud MSXDC G328.25−00.51, located at a distance of 2.5 kpc. The source was initially identified at 870 µm in the ATLASGAL survey [16-18] and later followed up with ALMA as part of the SPARKS project (Search for High-mass Protostars with ALMA Revealed up to Kilo-parsec Scales. Its systemic velocity of −43.1 km s^{-1} [19-20] and its mid-infrared quiescent nature strongly suggest a very early evolutionary stage, possibly preceding the emergence of an ultracompact H II region. Evidence for complex internal motions further indicates active mass accretion within the core. Furthermore, ALMA observations of the environments of G301.1364-00.2249A and G333.0162+00.7615 have revealed compact molecular cores with clear velocity gradients, indicating that rotational motion is a common feature of hot cores in the earliest stages of high-mass star formation [21, 22].

In this work, we present high-angular-resolution ALMA Band 7 observations of G328.2551−0.5321 targeting highly excited transitions of SO_2, CH_3OH and ^{34}SO. These molecular tracers allow us to investigate the small-scale kinematics and physical conditions of the hot molecular gas surrounding the high-mass protostar. Our analysis aims to characterize rotational structure, identify signatures of infall or disk-like motions, and provide new constraints on the earliest phases of massive star formation within this quiescent infrared dark cloud.

2. Observations and data reduction

The data analyzed in this study were retrieved from the Atacama Large Millimeter/submillimeter Array (ALMA) archive. Observations toward the star-forming region G328.2551−0.5321 (phase center: R.A. (J2000) = $15^h57^m59.791^s$, Dec. (J2000) = −53°58′00.560″) were carried out under project code 2018.1.01679.S between 2019 April 16 and 21. The array configuration provided baselines ranging from 37.7 m (L5) to 281.4 m (L80), yielding a maximum recoverable scale of 5.16″ and a primary beam of 17.06″. The total on-source integration time was 1632.96 s (≈ 0.45 hr), resulting in a synthesized beam size of 0.487″.

The correlator was configured to cover the 333.468–349.091 GHz frequency range (ALMA Band 7) with a total bandwidth of 16 GHz and a spectral resolution of 0.977 MHz, corresponding to a velocity resolution of 0.487 km s^{-1}. The achieved continuum sensitivity was 0.074 mJy beam^{-1}.

The raw visibility data were processed using the standard ALMA calibration pipeline (Pipeline-CASA54-P1-B, CASA version 5.4.0-70 42254M), which applies standard bandpass, flux and phase calibrations. The resulting calibrated measurement set was subsequently imaged and self-calibrated in the Common Astronomy Software Applications package (CASA) [23] to improve the signal-to-noise ratio.

3. Results and discussion

The 0.89 mm continuum emission toward G328.2551–0.5321 is shown in Figure 1. Continuum contours are drawn at 0.00267, 0.00405, 0.00615, 0.00934, 0.01418, 0.02152, 0.03267, and 0.04960 Jy beam^{-1}. The beam, indicated by the black ellipse in the lower-left corner, represents the angular resolution, while the white plus marks the continuum peak. From a two-dimensional Gaussian fit to the continuum emission performed in

CARTA, we derive a peak position of R.A. (J2000) = 15^{h}57^{m}59.799^s and Dec. (J2000) = −53°58′00.528″ ± 0.0043″. The fitted peak flux density is 0.0496 ± 0.0055 Jy beam^{-1}, with a deconvolved source size of 0.099 ± 0.010″ × 0.134 ± 0.016″ (major × minor axis). The integrated flux density is 0.141 ± 0.020 Jy.

Several masers and young stellar object (YSO) candidates are overlaid on the continuum map: Class I and II methanol masers and an OH maser are shown as colored triangles [24,25] the IRAS 15541–5349 YSO candidate is indicated with an orange dot, the extended green object (EGO) G328.25–0.53 is shown as a green dot and the massive core G328.2551–00.5321–MM1 is marked with a brown dot [26]. These objects are associated with the 0.89 mm continuum emission, but none of them coincides exactly with the continuum peak.

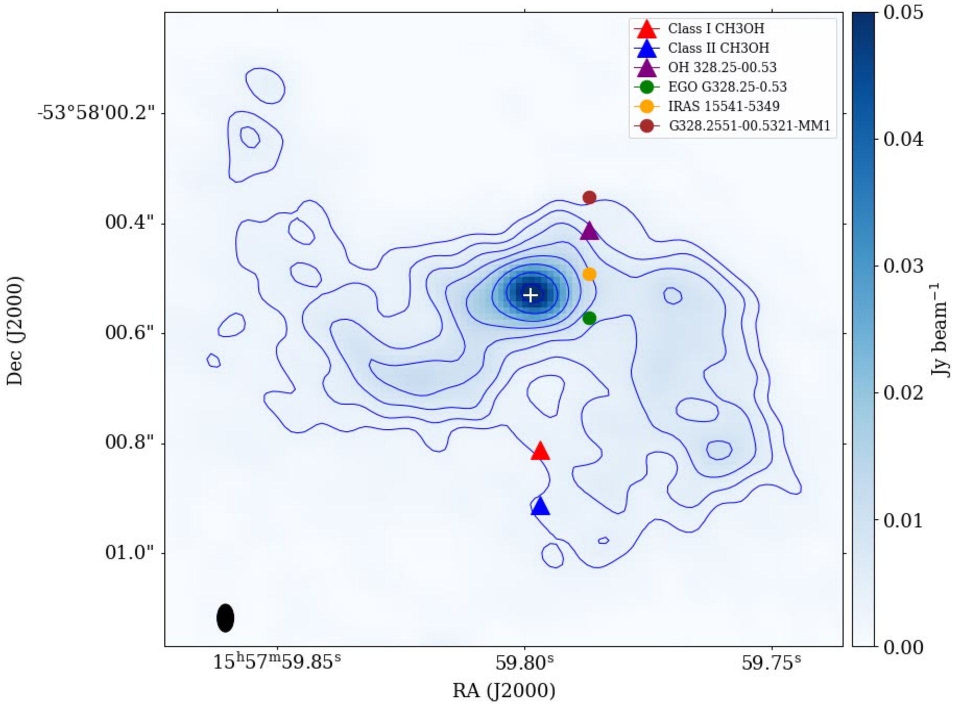

Fig.1. Continuum map toward G328.2551–0.5321 at 0.89 mm.

Figure 2 shows spectra of the SO_2 ($16_{4,12}$–$16_{3,13}$), CH_3OH ($12_{1,11}$–$12_{0,12}$ A) and ^{34}SO (7_8–6_7) molecular lines. Spectra taken directly at the continuum peak show noticeable asymmetry, likely caused by complex kinematic and structural effects near the emission maximum. To obtain representative line profiles, spectra were extracted from positions slightly offset from the continuum peak. These positions correspond to the intensity peaks of each molecular line in the integrated maps and cover regions about one synthesized beam in size. Gaussian profiles were fitted to all detected transitions. The spectral extraction and visualization were performed using CARTA [27]. The derived central upper-state energy (E_{up}/k), velocity (V_{LSR}), peak intensity (I_p) and full width at half maximum (FWHM; ΔV) are listed in Table 1.

Table 1. Observed line parameters toward G328.2551−0.5321

Molecule	Transition	Rest frequency (GHz)	E_u /k (K)	V_{LSR} (km/s)	I_p (Jy beam $^{-1}$)	ΔV (km s^{-1})
SO_2	16(4,12)–16(3,13)	346.523	166	−45.5 ± 0.12	0.7 ± 0.01	15 ± 0.3
CH_3OH	12(1,11)-12(0,12)A	336.864	197	−42.7 ± 0.06	0.8 ± 0.01	8.9 ± 0.14
^{34}SO	7(8) – 6(7)	333.902	81	−45.3 ± 0.07	0.29 ± 0.01	5.7 ± 0.17

Spectra extracted directly at the continuum peak exhibit noticeable asymmetry, likely due to complex kinematic and structural effects near the emission maximum. To obtain representative line profiles unaffected by these asymmetries, spectra were extracted from positions slightly offset from the continuum peak. These offsets correspond to the intensity maxima of each molecular line in the integrated maps and were taken from regions approximately one synthesized beam in size.

Figure 2 presents the averaged spectra of SO_2, CH_3OH, and ^{34}SO together with their Gaussian fits. The SO_2 line shows a slightly structured peak, with two closely spaced components, yet the profile remains broadly symmetric around the systemic velocity. The CH_3OH spectrum is well reproduced by a single Gaussian, exhibiting smooth and comparable blue and red wings. The optically thin ^{34}SO line displays a clean, symmetric Gaussian profile, indicating that it traces the intrinsic velocity field without significant radiative-transfer distortions. The generally symmetric shapes of all three lines suggest that the gas motions are dominated by ordered large-scale dynamics rather than irregular or multi-component structures.

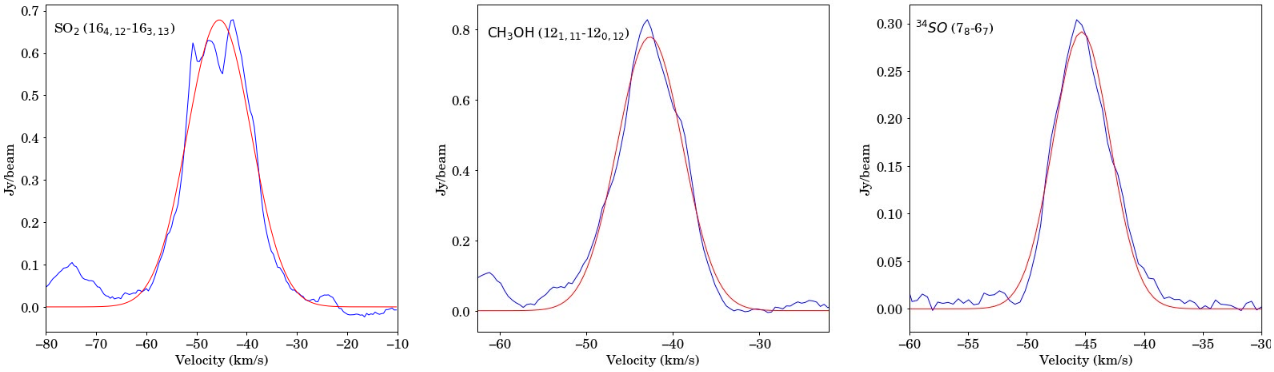

Fig.2. Molecular spectra with overlaid Gaussian fits. The blue curves represent the observed ALMA spectra, and the red curves show the multi-Gaussian fits.

Figure 3 shows the moment maps of integrated intensity, velocity and velocity dispersion, corresponding to moments 0, 1 and 2, of the $SO_2(16_{4,12}–16_{3,13})$, CH_3OH $(12_{1,11}–12_{0,12}$ A) and ^{34}SO $(7_8–6_7)$ emissions toward the G328.2551-0.5321 core. In the moment 0 map, the CH_3OH emission peak is shifted 0.089″ northeast of the continuum peak, with an integrated intensity of 12 Jy beam^{-1} km s^{-1}, whereas the ^{34}SO peak is offset 0.082″ to the northwest, reaching 4 Jy beam^{-1} km s^{-1}. The SO_2 emission peak coincides with the continuum peak and extends northward, attaining an integrated intensity of 15 Jy beam^{-1} km s^{-1}. The moment-1 maps of SO_2 $(16_{4,12}–16_{3,13}$; velocity range −51 km s^{-1} to −44 km s^{-1}) and ^{34}SO $(7_8–6_7$; velocity range −48 km s^{-1} to −39 km s^{-1}) display smooth west (blue-shifted) to east 4 (red-shifted) velocity gradients along PA = 98°, consistent with organized rotation. The corresponding moment-2 maps show enhanced turbulence near the core centers, with values of ~ 4–5 km^2 s^{-2} for SO_2 and ~ 10–15 km^2 s^{-2} for ^{34}SO. Both SO_2 and ^{34}SO show extended molecular line emission, indicating that these molecules are distributed over a relatively large region. In contrast, CH_3OH $(12_{1,11}–12_{0,12}$ A) exhibits compact emission coincident with the continuum peak, with a central velocity dispersion of ~7–7.5 km^2 s^{-2} that decreases outward, consistent with the findings of [25].

This compact morphology, spectral lines**,** combined with the observed velocity gradient, strongly supports the presence of a rotating structure, such as a circumstellar disk. To verify the velocity gradient seen in the moment-1 maps, a position–velocity (PV) diagram was extracted along PA = 98°, confirming that the emission follows the NE–SW direction.

Figure 4 presents the PV diagrams of the massive star-forming region G328.2551–0.5321 for the CH_3OH $(12_{1,11}–12_{0,12}$ A) and SO_2 $(16_{4,12}–16_{3,13})$ transitions. The velocity axes span roughly −55 km s^{-1} to −35 km s^{-1} for CH_3OH and −60 km s^{-1} to −35 km s^{-1} for SO_2. The systemic velocities, indicated by the dashed horizontal lines, are $V_0 \approx -45.135$ km s^{-1} for CH_3OH and $V_0 \approx -49.119$ km s^{-1} for SO_2. Similar PV structures observed in other massive cores, such as G333.6–0.2, exhibit clear velocity gradients along the major axis, providing strong evidence for the presence of rotating molecular envelopes or disk-like structures [28].

The dynamical mass (M_{dyn}) was estimated from the PV diagrams by applying the Keplerian rotation model, according to the following equation:

$$M_{dyn} = \frac{v^2 R}{G sin^2 i} \quad (1)$$

where v is the observed rotation velocity at an offset R, G is the gravitational constant, and i is the inclination angle of the disk (taken as 53.7° in this work).

The uncertainty in the dynamical mass was estimated by considering the propagation of errors in the main parameters of the Keplerian model, including the rotational velocity, radial distance, and disk inclination angle. Based on typical uncertainties in these quantities, the resulting uncertainty in the dynamical mass is on the order of 10–15%.

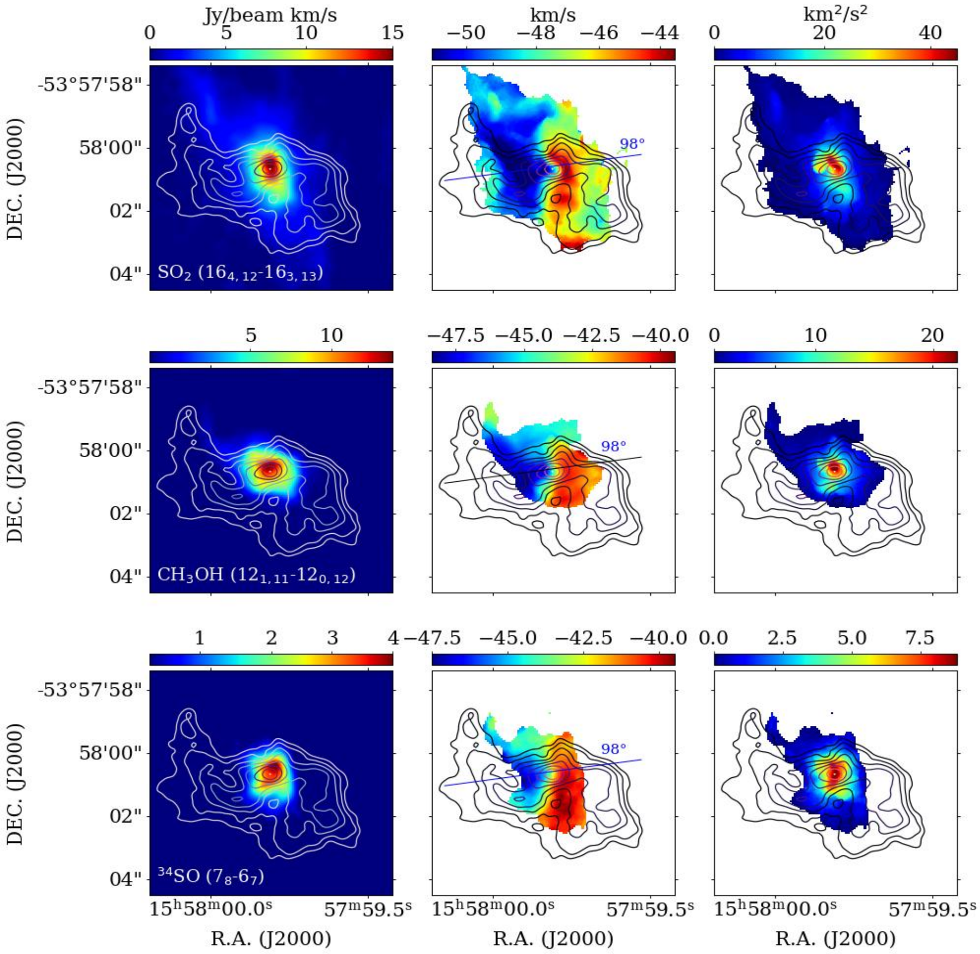

Fig.3. Moment 0, 1 and 2 maps of SO$_2$(16$_{4,12}$–16$_{3,13}$), CH$_3$OH (12$_{1,11}$–12$_{0,12}$ A) and ^{34}SO (7$_8$–6$_7$) emission toward G328.2551–0.5321 A. Contour levels are 0.00267, 0.00405, 0.00615, 0.00934, 0.01418, 0.02152, 0.03267 and 0.04960 Jy beam^{-1} km s^{-1}. The black ellipse in the lower-right panel denotes the synthesized beam.

The diagrams exhibit a pronounced, symmetric velocity gradient across the continuum major axis, with redshifted emission on one side and blue shifted emission on the other, producing the characteristic “butterfly” morphology expected for rotation. White curves on each panel represent a Keplerian disk model [29] with an inclination of $i \approx 53.7°$, which traces the bright emission ridge well. The inclination angle was derived from the deconvolved continuum ellipse. The fitted dynamical masses are $M \approx 20.5\ M_\odot$ for CH$_3$OH and $M \approx 23.2\ M_\odot$ for SO$_2$, indicating that the two tracers yield slightly different values. Small asymmetries in intensity and the presence of separate bright knots in SO$_2$ suggest that the two molecules likely trace somewhat different gas conditions or spatial regions within the rotating structure. These results are slightly higher but broadly consistent with the 10–20 M$_\odot$ range reported by [30], likely reflecting differences in tracer excitation and the adopted inclination.

Four transitions of CH$_3$OH have been detected toward G328.2551–0.5321. A rotation temperature diagram can therefore be used to estimate the rotational temperature and column density with Madrid Data CUBe Analysis.

The spectroscopic parameters of the detected CH$_3$OH transitions are listed in Table 2, including the transition designation, rest frequency, upper-state energy (E$_{up}$/k) and intensity. Figure 5 presents the rotational diagram for the methanol transitions observed toward the core.

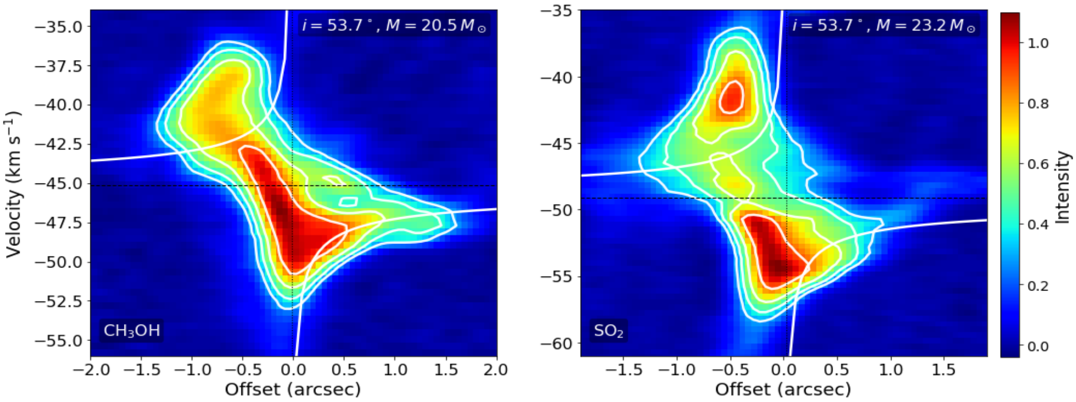

Fig.4. Position–velocity (PV) diagrams of the CH_3OH ($12_{2,11}$–$12_{0,12}$ A) and SO_2 ($16_{4,12}$–$16_{3,12}$) transitions toward G328.2551−0.5321, extracted along the major kinematic axis (i ≈ 53.7°). The white curves correspond to the Keplerian disk model.

Table 2. Parameters of CH_3OH (vt=0–2) molecular lines used for the rotational diagram analysis.

Molecule	Transitions	Rest Frequency (GHz)	E_{up}/k (K)	Peak intensity (K)	$\log_{10}(N_u/g_u)$
CH_3OH, vt=0–2	$3_{0,1}$–$2_{1,1}$	334.426571	125.51	0.53	5.7106
	$25_{3,1}$–$24_{2,1}$	334.679524	314.46	0.29	5.3496
	$2_{2,1}$–$3_{1,1}$	335.133570	1073.82	0.63	4.6465
	$9_{1,0}$–$8_{2,0}$	333.864722	44.67	0.05	5.6072

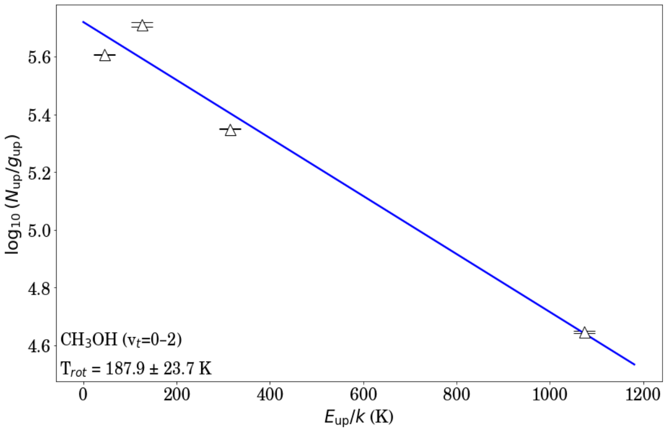

Fig.5. Rotational diagram of the observed CH_3OH transitions.

The uncertainties in the peak intensities, expressed as $\log_{10}(N_u/g_u)$ are indicated by triangles in the horizontal stripes of the data. The x-axis represents the upper-state energy E_{up}/k, expressed in Kelvin. A linear least-squares fit was applied to the data, yielding a rotational temperature of T_{rot} = 187.9 ± 23.7 K and a total column density of $N = 4.27 \times 10^{16}$ cm^{-2}. The uncertainty in the rotational temperature was derived directly from the standard error of the slope in the linear least-squares fit. Equation (2) demonstrates that the logarithm of the upper-level population normalized by its degeneracy, log (N_u/g_u), varies linearly with the upper-level energy E_u.

By plotting log (N_u/g_u) as a function of E_u/k_B, a linear fit can be applied to derive two key physical parameters: the rotational temperature from the slope and the total column density from the intercept.

$$log\left(\frac{N_u^{thin}}{g_u}\right) = -\left(\frac{loge}{T_{rot}}\right)\left(\frac{E_u}{k_B}\right) + log\left(\frac{N_{total}}{Q(T_{rot})}\right) \qquad (2)$$

In this approach, N_u/g_u is calculated from the observed line intensities using the rotational diagram method under the assumptions of local thermodynamic equilibrium (LTE) and optically thin emission. Accordingly, in the rotational diagram, the X-axis represents the upper-level energy E_u/k_B (in K), while the Y-axis corresponds to $\log(N_u/g_u)$, the logarithm of the column density per statistical weight [31].

4. Conclusion

High-angular-resolution ALMA observations of emission from highly excited molecular lines of CH_3OH, ^{34}SO and SO_2 toward the massive star-forming region G328.2551−0.5321 were carried out. The main results and conclusions are summarized below.

The 0.89 mm continuum peak of G328.2551−0.5321, together with surrounding Class I and II CH_3OH and OH masers, IRAS 15541–5349, EGO G328.25–0.53 and the massive core G328.2551−00.5321−MM1, reveals a complex, heterogeneous star-forming environment in which different tracers map distinct physical conditions and evolutionary stages around a central hub.

The moment-0 maps of molecular gas show that the molecular emission peaks are offset from the continuum peak. SO_2 and ^{34}SO are spatially extended across the envelope, whereas the CH_3OH emission is compact and centered on the continuum peak, indicating that methanol traces the densest and most compact region of the core.

The moment-1 maps of SO_2, CH_3OH and ^{34}SO reveal smooth and well-defined velocity gradients oriented from west (blue-shifted) to east (red-shifted) along PA = 98°, confirming the presence of an organized rotational motion within the core.

The position–velocity (PV) diagrams reveal a characteristic “butterfly”-shaped morphology, indicative of Keplerian rotation around a central massive source. Keplerian model fits yield dynamical masses of $M \approx 20.5\ M_\odot$ for CH_3OH and $M \approx 23.2\ M_\odot$ for SO_2, confirming the presence of a massive, rotating disk-like structure.

Rotational transitions of CH_3OH (v_t = 0–2) were detected toward G328.2551–0.5321. The rotational temperature is $T_{rot} = 187.9 \pm 23.7$ K and the total column density is $N = 4.27 \times 10^{16}$ cm^{-2}, indicating the presence of warm and dense gas characteristic of a hot molecular core.

These results demonstrate that G328.2551−0.5321 hosts a hot molecular core with a rotating disk, representing an active site of massive star formation.

Conflict of interest statement

The authors declare that they have no conflict of interest in relation to this research, whether financial, personal, authorship or otherwise, that could affect the research and its results presented in this paper.

CRediT author statement

Islyam Zh.B.: Conceptualization, Software, Writing - Original Draft; **Nodyarov A.S.:** Investigation, Formal analysis; **Demessinova A.M.:** Methodology, Validation; **Manapbayeva A.B.:** Visualization, Resources; **Kyzgarina M.T.:** Supervision, Writing - Review & Editing; **Zhumabay N.:** Data Curation, Software. The final manuscript was read and approved by all authors.

Funding

This research has been funded by the Science Committee of the Ministry of Science and Higher Education of the Republic of Kazakhstan (grant no. AP26102915)

Acknowledgements

This paper makes use of the following ALMA archival data: ADS/JAO.ALMA#2018.1.01679. S. ALMA is a partnership of ESO (representing its member states), NSF (USA), and NINS (Japan), together with NRC (Canada), MOST and ASIAA (Taiwan), and KASI (Republic of Korea), in cooperation with the Republic of Chile. The Joint ALMA Observatory is operated by ESO, AUI/NRAO, and NAOJ.

References

1 Nummelin A., Bergman P., Hjalmarson Å., Friberg P., Irvine,W. M., Millar T. J., Ohishi M., & Saito S. (2000) A three-position spectral line survey of Sagittarius B2 between 218 and 263 GHz. II. Data analysis. *The Astrophysical Journal Supplement Series*, *128*(1), 213–243. https://doi.org/10.1086/313376

2 Dunham M. K., Rosolowsky E., Evans N.J., II, Cyganowski C., & Urquhart J. S. (2011) The Red MSX Source survey: Ammonia and water maser analysis of massive star-forming regions. *The Astrophysical Journal*, *741*(2), 110–136. https://doi.org/*doi:10.1088/0004-637X/741/2/110*

.

3 Berdikhan D., Esimbek J., Henkel C., Zhou J., Tang X., Liu T., Wu G., Li D., He Y., Komesh T., Tursun K., Zhou D., Imanaly E., & Jandaolet Q. (2024) Ammonia observations of Planck cold cores. *Astronomy & Astrophysics*, *684*, A144. https://doi.org/10.1051/0004-6361/202348381

4 Sailanbek S., Esimbek J., Henkel C., Sobolev A. M., Ladeyschikov D. A., Berdikhan D., Wu G., Zhou J., Tang X., He Y., Li D., Tursun K., Zhou D., Ma Y., Komesh T., Ibraimov M., & Adilzhan K. (2025) Ammonia survey of the BGPS sources with the Nanshan 26-m telescope. *Monthly Notices of the Royal Astronomical Society*, *539*(4), 2987–3012. https://doi.org/10.1093/mnras/staf564

5 Imanaly E., Esimbek J., Baan W., Wu G., Zhou J., Li D., Tang X., He Y., Komesh T., Zhou D., Tursun K., Ma Y., Berdikhan D., Sobolev A. M., & Jandaolet Q. (2025) Formaldehyde in the Cygnus-X region. *Monthly Notices of the Royal Astronomical Society*, *542*(3), 2074–2086. https://doi.org/10.1093/mnras/staf1346

6 Komesh T., Esimbek J., Baan W., Zhou J., Li D., Wu G., He Y., Sailanbek S., Tang X., & Manapbayeva A. (2019) H_2CO and H110α observations toward the Aquila molecular cloud. *The Astrophysical Journal*, *874*(2), 172. https://doi.org/10.3847/1538-4357/ab0ae3

7 He Y.X., Henkel C., Zhou J. J., Esimbek J., Stutz A. M., Liu H. L., Ji W. G., Li D. L, Wu G., Tang X. D., Komesh T., & SailanbekS (2021) Extended HNCO, SiO, and HC_3N emission in 43 southern star-forming regions. *The Astrophysical Journal Supplement Series*, *253*(2), 44. https://doi.org/10.3847/1538-4365/abd0fb

8 Komesh T., Garay G., Henkel C., Omar A., Estalella R., Assembay Z., Li D., Guzmán A., Esimbek J., Huang J., He Y., Alimgazinova N., Kyzgarina M., Bekdaulet S., Zhumabay N., & Manapbayeva A. (2024) Infall motions in the hot core associated with the hypercompact H II region G345.0061+01.794 B. *The Astrophysical Journal*, *967*(1), 15. https://doi.org/10.48550/arXiv.2307.07459

9 Treviño-Morales S. P., Fuente A., Sánchez-Monge Á., Kainulainen J., Didelon P., Suri S., Schneider N., Ballesteros-Paredes J., Lee Y., Hennebelle P., Pilleri P., González-García M., Kramer C., García-Burillo S., Luna A., Goicoechea J., Tremblin P., Geen S. (2019) Dynamics of cluster-forming hub-filament systems: The case of the high-mass star-forming complex Monoceros R2. *Astronomy & Astrophysics*, *629*, A81. https://doi.org/10.1051/0004-6361/201935260

10 Zhang W., Zhou J., Esimbek J., Baan W., He Y., Tang X., Li D., Ji W., Wu G., Ma Y., Li J., Zhou D., Tursun K., & Komesh T. (2024) Kinematics and star formation of hub-filament systems in W49A. *Astronomy & Astrophysics*, *688*, A99. https://doi.org/10.1051/0004-6361/202348580

11 Ma Y., Zhou J., Esimbek J., Baan W., Li D., Tang X., He Y., Ji W., Zhou D., Wu G., Tursun K., & Komesh T. (2023). Gravitational collapse and accretion flows in the hub filament system G323.46-0.08. *Astronomy & Astrophysics*, *676*, A15. https://doi.org/10.1051/0004-6361/202346248

12 Li D., Henkel C., Kraus A., Tang X., Baan W., Esimbek J., Wang K., Wu G., Liu T., Sobolev A. M., Zhou J., He Y., & Komesh T. (2025) Evidence for core–core collision in Barnard 68. *The Astrophysical Journal*, *985*(2), 230. https://doi.org/10.3847/1538-4357/add326

13 Berdikhan D., Esimbek J., Henkel C., Zhou J., Tang X., Liu T., Wu G., Li D., He Y., Komesh T., Tursun K., Zhou D., Imanaly E., & Jandaolet Q. (2024) Ammonia observations of Planck cold cores. *Astronomy & Astrophysics*, *684*, A144. https://doi.org/10.1051/0004-6361/202348381

14 Abdullayev Z., Komesh T., Grossan B., Abdikamalov E., Maksut Z., Krugov M., Myrzakul S., & Tuiakbayeva D. (2025) Early-time optical spectral shape measurements of GRB 200925B. *Revista Mexicana de Astronomía y Astrofísica (Serie de Conferencias)*, *59*, 109–113. https://doi.org/10.22201/ia.14052059p.2025.59.20

15 Shimonishi T., Das A., Sakai N., Tanaka K. E. I., Aikawa Y., Onaka T., Watanabe Y., & Nishimura Y. (2020) Chemistry and physics of a low-metallicity hot core in the Large Magellanic Cloud. *The Astrophysical Journal*, *891*(2), 164. https://doi.org/10.3847/1538-4357/ab6e6b

16 Schuller F., Menten K. M., Contreras Y., Wyrowski F., Schilke P., Bronfman L., Henning T., Walmsley C. M., Beuther H., Bontemps S., Cesaroni R., Deharveng L., Garay G., Herpin F., Lefloch B., Linz H., Mardones D., Minier V., Molinari S., Motte F., Nyman L. Å., Reveret V., Risacher C., Russeil D., Schneider N., Testi L., Troost T., Vasyunina T., Wienen M., Zavagno A., KovacsA., Kreysa E., Siringo G., & Weiß A. (2009) ATLASGAL – The APEX Telescope Large Area Survey of the Galaxy at 870 µm. *Astronomy & Astrophysics*, *504*(2), 415–427. https://doi.org/10.1051/0004-6361/200811568

17 Csengeri T., Urquhart J. S., Schuller F., Motte F., Bontemps S., Wyrowski F., Menten K., Bronfman L., Beuther H., Henning T., Testi L., Zavagno A., & Walmsley M. (2014). The ATLASGAL survey: A complete sample of luminous clumps in the inner Galaxy. *Astronomy & Astrophysics*, *565*, A75. DOI:10.1051/0004-6361/201322434

18 Csengeri T., Bontemps S., Wyrowski F., Belloche A., Menten K. M., Leurini S., Beuther H., Bronfman L., Commerçon B., Chapillon E., Longmore S., Palau A., Tan J. C., & Urquhart J. S. (2018) ALMA survey of high-mass protostars revealed up to kilo-parsec scales (SPARKS). I. Indication for a centrifugal barrier in the environment of a single high-mass envelope. *Astronomy & Astrophysics*, *617*, A89. https://doi.org/10.1051/0004-6361/201832753

19 Csengeri T., Bontemps S., Wyrowski F., Megeath S. T., Motte F., Sanna A., Wienen M., & Menten K. M. (2017) The ATLASGAL survey: The sample of young massive cluster progenitors? *Astronomy & Astrophysics*, *601*, A60. https://doi.org/10.1051/0004-6361/201628254

20 Csengeri T., Belloche A., Bontemps S., Wyrowski F., Menten K. M., Bouscasse L. (2019) Search for high-mass protostars with ALMA revealed up to kilo-parsec scales. II. Complex organic molecules and heavy water in shocks around a young high-mass protostar. *Astronomy & Astrophysics*, *632*, A57. https://doi.org/10.1051/0004-6361/201935226

21 Assembay Zh., Komesh T., Garay G., Omar A., Esimbek J., Alimgazinova N., Kyzgarina M., & Murat Sh. (2022) ALMA observations of the environments of G301.1364-00.2249 A. *Proceedings of the Intern. Astronomical Union*, *18*(S380), 204–206. https://doi.org/10.1017/S1743921323002624

22 Komesh T., Omar A., Garay G., Assembay Z., Alimgazinova N., Zhumabay N., & Kyzgarina M. (2021) ALMA observations of the environments of G333.0162+00.7615. In T. Wong & W.-T. Kim, *Proceedings of the Intern.Astronomical Union*, 17, S362, 35–38. Cambridge University Press. https://doi.org/10.1017/S1743921323000121

23 McMullin J. P., Waters B., Schiebel D., Young W., & Golap K. (2007) *CASA architecture and applications. Astronomical Data Analysis Software and Systems XVI*, 376, 127. https://www.aspbooks.org/custom/publications/paper/

24 Caswell J. L., Fuller G. A., Green J. A., Avison A., Breen S. L., Brooks K. J., Burton M. G., Chrysostomou A., Cox J., Diamond P. J., Ellingsen S. P., Gray M. D., Hoare M. G., Masheder M. R. W., McClure-Griffiths N. M., Pestalozzi M. R., Phillips C. J., Quinn L., Thompson M. A., Voronkov M. A., Walsh A. J., Ward-Thompson D., Wong-McSweeney D., Yates J. A., & Cohen R. J. (2010) The 6-GHz methanol multibeam maser catalogue – I. Galactic Centre region, longitudes 345° to 6°. *Monthly Notices of the Royal Astronomical Society*, *404*(2), 1029–1060. https://doi.org/10.1111/j.1365-2966.2010.16339.x

25 McCarthy T., Ellingsen S., Breen S. L., Voronko M. A., Chen X. (2018). Detection of 84 GHz Class I methanol maser emission toward NGC 253. *The Astrophysical Journal Letters*, *867*(1), L4. https://doi.org/10.3847/2041-8213/aae82c

26 Csengeri T., Bontemps S., Wyrowski F., Megeath S. T., Motte F., Sanna A., Wienen M., & Menten K. M (2017) The ATLASGAL survey: The sample of young massive cluster progenitors? *Astronomy & Astrophysics*, *601*, A60. https://doi.org/10.1051/0004-6361/201628254

27 Cartavis. https://cartavis.org/ (accessed November 5, 2025).

28 Omar A., Abdirakhman A., Alimgazinova N., Kyzgarina M., Naurzbayeva A., Islyam Z., Turekhanova K., Demessinova A., & Manapbayeva A. (2025) ALMA observations of G333.6-0.2: Molecular and ionized gas environment. *Galaxies*, *13*(4), 73. https://doi.org/10.3390/galaxies13040073

29 Bosco F., Beuther H., Ahmadi A., Mottram J. C., Kuiper R., Linz H., Maud L., Winters J. M., Henning T., Feng S., Peters T., Semenov D., Klaassen P. D., Schilke P., Urquhart J. S., Beltrán M. T., Lumsden S. L., Leurini S., Moscadelli L., Cesaroni R., Sánchez-Monge Á., Palau A., Pudritz R., Wyrowski F., & Longmore S. (2019) Fragmentation, rotation, and outflows in the high-mass star-forming region IRAS 23033+5951: A case study of the IRAM NOEMA large program CORE. *Astronomy & Astrophysics*, *629*, A10. https://doi.org/10.1051/0004-6361/201935318

30 Csengeri T., Bontemps S., Wyrowski F., Belloche A., Menten K. M., Leurini S., Beuther H., Bronfman L., Commerçon B., Chapillon E., Longmore S., Palau A., Tan J. C., & Urquhart J. S. (2018) Search for high-mass protostars with ALMA revealed up to kilo-parsec scales I. Indication for a centrifugal barrier in the environment of a single high-mass envelope. *Astronomy & Astrophysics*, *617*, A89. https://doi.org/10.1051/0004-6361/201832753

31 Martín S., Martín-Pintado J., Blanco-Sánchez C., Rivilla V. M., Rodríguez-Franco A., & Rico-Villas F. (2019) Spectral line identification and modelling (SLIM) in the Madrid Data CUBe analysis package: Interactive software for data cube analysis. *Astronomy & Astrophysics*, *631*, A159. https://doi.org/10.1051/0004-6361/201936144

AUTHORS' INFORMATION

Islyam, Zh.B. — Master's student, Faculty of Physics and Technology, Al-Farabi Kazakh National University, Almaty, Kazakhstan; Scopus Author ID: 60077235000; https://orcid.org/0009-0006-5496-4501; islyamovzhomart@gmail.com

Nodyarov, A.S. – PhD, Senior Lecturer, Al-Farabi Kazakh National University, Almaty, 050040, Kazakhstan, Scopus Author ID: 57893764100; https://orcid.org/0000-0002-0045-5457; nodyarov.atilkhan@gmail.com.

Demessinova, A.M. — PhD, Senior lecturer, Faculty of Physics and Technology, Al Farabi Kazakh National University, Almaty, Kazakhstan; Scopus Author ID: 57211859262; https://orcid.org/0000-0001-5049-9338; aizat.dem@gmail.com

Manapbayeva, A.B. — Senior Researcher, Institute of Experimental and Theoretical Physics; Senior lecturer, Kazakh National Women's Teacher Training University, Almaty, Kazakhstan; Scopus Author ID: 57205165517; https://orcid.org/0000-0002-0322-1509; manapbayeva.arailym@gmail.com

Kyzgarina, M.T. — PhD, Senior lecturer, Faculty of Physics and Technology, Al Farabi Kazakh National University, Almaty, Kazakhstan; Scopus Author ID: 35146124400; https://orcid.org/0000-0002-4103-7657; meir83physics@gmail.com

Zhumabay, N — PhD student, Abai Kazakh National Pedagogical University, Almaty, Kazakhstan; Scopus Author ID: 58420497400; https://orcid.org/0009-0008-7100-008X; nurman-0906@mail.ru

.

EURASIAN PHYSICAL TECHNICAL JOURNAL

2026, Volume 23, No.1 (55)

https://doi.org/10.31489/2026N1/154-161

Received: 24/09/2025 Revised: 26/12/2025 Accepted: 19/03/2025

Original Research Article

UDC 535.215.5

IMPROVE THE PHOTOVOLTAIC PANELS BY ADVANCE COOLING USING DISTILLED WATER AND COPPER NANOPARTICLES

Sultan Khalid F.[1], Fadel Hiba S.[2], Jaddoa A.A.[1]*

[1] Electromechanical Engineering college, University of Technology, Iraq, Baghdad
[2] Al – Turath University, Iraq, Baghdad
**Corresponding author:* ameer.a.jaddoa@uotechnology.edu.iq

Abstract. *This study aimed to cool photovoltaic panels (monocrystalline and polycrystalline) using advanced cooling techniques with pure water and copper nanoparticles. The problem addressed by the current study is the high temperature in solar panels, and this problem is addressed by using one of the advanced cooling methods using nanomaterials. The high temperature harms the performance of photovoltaic panels, so cooling them is important until the high temperature leads to a decrease in their efficiency. Nanoparticles have been identified as one of the most effective methods in cooling photovoltaic panels because of their properties that can help improve the efficiency of photovoltaic panels. This study aimed to cool photovoltaic panels (monocrystalline and polycrystalline), and K – type thermometers were used to measure the side temperature. The back of each panel every half hour and the use of a Multi meter digital to measure current and voltage per half hour and a solar radiation meter to measure the intensity of solar radiation. In general, monocrystalline panels achieved better than polycrystalline panels and the best improvement of output power was when using Nano fluid at a concentration of 5%. The output power of monocrystalline and polycrystalline panels (76, 81, 85, 89W) (65.48, 70, 74.5, 76W) respectively when using distilled water and Nano fluid at a concentration of (1, 3, 5 %).*

Keywords: Photovoltaic, Thermal, Cooling, Nanoparticles, Concentration, Monocrystalline and Polycrystalline

1. Introduction

Burning fossil fuels saves 81 % of energy around the world, and the combustion of fossil fuels leads to changes in the weather, depletion of the weight layer and the emission of toxic gases that affect humanity [1]. Solar energy is an alternative to fossil fuels by generating electricity that can help reduce compared to alternative energy sources, fossil fuels have lower running costs and require less maintenance, contributing to global warming and other environmental concerns sources [2]. Photovoltaic panels are an important component of global power generation and are used in a wide range of household applications. Temperature is one of the factors most affecting the performance of photovoltaic panels [3], the performance of photovoltaic panels in factories is tested at a 25 ^{0}C temperature and solar radiation of 1000 W/m^2, which is called standard test conditions [4]. The production of solar panels changes dramatically when any change occurs in the surrounding environment [5] any increase in the temperature of the surrounding environment causes an increase in the temperature of the photovoltaic panel [6]. In addition, not all light falling on the photovoltaic panel turns into electricity [7]. A large part of the solar radiation is converted into heat that affects the performance of the panels, so they are cooled to improve their efficiency [8]. As a result, PV/T technology was developed to capture the extra heat produced by the cells in order to lower the temperature of the solar panel and increase overall energy conversion efficiency. Various fluids were utilized in the ducts on the back of the solar panels to circulate liquids and lower the temperature of the panels. or by sprinklers [9]. In the recent period, the use of nano liquids due to their heat transfer properties has increased significantly due to their thermal conductivity compared to other liquids [10]. It was used in many fields in electrical energy; photovoltaic energy has been proven effective in enhancing the photovoltaic/thermal system's efficiency in terms of testing nanoparticle concentrations, size, type, and basic fluids [11]. Adun et al. [12] used trinity nanofluids, a novel kind of liquid made up of three different kinds of nanoparticles combined with a base liquid. In water, the researchers introduced nano – Al_2O_3 – ZnO – Fe_3O_4. The greatest measured electrical efficiency was 13.75 %; the trinary PV/T system's PV panel temperature dropped by 8.81 ^{0}**C**. Govind S. Menon et al. [13] worked on evaluating hybrid photovoltaic system comprising tiny tubes mounted atop a solar panel and a plate on the back wall of the panel and cooling it using water and copper oxide nanofluids. The results showed that the average surface temperature of the board was 68.4 °C since the test was conducted during midday without cooling, which is the first case. At 12.98 %, the maximum electricity efficiency was attained. The cooling system was connected to the rear plate's wall. The second instance utilized water as the coolant, while the third case employed nano – fluid; all cases had the same operating parameters. The results showed that employing water and nanofluids increased the electricity efficiency to 14.58 % and 17.61 %, respectively. This study aimed to cool photovoltaic panels (mono crystalline and poly crystalline) through advance cooling using pure water and copper nanoparticles.

2. Methods of experimental work

2.1. Study location

Experimentation and evaluation of photovoltaic (PV) panels was conducted in Baghdad Al – Dora Governorate. The photovoltaic module (mono crystalline and polycrystalline) in this experiment was tilted at an angle of 30 south.

2.2. Experimental work setup

The experimental setup includes two photovoltaic panels (mono crystalline and poly –crystalline). The specifications of the panels are shown in Table 1. The purpose of using two panels is to compare the performance of the panels and to show which one is better in terms of performance. They are fixed on iron structures at an angle of 30^0. The panels were modified by adding copper tubes coated with nano – zirconia oxide with a grain size of 25nm.

Table 1. Specifications of the photovoltaic panel

	Polycrystalline, based PV module	Monocrystalline, based PV module
Maximum power	100 W	130 W
Open-circuit voltage	17 V	21.24 V
Short-circuit current	5.88 A	8.09 A
Voltage at maximum power	21.5 V	18 V
Current at maximum power	6.55 A	7.22 A
Standard test circumstances	1000 W/m^2, AM 1.5, 25 ^{0} C	1000 W/m^2, AM 1.5, 25 ^{0} C

The tubes are fixed on the back of the photovoltaic panels and measuring instruments the intensity of solar radiation using a type of energy meter (SM – 206). Measuring the ambient temperature by a temperature sensor type (DHT22) as well as measurement of current and voltage by means of a digital millimeter (SZ305) and measuring the cell temperature by a digital temperature sensor with a length of 1 meter Type (DS18B20).

2.3. Study location

To create the Nano fluid, an equivalent volume of 50 nm Cupper nanoparticles (Cu) was mixed together with clean water. To guarantee the dissociation of any aggregates, the mixes were separately guided and then further homogenized using sonication at 100 kHz and 300 W at 25 to 30 for two hours. To chill the fluids and stop overheating, the flasks were placed in an ice bath while being sonicated. Table 2 indicates the properties of nano fluids (Cu (50 nm) + DW).

Table 2. Properties of nanoparticles and distilled water

Basic fluid	ρ (kg \ m^3)	Cp (J \ kg. k)	K (W \ m. k)	β (*10^5 k^{-1})	α (*10^5) m^2/s
Distilled Water	997.1	4179	0.613	21	–
Nanoparticles Cupper (Cu)	8933	385	401	1.67	11.7

2.4 Thermo physical properties

2.4.1. Electrical Performance

The ratio of the highest electrical power of a PV module to the generation of solar radiation and module area. As shown in eq. (1) [15]:

$$\eta e = \frac{P}{A \times B} \tag{1}$$

$$P = I * V \tag{2}$$

2.4.2. Electrical performance (or PV module efficiency η_e)

The efficiency of converting sunlight into electricity, defined as the ratio of the maximum output power (P) to the product of solar radiation (B) in W/m² and the module area (A, in m²), is measured by the formula:

$$\eta \mathrm{e} = \frac{\mathrm{P}}{\mathrm{A} \times \mathrm{I}} ,$$

with *P* typically is representing *P* max = I mp × Vmp.

Factors Affecting Performance: The electrical output is heavily influenced by solar irradiance, ambient temperature, and cell temperature, which can significantly alter maximum power voltage.

Efficiency Range: Typical commercial PV module efficiency generally ranges from roughly 10% to over 20%, depending on the technology (mono crystalline vs. polycrystalline).

Performance Metrics: While efficiency is a measure of instantaneous conversion, performance ratio (PR) is often used to assess the overall quality of a PV plant, independent of location .

This performance index is crucial for evaluating how well a solar system converts sunlight into electricity under various environmental conditions.

2.5.3. Thermo physical properties of nanofluids

To determines the physical parameters of the nanofluids and compare the measured properties with Nanofluids. At the bulk average temperature of nanofluids, the fluid's dynamics and physical characteristics were approximated using the following equations [16 – 19]. The fraction's size (φ) can be used to calculate the nanofluid characteristics. Utilizing an Equation (3):

$$\varphi \% = \frac{\frac{W_{np}}{\rho_{np}}}{\frac{W_{np}}{\rho_{np}} + \frac{W_{bf}}{\rho_{bf}}} \times 100 \tag{3}$$

To calculate the density of Nanofluids, the following equation was used (4):

$$\rho_{\mathrm{nf}} = (1 - \varphi)\rho_{\mathrm{bf}} + \varphi\, \rho_{\mathrm{np}} \tag{4}$$

The specific heat capacity of Nanofluids was evaluated as follows:

$$C_P,nf = \frac{(1-\varphi)\rho_{bf}\,C_{bf} + \varphi\,\rho_{np}\,C_{np}}{p_{nf}} \tag{5}$$

To determine nanofluids' theoretical thermal conductivity, the following equation was used:

$$K_{nf} = k_{bf}\left[\frac{K_{np}+2K_{bf}+2\varphi\,(K_{np}-K_{bf})}{k_{np}+2K_{bf}-\varphi(K_{np}-K_{bf})}\right] \tag{6}$$

To determine nanofluids' theoretical thermal viscosity, the following equation was used:

$$\mu_{nf} = \frac{\mu_{bf}}{(1-\varphi)\ 2.5} \tag{7}$$

3. Results and discussion

3.1. Solar radiation and ambient temperature

Fig. 1 shows solar radiation per half hour on experimental days from 8:30 AM to 2:00 PM we notice that solar radiation increases from early morning until it reaches a peak in the middle of the day and decreases throughout the afternoon Fig. 2 shows the ambient temperature and the temperature begins to rise gradually until reaches its peak at 1:30 PM.

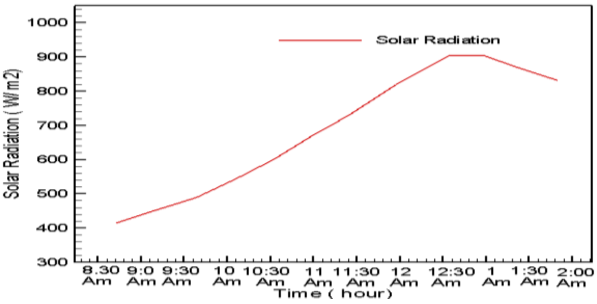

Fig.1. Solar radiation

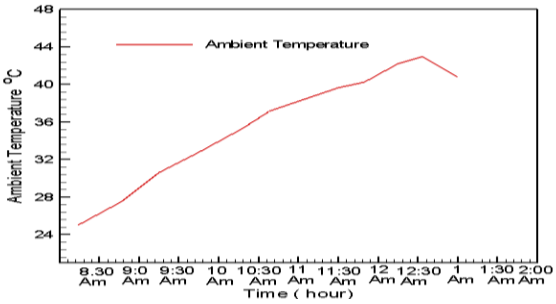

Fig.2. Ambient temperature

3.2. Effect of Nano fluidics of Temperature PV panel

The fig. 3 shows the temperatures of the cooled monocrystalline and polycrystalline photovoltaic panels. It is shown that when using Cu and water, the temperature of the panel decreases. At a concentration of 5 %, the minimum temperature is recorded, and at a concentration of 1 %, 3 % and distilled water.

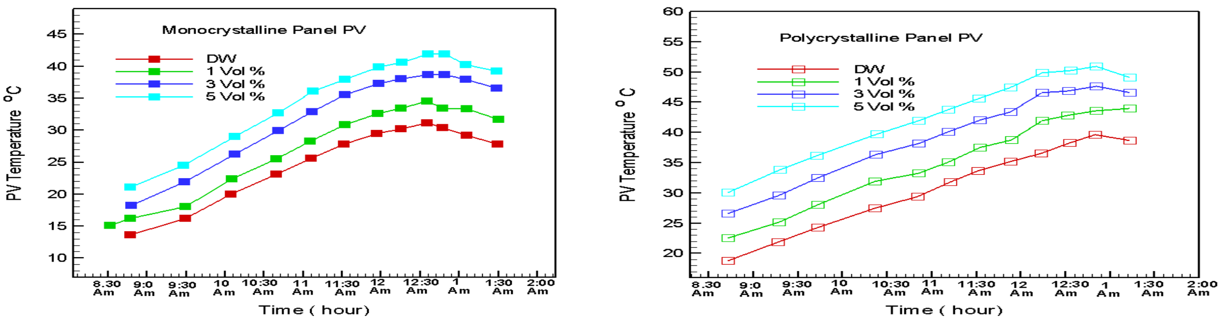

a) b)

Fig.3. Monocrystalline (a) and polycrystalline (b) panel PV surface Temperature with cooling at various Cu concentration values and distilled water

The reason for the decrease in temperature is that the addition of nanoparticles at different concentrations leads to heat transfer due to its high thermal conductivity.

3.3. Effect of Nano fluidics of Temperature PV panel

Photovoltaics consume about 20% of solar radiation and convert the rest into heat. Fig. 4 displays voltage over time when cooling using distilled water and Cu (50 nm) at three concentrations of monocrystalline and polycrystalline panels.

We notice a noticeable increase in voltage and it increases more and more than the increase in nanofluid concentrations and less Bima when using water distilled in cooling, decrease the voltages when by increasing temperature significantly and increase slightly with increasing solar radiation over time, and use of nanofluids in cooling led to lowering the temperature of the board and thus increasing the voltage.

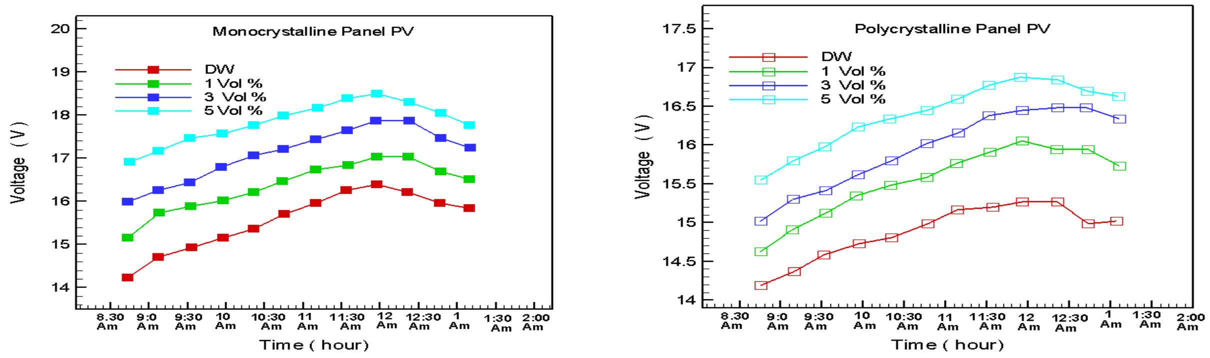

a) b)

Fig.4. a) monocrystalline and b) polycrystalline panel Variations of voltage with cooling at various Cu concentrations values and distilled water.

Fig.5 shows the electric current when cooling with distilled water and Cu (50 nm) at three concentrations of 1, 3, 5% mono crystalline and polycrystalline panels We note an increase in electric current for two reasons: 1 – Increasing solar radiation, which leads to the flow of more and more electrons; 2 – cooling using distilled water and Cu (50 nm) at three concentrations of 1, 3, 5 %.

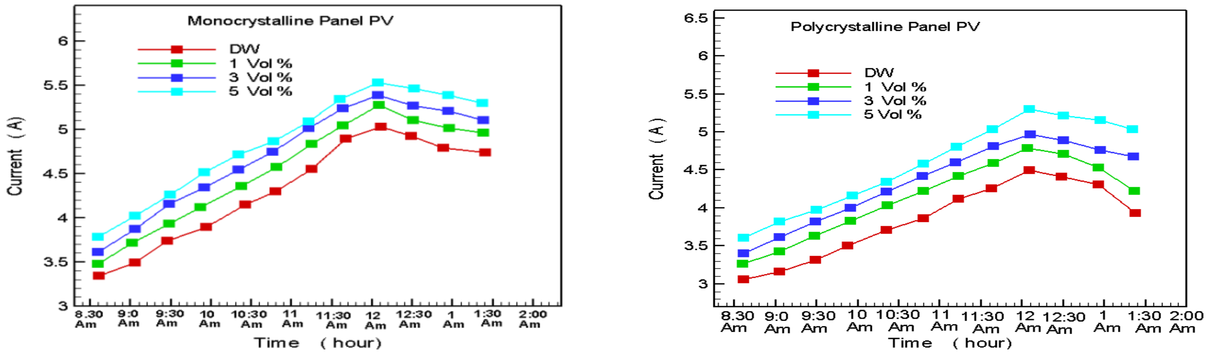

a) b)

Fig.5. monocrystalline and b) polycrystalline panel Variations of current with cooling at various Cu concentrations values and distilled water.

The fig. 6 displays the electrical power when using distilled water and Nano fluid Cu (50 nm) at three concentrations of 1, 3, 5 %. The electrical power also increases with the increase in solar radiation, where more and more electrons are emitted and more current and voltages are generated, in addition to that, the addition of nanofluids Cu (50nm) affects the productive capacity, as it increases with increasing concentration, as the highest value of the produced capacity was at a concentration of 5 % and the lowest value when using distilled water.

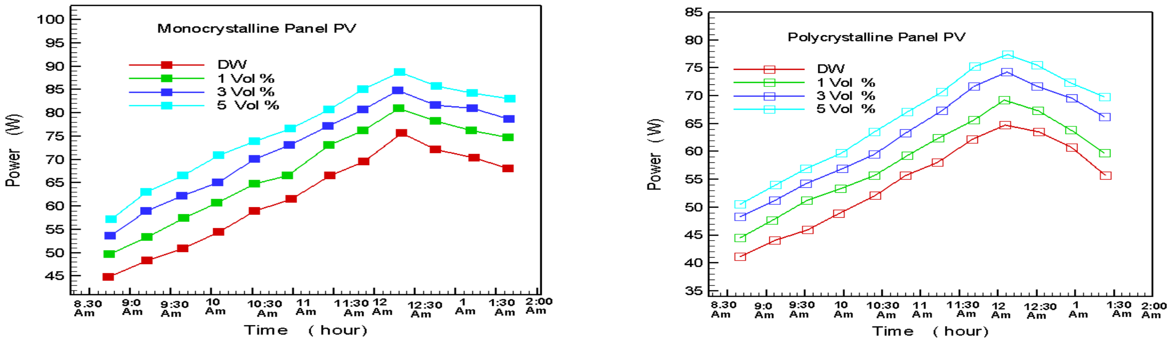

a) b)

Fig.6. Monocrystalline (a) and polycrystalline (b) panel electrical power with cooling (water and various values of Cu concentrations nano fluid as cooling fluid).

Fig. 7 shows the electrical efficiency when cooling with distilled water and nanofluid Cu (50nm) at three concentrations of 1, 3, 5 %

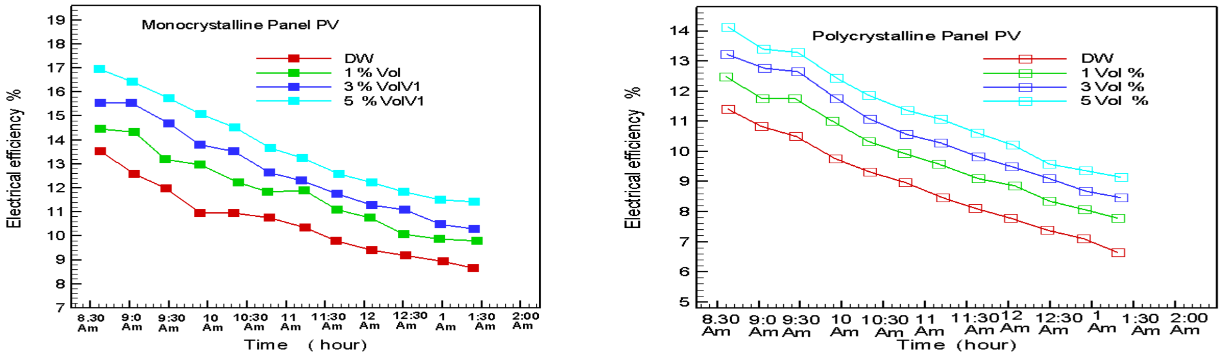

a) b)

Fig.7. Monocrystalline (a) and polycrystalline (b) panel electrical efficiency with cooling (water and various values of Cu concentrations nano fluid as cooling fluid).

The efficiency depends on solar radiation and the panels' temperature. We note that the efficiency values decrease over time as a result of increasing the temperature of the panel and that adding Cu (50 nm) leads to heat withdrawal and thus improves its efficiency.

4. Conclusions

1. The comparison showed that monocrystalline panels perform better than polycrystalline panels in all conditions.
2. Output power for mono crystalline panels was higher than that of polycrystalline panels due to cooling by Nano fluids and distilled water
3. The results showed the performance of nanofluids in cooling the photovoltaic panels, reducing their temperature and increasing the electrical efficiency of the three concentrations compared to distilled water due to their high thermal conductivity.
4. The comparison showed that the best performance was achieved during the cooling of photovoltaic panels using copper nanofluids at a concentration of 5 %.

Conflict of interest statement

The authors declare that they have no conflict of interest in relation to this research, whether financial, personal, authorship or otherwise, that could affect the research and its results presented in this paper.

CRediT author statement

Sultan Kh.F.: Writing – original draft, Investigation, Formal analysis, **Jaddoa A.A.:** Methodology, Formal analysis, Writing –review & editing, **Fadel H.S.:** Supervision, Funding acquisition, Conceptualization**.** The final manuscript was read and approved by all authors.

References

1 Raza M.Q., Nadarajah M., & Ekanayake C. (2016) On recent advances in PV output power forecast. *Solar Energy*, 136, 125–144. https://doi.org/10.1016/j.solener.2016.06.073

2 Murtadha T.K. (2023) Effect of using Al_2O_3/TiO_2 hybrid nanofluids on improving the photovoltaic performance. *Case Studies in Thermal Engineering*, 47, 103112. https://doi.org/10.1016/j.csite.2023.103112

3 Lamnatou C., Chemisana D. (2017) Photovoltaic/thermal (PVT) systems: A review with emphasis on environmental issues. *Renewable Energy*, 105, 270–287. https://doi.org/10.1016/j.renene.2016.12.009

2 Rathore N., Panwar N.L., Yettou F., & Gama A. (2021) A comprehensive review of different types of solar photovoltaic cells and their applications. *International Journal of Ambient Energy*, 42, 1200 – 1217. https://doi.org/10.1080/01430750.2019.1592774

4 Shaaban A.M.A., Mosa M.A., El-Samahy A.A., & Abed K.A. (2023) Enhancing the performance of photovoltaic panels by cooling: A review. *International Review of Automatic Control*, 16(1), 26–43. https://doi.org/10.15866/ireaco.v16i1.23181

5 Siecker J., Kusakana K., & Numbi B.P. (2017) A review of solar photovoltaic systems cooling technologies. *Renewable and Sustainable Energy Reviews*, 79, 192 – 203. https://doi.org/10.1016/j.rser.2017.05.053

6 Abdullah M. A. Shaaban, Adel A El-Samahy, Magdi Mosa, Kamal Ahmed Abed. (2024) Investigation of water-cooled photovoltaic driven reverse osmosis desalination system. *Journal of International Society for Science and Engineering*, 6(1), 1–6. https://doi.org/10.21608/jisse.2024.278089.1088

6 Kumar K., Chatterjee S., & Agrawal S. (2023) A comprehensive review of photovoltaic thermal (PVT) technology: Performance evaluation and contemporary development. *Energy Reports*, 10, 2655–2679. https://doi.org/10.1016/j.egyr.2023.09.043

7 Alktranee M., Shehab M.A., Németh Z., Bencs P., & Hernadi K. (2023) Effect of zirconium oxide nanofluid on the behaviour of photovoltaic–thermal system: An experimental study. *Energy Reports*, 9, 1265–1277. https://doi.org/10.1016/j.egyr.2022.12.065

8 Thong Le Ba, Ahmed Baqer, Mohammed Saad Kamel, Gyula Gróf, Vincent Otieno Odhiambo, Vincent Otieno Odhiambo, Somchai Wongwises, Lezsovits Ferenc and Imre Miklós Szilágyi.(2022). Experimental Study of Halloysite Nanofluids in Pool Boiling Heat Transfer. *Molecules*, *27*(3), 729. https://doi.org/10.3390/molecules27030729

9 Adun H., Adedeji M., Ruwa T., Senol M., Kavaz D., & Dagbasi M. (2022) Energy – exergy –economic – environmental (4E) approach to assessing the performance of a photovoltaic-thermal system using a novel ternary nanofluid. *Sustainable Energy Technologies and Assessments*, 50, 101804. DOI:10.1016/j.seta.2021.101804

10 Menon G.S., Murali S., Elias J., Delfiya D.S.A., Alfiya P.V., & Samuel M.P. (2022) Experimental investigations on unglazed photovoltaic-thermal (PVT) system using water and nanofluid cooling medium. *Renewable Energy*, 188, 986 – 996. https://doi.org/10.1016/j.renene.2022.02.080

11 Holman J.P. (2008) Heat Transfer (8th ed.). Available to: https://ia601501.us.archive.org/7/items/JackP.HolmanHeatTransferTenthEdition/%5BJack_P._Holman%5D_Heat_Transfer%2C_Tenth_Edition.pdf

12 Elminshawy, Nabil A.S. Elminshawy, Mohammad Faroug Addas, Mohamed Elghandour, (2019). Experimental investigation of a V-trough PV concentrator integrated with a buried water heat exchanger cooling system. *Solar Energy,* 193, 706–714. https://doi.org/10.1016/j.solener.2019.10.013

13 Chang M.H., Liu H.S., Tai C.Y. (2011) Preparation of copper oxide nanoparticles and its application in nanofluid. *Powder Technology,* 207(1-3), 378–386. https://doi.org/10.1016/j.powtec.2010.11.022

14 Yousefi, Tooraj,Veysi, Farzad, Shojaeizadeh, Ehsan, Zinadini, Sirus. (2011) An experimental investigation on the effect of Al_2O_3 – H_2O nanofluid on the efficiency of flat – plate solar collectors. Renewable Energy. https://ideas.repec.org/a/eee/renene/v39y2012i1p293-298.html

15 Sultan K.F., Ismail M.H., Anead H.S. (2024) Experimental Investigation of Evacuated Tubular Solar Collector Performance with (Cu/DW) Nano Fluid, *AIP Conference Proceedings*, 3092(1). https://doi.org/10.1063/5.0199706

16 Anead H.S., Sultan K.F., Khudhur A. (2023) An Experimental Assessment of The Thermal Performance of an Evacuated Tube Solar Collector by Using Cu Nanofluid, AIP Conference Proceedings, 2862(1). https://doi.org/10.1063/5.0172269

17 Jaddoa A.A., Sultan K.F., Jabal M.H. (2021) Energetic and Exergetic Assessment of Spiral Heat Exchanger Using Mineral and Oxide Mineral Oil Nanofluid. *International Journal of Heat and Technology*, 39, 2, 531 – 540. https://doi.org/10.18280/ijht.390223

18 Jaddoa A.A, Sultan K.F., Anead H.S. (2021) Energetic and exergetic assessment of the cooling efficiency of auto mobile radiator using mono and hybrid nanofluids. *International Journal of Heat and Technology*, 39(4), 1321-1327. https://doi.org/10.18280/ijht.390431

19 Sultan K.F., Jabal M.H., Jaddoa A.A. (2021) Performance assessment of the heat exchanger with and without a coating of hybrid nanoparticles the user cooling system in solar heating systems. *International Journal of Heat and Technology*, 39(5), 1460 – 1468. https://doi.org/10.18280/ijht.390507

AUTHORS' INFORMATION

Sultan, Khalid Faisal – PhD (Eng.), Professor, Electromechanical Engineering College, University of Technology, Baghdad, Iraq; Scopus Author ID: 572161335990; https://orcid.org/0000-0002-1986-0890

Fadel, Hiba Sami – Master (Eng.), Associate Professor, Electrical Techniques Engineering, AL - Turath University, Baghdad, Iraq; https://orcid.org/0009-0008-4084-3375

Jaddoa, Ameer Abed - PhD (Eng.), Professor, Electromechanical Engineering College, University of Technology, Baghdad, Iraq; Scopus Author ID: 57193803386; https://orcid.org/0000-0001-5158-1827